# Plasma spectroscopy

## for stationary and transient welding arcs containing metal-gas mixtures

Marina Kühn-Kauffeldt

UNIVERSITÄT DER BUNDESWEHR MÜNCHEN

Fakultät für Elektrotechnik und Informationstechnik

# Plasma spectroscopy for stationary and transient welding arcs containing metal-gas mixtures

Marina Kühn-Kauffeldt

Vollständiger Abdruck der von der Fakultät für Elektrotechnik und Informationstechnik der Universität der Bundeswehr München zur Erlangung des akademischen Grades eines

Doktor Ingenieur
(Dr.-Ing.)

genehmigte Dissertation.

| | |
|---|---|
| **1. Gutachter:** | Prof. Dr.-Ing. Jochen Schein<br>Universität der Bundeswehr München |
| **2. Gutachter:** | Prof. Gianluca Gregori Ph.D.<br>University of Oxford |
| **Vorsitzender des Promotionsausschusses:** | Prof. Dr. rer. nat. Mathias Richter<br>Universität der Bundeswehr München |

Die Dissertation wurde am 01.06.2015 bei der Universität der Bundeswehr München eingereicht und durch die Fakultät für Elektrotechnik und Informationstechnik am 05.11.2015 angenommen. Die mündliche Prüfung fand am 12.01.2016 statt.

# Danksagung

Eine Dissertation anzufertigen ist eine Einzelarbeit, jedoch kann mir sicherlich jeder Doktor bestätigen, dass dies nicht ohne eine starke Rückendeckung funktioniert. Deshalb möchte ich mich an dieser Stelle bei allen Menschen bedanken, die mich auf meinem langen Weg zum Dr. Ing. begleitet haben.

Der erste Dank gilt meinem Doktorvater, Professor Jochen Schein. Vielen Dank, Jochen, dass du mich als Doktorandin am Institut aufgenommen und mir die Freiheit gelassen hast mich in diversen Themengebieten des Instituts auszuprobieren, bis ich schlussendlich mein Dissertationsthema für mich entdeckt habe. Vielen Dank auch für die finanzielle Sicherheit, das angenehme Arbeitsumfeld, deine guten Ratschläge und die Zuversicht, dass es am Ende doch noch was wird!

Meinem Zweitgutachter, Professor Gianluca Gregori, danke ich für die Zeit, die er sich für das gründliche Lesen der Arbeit und den Prüfungstag selbst genommen hat. Ein herzlicher Dank gilt dem Vorsitzenden der Prüfungskommission, Professor Mathias Richter, der mich hervorragend durch alle Formalien der letzten Promotionsphase begleitet und mir auch so manch einen ausgefallenen Prüfungswunsch erfüllen konnte.

Ich danke auch einem brillanten Physiker und guten Kollegen José-Luis Marquès-López. Bereits im Studium hast du, José, meine Neugierde zur Plasmaphysik geweckt. Danke, dass du dir stets die Zeit genommen hast, mich mit exzellenten Erklärungen für kompliziertesten Sachverhalte zu begeistern. Ohne dein Wissen und deine aufmunternden Worte gewürzt mit einer guten Prise Humor wäre ich sicherlich nicht so weit in diverse Theorien vorgedrungen!

Ungemein schwieriger wäre mein Weg gewesen, hätte ich nicht auf die Erfahrungen der wissenschaftlichen Community zurückgreifen können. Vielen Dank an alle, die bereitwillig mit mir über die experimentellen Schwierigkeiten diskutiert und ihr Wissen geteilt haben. Insbesondere danke ich Professor Uwe Czarnetzki (Institut für Experimentalphysik V, RUB, Bochum), Dr. Antonio De Lorenzi und Dr. Roberto Pasqualotto (Consortio RFX, Padua, Italien) sowie Dr. Bernd Kurzan (IPP Max-Plank-Institut für Plasmaphysik, Garching) für ihre Ratschläge und Unterstützung. Herzlichen Dank an Dr.-Ing. Tobias Sander (Institut für Thermodynamik, UniBw München) für die Leihgabe der ICCD-Kamera, ohne die die Messungen am MSG Prozess nicht möglich gewesen wären!

Nicht möglich wäre die Durchführung der Experimente ohne das Werkstattteam mit dem charismatischen Werkstattmeister Ulrich Bayerle, das keines meiner Konstruktionswünsche unerfüllt lies. Vielen Dank euch Alexander Mai, Hermann Karl, Martin Goretzki, Günther Haderer und Walter Wagner für eure tatkräftige Unterstützung und hervorragende Arbeit.

Mit einer Hand lässt sich kein Knoten knüpfen und auch nicht erfolgreich forschen. Ich danke daher an dieser Stelle dem hervorragenden Kollegium des LPT, dessen Teil ich in den letzten Jahren sein durfte. Insbesondere danke ich Günter Forster für seine gemütliche Art und die großartige Starthilfe in Sache Thomsonstreuung und Sebastian Lange für die Fachsimpeleien über die Tücken der Lasermesstechnik. Danke, Stephan Zimmermann aka Zimbo, für deine "unermüdliche Überzeugungsarbeit" mir die Promotion hier am Institut schmackhaft zu machen und die stete tatkräftige Unterstützung bei allen experimentellen

Vorhaben und täglichen Laborproblemen. Ein großes Dankeschön gilt auch Jochen Zierhut für genial einfache Lösungen der Alltagslaborprobleme, Karsten Harz-Behrend für seinen mathematisch präzisen Blick in jeglichen Situationen und Professor Klaus Landes für das stets offene Ohr und seine Neugierde. Meinem Vakuumlabor-"Mitbewohner", Mathias Pietzka, danke ich für die unzähligen physikalischen Diskurse und natürlich für das exzellente Vakuum ;). Carmen und Stefan Kirner, Benjamin Bachmann, Erwan Siewert, Michal Szulc, Stefan Eichler und Silva Schein danke ich für die hilfreichen Diskussionen, tatkräftige Unterstützung in experimentellen Vorhaben auch über meine Promotionsarbeit hinaus und nicht zuletzt für die reibungslose Zusammenarbeit. Auch den Kollegen Alexander Atzberger, Matthias Bredack und Jörg Schaup, die ich erst zum Ende meiner Promotion kennenlernen durfte, sowie Dagmar Bergel und Cornelia Budach danke ich für eine tolle Arbeitsatmosphäre.

Was wäre ein Leben ohne Freunde? Da würde auch keine Dissertation nebenbei entstehen! Herzlicher Dank gilt meiner Capoeira Familie, den verrückten Impro-Elchen, dem VDEkistan Klan und nicht zuletzt meiner guten alten Düsseldorfer Connenction. Danke, dass ihr in all den Jahren für mich da wart, mich abgelenkt und aufgemuntert habt, wenn ich mal wieder im Motivationsloch gelandet bin!

Frei nach dem Motto das Beste kommt zum Schluss, möchte ich mich auch an dieser Stelle bei meiner Familie bedanken. Danke Mama, dass du nicht aufgegeben hast, als ich anfangs lieber rückwärts gelesen hab, mir etliche Male beharrlich das Bohrsche Atommodel am Küchentisch erklärt hast, den wahnsinnig wichtigen Schritt gewagt hast mich nach Deutschland zu bringen und mich in allen meinen Vorhaben unterstützt hast! Danke dir Thomas, dass du alles dafür getan hast, dass ich dieses Land mein Zuhause nenne kann und nicht zur guter Letzt dafür, dass du mir die Studienbroschüre der UniBW "untergejubelt" hast!

Was bleibt noch zu sagen?! Danke Marvin, dass du diese nicht immer einfache Zeit mit mir durchgestanden hast und dabei eine großartige Evolution durchgemacht hast – erst Student, dann Ehemann und jetzt auch noch Kollege!

**Abstract**

Shielded gas arc welding is an indispensable technology for joining all kinds of metals. In order to guarantee, that those processes fulfill high requirements for modern industrial applications, they take advantage of e.g. specific gas compositions or transient current phenomena for production of reliable welding joints. However, for a stable and safe process operation a profound understanding of the physics taking place in the arc plasma is needed. The level of knowledge for basic welding processes in stationary operating conditions has advanced in the past years. Yet, there is still a high demand for diagnostic techniques, which are able to resolve transient phenomena and measure parameters of plasmas containing gas mixtures or metal vapor.

In this work two plasma spectroscopy techniques, Thomson scattering and Stark broadening, have been applied for the investigation of plasma parameters in stationary as well as transient welding processes operated with different shielding gas mixtures and in the presence of metal vapor.

Thomson scattering uses scattering of the laser radiation by the free electrons in a plasma to provide information about their electron temperature and density. At first, it has been set up for the investigation of stationary gas tungsten arc welding (GTAW) processes with inert and molecular shielding gas mixtures. Thereafter, this technique has been extended for application to pulsed gas metal arc welding (GMAW) processes operated with aluminum and iron wire electrodes. It has been demonstrated, that this technique can be applied to transient GMAW processes in the presence of metal vapor. It has yielded spatially and temporally resolved electron density and temperature profiles without previous knowledge of plasma composition, the arc column shape and without the assumption of local thermal equilibrium (LTE). The measurement data could be additionally used for spatially and temporally resolved plasma composition estimation.

Stark broadening is a passive spectroscopic technique, which relates the width of resonance lines emitted by the plasma to the free electron temperature and density. The emission spectra of stationary GTAW processes operated with pure argon and with argon-helium gas mixture as well as the pulsed GMAW processes operated with aluminum as the wire electrode have been investigated by means of this technique. It has been successfully applied for the spatially and temporally resolved electron density determination without assumption of LTE. Temperature values have been additionally estimated, when LTE assumptions were taken into account.

The comparison of Thomson scattering and Stark broadening techniques has shown, that both methods deliver comparable results for electron density within the experimental error of the respective methods. Good agreement with the experimental results available in the literature could be also found for both techniques at least for the stationary processes, since not much data for transient processes exist.

**Zusammenfassung**

Schutzgasschweißen ist eins der wichtigsten Fügeverfahren. Um den hohen Anforderungen der modernen industriellen Anwendungen nachzukommen, werden hier z.B. spezielle Gasgemische oder transiente Effekte eingesetzt um verlässliche Schweißnähte zu erzielen. Für einen zuverlässigen Betrieb der Schweißlichtbögen, bedarf es jedoch eines tiefen Verständnisses der physikalischen Prozesse im Bogenplasma. In den letzten Jahren konnten bereits viele Erkenntnisse über die grundlegenden Vorgänge in den stationären Schweißprozessen gewonnen werden. Jedoch gibt es nach wie vor einen hohen Bedarf an Messverfahren, die Erkenntnisse über den Plasmazustand in transienten Prozessen, die Gasgemische oder Metalldampf beinhalten, liefern.

In dieser Arbeit wurden zwei plasmaspektroskopische Messverwahren, Thomson-Streuung und Stark Verbreiterung, zur Untersuchung von Plasmaparametern in stationären und transienten Schweißprozessen angewendet. Die Prozesse wurden sowohl mit unterschiedlichen Schutzgasgemischen als auch in der Metall-Schutzgas Atmosphäre betrieben.

Bei der Thomson-Streuung liefert die Streuung der Laserstrahlung an den freien Plasmaelektronen Information über die Elektronentemperatur und -dichte. Zunächst wurde dieses Verfahren auf stationäre Wolfram-Inertgas Schweißprozesse (WIG), die mit unterschiedlichen Gasgemischen betreiben wurden, angewendet. Anschließend wurde das Messverfahren auf die gepulste Metall-Schutzgas Schweißprozesse (MSG) mit Aluminium und Eisen Drahtelektroden ausgeweitet. Es wurde gezeigt, dass die Thomsons-Streuung für transienten MSG Prozesse, in denen Metalldampf entsteht, angewendet werden kann. Mit Hilfe der Streuspektren konnten örtlich und zeitlich aufgelöste Elektronentemperatur und -dichte Profile unabhängig von der Plasmazusammensetzung und ohne der Annahme des lokalen thermischen Gleichgewichts (LTG) gemessen werden. Die Messdaten konnten außerdem zu orts- und zeit-aufgelösten Rekonstruktion der Plasmazusammensetzung genutzt werden.

Stark Verbreiterung ist eine passive spektroskopische Methode, mit dessen Hilfe aus der Breite der Spektrallinien des Plasma-Emissionsspektrums die Elektronentemperatur und ?dichte bestimmt werden kann. Emissionsspektren sowohl der stationären WIG Prozesse unter Einsatz von Argon bzw. Argon-Helium als auch der gepulsten MSG Prozesse mit Aluminium wurden mit Hilfe von dieser Methode untersucht. Auf diese Weise konnte die Elektronendichte ohne die Annahme von LTG zeitlich und örtlich aufgelöst bestimmt werden. Elektronentemperatur konnte zusätzlich unter der Berücksichtigung der LTG Annahmen abgeschätzt werden.

De Vergleich der beiden Verfahren hat gezeigt, dass die Ergebnisse für die Elektronendichte im Rahmen der experimentellen Genauigkeit übereinstimmen. Diese Ergebnisse entsprechen ebenfalls den in der Literatur verfügbaren Werten für stationäre und transiente Schweißprozesse, soweit überhaupt Vergleichbare Messungen bereits veröffentlicht wurden.

# Contents

# Chapter 1

# Introduction

> *"In general we look for a new law by the following process. First we guess it. Then we compute the consequences of the guess to see what would be implied, if this law that we guessed is right. Then we compare the result of the computation to nature, with experiment or experience, compare it directly with observation, to see if it works. If it disagrees with experiment, it is wrong. In that simple statement is the key to science. It does not make any difference how beautiful your guess is. It does not make any difference how smart you are, who made the guess, or what his name is – if it disagrees with experiment, it is wrong."*
>
> Richard Feynman

Observation of nature is the key to all the knowledge that has been achieved by mankind. Without being able to sense nature we would not be able to describe and understand the world surrounding us. Our curiosity would never be aroused and all the inventions that seem so natural today, would simply not exist. No fire, no wheels, no electricity – no modern world that we live in.

It is the curiosity of Sir Humphry Davy, that we owe the first observation of an artificially generated electric arc. He first discovered it in 1800, while carrying out galvanic experiments with charcoals and a voltaic pile [1]. 87 years later, the first welding apparatus was patented by Benardos and Olszewski [2]. After its invention, electric arc welding has quickly become an indispensable tool for joining all kinds of metals. Nowadays welding processes are far more sophisticated. They take advantage of e.g. specific gas compositions or transient current phenomena in order to guarantee optimal conditions for the production of reliable welding joints for all kinds of metals. But for present, the modern welding processes have to fulfill higher requirements. Automation and operational safety have become essential features in industrial applications.

These high requirements cannot be fulfilled without a profound understanding of the physical principles behind the welding process. The plasma, being one of the key elements of this process, is its boon and bane. It provides the heat necessary for the melting and joining of materials, yet it makes the process description complicated. Although the understanding of basic welding processes in stationary operating conditions has advanced in the past years, many transient phenomena and effects involving mixing and the reaction of several chemical components still remain an open question.

Unlike today the observation, or in other words, experimental diagnostic methods, which once helped discover the electric arc, still remains an indispensable tool for unraveling the details of phenomena taking place in a welding plasma. Various techniques have been developed for the investigation of different aspects of the processes, allowing the characterization of temperature, density, velocity, composition and other properties of the

plasma. Still, up to now the most experimental works were focused on the investigation of stationary processes.

Consequently, there is still a high demand for diagnostic techniques, which are able to resolve transient phenomena and deliver parameters of plasmas containing different atomic species. When choosing a diagnostic method, it is mandatory to consider: the lesser assumptions are required to interpret the observation, the more reliable is the resulting information about the process.

Thomson scattering and Stark broadening are both techniques that can be adapted to measure spatially and temporally resolved plasma parameters. In contrast to other commonly applied methods, they do not depend on the plasma composition and do not require local thermal equilibrium assumption. Hence, both diagnostic concepts can be used to develop reliable and fast measurement systems, which are able to provide information about transient multi-element plasmas.

Since the computational capacity has considerably advanced in recent years, simulation has become a common approach for easier and faster prediction of the behavior of welding processes. But it has to be kept in mind that numerical calculations cannot replace experimental investigations until the unavoidable simplifications contained in every numerical model have been proved to be consistent with the experiment. This is especially the case for transient welding phenomena.

Before the focus of this work can be formulated, the overview of the two welding processes investigated in this work together with their conditions and requirements needs to be given. The following presentation of the processes also includes the review of diagnostic techniques, which are currently being applied for the investigation of welding plasmas.

## 1.1 Shielded gas arc welding processes

Generally speaking, welding describes the joining of materials by introducing an external energy source which transforms the material into plastic or liquid condition. An additional filler material with the same thermal properties as the workpiece might be used to fill the gap between the two workpieces to be joined [3].

The shielded gas arc welding belongs to the category of fusion welding processes. Here, an electric arc is ignited between a rode-like electrode and the workpiece by ionizing the shielding gas atmosphere which protects the workpiece from oxidation. The heat produced by the arc is transferred to the workpiece. This results in local fusing of the workpiece. Thus a weld pool is created which allows to join the two pieces of material.

The properties of the arc strongly influence the feasibility and the quality of the welding joint. The electric properties of the arc are described by the current voltage (I-U) characteristic. It mainly depends on the work function of the electrode materials, the arc column composition and the arc length [4]. Yet the capability of the arc to transport the heat from the electrode to the workpiece is only determined by the arc column composition. It consists of a mixture of the shielding gas and the metal vapor originating from the weld pool or the electrode. The gaseous components are at least partially ionized and hence are in the state of plasma. The properties of this plasma will be discussed in section 2.1.

The choice of the shielding gas is one of the key factors which influence the welding result. In general inert (e.g. Ar) or reactive (e.g. $CO_2$) shielding gases can be used depending on the workpiece materials. The main requirement is that the gas is not soluble in the weld pool in order to prevent pores or unwanted reactions inside the welding seam [5].

Besides the workpiece itself and the appropriate shielding gas a power supply, which is able to produce suitable arc voltage characteristics, is required in order to operate a welding process. For automation purposes it should be possible to regulate the output of the power supply in a feedback control loop [3]. There exists a variety of different designs, however nowadays the so called inverter power supply type is preferred. It uses

semiconductor rectifiers, which convert the incoming low frequency three-phase current to a high frequency AC signal. Therefore, small size transformers are sufficient in order to transform this input from high voltage and low current to high current and low voltage signal. Such power supplies are relatively small and hence transportable. Their output characteristic can be adapted for many operation modes such as direct current (DC) and alternating current (AC) while maintaining high efficiency [6].

For a specific welding process nominal values for arc current and voltage have to be defined by the user. In order to maintain stable operation conditions the power supply is provided with a feedback control, which regulates the output current according to the variation of the arc resistance [5]. However, the choice of suitable input current and voltage for a stable welding process requires profound knowledge of the material properties and arc characteristics. In order to facilitate the welding operation, typical characteristics data for different metals, electrodes, shielding gases and operation modes are stored in the control unit of the power supply [6].

### 1.1.1 Gas tungsten arc welding

The gas tungsten arc welding (GTAW) can be applied to join a wide range of metals. High quality welding joins can be reached for thin and tick materials. The technical drawback of the process is its relatively slow welding velocity in comparison to other techniques [3, 5].

The main feature of GTAW is the non-melting tungsten electrode, which is typically used as a cathode. As schematically shown in fig. 1.1 the arc is ignited between the tungsten cathode and the anodic workpiece. The main purpose of the arc is to provide a heat source which melts the workpiece. Since no material is transported through the arc itself,

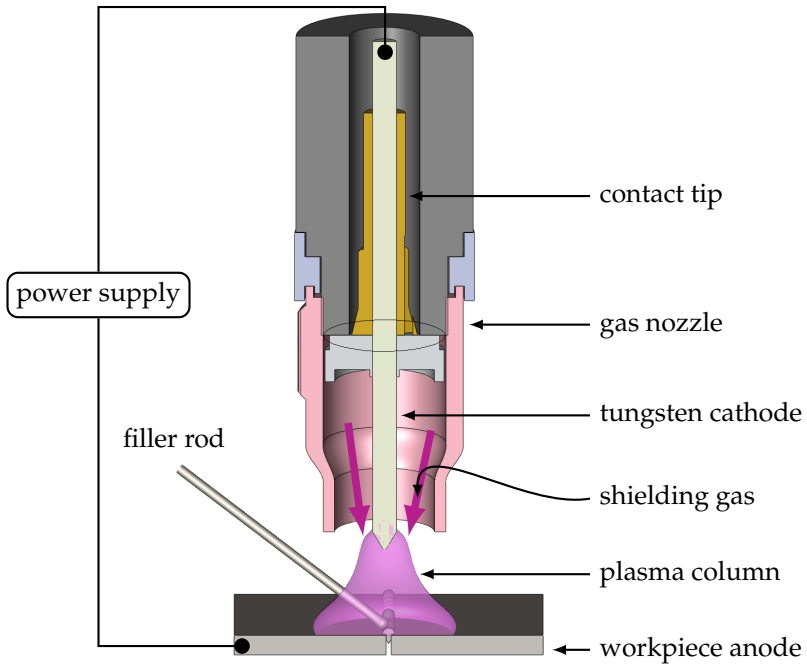


Figure 1.1: Schematic of a GTAW process.

the arc column composition mainly depends on the choice of the shielding gas. Metal vapor origin from the weld pool may entrain in the lower part of the arc column close to the workpiece surface. If required, an additional filler rod is inserted close to the workpiece in order to provide additional material for the welding joint.

The upper electrode is placed in a shroud - a gas nozzle providing the shielding gas atmosphere. Here only inert gases like argon and helium or gas mixtures of inert gases with low percentage of hydrogen or nitrogen are used to prevent the oxidation of the hot electrode tip. In order to decrease the work function of tungsten electrode and hence to increase the current density $1$ to $2\,\%$ rare-earth oxides (typically $ThO_2$, $ZrO_2$ or $LaO_2$) are added to the tungsten cathode. The shape of the electrode plays an important role since it determines the stability of the arc and so the quality of the resulting weld seam. Typically, a cone shape electrode is used. The angle of the cone is adjusted according to the magnitude of the current [5].

The GTAW processes are mostly operated with DC currents. In some cases pulsed current is used to achieve higher arc energy density or better control of the weld pool. For metals like aluminum or magnesium, which easily oxidize, AC currents are used in order to clean the surface from the previously formed oxide layer [6].

The parameters determining the GTAW process are the arc current, the shielding gas composition and flow rate, the distance of the electrodes and the welding speed. Typical currents range between $100$ and $400\,\mathrm{A}$ depending on the thermal properties and the thickness of the workpiece. If the welding torch position is fixed, the electrode distance remains constant during the process. Typical arc length values lie in the range of $1.5$ to $4\,\mathrm{mm}$ [3]. The arc is ignited using a high frequency or high voltage pulse in order to ionize the gas. After establishing the ionization channel the current is fixed and the arc voltage adapts to the existing conditions. The typical arc voltages are in the order of magnitude of $10\,\mathrm{V}$ [4].

### 1.1.2 Gas metal arc welding

Gas metal arc welding (GMAW) is one of the most wide spread arc welding processes [6]. It can be applied to a wide range of materials and is more cost-efficient than the GTAW process, without achieving the latter's quality of welding joint [3, 7].

Figure 1.2 shows a schematic setup of a GMAW process. In contrast to GTAW the arc burns between a melting wire electrode and the workpiece. The arc is ignited by producing a short circuit between the wire and the workpiece. Due to the Joule heating the electrode melts and evaporates, so that an arc can be formed [5]. As shown in fig. 1.2 the wire electrode is typically used as an anode while the workpiece poled as a cathode. The wire is contacted using a contact tip. It is as well shielded by a gas flow. As the wire electrode melts, no additional filler material is needed. The wire however has to be constantly fed into the arc by a wire feed driver.

GMAW processes can be operated in a DC, AC or in a pulsed mode depending on the type of the welding material. For example, for aluminum pulsed currents are used.

The main difference between the GTAW and GMAW processes is, that in the GMAW arc metal droplets are transferred from the electrode tip to the weld pool which has a significant influence on the arc column properties and the overall performance of the process. The distance between the wire electrode and the workpiece is not necessarily constant and should be adjusted by a control mechanism. Consequently, the arc characteristic not only depends on the current and the shielding gas. The wire diameter and the feed rate, which influence the distance between the electrodes, the amount of metal vapor present in the arc and the type of metal transfer also determine the characteristic of the arc. Depending on the resulting I-U working points different arc modes are possible. Figure 1.3 shows an example of GMAW of possible classification of different arc modes.

If the arc is operated in the DC mode, different arc types can be classified by the type of metal transfer in the arc, such as dip, globular or spray transfer, and the arc length

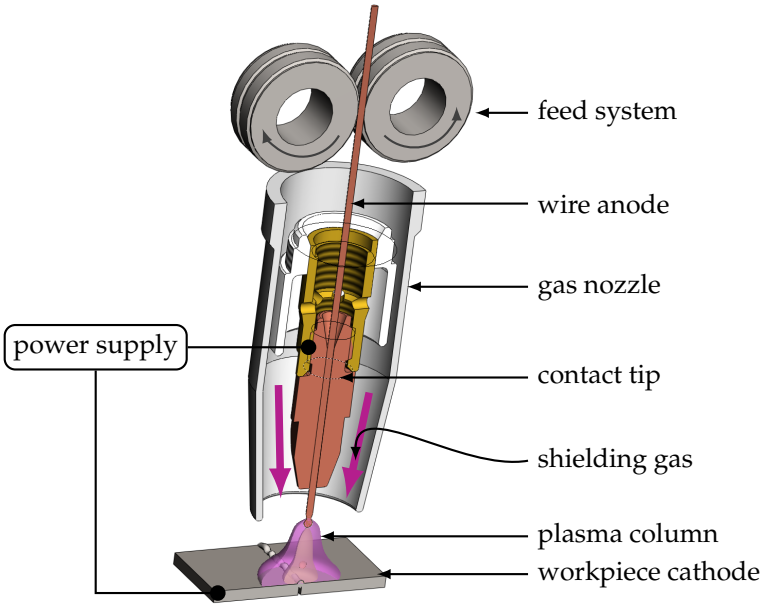


Figure 1.2: Schematic of a GMAW process.

(short or long) [3, 6]. Depending on the arc mode a short circuit may occur. Those modes are assigned to a narrow current and voltage range and are preferably used for specific welding conditions. For example, short arcs are typically applied for joining thin plates and spray arcs are used for welding of thick materials.

#### 1.1.2.1 Pulsed arc

When superposing low DC background current with high current pulses, the pulsed arc mode is obtained. As shown in fig. 1.3 it can cover a wide range of welding parameters. This arc mode is very stable and free of short circuits. It can be adjusted to produce one droplet per pulse. This type of arc can be applied to many materials like steel and aluminum.

Figure 1.4 shows a typical droplet transfer to the workpiece. In the low current phase (approx. $25$ to $80\,\mathrm{A}$) the wire electrode is heated and partially melted. However, no droplet is detached during this phase. During the high current phase the wire tip is further molten. On the downslope of the pulse the pinch effect forces the detachment of a droplet. The magnitude of the current in this phase depends on the feed rate and wire diameter. Depending on the material used the shape and the duration of the pulse can be additionally adjusted. The process can be operated with frequencies in the range of $25$ to $300\,\mathrm{Hz}$ [3, 9].

## 1.2 State of the art of diagnostics in welding processes

In terms of diagnostic objects one can divide the components of the welding process in two categories – the gaseous and liquid or solid targets. The latter implies electrodes and workpiece eventually including metal droplets detaching from a consumable electrode.

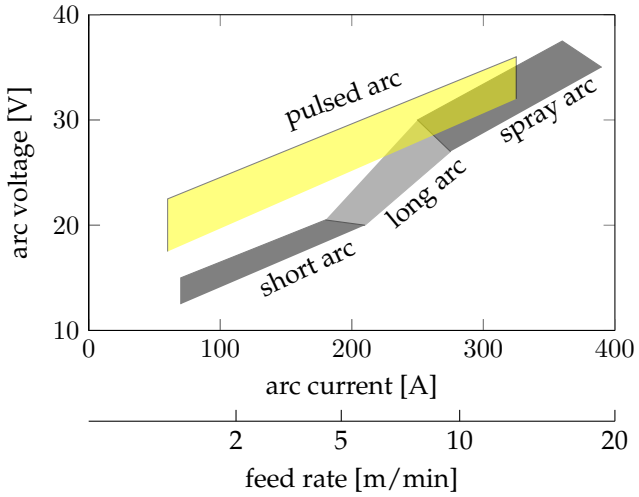


Figure 1.3: Example of a characteristic of the GMAW process operated with an iron alloy wire in a $Ar/CO_2$ atmosphere with a classification of different arc regimes depending on the arc current, voltage and the wire feed rate [adapted from 7].

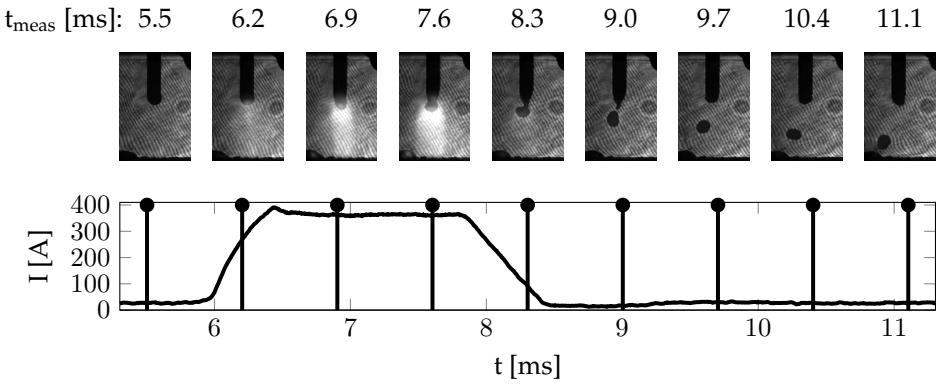


Figure 1.4: Shadowgraphy images of droplet transfer (top) during a high current pulse (bottom) in a pulsed arc operated with pure argon and Ge3Si1 iron wire [The shadwography images are taken from 8]

The solid or liquid components of the welding process are typically analyzed using non-invasive camera techniques. For example, electrode and droplet shape can be investigated using shadowgraph techniques [10–13], the weld pool and droplet temperature and viscosity by pyrometric methods [13–15]. In addition invasive methods such as thermocouples or calorimetry are applied to determine the weld pool temperature [14, 16]. The properties of the welding joint are typically investigated using metallography techniques [9].

The gaseous part of the welding process mainly consists of the arc plasma including the shielding gas flow. The flow can be visualized using particle image velocimetry or Schlieren technique[17]. The measurement of dynamic pressure provides the information about the arc column force and flow velocity on the workpiece surface [18].

Besides the monitoring of arc current and voltage, the arc itself is mainly characterized by its composition, temperature and density of the plasma column. To measure these parameters mainly three different types of diagnostics – electric probes, emission spec-

troscopy and laser assisted methods – are applied.

As electric probes typically Langmuir probes are used to measure the electron temperature, density and plasma potential in free burning arcs [19–21]. However, since this measurement method is invasive, special care has to be taken in order to protect the probe surface from melting. Moreover, in case the probe is inserted into the arc, it might mechanically or electrically disturb the process conditions.

Laser assisted techniques and emission spectroscopy methods are much more common as diagnostic tools for free burning arcs, which are discussed in the following.

### 1.2.1 Laser scattering diagnostics

Techniques based on interaction of laser radiation with plasma particles such as Thomson scattering are considered as the most reliable methods for temperature and density diagnostics in hot plasmas [22]. Originally developed for fusion processes these methods have been also utilized to measure plasma parameters in comparatively cooler thermal plasmas. Here mostly Thomson scattering technique was applied to obtain spatially resolved electron and ion temperature as well as density without assumption of local thermal equilibrium (LTE, see section 2.1.2) and the precise knowledge of plasma composition. Rayleigh scattering can also be applied for temperature diagnostic in the welding arc plasma [e.g. 23, 24]. However, since the Rayleigh scattering signal is dominant for the temperature range below $8000\,\mathrm{K}$ [21], the application of this technique in hotter plasma regions becomes difficult.

Thomson scattering has been widely applied for the investigation of GTAW processes [21, 24–32]. Moreover temperature and density measurements were also performed thermal plasmas generated by other technical devices. These include free burning model arcs [33–37], atmospheric plasma jets [38–42] and wall stabilized arcs [43–45].

Not only the plasma column region but also the boundary layers close to the electrodes can be investigated using this technique, if the laser is strongly focused. In this case special care has to be taken to suppress the stray light coming from the electrode surface [21, 44]. Yet high laser energy input may lead to an additional heating of the plasma and thus to overestimation of the electron temperature. In order to obtain correct electron temperatures it is necessary to correctly extrapolate the plasma parameters for conditions prevailing for zero laser pulse energy [45, 46]. Thus results comparable to other measurement methods are obtained [47].

Until now Thomson scattering measurements were mainly performed in pure argon atmosphere. Also processes operated with helium [32] and nitrogen [26] were investigated. The influence of metal vapor on the GTAW process was only studied by Terasaki et al. [30]. Yet no investigation of either welding processes in gas mixtures or GMAW processes, where high concentration of metal in the plasma is expected, were conducted so far.

However, investigations of other types of plasmas composed of different chemical species by means of Thomson scattering already exist. Measurements in circuit breaker devices, producing plasmas with similar parameters to the welding arcs, were performed by Tomita et al. [48]. Here a $Ar/SF_6$ gas mixture was used as a shielding gas. Moreover electron temperatures and densities in a free burning model arc, which were operated with a dry air shielding atmosphere with and without presence of metal vapor, were obtained [49, 50]. Thomson scattering was also applied to laboratory plasmas composed of gas mixtures yet with different electron temperature and density ranges than thermal plasmas. Here e.g. inductively coupled plasmas in Ar-$H_2$ or Ar-$N_2$ gas mixtures [51], argon microwave plasmas with $H_2$, $N_2$ $O_2$ or $CO_2$ admixtures [52, 53], laser induced plasmas in air [54] and vacuum discharges in tin vapor [55] were investigated.

Due to the relatively weak scattered signal high energy pulsed lasers are used. Yet even often light of several consecutive laser pulses has to be accumulated in order to obtain suitable signal to noise ratio. This makes the diagnostic of fluctuating processes a challenging

task. Still single shot Thomson scattering measurements were successfully performed in low density microwave plasmas in the temperature range of 10 000 to 20 000 K [56], in high density, high temperature laser induced plasmas [57, 58] and in the circuit breaker plasma [48]. For transient processes, such as pulsed vacuum discharges [59] or plasma streamer decays [60], time resolved measurements have been also conducted.

### 1.2.2 Emission spectroscopy diagnostics

Emission spectroscopy is the most frequently applied diagnostic technique for characterizing of temperature and density of the welding arc plasma. There exists a variety of different methods allowing the deduction of plasma parameters from the emission spectrum. Most methods however rely on the assumption of LTE and especially on the Boltzmann distribution of the excited states of bound electrons. Often the chemical composition of the arc has to be known and the emitted spectrum has to be optically thin. An overview of the applied methods can be found in [61].

Especially for GTAW arcs operated with pure argon as a shielding gas many spectroscopic studies have been carried out. For example, Haddad et al. or Thornton have applied the Fowler-Milne method in a pure argon arc [62–65]. Here relative radial distribution of one line is measured to deduce spatial temperature distribution by comparison with theoretical emission coefficient values. Originally developed for the application in pure Ar plasma it was also applied to plasmas with small impurities, e.g. the arc regions, where the presence of metal vapor is expected [66]. In addition Fowler-Milne method was further extended for use with plasmas in a gas mixtures as was first demonstrated in [67] for an Ar-$N_2$ shielding gas mixtures. It was moreover applied to investigate welding arcs operated with Ar-$H_2$ [68] and Ar-He gas mixtures [69–71]. With advancement in camera technology the Fowler-Milne method [72, 73] and the ratio methods [74] were adapted to the use with high speed cameras and narrow spectral bandwidth filters.

If the relative intensity of two different lines is measured, the so called ratio method [e.g. 75] or Boltzmann plot (for more than two lines) can be applied [e.g. 76]. The ratio of atom to ion lines can be interpreted using the Olsen-Richter method [77]. These methods directly yield the temperature of the excited species. In addition, they do not depend on the plasma composition. Therefore this method was preferably applied to GTAW processes with presence of metal vapor mainly evaporated from the molten anode [75, 76, 78–80]. Also GTAW arcs operated with Ar-He gas mixtures were investigated [71, 81, 82].

Absolute line intensities [79] can also be used to determine plasma temperature, while continuum intensity measurements were used to derive electron density and thus the species concentration [78, 80, 83]. Ratio of continuum to line intensities can also be used to derive plasma temperature [84]. These methods were as well applied to GTAW arcs in the presence of metal vapor origin from molten anode.

Measurement of the Stark width were also applied to deduce plasma density in GTAW processes [74, 85, 86]. The advantage of this method is that LTE assumptions are not necessarily need to be fulfilled. It is sufficient, if the assumption of Maxwellian velocity distribution of the electrons holds true. However as the dependence of the Stark width on the temperature cannot be always neglected, the plasma temperature has to be previously estimated or measured.

Spectroscopic techniques have also been applied to investigate GMAW plasma. Here mainly Boltzmann plot was used to measure plasma temperature in processes using iron based filler wires in DC [87, 88], pulsed processes [89]. It was also applied to pulsed processes operated with copper [90] and aluminum [9] wires. The Bartels method [91], which uses optically thick lines in order to deduce plasma temperature, and Olsen-Richter method were also applied by Goecke. Furthermore methods measuring absolute emission intensity [90] and high speed camera techniques with and without filters were applied for

visualization purposes [89, 90], estimation of plasma temperature and metal vapor concentration [92].

For the application of Stark broadening to the GMAW plasmas two different approaches can be distinguished. Analogously to investigations conducted with GTAW arcs, Rouffet et al. determined electron density in pulsed GMAW arc operated with iron wire by estimating the plasma temperature of $10^4$ K. A different approach originally, applied on microwave plasmas [93–95], suggests evaluation of the broadening width of at least two lines. It allows a simultaneous determination of the temperature and density of the plasma. This method was applied for DC GMAW arcs operated with iron [88, 96, 97].

## 1.3 Focus and structure of the thesis

A review of current literature reveals that there is still a need of experimental data for welding processes with multi-element transient plasmas. It has been previously demonstrated, that Thomson scattering and Stark broadening can be applied for the investigation of stationary welding processes. Both methods can provide electron temperature and density values, which are shown to be consistent with other experimental data. Moreover, they require fewer assumptions than other spectroscopic methods. In particular, for the validity of both methods neither local thermal equilibrium assumptions nor the knowledge of the plasma composition is required.

Still, Thomson scattering and Stark broadening have been only rarely or not at all applied for the investigation of transient multi-element welding plasmas e.g. present in a pulsed GMAW process. Therefore, the aim of this work is to develop two reliable systems for the diagnostic of plasma parameters by Thomson scattering and Stark broadening. The main goal is to apply those systems to transient welding processes operated with gas mixtures or in the presence of metal vapor.

The thesis is divided into five major sections. First of all, the basic properties and concepts of the description of the plasma state relevant for welding processes are introduced in chapter 2. Subsequently, the theory of the applied diagnostic techniques is presented in chapter 3. In this chapter the formulas used for the calculation of the Thomson scattering spectra is derived. The conditions which have to prevail for successful application of this method in the welding plasmas are discussed as well. Thereafter the spectral line broadening with the focus on Stark broadening is presented. Theoretical descriptions of linear and quadratic Stark effects, as well as the conditions, which has to be valid in order to use this technique for electron density and temperature diagnostics, are given.

The experimental setup for Thomson scattering and Stark broadening techniques is presented in chapter 4. Here the choice of the experimental components, the techniques used for the data evaluation and the investigated process parameters are discussed. In chapter 5 the results of both diagnostic techniques are presented, compared to each other and to the experimental and simulated data available in the literature. The focus remains on the detection of changes caused by the metal vapor and on tracking transient effects during pulsed GMAW. Moreover, the plasma composition is reconstructed for particular cases using the data gained with the Thomson scattering method. Finally, the results of this work are summarized in chapter 6. Additionally, comments on possible improvements and applicability of the diagnostic techniques in industrial processes are given in that final chapter.

# Chapter 2

# Plasma in welding processes

Since the focus of the investigations is on the arc column plasma, an overview of the general plasma properties and the properties of thermal plasma generated in the welding arc is given in this chapter.

## 2.1 General plasma properties

Plasma is often defined as fourth state of matter. In general, this state is characterized by the presence of a considerable amount of free moving charges. For example it arises from the gaseous state, when ionization processes take place. In contrast to a gas, in a plasma in addition to molecules and atoms also ions and electrons are present. This makes the plasma an electrically conducting medium [98]. Besides the direct collisions between particles, charged species can take influence on each others trajectories by means of the Coulomb force. A sufficient amount of charged particles in a volume will cause the collective behavior of the plasma. This means, that a single particle is not only influenced by direct collisions but also by the long range Coulomb force of other charged species [99].

Generally speaking, collisions play an important role for the description of the plasma state. The distinction is essentially made between elastic and inelastic collisions. The latter change the kinetic energy of a particle. Examples for inelastic collisions are ionization of the plasma or excitation of heavy particles (atoms and ions), which finally leads to photon emission. During elastic collisions the total kinetic energy of a particle remains unchanged, while its direction and the velocity are influenced by the interaction. The particle collision frequency can be defined as

$$f_{col} = n_q \sigma_{col} v_q \tag{2.1}$$

with $n_q$ the density of interacting species with a charge $q$ and $v_q$ the particle velocity. The effective cross section $\sigma_{col}$ depends on the type of interacting particle. In the simplest case, when at least one of the particles is not charged, the interaction is comparable to collisions between billiard balls with $\sigma_{col} = \pi r^2$, where $r$ is the effective radius of the particles. The situation however becomes more complicated, if both participants of the collision are charged. At this point the long range Coulomb force of the particles comes into play [98]. In contrast to billiard-like collisions the trajectory of colliding particles is not straight, but it is steadily changing during the collision process. This enlarges $\sigma_{col}$ yet makes its estimation more complicated. A plasma state is often described as collisionless or collision dominated. However, this characterization has to be conducted with respect to the timescale of the phenomenon on which the collisions may take impact.

Whenever speaking of particles collisions the particle motion is implied. In a plasma it is determined by several components. One of those components is the kinetic energy

$E_{kin} = m_q v_q^2/2$ depending on the particle's mass $m_q$ and velocity $v_q = |\vec{v_q}|$. Moreover, the particle's trajectory and velocity can be influenced by the electric or magnetic field.

Particles in an unbound state, a gas or a plasma, have all kind of velocities. If their number is high enough, they can be described using the concept of probability distribution functions. Since in a plasma different sources of particle motion have to be considered, it is impossible to define a general velocity distribution function.

Yet in the case of absence of strong magnetic and electric fields, several simplifications can be made. Here the plasma density and hence the collision frequency is assumed to be sufficiently high and the interaction between the particles almost instantaneous. In this case the probability to find a particle in an energy state $E_{u,q}$ is proportional to the ratio of Boltzmann distribution

$$f(E_{u,q}) \propto \exp\left(-\frac{E_{u,q}}{k_B T_q}\right) \tag{2.2}$$

with $k_\mathrm{B}$ being the Boltzmann constant. When substituting $E_{u,q} = m_q v_q^2/2$ the velocity distribution of the species with a charge $q$ can be derived. Thus the Maxwell-Boltzmann distribution is obtained

$$f(v_q)d = 4\pi v_q^2 \left(\frac{m_q}{2\pi k_\mathrm{B} T_q}\right)^{3/2} \exp\left(-\frac{m_q v_q^2}{2k_\mathrm{B} T_q}\right) dv_q. \tag{2.3}$$

The temperature of each particle type in a gas or in a plasma is defined as their average kinetic energy

$$\frac{3}{2} k_\mathrm{B} T_q = \frac{1}{2} m \overline{v_q^2}, \tag{2.4}$$

where $\overline{v_q^2}$ is the mean square three-dimensional velocity vector [98]. This allows to derive Dalton's ideal gas law

$$p = \sum_q n_q k_\mathrm{B} T_q \tag{2.5}$$

with $p$ the local pressure, $n_q$ the particular species density and $T_q$ its corresponding temperature.

Although the electrons and ions are separated, the overall charge within the plasma volume equals zero. This is also called the principle of quasineutrality. The electrons gather around the ions and so macroscopically shield their electric field with respect to the observer. The characteristic length at which the microscopic deviations from the quasineutrality are still "visible" is described by the Debye length

$$\lambda_D = \left(\frac{\varepsilon_0 k_\mathrm{B} T_e}{n_j e^2}\right)^{1/2}, \tag{2.6}$$

where $\varepsilon_0$ is the vacuum permittivity, $e$ the electron charge and $T_e$ the electron temperature. $\lambda_D$ has to be much smaller than the volume expansion of the plasma in order to assure collective behavior of the charge carriers. Another characteristic of the plasma describing the electron oscillation around their equilibrium position, is the plasma frequency [99]

$$\omega_{pe} = \sqrt{\frac{n_e e^2}{\varepsilon_0 m_e}}. \tag{2.7}$$

Here $n_e$ denotes the electron density and $m_e$ the electron mass. This frequency also corresponds to the upper frequency limit for electromagnetic waves to be compensated by the charged particles within the plasma. At a still higher frequency than the plasma frequency an electromagnetic wave can no longer be screened out by the plasma. This effect makes it possible, that e.g. the laser radiation, which frequency lies above the thermal plasma frequency can propagate in a plasma and interact with the free electrons.

### 2.1.1 Thermal equilibrium

Plasmas generated under atmospheric pressure are often described using the concept of the *thermal equilibrium* (TE) assumption. This implies, that the macroscopic state of the plasma can be described, if the temperature, density and chemical composition within the plasma volume are known. On the microscopic level it comprises, that mainly four processes are in equilibrium with their reverse process – the kinetic energy exchange between the particles, the de-/excitation, the ionization/recombination and the absorption and emission of radiation. This is called the principle of detailed balancing. Moreover, all the particles in the volume are described by a single temperature $T$ [100].

In TE distribution functions are used to describe e.g. the kinetic or excitation equilibrium. The velocities of the free particles can be described using the Maxwell-Boltzmann distribution given in eq. (2.3). The fraction or probability of particle species $j$ in an excited state $u$ within an ensemble in equilibrium is given by the Boltzmann distribution

$$\frac{n_{u,q}}{n_{g,q}} = \frac{g_{u,q}}{Z_q} \exp\left(-\frac{E_{u,q} - E_{g,q}}{k_\mathrm{B} T}\right) \tag{2.8}$$

with $n_{g,q}$ the density of the ground state, $n_{u,q}$ the density of the excited state, $g_{u,q}$ its statistical weight and $E_{u,q}$ the energy of the excited state of the species with a charge $q$. The partition function $Z_q$ describing the number of possible bound states up to the ionization limit can be calculated by

$$Z_q = \sum_u g_{u,q} \exp\left(-\frac{E_{u,q}}{k_\mathrm{B} T}\right). \tag{2.9}$$

The ionization recombination balance (i.e. equal number of ionizations as well as of recombinations) is described by the Saha-Eggert equation, which specifies the rate $K_{j+1}$ between single ionization stages

$$K_{j+1} = \frac{n_e n_{j+1}}{n_j} = \frac{Z_e Z_{j+1}}{Z_j} \left(\frac{2\pi m_e k_\mathrm{B} T}{h^2}\right)^{3/2} \exp\left(-\frac{E_{j+1} - \Delta E_{j+1}}{k_\mathrm{B} T}\right). \tag{2.10}$$

Here the indices $j$ and $j+1$ denote ions in $j^{th}$ and $j+1^{th}$ ionization stage. Index $e$ denotes the electrons, $m_e$ the electron mass and $h$ Planck's constant. The electrons can only have two states due to different electron spins. Hence, for the electron partition function $Z_e = 2$ is valid. $E_{j+1}$ indicates the ionization energy, while $\Delta E_{j+1} = \frac{je^2}{4\pi\varepsilon_0 \lambda_D}$ delivers the correction of this value due to Coulomb field of the surrounding ions [101].

The conservation of the radiation implies, that the absorption and spontaneous emission processes are balanced. The balance is described by the Planck's law of radiation relating the intensity $B_\lambda$ of blackbody radiation in equilibrium to the radiation wavelength $\lambda$ and the temperature $T$

$$B_\lambda(T) d\lambda = \frac{2hc^2}{\lambda^5} \frac{1}{\exp\left(\frac{hc}{\lambda k_\mathrm{B} T}\right) - 1} d\lambda. \tag{2.11}$$

Here $c$ denotes the speed of light [102].

However, in laboratory conditions the thermal equilibrium cannot be reached, since not all energy within a plasma can be conserved. For example, the temperature of the radiation produced by a plasma is lower than the temperature described in eq. (2.11). Moreover, the surrounding of the plasma volume is not maintained at the plasma temperature. Hence a part of the energy is lost to the surrounding through radiation or collision with particles [98, 100, 102].

### 2.1.2 Deviations from thermal equilibrium

If some requirements for the state of thermal equilibrium cannot be reached, this does not necessarily mean that the other equilibrium conditions are affected. Typically, the conservation of radiation cannot be fulfilled in real conditions. However, the energy loss through radiation, which affects the Planck's radiation law, is relatively small compared to the energy exchange through collisions between particles. Hence it can be assumed, that the other processes in the plasma are still in microscopic equilibrium and the equilibrium conditions are still valid, if some modification are introduced.

In a real plasma e.g. spatial temperature gradients are always present due to interaction of the plasma with the surrounding. It is impossible to define one temperature for the whole plasma volume. However, if the different particle species can reach equilibrium conditions fast enough, the plasma is in the state of the *local thermal equilibrium* (LTE). In this case the time between collisions is considerably smaller than the time the particles need to diffuse between regions with different temperatures. Under these conditions the plasma is also characterized as collision dominated. Again, it is still required, that locally electrons and heavy particles have the same temperature. Furthermore, the Maxwell-Boltzmann distribution, as well as the Saha-Eggert equation and the Boltzmann statistics are used as descriptions of the local particle state. Yet in contrast to section 2.1.1 the radiation and the particles cannot be characterized by the same temperature.

Further deviations from equilibrium are possible, if the electrons and the heavy particles are subject to different forces. This is often described as two temperature LTE. For example, such states exist in a plasma induced by a relatively high current. In this case the more mobile electrons quickly adopt the energy from the electric field. Since due to the mass difference the energy transfer from electrons to heavy particles via collisions is not very efficient, the heavy particle temperature is lower than the electron temperature. As a result the electrons and heavy particles have different Maxwell-Boltzmann distribution functions.

The ionization recombination and de-/excitation equilibria are however maintained. The heavy particles are excited or ionized by collisions with electrons rather than with ions, as the electron velocity is much higher. Therefore, for sufficiently high electron densities eqs. (2.8) and (2.10) are still valid when the total plasma temperature $T$ is replaced by electron temperature $T_e$ [103, 104].

If charge drift out of the plasma region becomes significant, the ionization/recombination balance is disturbed. The de-/excitation balance is also disturbed since the lower population levels tend to be underpopulated. The plasma can be then described by the so called partial LTE model, when the Saha-Eggert equation and the Boltzmann distribution are only valid for the upper excitation levels. This implies, that the electron temperature $T_e$ corresponds to the excitation temperature of upper energy levels the emitting species [98, 100, 102].

## 2.2 Properties of welding plasmas

The plasma in the welding process is created by the free burning electric arc, which partially or completely ionizes the fast flowing shielding gas. The ionization has to be sufficient to conduct the current from the cathode to the anode [4]. The arc is gas stabilized and is typically operated with currents above $50\,\mathrm{A}$ at pressures higher than $10^4\,\mathrm{Pa}$ [98].

The arc can be divided in three regions: the cathode fall, the anode fall and the arc column, as schematically shown in fig. 2.1. The cathode and anode fall regions are located at the corresponding electrodes. Their thickness are typically very small compared to the arc column region [4, 106]. They are characterized by the presence of a high electric field above $10^4\,\mathrm{V/m}$ and hence a high voltage gradient, which leads to acceleration of the free electrons [106, 107]. Therefore, no LTE can be established in this regions [105].

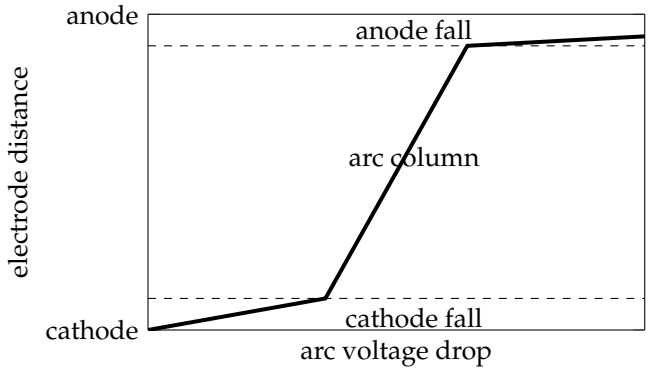


Figure 2.1: Schematic voltage distribution along the arc hight [adapted from 4, 105].

The arc column forms the largest region of the arc. The plasma in the arc column is often characterized as thermal, which implies a relatively low temperature high density plasma close to the state of thermal equilibrium [98]. In this region weak almost homogeneous electric fields below $10^3\,\mathrm{V/m}$, electron densities above $10^{20}\,\mathrm{m}^{-3}$ and temperatures in the range of $1 \times 10^4\,\mathrm{K}$ are typical [104].

The Joule effect is mainly responsible for the transport of the external energy to the free electrons. The latter transfer the energy to the heavy particles via elastic collisions. The electrons are as well responsible for the inelastic collisions leading to ionization and excitation of heavy particles [104]. For observation times in the range of $\mu\mathrm{s}$ or higher the plasma can be assumed as collision dominated. For typical collision frequencies above $10\,\mathrm{GHz}$, at least $10^4$ collisions would have occurred during the observation time window. This allows the use of statistical models for description of the particle behavior. In this case the energy distribution of all particle types in the arc column plasma is described by Maxwellian distributions. Ideally even equal electron and heavy particle temperatures can be assumed, so that LTE assumption as described in section 2.1.2 is still valid. Yet when reducing the observation timescale to e.g. $\mathrm{ns}$ the influence of the collision can be neglected.

Deviation from LTE in the arc column may occur, if the electric field rises. In this case the electron velocity becomes too fast and the collisions with heavy particles not sufficiently frequent. This may lead only to partial energy transfer from electrons to the heavy particles, which results in a two temperature equilibrium. If the electric field is further increased, the energy distribution function may even deviate from a Maxwellian type [98, 104].

The thermodynamic properties of the arc plasma such as enthalpy or specific heat are mainly determined by the plasma composition. Assuming the validity of LTE and a homogeneous pressure distribution in the plasma column the temperature dependent concentration of single species in the plasma can be reconstructed using the Saha equation eq. (2.10) and Dalton's law eq. (2.5) [98, 104]. If the arc column is composed of different chemical species, a correlation between the temperature, electron density and specific plasma composition can be calculated.

The radiation produced by the arc column is also temperature dependent in LTE. In the hot regions of the plasma it is the main source of energy loss. In the outer regions the radiation escaping from the inner hot regions might become an additional local energy source due to absorption phenomena [4, 98, 104]. In the hot regions different methods can be applied in order to deduce plasma parameters such as temperature and electron density from the measured radiation (see section 3.2).

# Chapter 3

# Optical diagnostics theory

In this chapter the respective theoretical models for the two optical diagnostic methods used in this work are discussed. Both diagnostic methods are based on the interaction of radiation with free electrons present in the plasma, which allows determining temperature and density of free electrons. First the theory of scattering of electromagnetic radiation in a plasma, on which Thomson scattering technique is based, is discussed. Afterwards the mechanism responsible for the Stark broadening effect of spectral lines is introduced.

## 3.1 Scattering of electromagnetic radiation in a plasma

The scattering of electromagnetic radiation in a plasma is based on the interaction of free or bound charges with the electric and magnetic field of the incident wave. Depending on the energy of the incident radiation, the type of particle the wave interacts with and the amount of energy transmitted to the particle multiple types of scattering can be distinguished. In general scattering processes can be divided in inelastic and elastic scattering. During inelastic scattering process a part of the energy of the incident wave is transmitted to the scattering particle. Examples for such processes are Compton and Raman scattering.

In contrast to the previous case elastic scattering implies energy conservation, whereas the direction of propagation, frequency and amplitude of the incident wave can be changed. The most prominent elastic scattering phenomenon is Rayleigh scattering. The incident radiation is scattered by the bound electrons of particles, which are much smaller than the wavelength of the incident waves. For example sunlight passing through the earth atmosphere is Rayleigh scattered, which gives the sky its characteristic blue color during the day and orange-red color when the sun goes down.

Another example for elastic scattering, on which this work mainly focuses, is Thomson scattering. It is triggered by the free electrons present in the plasma. The electrons are accelerated by the electric field of the incident wave, which leads to the characteristic scattered spectrum. It mainly depends on the velocity and position of the charges within the volume, where scattering occurs. This allows deriving mean average plasma parameters such as temperature and density.

In the following sections the derivation of the scattered power spectrum produced by the free electrons in the plasma is sketched. Therefore, firstly the electric field of a single accelerated charge is described. Since in a plasma light is scattered by a charge collective, the relation between the electron density and the scattered power spectrum is established. Finally, by applying Salpeter approximation [108] for the case of Maxwellian velocity distribution of the particles in the plasma, the general expression for the scattered radiation can be simplified. This delivers an equation, which can be used for the calculation of scattered spectra in welding arcs.

The derivations described here are mainly based on the work presented in [109], where all the detailed calculations can be found.

### 3.1.1 Requirements and boundary conditions for Thomson scattering

Before performing the calculation of the scattered radiation, it is necessary to define the conditions under which it is sensible to apply Thomson scattering diagnostics. Here the incident radiation is denoted by the index $I$ and the scattered radiation by the index $S$. The following conditions have to be fulfilled:

1. For the frequency of incident radiation $\omega_I > \omega_{pe}$ must be valid, where $\omega_{pe}$ is the plasma frequency of the free electrons within the plasma. This condition assures, that the electrons in the plasma cannot shield the oscillating electric field of the incident electromagnetic wave and cancel it out. Generally speaking, the timescale, at which the incident electric field oscillations take place, must be the smallest timescale in the system. Consequently, all processes inside the plasma can make an impact on the scattered radiation.

2. The incident radiation must not change the state of the plasma. This may happen, if the velocity achieved by the acceleration of the charges in the electric field is in the range of thermal velocity of the charges. This effect can be estimated by the relation

$$v_e = \left(\frac{k_\mathrm{B} T_e}{m_e}\right)^{1/2} \ll \frac{e|\vec{E}_{I,0}|}{m_e \omega_I}. \tag{3.1}$$

   with $|\vec{E}_{I,0}|$ the amplitude of the incident electric field

3. The plasma has to be quasineutral in the observed volume $V$. Thus it must contain $N$ electrons and $N/Z$ ions within $V$.

4. For the observing distance $R \gg V^{1/3}$ and $R \gg \lambda_I$ (the wavelength of incident radiation) has to apply. In this case the small-angle approximation is valid.

5. Scattering on positive ions is not considered. Due to the much greater mass the scattered radiation power is negligible.

6. Plasmas investigated in this work are in general non relativistic, thus $\frac{v}{c} \to 0$ for all velocities $v$ and the speed of light $c$.

7. The influence of an external magnetic field is not considered here.

8. In general, the plasma is assumed to be collisionless on the timescale of the incident radiation frequency.

The justification, that the requirement 8 is valid in welding plasmas, can be easily obtained when comparing the typical frequencies prevailing in the plasma. Inside a welding plasma arc temperature in the range of $15\,000\,\mathrm{K}$ is expected. In this case a fully ionized plasma can be assumed. Hence assuming $n_e = n_i$ the electron density can be estimated from eq. (2.5) yielding $2.4 \times 10^{23}\,\mathrm{m}^{-3}$. The corresponding plasma frequency is then equal to $\omega_{pe} \approx 2.8 \times 10^{13}\,\mathrm{rad/s}$, which is several orders of magnitude lower than the incident laser frequency $\omega_I = 3.5 \times 10^{15}\,\mathrm{rad/s}$. Hence no shielding of the incident radiation can be produced by the plasma. On the other hand, the collision frequency between the electrons and other charged particles within the plasma can be estimated by eq. (2.1). In this case the thermal electron velocity $v_e = \sqrt{\frac{k_\mathrm{B} T_e}{m_e}}$ and $\sigma_{col} = \pi \lambda_{Landau}^2$ the scale for the cross section of electrostatic interactions between the charged particles are used. Here the Landau

length scale, which defines the scattering cross section, describes the separation, at which electrostatic interactions have the same strength as the thermal energy:

$$\lambda_{Landau} = \frac{e^2}{4\pi\varepsilon_0}\frac{1}{k_\mathrm{B}T_e} \tag{3.2}$$

From that $f_{col} = 4.5 \times 10^{11}\,\mathrm{s}^{-1}$ results, which is again several orders of magnitude lower, than the laser frequency. Consequently, the free electrons in the plasma react many times more frequently to the laser before having the opportunity to collide among themselves. Hence, under these circumstances the assumption of a collisionless plasma is justified.

### 3.1.2 Radiation scattered by a single charge

It is commonly known, that a charge is a source of electric field. The motion and the position of the charge strongly influence that field, which can be detected by the observer. While in the static case it can be simply described by Coulomb's law, the situation becomes more difficult whenever a charge is in motion. In this case Maxwellian equations are needed to derive the appropriate relation:

$$\begin{aligned} &\text{Gauss' law (electric field): } \vec{\nabla}\cdot\vec{E} = \frac{\rho}{\varepsilon_0} \qquad \text{Gauss' law (magnetic field): } \vec{\nabla}\cdot\vec{B} = 0 \\ &\text{Faraday's law: } \vec{\nabla}\times\vec{E} = -\frac{\partial\vec{B}}{\partial t} \qquad \text{Ampère's law: } \vec{\nabla}\times\vec{B} = \mu_0\vec{j} + \mu_0\varepsilon_0\frac{\partial\vec{E}}{\partial t} \end{aligned} \tag{3.3}$$

Here $\vec{E}$ and $\vec{B}$ denote the electric and magnetic fields, $\rho$ the total charge density, $\vec{j}$ the total current density and $\varepsilon_0$ and $\mu_0$ the vacuum permittivity and permeability. The combination of Ampère's and Faraday's law delivers the dependence between $\vec{E}$ and $\vec{j}$:

$$\vec{\nabla}\times(\vec{\nabla}\times\vec{E}) + \mu_o\varepsilon_0\frac{\partial^2\vec{E}}{\partial t^2} = -\mu_0\frac{\partial\vec{j}}{\partial t}. \tag{3.4}$$

The expression for current density caused by a single charge, which is accelerated by the electric field of an incident wave, can be simplified as $\vec{j} = e\vec{v}(t')$. Here $t'$ denotes the time of scattering event. The solution of eq. (3.4) is extensively discussed in [110]. In the non-relativistic case the influence of the magnetic field can be neglected. For an electron the general solution for time and spatially resolved scattered electric field is given by

$$\vec{E}_S(R,t) = \frac{e}{4\pi\varepsilon_0 c^2 R}[\vec{s}\times(\vec{s}\times\frac{d\vec{v}}{dt'})]. \tag{3.5}$$

Herein $R$ indicates the observer's distance, $\vec{i}$ and $\vec{s}$ the unit direction of the incident and the scattered wave at the time $t > t'$.

Figure 3.1 illustrates the relation between the scattering event and the observer. According to the principle of relativity the information about the scattering event has to travel the distance $R$ before it can be detected. Consequently, one observes the scattering event not until the time interval $t - t' = \frac{R'}{c}$ has passed. Since the distance $R'$ between the observer and scattering charge is much bigger than the typical range of the charge movement $\vec{r}$, it can be assumed, that

$$t - t' \simeq \frac{|R - \vec{s}\cdot\vec{r}(t')|}{c} \tag{3.6}$$

with $\vec{r}(t') = \vec{r}(0) + \vec{v}(t')t'$ implied.

Furthermore, it can be assumed, that for the moving charge $e$ the second Newton's law is valid:

$$\vec{F} = m\vec{a} = m_e\frac{d\vec{v}}{dt'} = e\vec{E}(r,t). \tag{3.7}$$

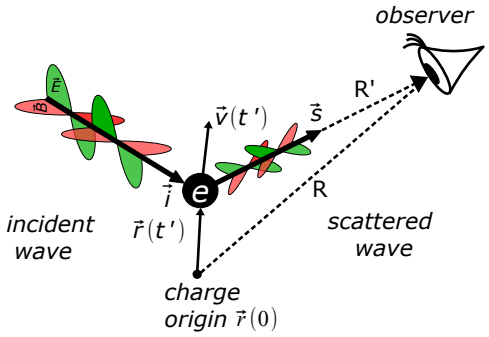


Figure 3.1: The scattering event initiated by a single charge $e$.

The electric field of a monochromatic electromagnetic wave can be described as

$$\vec{E}_I(r,\tau) = \vec{E}_{I,0}\cos(\vec{k}_I \cdot \vec{r} - \omega_I t'). \tag{3.8}$$

Here $|\vec{k}_I| = 2\pi/\lambda_I$, $\lambda_I$ and $\omega_I$ denote respectively the incident wave number, wavelength and frequency. Hence, when combining eqs. (3.5) to (3.8) the scattered electric field of a single charge accelerated by the field of the incident monochromatic radiation is obtained as follows:

$$\vec{E}_S(R,t) = \frac{e^2}{4\pi\varepsilon_0 m_e c^2 R}\left\|\vec{s}\times(\vec{s}\times\vec{E}_{I,0})\right\|\cos(k_S R - \omega_S t - \vec{k}\cdot\vec{r}(0))$$
$$\text{with } \omega_S = \omega_I\frac{1-\vec{i}\frac{v}{c}}{1-\vec{s}\frac{v}{c}}, \quad \vec{k}_S = \omega_S\vec{s} \quad \text{and} \quad \omega = \omega_S - \omega_I = \vec{v}\cdot(\vec{k}_S - \vec{k}_I) = \vec{v}\cdot\vec{k}. \tag{3.9}$$

Here $r_e = \frac{e^2}{4\pi\varepsilon_0 m_e c^2}$ is the classical electron radius. A typical observer however does not "see" the electric field of the scattered wave but its power density scattered within a solid angle. The power of the electromagnetic wave can be derived from the Poynting vector, which quantifies power per unit area of an electromagnetic wave [111].

$$\vec{S} = \frac{1}{\mu_0}\vec{E}\times\vec{B} = |\vec{S}|\vec{s} = \sqrt{\frac{\epsilon_0}{\mu_0}}|\vec{E}^2|\vec{s} \tag{3.10}$$

In combination with eq. (3.9) it leads to an expression for scattered power

$$dP_S(\vec{R},t) = \vec{S}\cdot d\vec{A} = \sqrt{\frac{\varepsilon_0}{\mu_0}}|\vec{E}_S(\vec{R},t)|^2\cdot R^2 d\Omega \;\Leftrightarrow$$
$$\frac{dP_S(\vec{R},t)}{d\Omega} = \sqrt{\frac{\varepsilon_0}{\mu_0}}|\vec{E_{I,0}}|^2 r_e^2\left[\vec{s}\times\left(\vec{s}\times\frac{\vec{E}_{I,0}}{|\vec{E}_{I,0}|}\right)\right]^2\cos^2(k_S R - \omega_S t - \vec{k}\cdot\vec{r}(0)). \tag{3.11}$$

Using the relation $\frac{1}{\mathcal{T}}\int_0^{\mathcal{T}}\cos^2\left(\frac{2\pi}{\mathcal{T}}t\right)dt = \frac{1}{2}$ and the expression for the power of the incident radiation $P_I = A\sqrt{\frac{\varepsilon_0}{\mu_0}}\frac{E_{I,0}^2}{2}$ with $A$ the radiated surface the time-averaged scattered power per solid angle $\Omega$ is obtained

$$\frac{dP_S(\vec{R})}{d\Omega} = \frac{P_I}{A}r_e^2\left[\vec{s}\times\left(\vec{s}\times\frac{\vec{E}_{I,0}}{|\vec{E}_{I,0}|}\right)\right]^2. \tag{3.12}$$

### 3.1.3 Radiation scattered by the charge ensemble within a plasma

In a plasma a charge ensemble consisting of electrons and ions is present. Thus scattered radiation observed in a plasma at an angle $\theta$ in relation to the incident radiation origins from a scattering volume V with a certain electron distribution as illustrated in figure 3.2.

Generally speaking, the microscopic distribution of an ensemble of a species with a charge $q$ can be described by a sum over all possible positions and velocities present in the investigated volume:

$$F_q(\vec{r},\vec{v},t) = \sum_S \delta(\vec{r}-\vec{r}_S(t))\delta(\vec{v}-\vec{v}_S(t)) \tag{3.13}$$

This definition implies, that $F_q$ follows the movement of every single particle in the volume $V$. When performing Thomson scattering measurements, the scattered radiation is detected over a finite time interval and volume. This allows deriving time and space averaged parameters such as electron density and temperature, which do not require the knowledge about the position and velocity of every single interacting particle. To consider this idea in the theoretical calculations the concept of ensemble average of a quantity $Q(x)$ is introduced as

$$\langle Q(x)\rangle = \frac{\int Q(x) f_Q(x) dx}{\int f_Q(x) dx}, \tag{3.14}$$

where $f_Q(x)$ is the probability to find the quantity $Q$ in the state $x$. Following this concept it can be assumed, that all the particles in the ensemble have a similar stochastic behavior and that their position and velocity can be predicted by a probability function. Consequently, to predict the behavior of the ensemble it is enough to describe, what the single particles on average will do. The ensemble average can be also considered as a time average on the timescale of the measurement.

The definition in eq. (3.13) can be first applied to express the total electric field scattered by the charge collective in the volume $V$ using eqs. (3.5) and (3.13)

$$E_S^T(R,t) = \iint F_q(\vec{r},\vec{v},t) E_S(R,t) d^3\vec{v} d^3\vec{r}. \tag{3.15}$$

Further, the electron density can be defined as

$$n_e(\vec{r},t) = \int F_e(\vec{r},\vec{v},t) d^3\vec{v}. \tag{3.16}$$

In an experiment a frequency resolved spectrum of the scattered power radiation is detected. Hence, it is necessary to transform the quantities in to the spectral range by applying the Fourier transformation. The combination of the Fourier transformed eq. (3.12) with

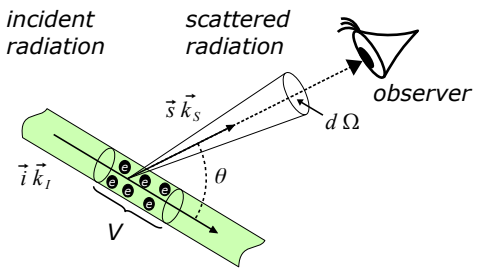


Figure 3.2: The scattering geometry in a volume $V$ on an electron charge collective.

the definition of the total scattered electric field eq. (3.15) delivers the frequency dependent scattered power per solid angle

$$\frac{d^2P_S(R,\omega_S)}{d\omega_S d\Omega} = \frac{P_I}{A} r_e^2 \left[\vec{s} \times \left(\vec{s} \times \frac{\vec{E}_{I,0}}{|\vec{E}_{I,0}|}\right)\right]^2 NS(\vec{k},\omega) \tag{3.17}$$

with frequency shift $\omega$ and shift wavenumber $\vec{k}$ as defined in eq. (3.9), $N$ the total number of electrons and the spectral density function $S(\vec{k},\omega)$ defined as the ensemble average of the autocorrelation spectrum of the electron density

$$S(\vec{k},\omega) = \lim_{\mathcal{T},V\to\infty} \frac{1}{\mathcal{T}V} \left\langle \frac{\left|n_e(\vec{k},\omega)\right|^2}{n_{e0}} \right\rangle. \tag{3.18}$$

Here $\mathcal{T}$ denotes a time interval with $n_{e0} = V/N$ the initial electron density in a volume $V$.Equation (3.17) points out, that the experimentally detected signal is the time-averaged value of $n_e(\vec{k},\omega)$.

In order to further specify the scattered spectrum an expression for $n_e(\vec{k},\omega)$ needs to be derived. This can be done by considering the rate of change for the number of particles in a plasma volume. It can be described using the distribution function of the electrons.

In general the distribution function $F_q$ of a species with a charge $q$ has to satisfy

$$\frac{\partial F_q}{\partial t} + \vec{v} \cdot \frac{\partial F_q}{\partial \vec{r}} + \vec{a} \cdot \frac{\partial F_q}{\partial \vec{v}} = 0. \tag{3.19}$$

In this case, according to eq. (3.7), the particle acceleration is given by $\vec{a} = \frac{q\vec{E}(r,t)}{m}$. Here the movement of the charges due to the total electric field created both through an external action as well as through the redistribution of the plasma charges is taken into account. The interaction of the particles among themselves is assumed to be small and is consequently neglected here. Depending on how $F_q$ is defined, this equation is known as Boltzmann, Vlasov or Klimonovich equation. These equations are discussed in detail in the appendix of [109].

For the description of the electric field Gauss law, as given in eq. (3.3), is used. It can be combined with the definition from eq. (3.16). Here however, all charge species contributing to $\vec{E}$ have to be considered as follows:

$$\vec{\nabla} \cdot \vec{E} = \frac{\rho(\vec{r},t)}{\varepsilon_0} = \frac{1}{\varepsilon_0} \sum_q q \int F_q(\vec{r},\vec{v},t) d^3\vec{v}. \tag{3.20}$$

By integrating and differentiating eq. (3.20) in the Fourier domain the following expression for $\vec{E}$ is obtained:

$$\vec{E} = \frac{\hat{\imath}\vec{k}}{\varepsilon_0 k^2} \sum_q q \int F_q(\vec{r},\vec{v},t) d^3\vec{v}. \tag{3.21}$$

Here $\hat{\imath}$ denotes the imaginary unit. The way, in which the distribution function has been defined in eq. (3.13), makes the solution satisfying eq. (3.19) complicated. In this case it would be necessary to derive the trajectory of every single particle in the volume. A solution can only be obtained, if the average behavior of all particles is considered.

In the simplest case, where the charges are homogeneously distributed in the scattering volume and do not interact with each other, no scattered radiation would be detected by the observer. Thus, it would be always possible to find pairs of scattered waves, which cancel each other out. Yet if it is assumed, that the electron positions fluctuate at a microscopic level, it would become possible to observe a net scattering signal. Therefore, $F_q$ can be expressed as

$$F_q(\vec{r},\vec{v},t) = F_{q,0}(\vec{r},\vec{v},t) + F_{q,1}(\vec{r},\vec{v},t) \tag{3.22}$$

with an average state distribution expressed by $F_{q,0}$ and its microscopic fluctuation distribution $F_{q,1}$. In the stationary undisturbed state the species distribution only depends on $\vec{v}$. Hence, $F_{q,0}$ can be related to the distribution $f_q(v)$ weighted by the initial homogeneous density of the species with a charge $q$:

$$F_{q,0}(\vec{v}) = n_{q0} f_q(v), \text{ with } n_{q0} = N/V. \tag{3.23}$$

By firstly assuming the absence of external electric field and collisions eq. (3.19) can be expressed as

$$\frac{\partial F_{q,1}}{\partial t} + \vec{v}\cdot\frac{\partial F_{q,1}}{\partial \vec{r}} + \frac{q}{m}\vec{E}_1\cdot\frac{\partial F_{q,0}}{\partial \vec{v}} = 0. \tag{3.24}$$

Here the deviation from stationary state is responsible for a formation of the electric micro-field $\vec{E}_1$

$$\vec{E}_1 = \frac{\hat{\imath}\vec{k}}{\varepsilon_0 k^2}\sum_q q\int F_{q,1}(\vec{r},\vec{v},t)d^3\vec{v}.$$

Now an expression for the electron density $n_e$ can be derived. Therefore, the following is valid. The plasma volume $V$ is composed of electrons (denoted by the subscript $e$) with a charge $q_e = -e$ and ions (denoted by the subscript $i$) with $q_i = Ze$ with $Z$ the mean charge-ionization state and corresponding densities $n_e$ and $n_i$. In order to fulfill the condition of quasineutrality $n_e = Zn_i$ is valid on the average. Yet on the microscopic scale the total charge density $\rho_1$ can deviate from zero at the length scale below the Debye length, which is the reason for the existence of the micro-field $\vec{E}_1$ with

$$\rho_1 = Zen_i - en_e. \tag{3.25}$$

Application of Fourier-Laplace transform [1] to $\frac{\partial F_{q,1}}{\partial t}$ simplifies to

$$\int_{-\infty}^{\infty}\int_{0}^{\infty}\exp(\hat{\imath}\vec{k}\cdot\vec{r})\exp(-(\hat{\imath}\omega+\gamma))\frac{\partial F_{q,1}}{\partial t}d^3\vec{r}dt = -F_{q,1}(\vec{k},\vec{v},0) + (\hat{\imath}\omega+\gamma)F_{1,q}(\vec{k},\vec{v},\omega)$$

and for $\frac{\partial F_{q,1}}{\partial \vec{r}}$ to

$$\int_{-\infty}^{\infty}\int_{0}^{\infty}\exp(\hat{\imath}\vec{k}\cdot\vec{r})\exp(-(\hat{\imath}\omega+\gamma))\frac{\partial F_{q,1}}{\partial \vec{r}}d^3\vec{r}dt = -\hat{\imath}\vec{k}F_{1,q}(\vec{k},\vec{v},\omega).$$

If additionally considering, that $F_{q,0}(\vec{v})$ is not a function of time and space, eq. (3.24) delivers a solution for the distribution function $F_{q,1}$:

$$F_{q,1}(\vec{k},\vec{v},\omega) = \frac{-\hat{\imath}F_{q,1}(\vec{k},\vec{v},0) - \frac{q\vec{k}}{m\varepsilon_0 k^2}\rho_1(\vec{k},\omega)\cdot\frac{\partial F_{q,0}}{\partial \vec{v}}}{\omega - \vec{k}\cdot\vec{v} - \hat{\imath}\gamma}. \tag{3.26}$$

By inserting eqs. (3.23) and (3.26) into eq. (3.16), an expression for $n_e$ and $n_i$ is obtained.

$$n_{e,1}(\vec{k},\omega-\hat{\imath}\gamma) = -\hat{\imath}\sum_{j=i}^{N}\frac{e^{\hat{\imath}\vec{k}\cdot\vec{r}_j(0)}}{\omega-\vec{k}\cdot\vec{v}_j(0)-\hat{\imath}\gamma} + \frac{\chi_e(\vec{k},\omega)\rho_1(\vec{k},\omega)}{e} \tag{3.27}$$

$$n_{i,1}(\vec{k},\omega-\hat{\imath}\gamma) = -\hat{\imath}\sum_{l=i}^{N/Z}\frac{e^{\hat{\imath}\vec{k}\cdot\vec{r}_l(0)}}{\omega-\vec{k}\cdot\vec{v}_l(0)-\hat{\imath}\gamma} - \frac{\chi_i(\vec{k},\omega)\rho_1(\vec{k},\omega)}{Ze} \tag{3.28}$$

[1] Here $\gamma = \frac{1}{T} > 0$ is introduced in order to ensure, that the Laplace integral converges in the case it would not converge for $\gamma = 0$. For the final calculation of $S(\vec{k},\omega)$ $\gamma \to 0$ will be considered.

with electron and ion susceptibilities $\chi_e$ and $\chi_i$ described by

$$\chi_e(\vec{k},\omega) = \int_{-\infty}^{\infty} \frac{e^2 n_{e0}}{m_e \varepsilon_0 k^2} \frac{\vec{k}\cdot\frac{\partial f_e}{\partial \vec{v}}}{\omega - \vec{k}\cdot\vec{v} - \hat{\imath}\gamma} d^3\vec{v}, \tag{3.29}$$

$$\chi_i(\vec{k},\omega) = \int_{-\infty}^{\infty} \frac{Z^2 e^2 n_{i0}}{m_i \varepsilon_0 k^2} \frac{\vec{k}\cdot\frac{\partial f_i}{\partial \vec{v}}}{\omega - \vec{k}\cdot\vec{v} - \hat{\imath}\gamma} d^3\vec{v}. \tag{3.30}$$

The substitution of eq. (3.25) into eq. (3.27) delivers

$$n_{e,1}(\vec{k},\omega-\hat{\imath}\gamma) = -\hat{\imath}\left[\sum_{j=i}^{N} \frac{e^{\hat{\imath}\vec{k}\cdot\vec{r}_j(0)}}{\omega - \vec{k}\cdot\vec{v}_j(0) - \hat{\imath}\gamma} - \frac{\chi_e}{\epsilon}\sum_{j=i}^{N} \frac{e^{\hat{\imath}\vec{k}\cdot\vec{r}_j(0)}}{\omega - \vec{k}\cdot\vec{v}_j(0) - \hat{\imath}\gamma} + \right.$$
$$\left. + \frac{Z\chi_e}{\epsilon}\sum_{l=i}^{N/Z} \frac{e^{\hat{\imath}\vec{k}\cdot\vec{r}_l(0)}}{\omega - \vec{k}\cdot\vec{v}_l(0) - \hat{\imath}\gamma}\right]. \tag{3.31}$$

Equation (3.31) has three terms contributing to the fluctuating electron density. They can be interpreted as follows. The first term describes the contribution of free electrons, which are not perturbed by the interaction with other particles in the plasma. This term determines the spectrum in the noncollective mode. The second term describes contribution of electrons interacting with other free electrons due to the Coulomb force. This part mainly contributes to the spectrum in the collective scattering mode. The last part of the expression is known as the ion feature, which origins from the interaction of electrons and ions.

By means of $\chi_e$ and $\chi_i$ the longitudinal dielectric function $\epsilon(\vec{k},\omega)$ is defined:

$$\epsilon(\vec{k},\omega) = 1 + \chi_e(\vec{k},\omega) + \chi_i(\vec{k},\omega). \tag{3.32}$$

Finally $S(\vec{k},\omega)$ is obtained by inserting eq. (3.31) into eq. (3.18). It can be simplified to

$$S(\vec{k},\omega) = \frac{1}{k}\left|1 - \frac{\chi_e}{\epsilon}\right|^2 f_e\left(\frac{\omega}{k}\right) + \frac{Z}{k}\left|\frac{\chi_e}{\epsilon}\right|^2 f_i\left(\frac{\omega}{k}\right). \tag{3.33}$$

$f_e\left(\frac{\omega}{k}\right)$ and $f_i\left(\frac{\omega}{k}\right)$ represent velocity distributions in the direction of $\vec{k}$ according to definition in eq. (3.9).

The absolute value of the shift wave number $|\vec{k}|$ can be derived from the scattering diagram illustrated in fig. 3.3:

$$|\vec{k}| = \left(|\vec{k}_S|^2 + |\vec{k}_I|^2 + 2|\vec{k}_S||\vec{k}_I|\cos(\theta)\right)^2. \tag{3.34}$$

For the non relativistic case ($v/c \ll 1$), $|\vec{k}_S| \simeq |\vec{k}_I|$ can be assumed from the definition in eq. (3.9), which delivers

$$k = |\vec{k}| \simeq 2|\vec{k}_I|\sin(\theta/2) = 2\left|\frac{\omega_I}{c}\right|\sin(\theta/2) = \frac{4\pi}{\lambda_I}\sin(\theta/2). \tag{3.35}$$

### 3.1.4 Salpeter approximation

So far an expression for $S(\vec{k},\omega)$ with a general electron and ion distribution functions $f_e$ and $f_i$ has been derived. Now the special case of the plasma close to LTE will be examined. It can be assumed that the electron and ion velocity distributions are Maxwellian. For simplicity only a one dimensional distribution for each species is used here:

$$f_e(v)dv = \left(\frac{1}{\pi v_e^2}\right)^{1/2}\exp\left(-\frac{v^2}{v_e^2}\right)dv \text{ and } f_i(v)dv = \left(\frac{1}{\pi v_i^2}\right)^{1/2}\exp\left(-\frac{v^2}{v_i^2}\right)dv. \tag{3.36}$$

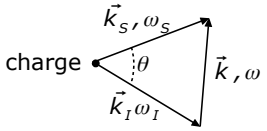


Figure 3.3: Wave vector diagram for the scattering of the radiation.

with $v_e$ as electron and $v_i$ as ion thermal velocities

$$v_e = \left(\frac{2k_\mathrm{B}T_e}{m_e}\right)^{1/2} \text{ and } v_i = \left(\frac{2k_\mathrm{B}T_i}{m_i}\right)^{1/2}.$$

When inserting eq. (3.36) into eq. (3.33), the susceptibility functions in eqs. (3.29) and (3.30) can be explicitly calculated. For the susceptibility $\chi_q$ of the species with a charge $q$ with the thermal velocity $v_q$ one obtains

$$\begin{aligned}
\chi_q(\vec{k},\omega) = & \int_{-\infty}^{\infty} \frac{q^2 n_{e0}}{m_q \varepsilon_0 k^2} \frac{1}{\sqrt{\pi} v_q} \frac{k\left(-\frac{2v}{v_q^2}\exp\left(-\frac{v^2}{v_q^2}\right)\right)}{\omega - kv - \hat{\imath}\gamma} dv \\
= & \left(\frac{1}{k\lambda_{\mathrm{D}q}}\right)^2 \frac{1}{v_q\sqrt{\pi}} \int_{-\infty}^{\infty} \frac{kv\exp\left(-\frac{v^2}{v_q^2}\right)}{-\omega + kv + \hat{\imath}\gamma} dv \left| \begin{smallmatrix} x=\frac{v}{v_q} \\ x_q=\frac{\omega}{kv_q} \\ \alpha=k\lambda_{\mathrm{D}q} \end{smallmatrix} \right. \\
= & \frac{\alpha^2}{\sqrt{\pi}} \int_{-\infty}^{\infty} \frac{x\exp\left(-x^2\right)}{-x_q + x + \hat{\imath}\frac{\gamma}{kv_q}} dx
\end{aligned}$$

Using Cauchy theorem the last integral can be simplified to

$$Rw(x_q) + \hat{\imath}Iw(x_q) = 1 - 2x\exp(-x_q^2)\int_0^{x_q} \exp(p^2)dp - \hat{\imath}\pi^{1/2}x\exp(-x_q^2). \tag{3.37}$$

The detailed derivation can be found in [38]. Now $\chi_e$ and $\chi_i$ can be expressed as

$$\begin{aligned}
\chi_e(\vec{k},\omega) &= \alpha^2\left[Rw(x_e) + \hat{\imath}Iw(x_e)\right] \\
\chi_i(\vec{k},\omega) &= \alpha^2\frac{ZT_e}{T_i}\left[Rw(x_i) + \hat{\imath}Iw(x_i)\right] \qquad (3.38) \\
x_e = \frac{\omega}{kv_e},\ x_i &= \frac{\omega}{kv_i} \text{ and } \alpha = \frac{1}{k\lambda_{De}} \qquad (3.39)
\end{aligned}$$

with $k$ and $\omega$ as defined in eqs. (3.9) and (3.35) and $x_e$ and $x_i$ the normed frequency scales and $\lambda_{\mathrm{D}e}$ the Debye length of the plasmas free electrons. The imaginary part of the susceptibility function is also known as Landau damping term, which describes the energy exchange between the electromagnetic wave and the particles. Now eq. (3.33) can be written as

$$S(\vec{k},\omega) = S_e(\vec{k},\omega) + S_i(\vec{k},\omega) = \frac{1}{\sqrt{\pi}v_e k}\left|\frac{1+\chi_i}{1+\chi_e+\chi_i}\right|^2 e^{-x_e^2} + Z\frac{1}{\sqrt{\pi}v_i k}\left|\frac{\chi_e}{1+\chi_e+\chi_i}\right|^{1/2} e^{-x_i^2}. \tag{3.40}$$

Here $S_e(\vec{k},\omega)$ and $S_i(\vec{k},\omega)$ denote the electron and the ion feature of the scattering spectrum. The electron feature contains the interaction of the incident radiation with the free electrons in the plasma, as described by the first two terms of eq. (3.31). The ion feature expresses the interaction of the ion as given in the third term of eq. (3.31).

In order to further simplify eq. (3.40) a closer look at the numerical behavior of the eq. (3.37) can be taken. For $x \to \infty$ both $Rw(x)$ and $Iw(x)$ converge towards zero as illustrated in fig. 3.4. The relevant contribution to the electron feature arises from these contributions close to $x_e \simeq 1$. This contribution corresponds to the high frequency part of the spectrum ($\omega \gg \omega_{pi} = \sqrt{\frac{n_i e^2}{m_i \varepsilon_0}}$, while $\omega \gtrsim \omega_{pe}$ due to very small $\frac{m_e}{m_i}$). For this part of the spectrum $x_i \gg 1$, so that the $\chi_i \to 0$ is valid. Thus, the electron feature $S_e(\vec{k},\omega)$ simplifies to

$$S_e(\vec{k},\omega) \simeq \frac{1}{\sqrt{\pi} v_e k} \left| \frac{1}{1+\chi_e} \right|^2 e^{-x_e^2}. \tag{3.41}$$

It should be considered, that this approximation is only valid for high frequencies. At low frequencies the ions may influence the spectrum depending on the order of $T_e/T_i$.

For the ion feature of the scattering spectrum similar simplifications can be applied. For the case $x_e/x_i = \sqrt{m_e T_i / m_i T_e} \ll 1$ the relevant contribution of the ion feature ranges in the order of $x_i \simeq 1$ so that $x_e$ is close to zero. Consequently, $Rw(x_e) \simeq 1$ and $Iw(x_e) \simeq 0$ can be assumed, so that the expression for $S_i(\vec{k},\omega)$ simplifies to

$$S_i(\vec{k},\omega) \simeq \frac{Z}{\sqrt{\pi} v_i k} \left| \frac{\alpha^2}{1+\alpha^2+\chi_i} \right|^2 e^{-x_i^2}. \tag{3.42}$$

Equations (3.41) and (3.42) imply, that the ion and the electron features are spectrally separated from the central wavelength and from each other. Figure 3.5 visualizes this separation for a scattering spectrum arising from a typical welding plasma. Here $\lambda_I$=532 nm is chosen. It is the central wavelength of an Nd:YAG laser - a typical radiation source for Thomson scattering measurements. In this example the ion feature can be found close to $\lambda_I$, at a distance in the range of 10 pm. The electron feature however is located further away, at a distance in the range of 1 nm.

The scattering spectrum $S(\vec{k},\omega)$ can also be written as a function of wavelength. Using the relation $\omega\lambda = 2\pi c_0$ and the approximation $\omega_s \simeq \omega_i$ for a non relativistic plasma, one

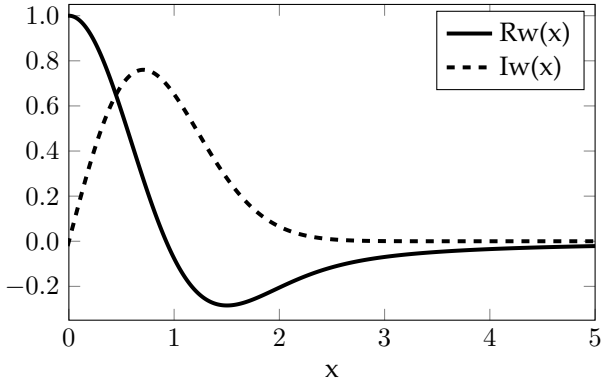


Figure 3.4: Real part Rw(x) and imaginary part Iw(x) of the plasma dispersion function (eq. (3.37)).

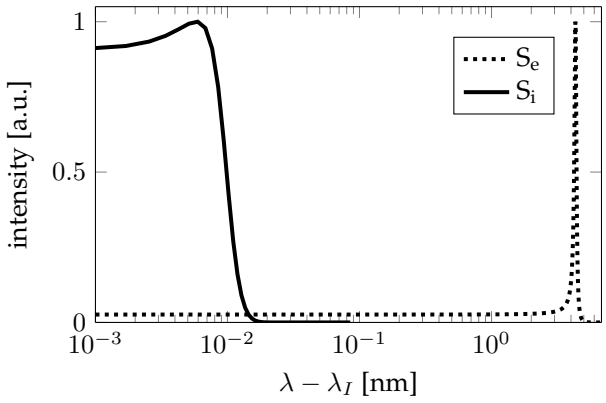


Figure 3.5: Example of an electron and ion feature of the Thomson scattering spectrum for an argon plasma with $Z = 1$, $T_e = T_i = 1.5 \times 10^4\,\mathrm{K}$ and $\alpha = 3$. Here $\lambda_I = 532\,\mathrm{nm}$ and $\theta = 90°$ are chosen. Note the logarithmic scale in the wavelength shift.

obtains

$$\begin{aligned} \lambda = \lambda_S - \lambda_I &= x_e a \frac{2\lambda_I \sin(\theta/2)}{c} && \text{for the electron feature and} \\ &= x_i b \frac{2\lambda_I \sin(\theta/2)}{c} && \text{for the ion feature.} \end{aligned} \tag{3.43}$$

As already stated in section 3.1.3, two modes of Thomson scattering – *noncollective* and *collective* - can be distinguished. In the case of Salpeter approximation these modes can be characterized by the parameter $\alpha$. For $\alpha < 1$ the shape of $S_e(\vec{k}, \omega)$ becomes Gaussian. It mainly reflects the thermal fluctuation of the electrons, whereas for $\alpha \geq 1$ the influence of charges interaction becomes visible in the spectrum, as illustrated in fig. 3.6.

The Salpeter approximation does not hold for $S_i$, if $T_e/T_i$ considerably larger than 1 or an electron motion is present. This typically occurs, when considerable currents flow through the plasma. Here the electrons, which are much lighter than the ions, have a drift velocity $\vec{v_d}$ in the direction of wave vector $\vec{k}$. This modifies the electron velocity distribution to

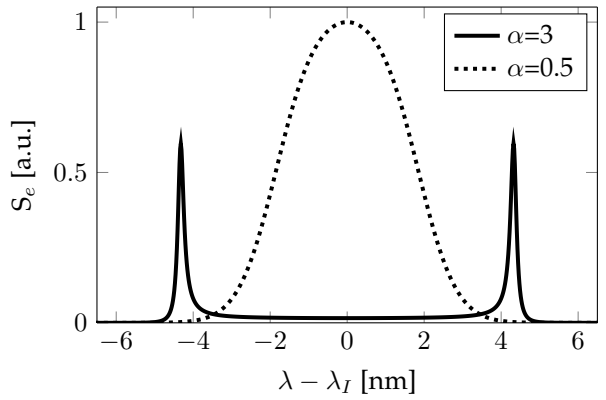


Figure 3.6: Example of the electron feature $S_e$ calculated for $T_e = 1.5 \times 10^4\,\mathrm{K}$ in the collective mode ($\alpha = 3$) and noncollective mode ($\alpha = 0.5$). Here $\lambda_I = 532\,\mathrm{nm}$ and $\theta = 90°$ are chosen.

$$f_{e,v_d} = \left(\frac{1}{\pi a^2}\right)^{1/2} \exp\left(-\frac{(v-v_d)^2}{a^2}\right) = f_e(v-v_d).$$

With the normalized frequency shift due to the drift $x_d = \frac{\vec{v_d}\cdot\vec{k}}{ka}$ the electron feature of the Thomson scattering spectrum given in eq. (3.40) can be rewritten as

$$S_e(\vec{k},\omega) \simeq \frac{1}{\sqrt{\pi}ak}\left|\frac{1}{1+\alpha^2\left(Re(x_e-x_d)+\hat{\imath}Iw(x_e-x_d)\right)}\right|^2 e^{-(x_e-x_d)^2}. \tag{3.44}$$

Hence the electron feature is simply Doppler shifted around the central wavelength, while the shape remains unchanged. The situation is however different for the ion feature. Here the scattering spectrum is given by

$$S_i(\vec{k},\omega) \simeq \frac{1}{\sqrt{\pi}bk}\left|\frac{\alpha^2\left(Re(x_e-x_d)+\hat{\imath}Iw(x_e-x_d)\right)}{1+\alpha^2\left(Re(x_e-x_d)+\hat{\imath}Iw(x_e-x_d)+\frac{ZT_e}{T_i}\left(Re(x_i)+\hat{\imath}Iw(x_i)\right)\right)}\right|^2 e^{-(x_i)^2}. \tag{3.45}$$

This results in an asymmetric ion feature as illustrated in fig. 3.7.

In order to estimate a possible shift of the electron feature and the asymmetry of the ion feature the drift velocity of the electrons in the welding arc column needs to be estimated. For currents in the order of $100\,\mathrm{A}$ and an arc diameter of $5\,\mathrm{mm}$ current densities in the order of $10\,\frac{\mathrm{A}}{\mathrm{mm}^2}$ can be expected. The absolute value of the current density $j$ is given by

$$j = en_e v_d.$$

For a typical density of $n_e = 10^{23}\,\mathrm{m}^{-3}$ one obtains a drift velocity of $v_d \approxeq 6\times10^2\,\mathrm{m/s}$. This corresponds to a maximum normalized shift of $x_d = 0.001$ at $T = 1.5\times10^4\,\mathrm{K}$. At the scattering angle of $\theta = 90°$ and $\lambda_I = 532\,\mathrm{nm}$ this is equivalent to the wavelength shift of $S_e$ by $\Delta\lambda \approxeq 2\,\mathrm{pm}$, which cannot be resolved by an ordinary spectrometer with a typical wavelength range. As can be seen in fig. 3.7 almost no asymmetry is visible for $x_d$ of this order for the ion feature $S_i$.

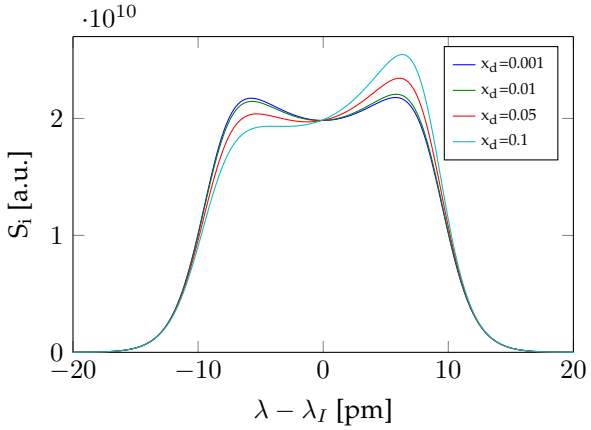


Figure 3.7: Ion feature for different normed frequency drifts $x_d$ for an argon plasma with $Z = 1$, $T_e = T_i = 1.5\times10^4\,\mathrm{K}$ and $\alpha = 3$.

## 3.2 Spectral line broadening in plasmas

In contrast to gaseous states the plasma state can be easily recognized by the human eye. The reason is simple - plasma glows. The radiation emitted by a plasma can deliver information about its current state without disturbing the measuring object by any kinds of probes. Here various radiation characteristics, such as absolute intensity values of lines, line ratios or shapes, can be evaluated in order to deduce e.g. plasma temperature and density. Although the detection of the radiation is relatively straightforward, the evaluation of the obtained data often involves a detailed model of the plasma with numerous assumptions to be fulfilled.

The following section focuses on the analysis of the line shape as a diagnostic technique for plasma temperature and density determination. First the general process of emission of radiation by atoms and ions in a plasma will be briefly discussed. Thereafter, different types of line broadening mechanisms will be presented. The theory of the Stark effect is discussed in more detail. Here the mechanisms responsible for the linear and quadratic Stark effect are derived using the quantum mechanical description of the line emission phenomena and the interaction of the emitting species with the surrounding plasma particles. Finally, the particular cases describing the line profiles of argon and hydrogen lines are discussed. The discussion of the quantum mechanical phenomena presented in this section is based on the works of Schiff and Griem [101, 112].

### 3.2.1 Emission of electromagnetic radiation in a plasma

There are several processes responsible for the radiation produced by a plasma. However, the process delivering most of the radiation energy is the line radiation arising from the electrons bound inside the atoms or ions. Here a photon is emitted, when a bound electron makes a transition from an excited energy level $E_m$ to a lower level $E_n$. According to the principle of conservation of energy the frequency of the photon is given by [102]

$$\nu_{mn} = \frac{E_m - E_n}{h}. \tag{3.46}$$

The spectral line arising from this transition is described by the emission coefficient of the transition $m \to n$ is defined as the energy emitted per unit solid angle and unit time

$$\varepsilon_{m\to n} = \frac{h\nu_{mn}}{4\pi} A_{m\to n} n_m \mathcal{L}(\nu). \tag{3.47}$$

Here $n_m$ denotes the density of the upper energy level $E_m$, whereas the Einstein coefficient $A_{m\to n}$ describes the transition probability rate of a specific transition. $\mathcal{L}(\nu)$ is the spectral profile of the emitted line. Typically, it is given as a normalized function of angular frequency $\omega = 2\pi\nu$ with

$$\int_{-\infty}^{\infty} \mathcal{L}(\omega) d\omega = 1. \tag{3.48}$$

In the majority of cases the line shapes are described by the Lorentz profile $\mathcal{L}_{\mathrm{Lor}}$ or by the Gauss profile $\mathcal{L}_{\mathrm{G}}$:

$$\mathcal{L}_{\mathrm{Lor}}(\omega) = \frac{1}{\pi} \frac{\delta/2}{(\omega - \omega_0)^2 + (\delta/2)^2} \qquad \text{with } \Delta\omega_{\mathrm{Lor}} = \delta, \tag{3.49}$$

$$\mathcal{L}_{\mathrm{G}}(\omega) = \frac{1}{\sigma\sqrt{2\pi}} \exp\left[-\frac{1}{2}\left(\frac{\omega - \omega_0}{\sigma}\right)^2\right] \qquad \text{with } \Delta\omega_{\mathrm{G}} = \sigma\sqrt{8\ln 2}. \tag{3.50}$$

Here $\Delta\omega$ represents the full width half maximum (FWHM) of the line profile. Experimentally the line shape is measured as a function of wavelength. If $\Delta\lambda \ll \lambda_0$, then

$$\mathcal{L}(\lambda) = \frac{2\pi}{\lambda_0^2}\mathcal{L}(\omega) \tag{3.51}$$

is valid. If several effects with different line profiles influence the transition process, then the resulting line profile is give as the convolution of the single profiles

$$\mathcal{L}(\omega) = \mathcal{L}_1(\omega) * \mathcal{L}_2(\omega) = \int \mathcal{L}_1(\tau) \cdot \mathcal{L}_2(\omega - \tau) d\tau. \tag{3.52}$$

The convolution of Lorentzian and Gaussian line profiles results in the Voigt profile.

$$\mathcal{L}_{\mathrm{V}}(\omega) = \mathcal{L}_{\mathrm{Lor}} * \mathcal{L}_{\mathrm{G}} \tag{3.53}$$

The Voigt profile can be approximated by the pseudo-Voigt function defined as a linear combination fo the Gaussian and Lorentzian profiles [113]:

$$\mathcal{L}_{\mathrm{pV}}(\omega) = \eta\mathcal{L}_{\mathrm{Lor}}(\omega) + (1-\eta)\mathcal{L}_{\mathrm{G}}(\omega) \text{ with } 0 < \eta < 1 \tag{3.54}$$

The advantage of the pseudo-Voigt profile is, that it is more convenient for fitting purposes than the original definition of the Voigt profile. The deviation of the two functions lies below $1\,\%$, which delivers an acceptable accuracy.

### 3.2.2 Types of line broadening

The particular shape of a spectral line strongly depends on the circumstances under which the photon is emitted. There are several types of broadening mechanisms, which can take place in a plasma.

In the first place all the emitted lines are broadened due to the Heisenberg's uncertainty principle. It relates the uncertainty of the lifetime of an excited state to the uncertainty of the difference between the upper and lower energy state. In accordance with this principle the shape of the emitted line is not an ideal Dirac's delta function, but is already naturally broadened. However, the width achieved by the *natural broadening* usually does not exceed $10^{-5}\,\mathrm{nm}$ [114]. Thus, in the experiment the natural broadening does not need to be considered, since when convoluted with the apparatus function of the spectrometer, which usually lies in the order of $10^{-2}\,\mathrm{nm}$, it has no measurable influence on the final line shape.

The *Doppler broadening* has a considerably higher impact on the shape of the emitted line. It originates from the movement of the emitter relative to the observer, which leads to a shift of the emitting frequency. If the emitter with a charge $q$ moves with a velocity $v_q$ towards the detector, then the frequency shift is obtained from

$$\omega = \omega_0 + \omega_0\frac{v_q}{c}. \tag{3.55}$$

The profile of the line broadened by the Doppler effect can be derived from the following relation [102, 115]:

$$\mathcal{L}(\omega)d\omega = f(v_q)dv_q. \tag{3.56}$$

By assuming a one dimensional Maxwellian velocity distribution as given in eq. (3.36) a Gaussian profile is obtained for a Doppler broadened line:

$$\mathcal{L}(\omega) = \frac{c}{\omega_0}\sqrt{\frac{1}{\pi\overline{v_q}}}\exp\left[-\left(\frac{c}{\overline{v_q}}\frac{\omega-\omega_0}{\omega_0}\right)^2\right] \tag{3.57}$$

$$\text{with } \Delta\omega = \frac{\overline{v_q}\omega_0}{c}\sqrt{4\ln 2} = \omega_0\sqrt{\frac{8\ln 2 k_{\mathrm{B}}T_q}{m_q c^2}}.$$

Here $\overline{v_q}$ and $T_q$ represent the thermal velocity and temperature of the species with a charge $q$.

For a plasma with the thermalized velocity distribution of different species one can easily estimate the expected broadening line width. Figure 3.8 shows the calculated Doppler width $\Delta\lambda_{\mathrm{Dop}}$ in comparison to the width $\Delta\lambda_{\mathrm{Dop*App}}$ resulting from the Doppler and apparatus profiles in the relevant temperature range from $5000$ to $24\,000\,\mathrm{K}$ for an Ar I emitter in a pure argon plasma. It can be clearly seen, that the resulting width $\Delta\lambda_{\mathrm{Dop*App}}$ does not significantly change with increasing temperature. Hence the Doppler broadening can be neglected, when evaluating line profiles emitted in welding plasmas with the given apparatus profile.

In the two previous cases the broadening of the spectral line is caused by the state of the emitter itself. Pressure broadening occurs, if the surrounding particles influence the emitter. Depending on the type of the perturbing particle different types of pressure broadening are distinguished. *Resonance broadening* is caused by the interaction of particles of the same type during a resonant transition. If neutral unlike particles influence the ground state level of the emitting species, *van-der-Waals broadening* is present. In welding plasmas the broadening width resulting from both resonance and van-der-Waals mechanisms is smaller than the Doppler broadening width. For example, for the Ar I $696.5\,\mathrm{nm}$ line the impact of van-der-Waals broadening lies in the range of $1\,\mathrm{pm}$ [97]. Similar estimation is obtained for the hydrogen lines. For $H_\alpha = 656.3\,\mathrm{nm}$ and $H_\beta = 486.1\,\mathrm{nm}$ the van-der-Waals broadening width lies in the range of $1$ to $9\,\mathrm{pm}$ [116, 117]. Hence the influence of these broadening effects can be neglected as well.

Stark effect describes line broadening caused by charged particles, namely electrons or ions, in the plasma. Under the conditions which prevail in welding plasmas, this type of broadening mostly determines the shape of the emitted line. There is no general solution estimating the spectral line shape caused by the Stark effect. This originates from the fact, that the resulting line shape strongly depends on the atomic structure of the emitter and the types, if interaction of the emitter with its surrounding. Mainly two approaches, the impact and quasi-static approximation, form the basic concept for the description of the resulting spectral line shape. This is discussed in the following.

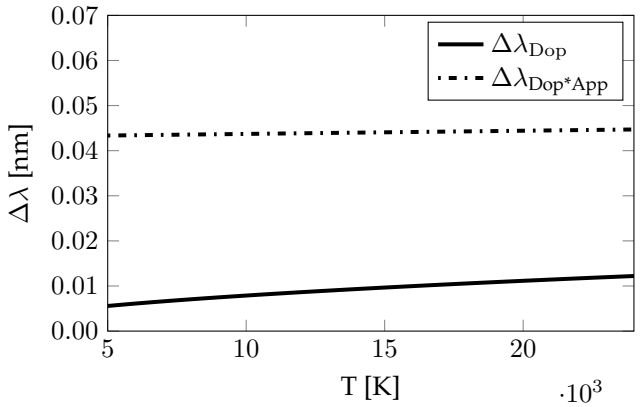


Figure 3.8: Doppler broadening width calculated for the Ar I resonance line ($\lambda_0 = 696.5\,\mathrm{nm}$) emitted in a pure argon plasma in dependence of the temperature (solid line); Doppler broadening width convoluted with the apparatus function with the instrumental width $\Delta\lambda_{\mathrm{App}} = 0.043\,\mathrm{nm}$ (dashed line).

### 3.2.3 Quantum mechanical description of spontaneous line emission

In order to predict the influence of the surrounding electrons, ions and atoms on the line shape quantum theoretical description of the radiation process is used.

In general the current state of the physical system is described by the Schrödinger equation.

$$\hat{\imath}\hbar\frac{\partial}{\partial t}\varphi_n(x,t) = H(\underline{p},\underline{q})\varphi_n(x,t). \tag{3.58}$$

Here $\varphi_n(x,t)$ is the state function, which is also denoted as $|n\rangle$. $H(\underline{p},\underline{q})$ is the Hamiltonian operator describing the energy of the system as a function of the momentum operator $\underline{p}$ and position operator $\underline{q}$. For $H(\mathfrak{p},\mathfrak{q})$ the Hamiltonian equation of motion

$$\frac{\partial q}{\partial t} = \frac{\partial H}{\partial p} \text{ and } \frac{\partial p}{\partial t} = -\frac{\partial H}{\partial q} \tag{3.59}$$

are valid. The probability distribution of finding a particle in a state $|n\rangle$ is given by

$$f_n(x,t) = \varphi_n^*(x,t)\varphi_n(x,t) \tag{3.60}$$

with

$$\langle n|n\rangle = \int_{-\infty}^{\infty} \varphi_n^*(x,t)\varphi_n(x,t)dx = 1. \tag{3.61}$$

The expectation value for a macroscopic measurement of the state $\varphi$ by means of the measurable variable/operator $\underline{A}$ corresponds to

$$\langle n|A|n\rangle = \int_{-\infty}^{\infty} \varphi_n^*(x,t)\underline{A}(\underline{p},\underline{q})\varphi_n(x,t)dx. \tag{3.62}$$

Such variable might be space or momentum operators themselves. E.g. the action of the position operator $\underline{q}$ on the state $|n\rangle$ just "reads" the space coordinate for that space: $\underline{q}|n\rangle = x|n\rangle$.

An unperturbed bound electron within an atom can be described using the following approach. Its state function is assumed to be defined as a product of the temporal and spatial components:

$$\Phi_n(x,t) = \exp(-\hat{\imath}E_n t/\hbar)\varphi_n(x). \tag{3.63}$$

Here $E_n$ denotes the energy level of the electron. It is assumed, that for different energy levels

$$\langle n|m\rangle = \begin{cases} 1 & n = m \\ 0 & n \neq m \end{cases} \tag{3.64}$$

is valid, corresponding to the case of no energy degeneracy (each state has different energy).

Whenever a perturbation is introduced the Hamiltonian $H$ is described as

$$H = H_0 + H_{int}. \tag{3.65}$$

$H_0$ is the Hamiltonian of the unperturbed and $H_{int}$ of the perturbed system. The following expansion can be applied to solve the Schrödinger equation

$$\Phi_n(x,t) = \sum_m c_{nm}(t)\varphi_m(x) = \sum_m c_{nm}(t)\exp(-\hat{\imath}E_m t/\hbar)|m\rangle. \tag{3.66}$$

By inserting eq. (3.66) into eq. (3.58) a differential equation of the first order is obtained. Under the assumption of initial condition $c_{nm}(t=0) = 1$ and if the magnitude of perturbation is small compared to the unperturbed state, it is possible to obtain the solution

for $c_{nm}$. Therefrom *Fermi's golden rule* can be formulated. It gives the probability per unit time for a transition of an electron from the state $|m\rangle$ to the state $|n\rangle$. For the first order approximation it delivers

$$\frac{|c_{nm}|^2}{t} = \frac{2\pi}{\hbar} \left|\langle n| H_{int} |m\rangle\right|^2 D(E_n) \tag{3.67}$$

with $D(E_n)$ the density of final states with an energy $E_n$ or, in other words, the number of photons emitted within the frequency $\omega_{nm}$. If $\langle n|H_{int}|m\rangle = 0$, the second order approximation must be used

$$\frac{|c_{nm}|^2}{t} = \frac{2\pi}{\hbar} \left| \sum_{n'} \frac{\langle n| H_{int} |n'\rangle \langle n'| H_{int} |m\rangle}{E_m - E_{n'}} \right|^2 D(E_n). \tag{3.68}$$

Now, in order to describe the probability of a transition of an electron from energy level $E_m$ to $E_n$ in the presence of an external field generated by surrounding electrons or ions the Hamiltonian of this system has to be formulated as

$$H_{tot} = H_{part,0} + H_{rad} + H_{int}. \tag{3.69}$$

The Hamiltonian of the electromagnetic radiation $H_{rad}$ is given by

$$H_{rad} = \int_V \left[ \frac{\varepsilon_0}{2} \vec{E}^2 + \frac{1}{2\mu_0} \vec{B}^2 \right] d^3\vec{x} \tag{3.70}$$

and contributes to the unperturbed Hamiltonian $H_0$. The Hamiltonian of an unperturbed bound electron is composed of its kinetic and potential energy

$$H_{part,0} = \frac{\underline{p}_0^2}{2m_e} + E_{pot}(\underline{q}). \tag{3.71}$$

However it needs to be taken into account, that the momentum $\underline{p}$ can be influenced by the external electromagnetic field, which introduces the perturbation. In the quantum-mechanical description the compact formulation of the electromagnetic field with a vector $\vec{A}(\underline{q}, t)$ and the scalar potential $\phi$ with

$$\begin{aligned} \vec{E} &= -\frac{\partial \vec{A}}{\partial t} - \nabla\phi, \\ \vec{B} &= \vec{\nabla} \times \vec{A} \end{aligned} \tag{3.72}$$

is used. This allows the formulation of a momentum of a bound electron under the influence of electromagnetic field as

$$\underline{p} = m_e \frac{\partial \underline{q}}{\partial t} - e\vec{A} = \underline{p}_0 - e\vec{A} \tag{3.73}$$

and the potential energy as

$$E_{pot} = E_{pot,0} - e\phi. \tag{3.74}$$

By combining eqs. (3.69), (3.71) and (3.73) and by setting $\phi = 0$ (Gauge invariance) the Hamiltonian of the perturbed electron is obtained:

$$H_{tot} = \frac{\left(\underline{p} + e\vec{A}\right)^2}{2m_e} + E_{pot}(\underline{q}) + H_{rad} = \underbrace{\frac{\underline{p}^2}{2m_e} + E_{pot}(\underline{q})}_{H_{part,0}} + H_{rad} + \underbrace{\frac{e\underline{p}\vec{A}}{m_e} + \frac{\left(e\vec{A}\right)^2}{2m_e}}_{H_{int}}. \tag{3.75}$$

Since $H_0 \gg H_{int}$ is required, the term with $e^2$ can be omitted, so that

$$H_{int} = \frac{e\underline{p}\vec{A}}{m_e} \tag{3.76}$$

can be assumed. $H_{int}$ describes the interaction of the free charges with the atomic electric dipole formed by the emitting bound electron.

It is possible to define $\vec{A}(\underline{q}, t)$ in the simple electromagnetic configuration with a planar electromagnetic wave propagating along the spatial direction $z$, while the charges interaction can be assumed as weak ($\vec{j} = 0$ and $\rho = 0$):

$$\vec{A}(\underline{q}, t) = \begin{pmatrix} A_x(z,t) \\ 0 \\ 0 \end{pmatrix} \text{ with } A_x(z,t) = \frac{A_\omega(t)\exp(\hat{\imath}kz) + A^*_\omega(t)\exp(-\hat{\imath}kz)}{\sqrt{2}}. \tag{3.77}$$

Here $A^*_\omega(t)$ is the conjugate-complex of $A_\omega(t)$. The latter is chosen so, that $\frac{A_\omega}{dt} = -\hat{\imath}\omega A_\omega$. Now the Hamiltonian of the electromagnetic radiation can be expressed using $\vec{A}(\vec{x}, t)$. Hereby the integration is performed in a volume $V = l^3$. For this case eq. (3.70) simplifies to

$$\begin{aligned} H_{rad} =& \int_V \left[ \frac{\varepsilon_0}{2} \left( \frac{-d\vec{A}(\vec{x,t})}{dt} \right)^2 + \frac{1}{2\mu_0} \left( \vec{\nabla} \times \vec{A}(\vec{x,t}) \right)^2 \right] d^3\vec{x} \\ \underset{\text{eq. (3.3)}}{=} & -\frac{l^2\omega^2\varepsilon_0}{2} \int_{-l/2}^{l/2} \left[ A^2_\omega \exp(\hat{\imath}2kz) + A^{*2}_\omega \exp(-\hat{\imath}2kz) - A^*_\omega A_\omega - A_\omega A^*_\omega \right] dz \\ =& \frac{l^3\omega^2\varepsilon_0}{2} \left( A^*_\omega A_\omega + A_\omega A^*_\omega \right) = \frac{\hbar\omega}{2} \left( \sqrt{\frac{l^3\varepsilon_0\omega}{\hbar}} A^*_\omega \sqrt{\frac{l^3\varepsilon_0\omega}{\hbar}} A_\omega + \sqrt{\frac{l^3\varepsilon_0\omega}{\hbar}} A_\omega \sqrt{\frac{l^3\varepsilon_0\omega}{\hbar}} A^*_\omega \right). \end{aligned}$$

The upper Hamiltonian is analogous to that of a harmonic oscillator [112]. Hence the radiation can be treated as a harmonic oscillator with a corresponding operator $A_\omega$.

Since the Hamiltonian of the unperturbed particle and the radiation are treated as a sum of uncoupled subsystems, the total state of the emitting particle with an electron transition from $E_m$ to $E_n$ can be seen as a product of the particle and radiation states. The combination of this idea with eqs. (3.46), (3.59) and (3.76) allows the following transformation:

$$\left| \langle n | H_{int} | m \rangle \right| = \left| \left\langle n \left| \frac{e\partial\underline{q}\vec{A}}{\partial t} \right| m \right\rangle \right| = \sin\vartheta \sqrt{\frac{\hbar\omega_{nm}}{2l^3\varepsilon_0}} \left| \langle n | e\underline{q} | m \rangle \right| \tag{3.78}$$

with $\vartheta$ the angle between $\underline{q}$ and the direction of the emitted photon. Here again the $e^2$ terms were omitted.

The final result for the transition rate between the initial and final states according to the Fermi's Golden Rule requires the calculation of the density of states $D(E_n)$ for the final energy $E_n$. It can be done by integrating over allowed $\underline{p}$ values within a volume $l^3$. From the uncertainty relation $d\underline{q} \cdot d\underline{p} \gtrsim h$ follows

$$D(E_n)dE_n = g_n \frac{l^3 p^2}{h^3} \underline{p}^2 d\underline{p} 2\pi \sin\vartheta d\vartheta.$$

Here $g_n$ is the number of polarizations of a photon. Using the relation between the momentum and the energy of a photon $p = \frac{E_{photon}}{c} = \frac{\hbar\omega_{nm}}{c}$ one obtains

$$D(E_n) = g_n \frac{l^3\omega^2_{nm}}{4\pi^2\hbar c^3} \sin\vartheta d\vartheta. \tag{3.79}$$

When inserting eqs. (3.78) and (3.79) in eq. (3.67) and integrating over all possible $\vartheta$ the first order approximation of Fermi's golden rule can be simplified to

$$\frac{|c_{nm}|^2}{t} = g_n \frac{\omega_{nm}^3}{3\pi\varepsilon_0\hbar c^3} \left|\langle n| e\underline{q} |m\rangle\right|^2 . \tag{3.80}$$

$\frac{|c_{nm}|^2}{t}$ corresponds to the Einstein coefficient in eq. (3.47). Now the power radiated during the transition $m \to n$ can be expressed as

$$P_{rad} = \frac{|c_{nm}|^2}{t} \hbar\omega_{nm}. \tag{3.81}$$

### 3.2.4 Impact approximation of the linear Stark effect

The first order approximation of Fermi's golden rule (eq. (3.67)) delivers the following expression for the spectral distribution of the radiated power of a single atom:

$$\frac{dP_{rad}}{d\omega} = g_n \frac{\omega_{nm}^4}{3\pi\varepsilon_0 c^3} \left|\langle n| e\underline{q} |m\rangle\right|^2 \delta\left(\omega - \omega_{nm}\right). \tag{3.82}$$

Hence, the line shape produced by a photon of a single atom would correspond to a Dirac's delta function. However, in a plasma an ensemble of spatially distributed emitters is present. Since each position operator is acting at a different time, the line shape produced by such an ensemble will no longer be a delta function. The emitted power of the whole ensemble is described by

$$\frac{dP_{rad}}{d\omega} = g_n \frac{\omega_{nm}^4}{3\pi\varepsilon_0 c^3} \left|\langle n| e\underline{q} |m\rangle\right|^2 \mathcal{L}(\omega) \tag{3.83}$$

with the line shape $\mathcal{L}(\omega)$, for which the definition in eq. (3.48) applies. In order to define $\mathcal{L}(\omega)$ the state function $\Phi$ describing the state of the emitter collective is used. In this case the expression $\langle n| eq |m\rangle$ can be replaced by $\langle \Phi_n| \sum_a e\underline{q}_a |\Phi_m\rangle$ with a position operator $\underline{q}_a$ acting on specific atom $a$ in the collective. Now the line shape can be defined as

$$\mathcal{L}(\omega) = \lim_{\mathcal{T}\to\infty} \frac{\left| \int_{-\mathcal{T}/2}^{\mathcal{T}/2} \exp\left(-\hat{\imath}\omega t\right) \langle \Phi_n| e \sum_a \underline{q}_a |\Phi_m\rangle \, dt \right|^2}{2\pi\mathcal{T} \left|\langle n| e\underline{q} |m\rangle\right|^2}. \tag{3.84}$$

#### 3.2.4.1 Derivation of the Lorentzian line profile

In order to derive the line profile some assumptions are necessary. The perturbation of the bound electron transition is supposed to be mainly caused by the free electrons in the plasma. The electric field of the moving electron passing an emitting atom thus shifts its energy levels. In the impact approximation this effect is treated as elastic collisions between the free electrons and emitting atoms. The atoms are static compared to the free electrons, which are supposed to be moving on a straight line. The collisions are assumed to be instantaneous. This implies, that the duration time of the collision is much smaller than the time between two sub-sequential collisions. More over the collisions are supposed to be statistically independent [102, 115, 118]. Equivalently to eq. (3.63)

$$\langle \Phi_n| \sum_a e\underline{q}_a |\Phi_m\rangle = \varphi(t) \langle n| e\underline{q} |m\rangle \tag{3.85}$$

is defined. Inserted into eq. (3.84) and using the Parseval's relation the definition delivers

$$\begin{aligned}\mathcal{L}(\omega) &= \frac{1}{2\pi}\int_{-\infty}^{\infty}\exp\left(-\hat{\imath}\omega\tau\right)\left[\lim_{T\to\infty}\frac{1}{\mathcal{T}}\int_{-\mathcal{T}/2}^{\mathcal{T}/2}\varphi^*(t')\varphi(t+\tau)dt'\right]d\tau \\ &= \frac{1}{2\pi}\int_{-\infty}^{\infty}\exp\left(-\hat{\imath}\omega\tau\right)\mathcal{C}(\tau)d\tau. \end{aligned} \tag{3.86}$$

$\mathcal{C}(t)$ can be interpreted as the correlation function of the emitted light amplitude. Since however $\mathcal{L}(\omega)$ is supposed to be real, the correlation function must fulfill $\mathcal{C}(-\tau) = \mathcal{C}^*(\tau)$ [101]. Here again $^*$ denotes the conjugate-complex. This simplifies eq. (3.86) to

$$\mathcal{L}(\omega) = \frac{1}{\pi}\mathrm{Re}\left\{\int_0^{\infty}\exp\left(-\hat{\imath}\omega\tau\right)\mathcal{C}(\tau)d\tau\right\}. \tag{3.87}$$

$\varphi(t)$ describes the oscillation of the atoms in time and can be assumed as

$$\varphi(t) = \exp\left(\hat{\imath}\omega_{nm}t + \hat{\imath}\int_{-\infty}^{t}\kappa(t')dt'\right) = \exp\left(\hat{\imath}\omega_{nm}t + \hat{\imath}\eta(t)\right). \tag{3.88}$$

The variation of the unperturbed oscillation frequency $\omega_{nm}$ arises due to collisions with perturbing particles, which leads to the phase shift $\kappa(t')$. The total phase shift $\eta(t)$ is simply defined by the integral over all phase shifts, which occurred until the time $t$. Under the previously stated assumptions it is possible to derive the line shape of the emitted line by calculating $\mathcal{C}(t)$ [115, 119]. By inserting eq. (3.88) into eq. (3.86) the following expression for $\mathcal{C}(\tau)$ is obtained

$$\begin{aligned}\mathcal{C}(\tau) &= \lim_{\mathcal{T}\to\infty}\frac{1}{\mathcal{T}}\int_{-\mathcal{T}/2}^{\mathcal{T}/2}\exp\left(-\hat{\imath}\omega_{nm}t' - \hat{\imath}\eta(t')\right)\exp\left(\hat{\imath}\omega_{nm}(t'+\tau) + \hat{\imath}\eta(t'+\tau)\right)dt' \\ &= \exp(\hat{\imath}\omega_{nm}\tau)\lim_{\mathcal{T}\to\infty}\frac{1}{\mathcal{T}}\int_{-\mathcal{T}/2}^{\mathcal{T}/2}\exp\left(-\hat{\imath}\eta(t') + \hat{\imath}\eta(t'+\tau)\right)dt' \\ &= \exp(\hat{\imath}\omega_{nm}\tau)\mathcal{C}'(\tau). \end{aligned} \tag{3.89}$$

Assuming that the collisions are statistically independent $-\eta(t') + \eta(t'+\tau) = \eta_k$ is valid with $\eta_k$ a time independent random number. The time average is now replaced by the statistical average over the collision probability resulting in all possible phase shifts $\eta_k$. The collision probability $\mathcal{P}_{col}$ can be derived from definition in eq. (2.1) as

$$\mathcal{P}_{col} = f_e(v_e)n_e dv_e d\tau d\sigma. \tag{3.90}$$

Now $\mathcal{C}'(\tau)$ simplifies to

$$\mathcal{C}'(\tau) = \tau n_e\iint\exp\left(-\hat{\imath}\eta_k(\tau)\right)f_e(v_e)dv_e d\sigma = \langle\exp\left(-\hat{\imath}\eta_k(\tau)\right)\rangle. \tag{3.91}$$

In order to solve eq. (3.91) $\Delta\mathcal{C}'(\tau)$ is calculated.

$$\begin{aligned}\Delta\mathcal{C}'(\tau) &= (\mathcal{C}'(\tau+\Delta\tau) - \mathcal{C}'(\tau)) \\ &= -\mathcal{C}'(\tau)\left\langle 1 - \exp\left(\hat{\imath}\eta_k(\Delta\tau)\right)\right\rangle \\ &= -\mathcal{C}'(\tau)\Delta\tau n_e \iint \left(1 - \exp\left(\hat{\imath}\eta_k(\Delta\tau)\right)\right) f_e(v_e) dv_e d\sigma \\ \frac{\Delta\mathcal{C}'(\tau)}{\Delta\tau} &\overset{\Delta\tau\to d\tau}{=} \frac{d\mathcal{C}'(\tau)}{d\tau} = -\mathcal{C}'(\tau) n_e \langle v_e\sigma\rangle\end{aligned}$$

Here it is implied, that

$$\sigma = \sigma_{re} - \hat{\imath}\sigma_{im} = \int \left(1 - \exp\left(\hat{\imath}\eta_k(\Delta\tau)\right)\right) d\sigma. \tag{3.92}$$

Thus the obtained differential equation can be now solved delivering

$$\mathcal{C}'(\tau) = \exp\left(-n_e\langle v_e\sigma\rangle\tau\right). \tag{3.93}$$

Finally inserting eqs. (3.89) and (3.93) into eq. (3.87) one obtains

$$\begin{aligned}\mathcal{L}(\omega) &= \frac{1}{\pi}\mathrm{Re}\left\{\int_0^\infty \exp\left[\left(\hat{\imath}\omega_{nm} - \hat{\imath}\omega - n_e\langle v_e(\sigma_{re} - \hat{\imath}\sigma_{im})\rangle\right)\tau\right] d\tau\right\} \\ &= \frac{n_e\langle v_e\sigma_{re}\rangle}{\pi}\frac{1}{(\omega - \omega_{mn} - n_e\langle v_e\sigma_{im}\rangle)^2 + (n_e\langle v_e\sigma_{re}\rangle)^2}.\end{aligned} \tag{3.94}$$

The resulting line shape corresponds to the Lorentz profile (eq. (3.49)) with a FWHM $\Delta\omega = 2n_e\langle v_e\sigma_{re}\rangle$. Hence, on the one hand the resulting line width mainly depends on the velocity distribution prevailing for the perturbers in the investigated plasma and on the other hand the effective collision cross section. It is worth noting that under the collision assumption taken here, $\Delta\omega$ is directly proportional to $n_e$.

### 3.2.5 Quasi-static approximation of the Stark effect

In the previous case it has been assumed that the collision time is short compared to the timescale of the collision frequency, which is always valid for electrons as perturbers. Now the ion contribution to the perturbation of the emitting species should be considered.

Since the ions are much heavier than electrons, they move with a much lower velocity than the free electrons. Consequently, they can be assumed to be nearly static. The electric field produced by the ions is therefore considered to be static. This field modifies the upper and lower energy levels of the emitter. Thus the emitter frequency is no longer constant but a function of the position operator $\underline{q}$. The spatial dependency of $\omega_{nm}$ is described by

$$\omega_{nm}(\underline{q}) = \omega_{nm}(0) + C_{nm}\left|\vec{E}^k\right| \tag{3.95}$$

with $k = 1$ for the *linear*, $k = 2$ for the *quadratic* Stark effect and $C_{nm}$ the Stark coefficient [102]. The linear Stark effect is valid, when the first order approximation of Fermi's golden rule is non zero. This means that the electron distribution in the atom is not symmetric. In the case of symmetric electron distribution the quadratic Stark effect applies. In order to obtain the line profile $\mathcal{L}(\omega)$, eq. (3.84) has to be integrated over the probability to find the emitter in the position $\underline{q}$ [120]

$$\mathcal{L}(\omega) = \lim_{\mathcal{T}\to\infty} \frac{\left|\int_{-\mathcal{T}/2}^{\mathcal{T}/2} \exp\left(-\hat{\imath}\omega t\right) \int_{\underline{q}} \langle\Phi_n| e\sum_a \underline{q}_a |\Phi_m\rangle \mathcal{P}(\underline{q}) d\underline{q} dt\right|^2}{2\pi\mathcal{T}\left|\langle n| e\underline{q} |m\rangle\right|^2}. \tag{3.96}$$

Hence, the line shape depends on the shape of the field distribution. It can be expressed as

$$\mathcal{L}(\omega)d\omega = \mathcal{H}(\beta)d\beta. \tag{3.97}$$

$\mathcal{H}(\beta)$ gives the probability to obtain a certain microfield at a specific location in the plasma normalized to the maximum microfield with $\beta = \frac{\left|\vec{E}\right|}{\left|\vec{E}_0\right|}$. This probability function was first calculated by Holtsmark [121]. The calculation was made under the specific assumption, that the ions are uncorrelated. $\mathcal{H}(\beta)$ is described by the following equation:

$$\mathcal{H}(\beta) = \frac{2}{\pi}\beta \int_0^\infty \sin(\beta x)\exp(-x^{3/2}dx). \tag{3.98}$$

The maximum field strength is given by

$$\left|\vec{E}_0\right| = 2.603\frac{Ze}{4\pi\varepsilon_0}n_e^{2/3}. \tag{3.99}$$

According to Holtsmark distribution the spectral width of a line broadened due to the linear Stark effect is proportional to $n_e^{2/3}$. Moreover, it does not depend on temperature of the perturbers, since they are considered static. This approximation does not take into account, that in a plasma the ions interact with each other via the shielded Coulomb potential. Field distributions taking into account this interaction were calculated by Hooper [122, 123]. The resulting distributions depend on the dimensionless parameter $R$ defined as [102, 115]

$$R = \frac{R_0}{\lambda_D} = \frac{\sqrt[3]{\frac{3}{4\pi n_e}}}{\sqrt{\frac{\varepsilon_0 k_\mathrm{B} T}{e^2 n_e}}} \tag{3.100}$$

with $R_0$ the ion sphere radius. Here a slight temperature dependence originating for the Debye length $\lambda_D$ is introduced. Yet Hooper's approach is only suitable for weakly coupled plasmas. Since neither in the case of Holtsmark distribution nor in the case of the corrected distribution given by Hooper eq. (3.97) can be solved analytically, no direct relationship can be given for $\Delta\omega$. However approximate relations can be determined for the case of particular lines. A general discussion of the correlation among ions requires a full numerical simulation.

### 3.2.6 Particular cases

In the previous section general theories for calculation of the shape and the resulting width of broadened spectral lines were discussed. In this section the application to particular spectral lines, important for the investigations presented in this work, are discussed.

#### 3.2.6.1 Neutral argon lines

For the derivation of the linear Stark effect it is assumed, that the component of the first order approximation of Fermi's golden rule is non zero. This implies, that an electric dipole is induced during the transition of the emitting electron from the excited into the ground state.

However, argon atoms have a symmetric electron distribution due to their inert gas structure. This leads to $\langle n| H_{int} |m\rangle = 0$, so that the second order approximation is needed to calculate the electron transition probability. In other words, in order to induce an electric dipole on an argon electron structure two free electrons are needed. The interaction with the first free electron leads to a slight deformation of electron structure resulting in a

temporal dipole formation. The second free electron can then interact with the short lived dipole [112]. The second order interaction is known as quadratic Stark effect. Its impact on the broadening of a spectral line is much weaker than a linear effect. This can be easily seen, when taking a closer look on the perturbation Hamiltonian in eq. (3.76). It can be also written as

$$H_{int} = \frac{e\vec{p}\cdot\vec{A}}{m_e} = e\underline{\vec{q}}\cdot\vec{E} = \underline{\vec{d}}_{dip}\cdot\vec{E} \tag{3.101}$$

with $\underline{d}_{dip}$ the electric dipole momentum induced by the electric field $\vec{E} = \frac{e\vec{q}}{4\pi\varepsilon_0|\vec{q}^3|}$ of a free electron. For the linear case the perturbation strength is proportional to the distance $\frac{1}{\underline{q}^2}$. For the second order approximation the term $\frac{|c_{nm}|^2}{t}$ is proportional to $\frac{1}{\underline{q}^4}$, which is the reason for the weaker broadening. The spectral power can be expressed equivalently to eq. (3.82) when replacing probability coefficients in eq. (3.80) by eq. (3.68).

The main contribution to the broadening of the atomic argon lines can be estimated by the impact approximation yielding a relation for the broadening width as given in eq. (3.94). Yet the ion microfields, which are considered in the quasistatic approximation of the quadratic Stark effect, contribute as well to the broadening of the line profile. Their contribution to the broadening width lies in the range of up to $20\,\%$ for neutral emitters [124]. In this case the total line profile can be obtained from the convolution of impact broadening and quasistatic profiles. Since the quasistatic profiles cannot be given as an analytic function, the total profile has to be numerically estimated. Griem delivers an empirical formula for the profile width along with tables for parameters contained there in [125]:

$$\Delta\lambda_{Stark} = 2 * w\left(1 + 1.75a(1 - 0.75R)\right). \tag{3.102}$$

Here $w$ the profile half width in $\mathrm{nm}$ calculated for the electron density of $n_{e,0} = 10^{22}\,\mathrm{m}^{-3}$ as discussed in section 3.2.4.1. It has a slight temperature dependency and scales linearly with the electron density $n_e$. $a$ is the ion impact parameter. It is calculated for $n_{e,0}$, is as well temperature dependent and scales with $n_e^{1/4}$. $R$ is the quotient of the ion radius and the Debye length (as given in eq. (3.100)), which simplifies to $R = 0.009\frac{n_e^{1/6}}{\sqrt{T}}$. Hence, eq. (3.102) can be written as

$$\Delta\lambda_{Stark} = 2 * w(T_e) * \frac{n_e}{n_{e,0}}\left(1 + 1.75a(T_e)\left(\frac{n_e}{n_{e,0}}\right)^{1/4}\left(1 - 0.0068\frac{n_e^{1/6}}{\sqrt{T_e}}\right)\right). \tag{3.103}$$

The values for $w(T_e)$ and $a(T_e)$ are tabulated in the appendix A.1 for the lines used in this work.

There are other works dealing with the calculation of line shape of argon lines broadened by the Stark effect. Here the broadening width for neutral argon lines based on the combination of the two previously discussed approximations, the semi-classical perturbation formalism [126, 127] are determined. The results can be accessed via the on-line database STARK-B [128]. The fitting function for the calculation of the line width used in this work is as well tabulated in appendix A.1.

The Ar I $696.5\,\mathrm{nm}$ resonance line has been studied by Pellerin et al. [86]. Here the experimentally determined line width was correlated to temperature and density measurements with other spectroscopic methods. The results were compared to other available experimental data and to the theoretical spectral width estimation given by Griem [101]. Finally, a corrected spectral width formula was given as

$$\Delta\lambda_{Stark} = 0.0814\,\mathrm{nm}\frac{n_e}{10^{23}\,\mathrm{m}^3}\left(\frac{T_e}{13\,000\,\mathrm{K}}\right)^{0.3685}. \tag{3.104}$$

Here the experimental data for the temperature range of $13\,000$ to $24\,000\,\mathrm{K}$ and electron densities $n_e < 2\times10^{23}\,\mathrm{m}^{-3}$ was considered.

#### 3.2.6.2 Hydrogen atomic lines

The hydrogen Balmer series is probably the most studied one in terms of Stark broadening. Therefore, it is widely used as a diagnostic tool for different types of plasma. Already a trace of hydrogen produces a sufficiently strong resonance line signal, from which the Stark effect can be evaluated. The linear Stark effect applies to the hydrogen lines, which results in a rather strong broadening. Here both, the electrons and the ions, contribute to the broadening mechanism. Since the quasistatic effect is stronger than in the case of argon lines, the line profile often results in a shape, which cannot be described neither by a Lorentzian nor a Gaussian profile. Figure 3.9 shows an example of line profiles of the $H_\alpha = 656.3\,\mathrm{nm}$ and $H_\beta = 486.1\,\mathrm{nm}$ lines. While for the $H_\alpha$ the deviation from Lorentzian fit is slightly present only in the wings of the profile, so that the fit overestimated the Stark width only by $5\,\%$ the situation is clearly different for the $H_\beta$ line. Although the difference between the fit and the simulated profile reaches up to $25\,\%$, the width resulting from the Lorentzian fit only underestimates the simulated Stark width by $7\,\%$. Hence, for the estimation of the line width the Lorentz fit is still appropriate.

For light emitters like hydrogen ion dynamics might play a role. In order to predict the line profile it is necessary to consider the emitter environment, which requires a more complicated non-analytical model. Many approaches describing broadening and shifts of hydrogen and hydrogen like emitters have been developed in the last years. They can be categorized into the standard theory, where the impact approximation is combined with the quasistatic approximation [e.g. 130, 131] and simulation techniques [e.g. 129, 132]. The difference between the latter results in the way the problem is treated mathematically and which effects are taken into consideration. The resulting broadening width of some theoretical calculations for hydrogen lines are reviewed and compared with experimental data by Konjevic et al. [133]. The best correspondence of the model and the experiment for $H_\alpha$ is achieved for the model presented by Gigosos et al. [129],[134]. For the case of $H_\beta$ no significant difference between the models is observed. Also a comparison of the work Gigosos et al. [134] with a more complex model by Oks [135] considering indirect coupling of electrons to the ion microfields and direct coupling via acceleration of electron by ion fields delivers comparable results within the experimental error of these works.

The technique presented by Gigosos and coworkers is based on a Molecular Dynamics simulation approach, which assumes a plasma with Maxwellian temperature distribution of the particles. It considers the interaction of the particles via the Coulomb potential.

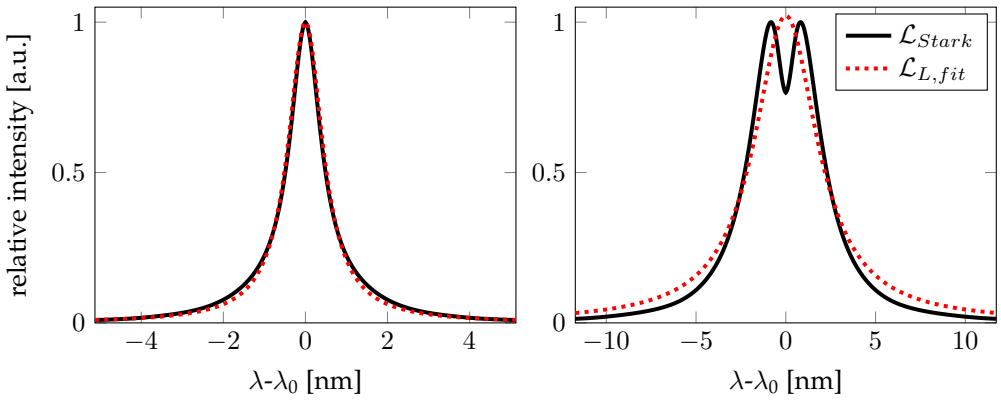


Figure 3.9: Spectral line profile of the stark broadened $H_\alpha$ (left) and $H_\beta$ (right) (solid black line) obtained from [129] for $T_e = 12\,399\,\mathrm{K}$, $n_e = 10^{23}\,\mathrm{m}^{-3}$ and $\mu = T_e/T_i = 1$ in comparison to a fitted Lorentzian line profile (dotted red line)

The influence of ions and electrons are calculated separately and numerically combined to determine the resulting broadening width. Two temperature effects are considered by introducing the parameter $\mu$ which represents the reduced mass of an emitter-perturber pair measured in the units of proton mass. In the case of hydrogen emitting in a heavy atom plasma (e.g. argon) with $T_e = T_i$, $\mu \simeq 1$, is valid. For higher values of $\mu$ two temperature effects can be considered by using $\mu = T_e/T_i$.

In [129] full line profiles for wide number of $n_e, T_e$ and $\mu$ are provided in electronic version, so that the data can be applied for the fitting purposes. However by considering, that the dependence of the broadening width on $\mu$ and $T_e$ is relatively weak, the electron density in the plasma can be estimated by the following formulas:

$$H_\alpha : \qquad n_e[\mathrm{m}^{-3}] = 10^{23} \cdot (\Delta\lambda_{Stark,HA}[\mathrm{nm}]/1.098)^{1.47135}, \tag{3.105}$$

$$H_\beta : \qquad n_e[\mathrm{m}^{-3}] = 10^{23} \cdot (\Delta\lambda_{Stark}[\mathrm{nm}]/4.8)^{1.46808}. \tag{3.106}$$

For the $H_\alpha$ line $\Delta\lambda_{Stark,HA}$ denotes the full width half area as defined in [129]. As has been shown in [133], the shape of the $H_\alpha$ line can be fitted by the Lorentzian profile. For this case $\Delta\lambda_{Stark}$ is a good approximation for $\Delta\lambda_{Stark,HA}$ so that eq. (3.105) can be used for the evaluation of the measurement with $\Delta\lambda_{Stark,HA} \simeq \Delta\lambda_{Stark}$.

Moreover, there exist other formulas approximating the electron density line width of $H_\alpha$ line. This relation was described by Büscher et al. [136], whereas the approximation formula can be found in [102]:

$$n_e[\mathrm{m}^{-3}] = (\Delta\lambda_{Stark}/2.8 \times 10^{-17})^{1/0.72}. \tag{3.107}$$

# Chapter 4

# Experimental setup

In the following chapter the experimental setups used in this work are described. In the case of Thomson scattering the focus is on the choice of particular experimental components and their impact on the measurement object. Moreover, the system alignment and synchronization as well as data processing are discussed.

Since the experimental setup for the Stark broadening is less complex, the discussion focuses on the data evaluation. Here single data processing steps such as deconvolution, Abel inversion and the interpretation of the resulting line width are explained.

## 4.1 Thomson scattering

In this work two setups for Thomson scattering measurement are implemented. The first setup is applied to investigate the GTAW arc process, which is supposed to be stationary. In the second step the pulsed GMAW arc is investigated. This requires modification of the original setup, because a temporal resolution is necessary. In the following, a general Thomson scattering setup for measurements in welding plasmas will be briefly presented. Afterwards the single components of the setup and the difference between the two setups will be discussed.

### 4.1.1 General Thomson scattering setup

Figure 4.1 shows the general setup of the Thomson scattering diagnostic. It can be divided in two parts, the sender and the receiver module. The sender module contains a pulsed Nd:YAG (neodymium-doped yttrium aluminum garnet) laser in the second harmonic mode with a central wavelength of $\lambda_I = 532\,\mathrm{nm}$ (MINILIGHT II, CONTINUUM). The

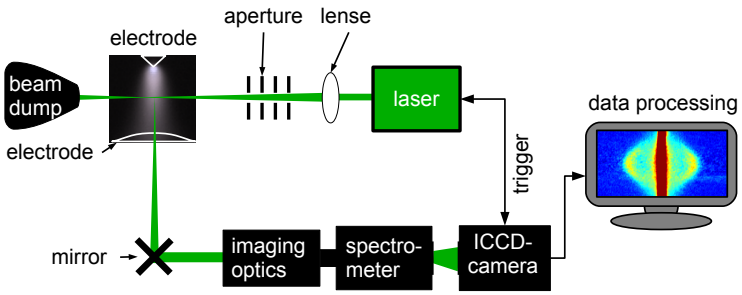


Figure 4.1: General Thomson scattering setup for electron temperature and density measurement in a welding arc.

laser beam is focused on the arc column using a biconvex lens with the focal length of $f = 150\,\mathrm{mm}$ and a diameter of $d = 50\,\mathrm{mm}$. It is aligned perpendicular to the vertical arc axis and enters the arc column in the center. In order to minimize parasitic reflections originating from the lens surface apertures are installed after the lens. The expanded laser beam is trapped in a beam dump, which is installed behind the measurement object. The sender module remains identical for both investigated processes.

The receiver module contains an imaging optics, which detects the scattering at an angle of $\theta = 90°$ with respect to the incident beam. Two mirrors are used for the $90°$ image rotation. In this manner the horizontally oriented plasma cross line volume radiated by the laser can be imaged on the vertically oriented spectrometer slit. An imaging system projects the rotated plasma image on the slit of a spectrometer. The resulting spectrum is recorded by an intensified charge-coupled device (ICCD) camera positioned at the image plane of the spectrometer. The particular receiver module design for the different processes however has some differences. The choice of components for the two setups is discussed in detail in section 4.1.3.2.

A single Thomson scattering spectrum image delivers one-dimensional information along the radial (horizontal) direction. In order to obtain two-dimensional information the measurement has to be repeated at several vertical positions within the arc.

### 4.1.2 Laser

The laser is one of the key elements of the Thomson scattering diagnostic. It delivers the radiation, which initiates the Thomson scattering effect. The choice of the radiation source depends on the properties of the investigated plasma. Here mainly two parameters, the radiation wavelength and energy, play a crucial role.

First of all, the plasma investigated by the Thomson scattering needs to be optically thin in the region of the laser wavelength and the Thomson scattering signal. Ideally no strong atom or ion lines should be present in the wavelength interval, where the scattering signal is expected to be located. For the welding plasmas with electron temperatures in the range of $10^4\,\mathrm{K}$ and densities in the range of $10^{23}\,\mathrm{m}^{-3}$ the scattering signal is expected in the interval of approximately $532 \pm 5\,\mathrm{nm}$. In the case of pure Ar plasma as well as in presence of N, H, He or Al only weak Ar, N, Al atom and ion resonance lines are predicted according to the data provided in [137]. The continuum radiation is expected to be optically thin as well [138].

As can be seen for example in fig. 4.2, a spectrum of an Ar-Al plasma generated in the high current phase of the pulsed GMAW arc does not show any evidence of strong lines. This is however not the case, if iron vapor is present, which will be discussed in section 5.1.2.2.

Apart from the plasma itself, the laser light can be absorbed by fumes arising during the GMAW process. The fumes contain metal oxides and other byproducts. They form, if the metal is heated beyond its boiling point. The presence of fumes leads to a drastic signal reduction, which also reduces the intensity of the relatively strong Rayleigh scattering signal. The fumes can be also detected by a supplementary camera additionally surveying the GMAW process. Yet in experiments conducted in this work, no fumes were visible neither in the ICCD signal nor by the supplementary camera. Consequently, their influence can be neglected.

The incident laser power determines the scattering radiation power. Consequently, the laser has to provide sufficient power, for the scattered radiation power to exceed the radiation power of the background plasma itself. If the laser's energy exceeds a certain level, the incident radiation may also change the plasma properties by heating and ionizing the investigated plasma volume [42]. This makes it necessary to estimate to which extent the given incident laser radiation heats up the plasma volume (see section 4.1.2.1).

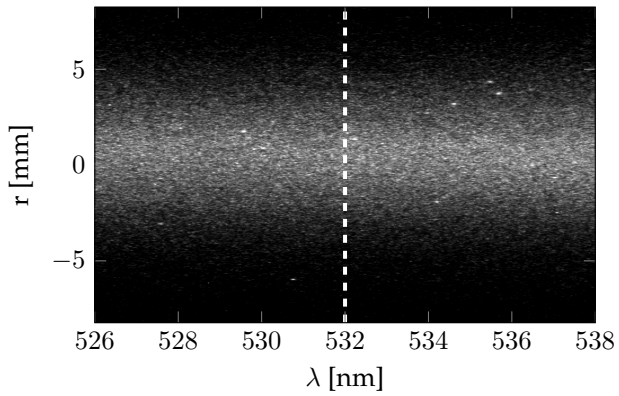


Figure 4.2: Spatially resolved spectrum of the Ar-Al plasma generated in a high current phase of the GTAW arc (exposure time: $5\,\mathrm{ns}$). The dashed white line indicates the position of the laser line.

Typically, total radiation power needed to achieve detectable Thomson scattering signal exceeds $1\,\mathrm{MW}$, so that acceptable $\mathrm{W/m^2}$ values can be yielded by focusing the laser. This requires the use of pulsed devices. Here the energy af a single laser pulse, the pulse duration and the final laser spot diameter determine the incident power per radiated area.

The repetition rate is of interest, if the signal of several Thomson scattering events is integrated on the camera chip. In this case a faster repetition rate is advantageous, as it allows to keep the chip background noise low, by using shorter accumulation times. This issue will be discussed in more detail in section 4.1.3.3.

The laser chosen for this work has a maximum energy of $25\,\mathrm{mJ}$ per pulse with a pulse duration of 3 to $5\,\mathrm{ns}$. The pulse repetition rate can be regulated from 1 to $15\,\mathrm{Hz}$. The initial laser beam spot diameter is $3\,\mathrm{mm}$ with a divergence of $< 3\,\mathrm{mrad}$ (full angle).

#### 4.1.2.1 Heat-up of the plasma by the laser radiation

For a proper description of the heating process initiated by the laser in the plasma, the cooling by the plasma itself has to be taken into account. This however requires a fluid dynamic modeling [46]. Yet, for a rough estimation of the plasma volume heat-up a more simple model, which does not consider cooling effects, is sufficient. It is assumed, that the increase of energy $\Delta E$ in the plasma can be expressed as the energy absorbed in the radiated plasma cross-section:

$$\Delta E = \frac{3}{2} k_B \Delta T_e = \frac{E_L}{\pi r_L^2} \frac{1}{n_e l_{IB}} \text{ with } l_{IB} = \frac{1}{\kappa_{IB}}$$

with $E_L$ is the laser energy, $r_L$ the laser beam radius and $l_{IB}$ the absorption length of the laser radiation in the plasma. This relation is used to obtain the relative electron temperature increase

$$\frac{\Delta T_e}{T_e} = \frac{2\kappa_{IB} E_L}{3 k_B T_e n_e \pi r_0^2}. \tag{4.1}$$

The absorption coefficient $\kappa_{IB}$ is given by

$$\kappa_{IB} = \left(\frac{32\pi}{27}\right)^{1/2} \frac{n_e n_i Z^2 \lambda_I^3}{h m_e^2 c^4} \left(\frac{e^2}{4\pi\varepsilon_0}\right)^3 \sqrt{\frac{m_e}{k_B T_e}} \left[1 - \exp\left(-hc/k_B T_e \lambda_I\right)\right] \bar{g}_{ff}(\lambda_I), \tag{4.2}$$

where $Z$ is the ion charge and $\bar{g}_{ff}$ the Gaunt factor for free-free transitions [45, 139, 140].

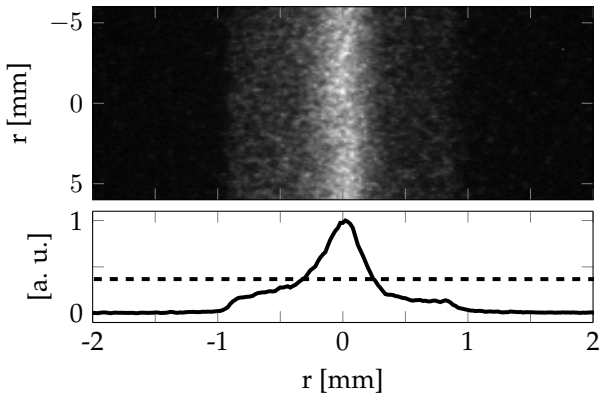


Figure 4.3: Top: Rayleigh scattering image of the focused laser beam in air with an open spectrometer slit; bottom: relative radial laser intensity (solid line) with the 1/e relative intensity level (dotted line).

For the evaluation of this formula two laser energies $E_L = 15mJ$ and $E_L = 25mJ$ are considered. The laser beam spot radius can be estimated by [141]

$$r_L = 0.5 f \vartheta \tag{4.3}$$

with $f$ the focal length of the focusing optics and $\vartheta$ the full divergence angle of the laser.

For the imaging optics used in this setup the estimation delivers a focused laser beam radius of $r_L = 225\,\mu\mathrm{m}$. Additionally, the focused laser beam spot radius is experimentally determined by recording Rayleigh scattering signal of the laser radiation in air with a fully open spectrometer slit, see fig. 4.3. $r_L \approx 280\,\mu\mathrm{m}$ is obtained from the half width $1/e$ maximum of the detected laser line. Therefrom it can be concluded, that the laser beam diameter is constant in the measurement volume.

The average value of the estimated and measured radii ($250\,\mu\mathrm{m}$) is used for the calculation. Moreover, a square laser pulse shape with duration of $4\,\mathrm{ns}$ and initial plasma conditions in LTE within electron temperatures from $5000$ to $25\,000\,\mathrm{K}$ are assumed. Figure 4.4(a) shows, that the relative maximum temperature increase with respect to the initial temperature of the unperturbed plasma does not exceed $6\,\%$ for $E_L = 15\,\mathrm{mJ}$. For $E_L = 25\,\mathrm{mJ}$ it ranges below $10\,\%$, which is still within the accuracy of the measurement. However, it was shown, that this formula overestimates the plasma heating [45, 46]. Thus, the actual increase of temperature within the plasma is smaller than the estimated values.

Furthermore, temperature profiles measured in a GTAW arc with $I = 150\,\mathrm{A}$ in an argon shielding gas atmosphere using laser pulses with a per pulse energy of $25\,\mathrm{mJ}$ and $15\,\mathrm{mJ}$ are compared. Figure 4.4(b) shows almost no difference between the temperatures evaluated from measurements with two different laser energies. This confirms that the plasma heating by the laser radiation can be neglected under the prevailing experimental conditions. For further investigation the laser pulse energy of $25\,\mathrm{mJ}$ is used.

### 4.1.3 Detection module

The main requirement for the detection module for Thomson scattering is to provide a sufficient signal to noise ratio (S/N) of the scattering signal. S/N depends on several factors, such as detector sensitivity, imaging optics efficiency and the signal integration time.

For stationary processes, such as the GTAW, the time needed for acquisition of the scattering signal is not a critical factor. Therefore, the signal can be accumulated over

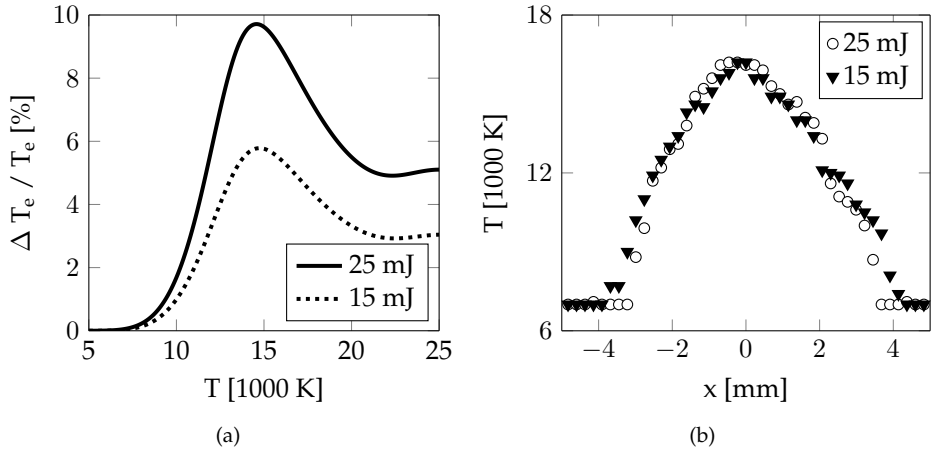


(a) (b)

Figure 4.4: (a) Evaluation of the plasma heating by a laser pulse with energies of 15 and 25 mJ and the radius of 250 $\mu$m. For these plasma conditions $\bar{g}_{ff}(\lambda_L) = 1.2$ is assumed [142]; (b) Temperature profiles measured using Thomson scattering method within the GTAW arc with $I = 150$ A, argon shielding gas atmosphere and laser pulse energies of 15 and 25 mJ.

several laser pulses, if it is necessary to compensate a non optimal configuration of the imaging optics or the detector. This advantage however cannot be utilized for transient and less stable processes such as the GMAW process. Here special care has to be taken to optimize the choice of imaging optics and the detector in order to be able to accumulate an evaluable signal in a minimum integration time.

In this work a setup for the investigation of the GTAW process was developed first. This setup was later adapted for the measurements in the GMAW process. Figure 4.5 shows the schematic of the two setups. Table 4.1 summarizes the main differences of the two setups, which are explained in detail in the following.

The main requirement for the imaging optics with regard to the optimal S/N is to deliver the best possible light transition and detection. The properties of the optics material

| **parameter** | **GTAW** | **GMAW** |
|---|---|---|
| *optics* | | |
| distance to the object | 1000 mm | 250 mm |
| $f/n$ | 12 | 2 |
| *detector* | | |
| image intensifier | GEN II | GEN III |
| quantum efficiency | 12 % | 50 % |
| exposure time | 10 ns | 5 ns |
| delay | 15 ns | 25 ns |
| gain | 85 % | 98 % |
| CCD sensor type | analog | digital |
| on chip integration | no | yes |
| number of integrations | 250 | 5 |

Table 4.1: Parameter overview for the scattering detection modules used for GTAW and GMAW processes.

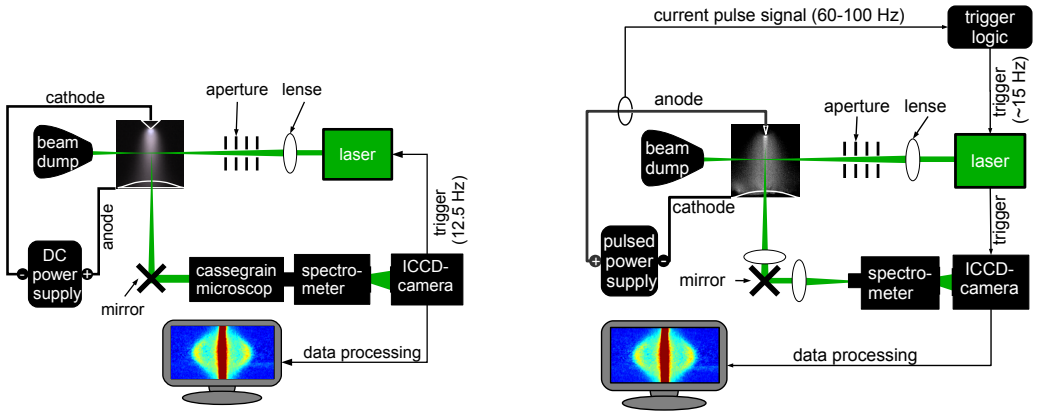


(a) GTAW (b) GMAW

Figure 4.5: Schematic of the Thomson Scattering setup for the (a) GTAW and (b) GMAW processes.

influence the light transition. Yet the main factors determining the light throughput are $l$, the distance to the object from imaging optics, and $d$, the optics diameter. Those parameters can be used to describe the solid angle, from which stray light can be collected. These two quantities can be combined to an f-number ($f/n$) with $n$ defined as

$$n = \frac{f}{d}. \tag{4.4}$$

Here the focal length of the optics $f$ mainly restricts a closest possible distance to the object. This definition allows comparing the light transmission of different components such as lenses, objectives, mirrors and spectrometers. In order to optimize the light throughput $f/n$ has to be minimized. However, it should be considered, that the light throughput is restricted by the largest $f/n$ of all the used components. Therefore, a closer look on the single components of the detection module is taken in the following.

#### 4.1.3.1 Spectrometer

A spectrometer with a Fastie-Ebert design and a focal length of $f = 250\,\mathrm{mm}$ is used in both setups. It is equipped with a plain diffraction grating with $1500\,\mathrm{grooves/mm}$ and a width of $58\,\mathrm{mm}$. The grating can be operated in the first or second diffraction order. In this experiment the first order is used. Figure 4.6 shows the schematic of the spectrometer design. It has only one spherical mirror, which collimates and focuses the incoming light from the adjustable entrance slit. A mask is introduced in order to prevent the reflection of unwanted parts of the spectrum. A stepping motor is used to define the output wavelength by changing the angle of the grating with respect to the entrance slit. Although this is a simple design, its imaging properties are sufficient, as long as the image is aligned on axis [102].

The $f/n$ of the spectrometer is approximately $f/4$. Here the grating width is the restricting parameter of the spectrometer optics. For the Thomson scattering measurement a slit width of $280\,\mu\mathrm{m}$ is used.

#### 4.1.3.2 Imaging optics

For the GTAW process a Cassegrain microscope combined with two mirrors ($179 \times 122\,\mathrm{mm}$) for image rotation is used as an imaging optics. Figure 4.7 shows the schematic drawing of

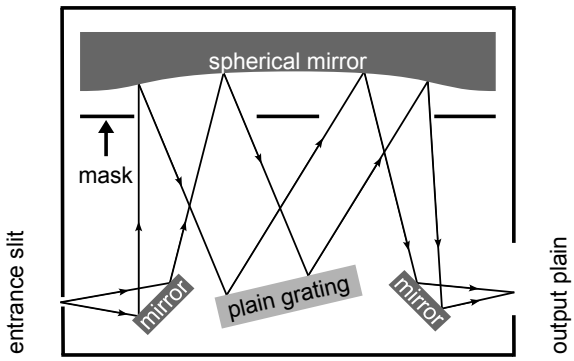


Figure 4.6: Schematic of a spectrometer with a Fastie-Ebert design.

the mirror as well as the lens configuration of the Cassegrain microscope QUESTAR QM1. Its main advantage is the compact close imaging optics adjustable to various distances. The close design also reduces the detection of parasitic light. QM1 is installed at a distance of $1000\,\mathrm{mm}$ from the measurement volume. The image is projected on the entrance slit of the spectrometer. $f/n$ of the used configuration is approximately $f/12$.

The comparison of $f/n$ of the spectrometer and the Cassegrain optics clearly indicates, that the imaging of the amount of stray light on the spectrometer slit may still be optimized in terms of increasing the solid angle of the optics and hence the light throughput.

For the GMAW setup the S/N ratio needs to be improved in order to minimize number of laser pulses necessary to achieve a detectable Thomson scattering signal. Therefore, QM1 is replaced by a combination of two lenses with a focal length of $250\,\mathrm{mm}$ and a diameter of $150\,\mathrm{mm}$ (see fig. 4.5(b)). The first lens is placed $250\,\mathrm{mm}$ away from investigated plasma volume. Thus, it generates a parallel optical path. The image is rotated using two plane mirrors. Finally, the arc is imaged on the spectrometer slit by placing the second lens $250\,\mathrm{mm}$ away from the spectrometer entrance slit resulting in a 1:1 image ratio. This configuration delivers an f-number in the range of $f/2$. Here the width of the mirrors ($d = 122\,\mathrm{mm}$) is the restricting element.

#### 4.1.3.3 Detector

Since the laser pulse duration is relatively short ($5\,\mathrm{ns}$) and the scattering signal is very weak, ICCD detectors with high quantum efficiency and short gating times are required. An image intensifier is typically composed of several functional parts. It includes a cathode coated with a photosensitive layer and a micro channel plate (MCP). The latter is an array

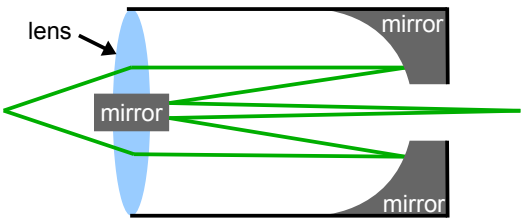


Figure 4.7: Schematic of the light path within a Cassegrain microscope.

of microscopic channel electron multipliers operated with adjustable high voltages in the range of $\mathrm{kV}$. The electrons coming out of the MCP are visualized by a phosphor screen [102]. Thus the amplified light is imaged on the CCD (charge-coupled device) sensor and can be electronically processed. Such system allows short exposure times and precise delay adjustment, both in the $\mathrm{ns}$ timescale.

The main criterion for the choice of the detector is its quantum efficiency in the desired wavelength range ($532\pm5\,\mathrm{nm}$). Other important features are the integration of the amplified signal on the CCD chip and the external trigger ability of the camera.

For the GTAW process the 4PICOS ICCD (STANFORD COMPUTER OPTICS) with an Gen II (S20) image intensifier is used. The intensifier is coupled to a CCD chip with an analog output (CCIR norm) using a distortion free relay lens. The quantum efficiency of the detector is approximately $12\,\%$ for $\lambda = 532\,\mathrm{nm}$. The intensifier is operated with $85\,\%$ of the maximum acceleration voltage. The exposure time is set to $10\,\mathrm{ns}$ with $15\,\mathrm{ns}$ delay with respect to the input trigger applied to the image intensifier.

The CCD chip readout can be performed with only either 50 half or 25 full frames per second, as the CCD readout frequency is internally fixed. The integration of the intensified signal on the CCD chip is only possible within maximum $20\,\mathrm{ms}$. Since the maximum laser repetition rate is only $15\,\mathrm{Hz}$, no on-chip integration can be achieved with this camera. Moreover, the CCD readout cannot be triggered and therefore the 4PICOS has to be operated as a master for synchronization purposes.

For the GMAW process PI-MAX2 ICCD detector (PRINCETON INSTRUMENTS) with an HBf GEN III image intensifier is used. It is coupled to a digital CCD chip by fused fiber optic bundle. The quantum efficiency of the system is $50\,\%$. The intensifier is operated with $98\,\%$ of the maximum acceleration voltage. The exposure time is set to $5\,\mathrm{ns}$ in order to minimize plasma background radiation. The delay is adjusted to $25\,\mathrm{ns}$ with respect to the input trigger.

In the single chip exposure mode the CCD readout is limited to 10 frames per second, if the full chip area is used. By reducing the readout area higher readout rates can be achieved. The camera can be also operated in the multiple chip exposure mode. This feature allows an on chip integration of the intensified image signal without a permanent CCD chip readout. In this case the image intensifier is externally triggered with a frequency of up to $5\,\mathrm{kHz}$. In the meantime the CCD chip read out is attenuated by the software. The different modes allow to operate the camera as a slave and as a master for synchronization purposes.

Moreover, aa supplementary high speed camera (PCO.1200 S) equipped with a ZEISS MAKRO PLANAR 2/100 lens is installed in order to monitor the GMAW process. This allows the comparison of the arc shape of single shots during the integration period. The exposure time of this camera is set to $5\,\mu\mathrm{s}$ for the high current phase and to $50\,\mu\mathrm{s}$ for the low current phase. Neutral density filters in front of the lens prevent the over-saturation of the CCD. The current and the voltage of the arc are additionally monitored during the measurement.

### 4.1.4 System alignment

In order to ensure optimal light throughput of all the installed components they have to be properly aligned. Therefore, first the backward alignment using a solid state continuous laser ($\lambda_I = 532\,\mathrm{nm}$, $P = 1\,\mathrm{mW}$) is used. The laser is installed in the position of the ICCD camera. It is adjusted to pass the spectrometer and the imaging optics on their central axis. The heights of the Nd:YAG laser has to be adjusted so that the pulsed laser beam perpendicularly crosses the alignment laser beam. Finally the welding torch position is adjusted, so that the alignment laser beam hits the upper electrode. The desired vertical measurement position is adjusted by vertically shifting the welding apparatus. Figure 4.8 visualizes the backward alignment procedure.

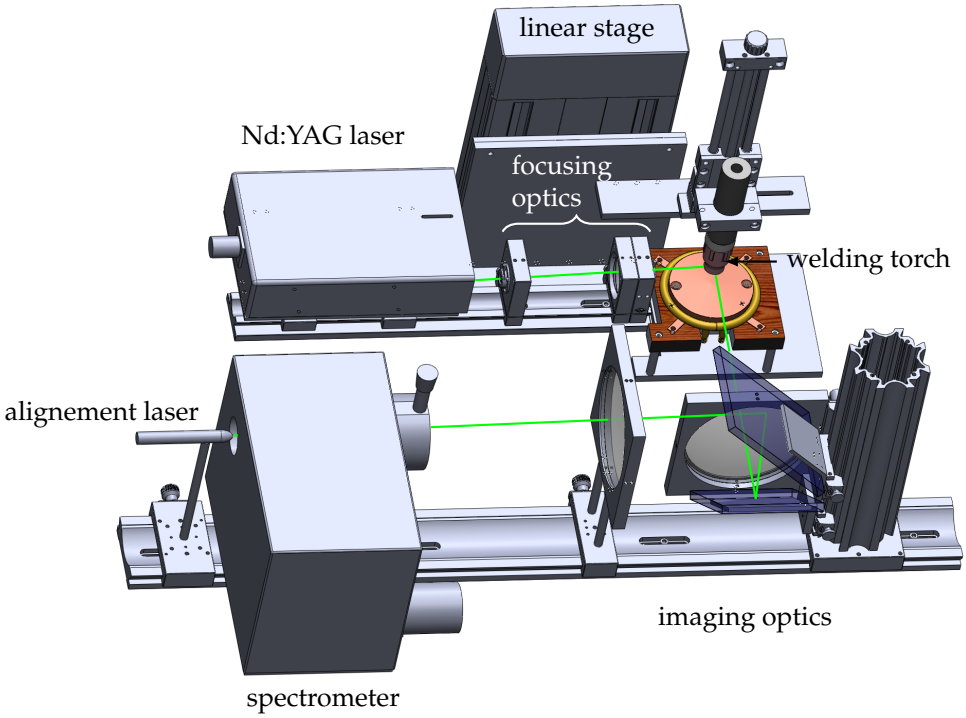


Figure 4.8: Visualization of the laser pass during a backward alignment procedure of the Thomson scattering setup for the GMAW process.

After the backward alignment, the laser is replaced by the ICCD camera. Now an image of the Rayleigh scattering signal of the pulsed laser in air can be recorded by the camera. It is used to verify the correct position of the laser beam with respect to the entrance slit of the spectrometer. Therefore, special care has to be taken not to damage the ICCD by reflections of the laser on the cathode or wire tip. The laser power has to be considerably reduced by using additional neutral density filters.

### 4.1.5 Process synchronization and data acquisition

As two different camera types are used in the investigated processes, two different synchronization setups are implemented.

For the GTAW process the CCD detector of the 4PICOS is operated in the *field mode* with the vertical synchronization output. This means, that even and odd rows of the CCD detector are alternately exposed. An image composed of either even or odd rows is called a half frame. Hence, a full frame is composed of two consecutively exposed even and odd half frames.

Figure 4.9 gives and overview for the process synchronization. 50 Hz CCD half frame readout signal (f-sync OUT) of the 4PICOS is used as the master signal. In order to match the frequency range of the laser the f-sync signal is reduced to 12.5 Hz by an external frequency divider. This signal is transmitted to the flash lamp trigger input of the Nd:YAG laser. The Q-switch trigger signal generated by the laser electronics is used to trigger the image intensifier of the ICCD camera (TRIG IN). The adjustment of the delay of the image intensifier via the control software of the camera allows synchronizing the gating time with the laser pulse.

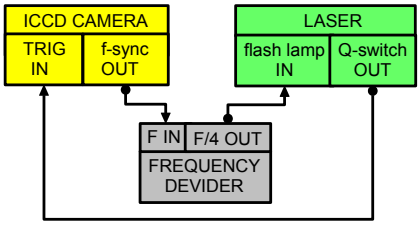


Figure 4.9: Synchronization schematic for the Thomson scattering measurement of the GTAW process.

Video signal of the CCD camera is acquired by a frame grabber (MVGAMMA-G, MATRIX VISION), which delivers full frame images to the camera software (4SPEC, STANDFORD COMPUTER OPTICS). A single laser pulse is not useful to deliver an image with a sufficient S/N ratio for the detection of the Thomson scattering signal. An evaluable image is generated from 250 exposed single images. Moreover, plasma background without laser radiation has to be recorded for 250 full frames while the laser output has to be mechanically blocked. This implies a total integration time of $40\,\mathrm{s}$ per particular measurement position. The consecutive acquisition of the images is possible with the camera software function "Aquire real-time series". The further processing of the image is discussed in section 4.1.6.

The GMAW process is a transient process, which requires temporal resolution of the measurement. This is realized by using an additional trigger logic as already indicated in fig. 4.5(b). Figure 4.10 visualizes the synchronization process in detail.

Here the current of the welding process is used as master signal. A Hall sensor (SS94A1F) is used to track the electric current pulse of the welding arc. The analog digital converter of the micro-controller board (ARDUINO DUE board with ATMEL SAM3X8E ARM CORTEX-M3 MCU processor) is used to detect a predefined level of the current pulse. The conditions of the threshold are programmed to detect the beginning of the high current phase. The analogue-digital converter of the micro-controller provides a $1\,\mathrm{MHz}$ sampling rate and a $12\,\mathrm{bit}$ resolution. It is fast and precise enough to deliver reproducible trigger points for the GMAW process with a maximum pulse rate of $100\,\mathrm{Hz}$. A temporal delay with a precision of $25\,\mathrm{ns}$ is generated using the counter functionality of the micro-controller. The delay function is needed in order to measure the Thomson scattering signal at different phases of the current pulse. Thus, temporally resolved measurements can be implemented.

The measurement trigger signal (DO, TTL standard) is transmitted to the flash lamp input trigger signal of the Nd:YAG laser. The Q-Switch trigger output is connected to the image intensifier gate trigger input (TRIG IN). The camera software is used to activate the on chip integration mode for the desired number of laser pulses and to adjust the delay of the laser pulse with respect to the gating time of the image intensifier. The readout of the CCD chip is automatically triggered by the camera software, when the preset number of pulses is reached. Due to higher the sensitivity of the camera and an improved imaging optics integration over only 5 laser pulses for the high current phase and 20 pulses for the

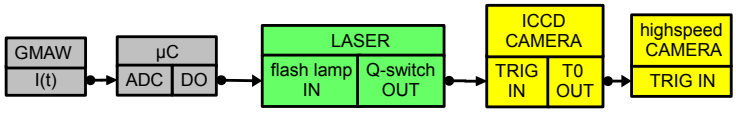


Figure 4.10: Synchronization schematic for the Thomson scattering measurement of the GMAW process.

low current phase are sufficient to deliver a scattering signal with an acceptable S/N. Here as well the plasma background is integrated for 5 or 20 laser pulses respectively, while the laser beam is mechanically blocked. The signal integration time is $0.33\,\mathrm{s}$ for the high current phase and $1.33\,\mathrm{s}$ for the low current phase.

Additionally, the high speed camera is triggered by the synchronization output of the ICCD camera (T0 OUT). An image is recorded, every time the image intensifier is triggered and the on chip integration is in process. Thus, a control image sequence for every measurement point is obtained.

### 4.1.6 Data processing and evaluation

Determination of the electron density and the temperature from the detected scattering signal requires several steps:

- wavelength calibration
- determination of instrumental function
- correction of the spectral line curvature
- generation of the convoluted theoretical Thomson scattering spectra
- plasma parameter determination from the fitted theoretical spectra

The data processing is performed using the MATLAB software. In the following each processing steps is discussed in detail.

#### 4.1.6.1 Wavelength calibration and instrumental function

The spectrometer used for Thomson scattering has to be calibrated for the use with different detectors. Since only a relative signal is needed to evaluate temperature and density from Thomson scattering, no absolute calibration is needed. Yet a spectral resolution calibration is still required for each detector. For this purpose a low pressure neon discharge lamp (PEN-RAY, LOT) is used. It provides a high accuracy discrete line spectrum with FWHM below $\mathrm{pm}$. Therefore, according to the specification of the lamp neon resonance lines with $\lambda_0 = 533.08, 534.11$ and $540.06\,\mathrm{nm}$ are used. The calibration yields a $0.04\,\mathrm{nm/pix}$ resolution for the 4PICOS and a $0.027\,\mathrm{nm/pix}$ for the PI-MAX2. In this case no pixel binning (combining a cluster of several pixels to one pixel) is used.

For each measurement series the wavelength calibration and the instrumental function determination are performed using the Rayleigh scattering signal of the Nd:YAG laser in air with the slit width set to $280\,\mu\mathrm{m}$. The intensity distribution can be approximated by a Gaussian distribution fitted to the measured intensities (see fig. 4.11). This function is used to further consider the instrumental broadening of the theoretical Thomson scattering spectra. FWHM values of $0.49\,\mathrm{nm}$ for the 4PICOS and $0.30\,\mathrm{nm}$ for the PI-MAX2 detectors are obtained.

In the detected Thomson scattering spectra the Rayleigh scattering part of the signal is used to determine the absolute wavelength position.

#### 4.1.6.2 Spectral line curvature correction

The path length difference for the light rays coming through the center and the end of the spectrometer slit results in a curved spectral line. This curvature needs to be corrected before further processing.

The correction can be calculated using the calibration image using the Rayleigh scattering signal of the Nd:YAG laser in air. A second order polynomial is fitted into the curved

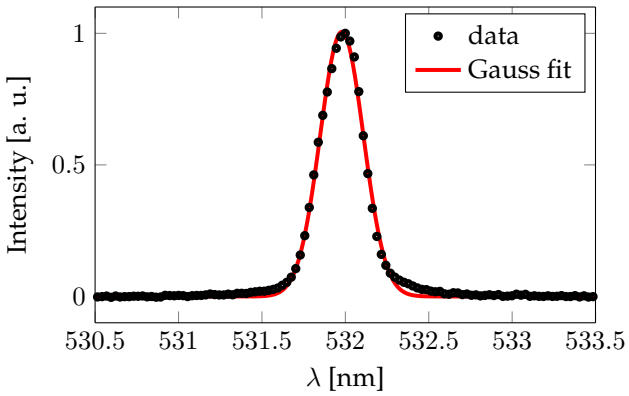


Figure 4.11: Example of the measured and fitted instrumental function of the Fastie-Ebert spectrometer when using the PI-MAX2 ICCD.

line shape using a least square fit algorithm as illustrated in fig. 4.12(a). Hence, the image can be "straightened" (fig. 4.12(b)) by shifting the pixel rows of the original image by the corresponding value of the resulting polynomial fit. This correction is applied to all measured spectra.

#### 4.1.6.3 Data preparation

Since two detector types are used in this work, slightly different data preparation procedures are necessary before plasma parameter can be finally evaluated from the Thomson scattering spectra

The data format provided by the 4PICOS frame grabber requires separation into single frames. One full frame contains two sub-sequentially recorded half frames. Since according to the synchronization type only every 4th half frame contains a signal, the full frame has to be split in two images in the post-processing. The frames can be sorted by evaluating the signal level in to exposed and unexposed frames. For each measurement positions 250 half frames containing laser radiation are recorded delivering 250 exposed

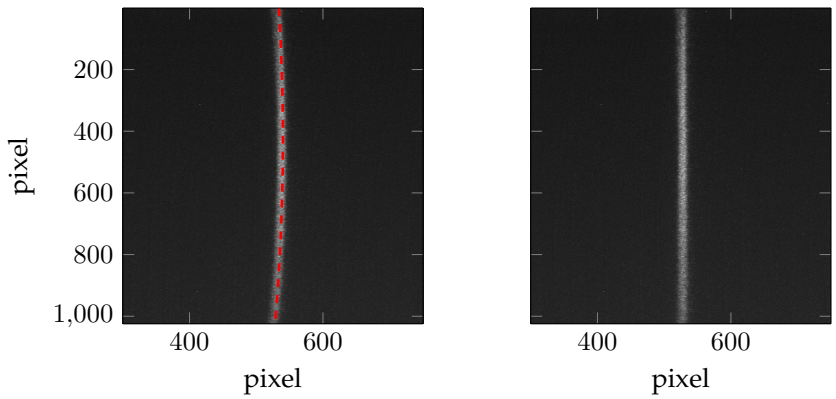


(a) uncorrected (b) corrected

Figure 4.12: (a) Uncorrected calibration image with respective polynomial fit marked with a red dashed line; (b) straightened calibration image.

frames, which are integrated into one image in order to enhance the signal. The unexposed half frames are used to determine the dark current signal of the CCD, which is subtracted from each exposed frame. Additionally, to the laser scattering signal 250 full frames with plasma background radiation are recorded and prepared in the same manner. The plasma background is then subtracted from the laser scattering signal.

PI-MAX2 delivers full frame TIF images which can be directly evaluated. For each measurement position laser scattering signal and plasma background signal are recorded. The CCD dark current signal is recorded separately, while no laser or plasma are operated. It is as well subtracted from each signal frame. No signal integration in the post-processing is necessary as the on-chip integration mode is used in this case.

Once the raw scattering signal is extracted, additional steps for noise reduction might be performed. The noise in the signal is on the one hand caused by the statistical CCD noise. On the other hand the fluctuation of the plasma radiation brings in an additional noise source. Singular value decomposition (SVD) with principal component analysis as described in [143] is used for noise reduction purposes. SVD is performed using an algorithm provided by MATLAB. Additionally, the noise level can be reduced by pixel binning in the direction of spatial resolution. Figure 4.13 shows an example of scattering spectrum image, which is prepared as described above. It can be used for plasma parameter determination in the next step.

#### 4.1.6.4 Plasma parameter determination

In order to determine electron temperature and density from the scattering spectrum eq. (3.41) needs to be fitted to the data. Moreover, convolution of the scattered signal with the instrumental functions needs to be considered.

When applying eqs. (3.35), (3.36) and (3.44) the electron feature $S_e$ can be expressed as a function of temperature $T_e$ and dimensionless parameter $\alpha$, which are suitable parameters for the fit procedure. In order to numerically evaluate $Rw(x)$, also known as Dawson integral (eq. (3.37)), a built in MATLAB routine `mfun('dawson',x)` is used. The instrumental broadening of the theoretical spectrum $S_e$ is considered by convolution of the latter with the instrumental function. Hence, the convoluted theoretical electron feature $S_{e,conv}$ is further used for the fit procedure.

Since the central wavelength is not filtered out in the experimental setup, it needs to be approximated by a fit function in order to obtain reliable fit results. Since this part of

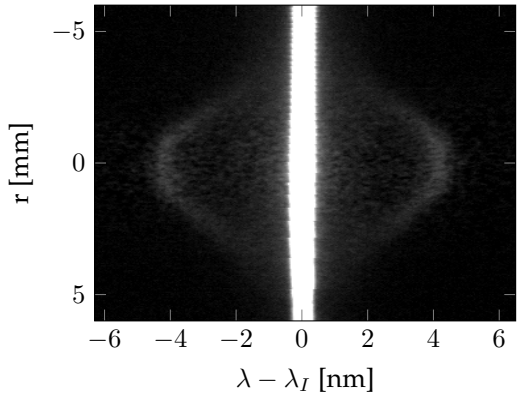


Figure 4.13: Example of the scattering spectrum data recorded in a GTAW process operated with argon with plasma and dark current background signal subtracted and 5 pixels binned together in vertical direction.

the spectrum is influenced by many phenomena, no analytical model can be formed. Best fit results are obtained, when the central region is fitted with a modified Pseudo-Voigt function

$$S_{center} = S_1 \left( \frac{c}{\pi} \frac{\delta/2}{(\omega - \omega_0)^2 + (\delta/2)^2} + (1-c) \exp\left[ -\frac{1}{2} \left( \frac{\omega - \omega_0}{\sigma} \right)^4 \right] \right). \tag{4.5}$$

The parameters of $S_{center}$ are independent from temperature or density and hence do not influence $S_{e,conv}$. The final fit function is defined as the sum of central wavelength and the convoluted electron feature:

$$S_{fit} = S_{e,conv}(T, \alpha) + S_{center}. \tag{4.6}$$

The fit is performed using a least square fit algorithm provided by the MATLAB function `lsqcurvefit`. This function allows simultaneous fitting of multiple parameters with predefined boundary conditions. Thus, for a successful fit physically and technically sensible boundary parameters need to be determined. Moreover, in order to assure an equal sensitivity of the fit algorithm to all parameters, it is useful to parametrize them to comparable orders of magnitude. Figure 4.14 shows an example of a result of a fitting procedure for an electron scattering spectrum. The signal is recorded in a GTAW process operated in argon shielding gas atmosphere. From the final fit parameters $T_e$ and $\alpha$ plasma parameters $T_e$ and $n_e$ can be calculated using eq. (2.6).

The result of the fit is sensitive to the choice of boundary conditions, initial value of the fitting parameter and the noise in the signal. Unfavorable combination of initial parameter and noise influence might lead to a false local minimum and hence to wrongly determined temperature and density values. Thus, an interactive evaluation tool (fig. A.3) is developed to correct the fitting results in such cases. Herewith it is possible to load a dataset together with the automatically evaluated temperatures and densities. Separate spatial points with a false automatically generated local minimum can be corrected by manually adjusting the geometric fitting parameters.

The measurement uncertainty mainly arises from the fluctuation of the measurement conditions and the precision of the fit algorithm. It is determined by calculated the standard deviation of at least three consecutive measurement results.

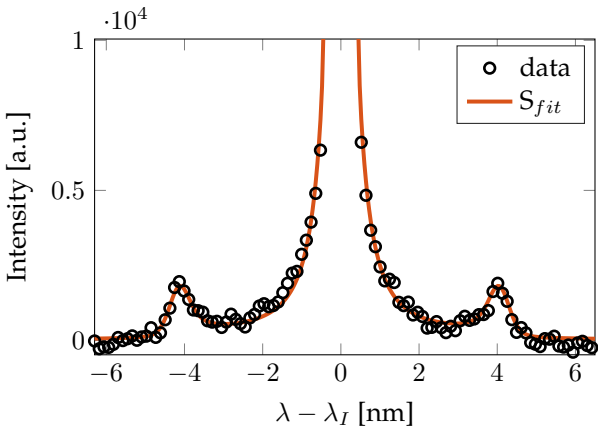


Figure 4.14: Example of the fitted spectrum $S_{fit}$ for a dataset recorder in a GTAW process operated in argon atmosphere.

## 4.2 Stark broadening

In contrast to Thomson scattering the same diagnostic setup can be used to record emission spectra for Stark broadening evaluation in GTAW and GMAW processes. In both processes mostly argon resonance lines are investigated. In the case of the GMAW process hydrogen Balmer lines are analyzed by adding a trace of molecular hydrogen to the shielding gas. The additional setup required for this investigation is described in section 4.2.2.

Since emission spectroscopy is a passive diagnostic technique, only a detection module, which is composed of an imaging optics, a spectrometer and a CCD camera, is necessary to obtain the desired signal. In particular the high wavelength resolution is crucial for the successful evaluation of the Stark broadening of spectral lines.

Figure 4.15 shows the schematic of the main setup for the Stark broadening measurement. As an imaging optics a collimator (NA=0.25, 633 nm alignment) in combination with an aperture are used to couple the emitted light into an optical fiber. Thus the light collected from the plasma volume with a cross section of 1 mm and the thickness of the whole plasma column is imaged on the slit of the spectrometer. The use of optical fiber implicates a greater flexibility concerning the positioning of the optics. The fiber guides the collected light to the entrance slit of the high resolution Echelle spectrometer (ARYELLE BUTTERFLY 400, LTB LASERTECHNIK BERLIN). The wavelength dispersed signal is recorded by a CCD detector.

Due to the use of the optical fiber only 0-dimensional information is recorded. In order to obtain a two dimensional signal different points of the plasma column have to be scanned. For the GMAW process monitoring the same high speed camera setup as for Thomson scattering is used.

### 4.2.1 Echelle spectrometer

In contrast to the spectrometer design described in section 4.1.3.1 an echelle spectrometer uses a grating with large groove spacing (typically 20 to 100 grooves/mm). This grating type is called the echelle grating. When using the high diffraction orders of this grating (10 to 100), high spectral resolution can be achieved. Typically, the orders overlap and have to be separated by a cross dispersing prism as shown in fig. 4.16. Additional mirrors are used to fold and image the spectrum on the grating and the CCD chip. The resulting spectral image consists of rows of spectra of different orders. In this manner a simultaneous recording of a large wavelength range with high spectral resolution is possible.

The ARYELLE 400 echelle spectrometer has a focal length $f = 400\,\mathrm{mm}$ with an aperture $f/10$. The visible spectral range of the device is 300 to 900 nm with a spectral resolving power of $15\,000\,\lambda/\mathrm{min}\,\mathrm{FWHM}$. This implies, that resolutions of 20 to 60 pm can be achieved. The entrance slit of the spectrometer is fixed to $50 \times 50\,\mu\mathrm{m}$.

As a detector ANDOR NEWTON CCD DU940P with the BU2 sensor is used. This is a full frame type CCD, which can be characterized by a high sensitivity and a suitable wide spectral range. It is possible to directly trigger the camera by a $50\,\Omega$ terminated TTL signal,

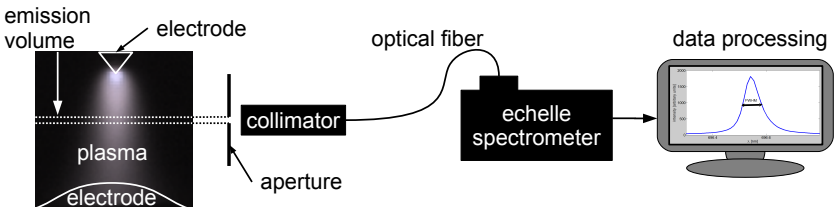


Figure 4.15: Schematic of the Stark broadening setup.

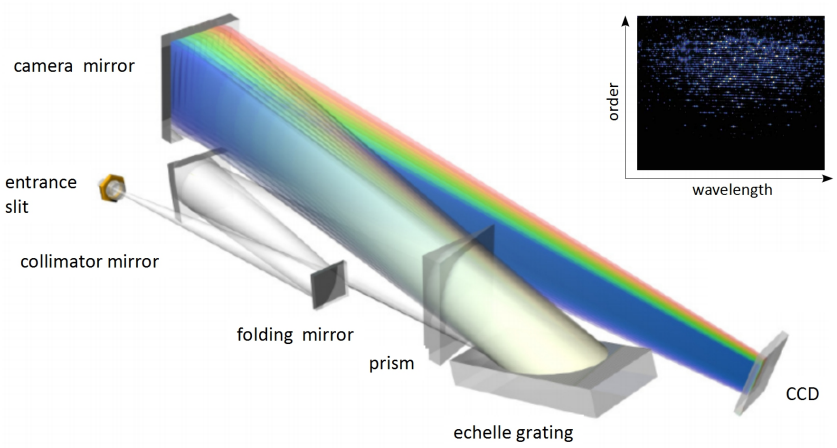


Figure 4.16: Schematic of the Echelle spectrometer as used for the ARYELLE 400 with a typical raw image of the echelle spectrum (upper right corner) [144]

which allows operating the spectrometer in the slave and master mode. A drawback of this CCD type is its minimum exposure time of $1\,\mathrm{ms}$. As a result a dark environment is needed for artifact-free images. To ensure, that no light is falling on the CCD sensor during the readout, a mechanical shutter is built in the ARYELLE 400 spectrometer. It has a response time in the range of $10\,\mathrm{ms}$ which can be taken into account via the software.

### 4.2.2 Detection of hydrogen Balmer lines

Due to the very low concentration of hydrogen in the plasma the intensity of the hydrogen Balmer lines is relatively weak compared to the argon resonance lines. The dynamic range of the CCD detector does not allow to detect weak and strong lines simultaneously. Besides the sensitivity of the detector at the exposure time of $1\,\mathrm{ms}$ is not sufficient to detect the hydrogen lines. Hence a detector with a higher sensitivity is needed.

The detection module originally used for the Thomson scattering diagnostic of the GMAW process (section 4.1.3) could be applied for detection of the hydrogen Balmer lines as shown in fig. 4.17. In this case the 4PICOS ICCD camera is used, because the PI-MAX2 was not available. Besides the higher detector sensitivity, the advantage of this setup are the shorter gating times in the range of $\mathrm{ns}$ and 1-dimensional spatial resolution, which allows a more precise temporal and spatial investigation of the process. Yet only hydrogen Balmer lines can be investigated here. Their broadening width is significant enough compared to the instrumental width of the spectrometer. This is not the case for neutral argon lines.

### 4.2.3 Process synchronization and data acquisition

As the GTAW process is operated in a stationary mode, no particular care has to be taken to synchronize the process with the spectrometer. The echelle spectrometer is operated with the shutter opening and closing at each exposure with exposure times of $6\,\mathrm{ms}$ and $40\,\mathrm{ms}$ respectively. The spectrometer automatically generates wavelength intensity data sets from recorded spectral images. In this case one dataset is an average of 5 consecutive measurements.

The spectrometer software can be additionally synchronized with the linear stages. An integrated script language allows to automate the measurement for several spatial measurement points.

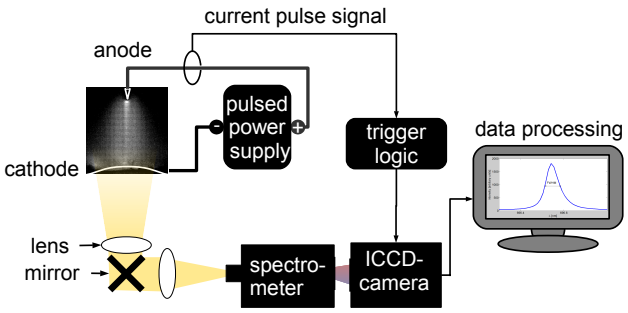


Figure 4.17: Schematic of an additional setup for the hydrogen Balmer lines detection in the GMAW process.

In contrast to the GTAW process the GMAW processes need to be synchronized with the measurement system in order to obtain temporally resolved results. Again the process itself is used as a master. As already described in section 4.1.5, the current signal is fed into a micro-controller, which generates a trigger signal for the spectrometer camera and an additional high speed camera. The schematic of the synchronization is illustrated in fig. 4.18.

Typically, the duration of the high current phase of a GMAW process is set to around $2\,\mathrm{ms}$. The CCD detector of the echelle spectrometer is however the limiting factor in terms of temporal resolution of this process. The minimum exposure time of $1\,\mathrm{ms}$ only allows time averaged measurements during the high current phase of the pulse. Moreover, the operation in the original configuration of the ARYELLE spectrometer turns out to be problematic due to the relatively high reaction times of the mechanical shutter ($>10\,\mathrm{ms}$). If the spectrometer is operated as a slave with the shutter opening and closing time at each exposure set to minimum, no light is detected at the CCD chip at an exposure time of $1\,\mathrm{ms}$. This can be explained by the fact, that the system does not consider the actual shutter delay. Hence, the shutter starts to close before it is completely open.

As already indicated in fig. 4.18, a workaround for this problem can be provided. Therefore, the spectrometer has to be operated as a slave, while the CCD shutter is permanently open. Simultaneously, a custom made piezo motor (X15G, ELLIPTEC) driven shutter is positioned in front of the aperture of the collimator. Thus a more flexible synchronization between the trigger signal and the shutter can be implemented. This shutter has a closing time of $3\,\mathrm{ms}$ and can be triggered simultaneously to the CCD camera of the spectrometer. Thus it can be achieved that a signal is detected for exposure times of $1\,\mathrm{ms}$ with a minimum distortion of the CCD chip during the readout.

The 4PICOS ICCD used in the additional setup is operated in the field mode with the

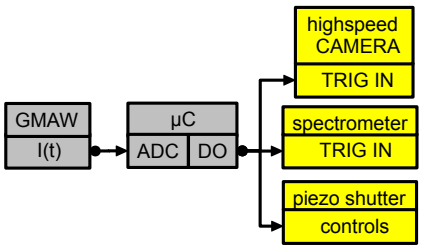


Figure 4.18: Synchronization schematic of the Stark broadening setup for the GMAW process.

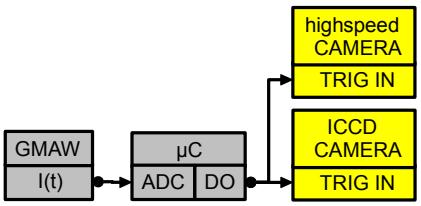


Figure 4.19: Synchronization schematic of the additional setup for the Stark broadening measurement of hydrogen Balmer lines in the GMAW process.

vertical synchronization output. The exposure time is set to $140\,\mathrm{ns}$ and the gain to $45\,\%$. The ICCD has to be synchronized with the GMAW process as well. The problem here is, that the CCD readout cannot be synchronized with other processes. Therefore, only the image intensifier is triggered by the micro controller (fig. 4.19) signal. The CCD is operated with the internal frequency of $50\,\mathrm{Hz}$. The image sequence delivered by the software contains a series with exposed and unexposed half frames. Since the emission signal is sufficiently strong the unexposed half frames can be easily filtered out in the post-processing.

### 4.2.4 Data processing and evaluation

In order to derive the electron density and the temperature from the raw measurement data several steps are necessary:

- wavelength calibration of the data
- determination of instrumental function
- deconvolution of other broadening effects
- local emissivity determination (Abel transform)
- line width determination
- plasma parameter assignment from the line width data

The data processing is performed using a MATLAB script. In the following each processing step is discussed in detail.

#### 4.2.4.1 Wavelength calibration and instrumental function

Wavelength calibration is necessary in order to assign wavelength scale to the images recorded by the detector of the spectrometer. For this purpose the integrated mercury lamp of the ARYELLE spectrometer is used. The spectrometer software can automatically execute the calibration procedure before the measurement. In the additional setup the 4PICOS ICCD is calibrated using a neon Pen-Ray lamp. The spectrum of the lamp provided by the manufacturer can be used to identify the detected lines and thus to calculate the resolution and the wavelength scale in the desired wavelength range.

For the measurement of the instrumental function an argon PEN-RAY lamp for argon resonance lines and a low pressure hydrogen gas lamp for hydrogen Balmer lines are used. The instrumental function is fitted by a Gaussian distribution (fig. 4.20), which is used for the deconvolution of the data. Table 4.2 contains the measured FWHM values for the corresponding resonance lines. The results correspond approximately to the values given in the data sheet. The argon lines are detected using the ARYELLE spectrometer, whereas the hydrogen lines are analyzed using the additional setup.

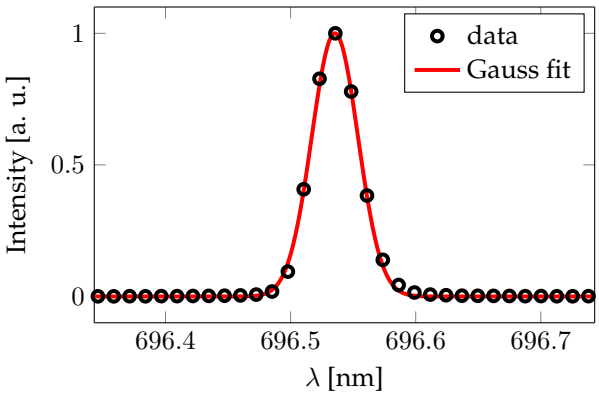


Figure 4.20: Example of measured and fitted instrumental function of the ARYELLE 400 spectrometer.

| **line** | H-$\alpha$ | H-$\beta$ | Ar I | Ar I | Ar I | Ar I |
|---|---|---|---|---|---|---|
| $\boldsymbol{\lambda_0}$ | 486.13 | 656.28 | 696.54 | 738.40 | 763.51 | 794.82 |
| **FWHM [nm]** | 0.275 | 0.275 | 0.043 | 0.045 | 0.058 | 0.059 |

Table 4.2: Instrumental width of the investigated resonance lines.

#### 4.2.4.2 Data preparation

Before the line width can be evaluated from the measured spectra, it needs to be preprocessed. This may include signal integration and binning, noise filtering and background subtraction.

The ARYELLE spectrometer software directly delivers a spectrum, which is already preprocessed by the internal software. The preprocessing includes dark current subtraction and transformation of the image into the wavelength spectral intensity dataset.

The image data provided by the 4PICOS ICCD first needs to be sorted into the exposed and unexposed half frames by evaluation of maximum signal level of each frame. The unexposed half frames are used to determine the dark current signal of the CCD chip, which is subtracted from each exposed half frame. After sorting curvature correction is performed for each half frame as described in section 4.1.6.2.

If required, noise reduction using the SVD technique (see section 4.1.6.3) can be applied. The noise sources for the Stark broadening are of the same origin as for Thomson Scattering. Additionally, noise level can be reduced by pixel binning in the direction of spatial resolution.

#### 4.2.4.3 Deconvolution of instrumental broadening

As previously discussed in section 3.2.2, apart from Stark effect instrumental broadening takes the main influence on the line shape. Before proceeding with the evaluation, impact of this broadening effect on the line shape needs to be removed by deconvolution. If a Lorentzian shape is assumed for the Stark broadened line profile with a FWHM $w_L$, the convoluted line profile can be described by the Voigt function with a FWHM $w_V$. The width of the Lorentzian profile can be reconstructed by the following empirical formula[133]

$$w_V = 0.5346 \times w_L + \left(0.2169 \times w_L^2 + w_G^2\right)^{1/2} \tag{4.7}$$

with $w_G$ the FWHM of the instrumental function approximated by a Gaussian profile. The advantage of this approach compared to numerical deconvolution methods is the much shorter computation time with relative error of the approximation below $1\,\%$. The detected noise is more over smoothened and does not influence further evaluation steps. An example of the development of the relative deviation of the approximated Lorentz profile width is shown in fig. 4.21. Here an instrumental function with $w_G = 0.043\,\mathrm{nm}$ is used.

In order to perform the deconvolution first the pseudo-Voigt profile (eq. (3.54)) is fitted to the measured data using a nonlinear least squares fit procedure (MATLAB function `lsqcurvefit`). The fit function includes the assumed line profile together with the contribution of the continuum radiation. In most cases a first order polynomial is used to approximate the continuum radiation. An example of a fitted and deconvoluted profile can be seen in fig. 4.22.

From the fitted Voigt profile $w_V$ is determined by interpolating the obtained profile at half maximum. Subsequently, $w_L$ is calculated from eq. (4.7) and is further used to generate a deconvoluted Lorentzian line profile.

In the case of the $H_\beta$ several Ar I, Ar II and Mn II lines are present in the spectral region, as can be seen in fig. 4.23. In this case the fit function can be formulated as a sum of several lines and the continuum radiation. Here Ar I line with $\lambda_0 = 479.40\,\mathrm{nm}$ Ar II lines with $\lambda_0$ =480.6, 484.78, 486.59, 486.75 and $487.98\,\mathrm{nm}$ and Mn I and Mn II lines with $\lambda_0$ =482.35, $480.69$ and $481.16\,\mathrm{nm}$ can be identified by means of the NIST database [137]. The lines are assumed not to be considerably broadened. Therefore, they can be fitted by a Gaussian line profile with a line width close to the instrumental profile width. The continuum is fitted by a second order polynomial function. Since not all weak lines can be identified the fit region is restricted as illustrated in fig. 4.23.

#### 4.2.4.4 Abel inversion

For the evaluation of the local plasma density and temperature local emissivity values $\varepsilon$ are necessary. However, the quantity detected by the CCD chip is integrated over the line of sight, which is also known as radiance. It is defined as

$$L = \int \varepsilon(s) ds \tag{4.8}$$

with $s$ denoting the location inside the arc. If the plasma radiation is assumed to be optically thin and the plasma column axially symmetric, the local emissivity $\varepsilon(r)$ can be

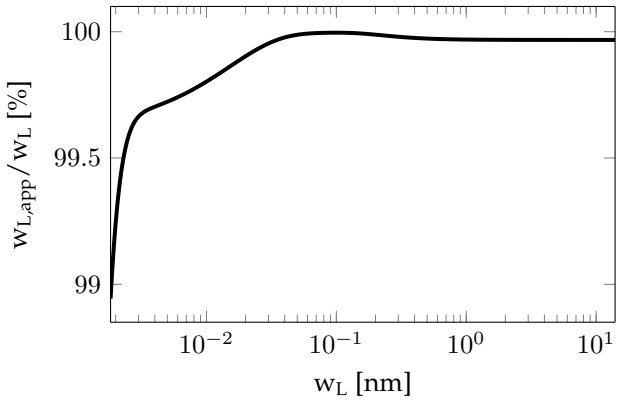


Figure 4.21: Relative deviation of the approximated deconvoluted width $w_{L,app}$ of a Lorentz profile convoluted by the instrumental function with $w_G = 0.043\,\mathrm{nm}$ compared to the original Lorentz profile width $w_L$.

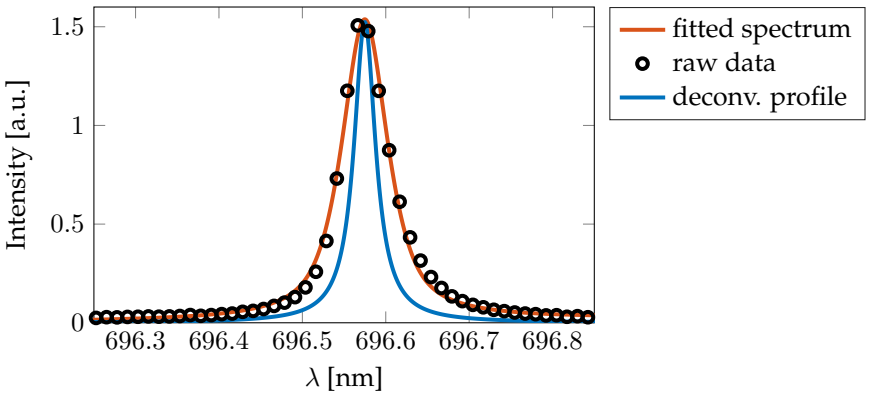


Figure 4.22: Example of a fitted pseudo-Voigt profile under consideration of continuum radiation (1st order polynomial approximation) and a resulting deconvoluted line profile assuming a Gaussian instrumental function with $w_G = 0.043\,\mathrm{nm}$.

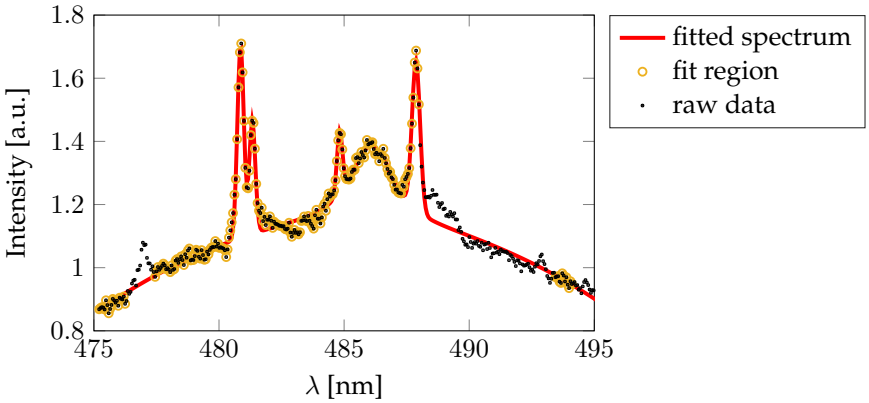


Figure 4.23: Example of a measured and fitted spectrum in the region of $H_\beta$ line.

expressed as a function of the radius of the plasma column. In a two dimensional case the radiance can be interpreted as a projection of the two dimensional radially symmetric emissivity field on one axis. Using the polar coordinates with $r = \sqrt{x^2 + y^2}$ one obtains

$$L(y) = \int_{-\infty}^{\infty} \varepsilon(r)dx = 2\int_{y}^{\infty} \varepsilon(r)\frac{r}{\sqrt{r^2 - y^2}}dr. \tag{4.9}$$

The last equation can be solved to obtain local emissivity distribution using the Abel inversion [102]

$$\varepsilon(r) = -\frac{1}{\pi}\int_{r}^{\infty} \frac{dL(y)}{dy}\frac{dy}{\sqrt{y^2 - r^2}}. \tag{4.10}$$

If the light intensity is approximated by an analytical function, the local emissivities can be calculated directly. Here the following emissivity radial profile is assumed

$$\varepsilon(r) = A(1 + cr^2)\exp\left(-\frac{r^2}{2\sigma^2}\right). \tag{4.11}$$

Inserted into eq. (4.9) the integration delivers

$$L(y) = \int_{-\infty}^{\infty} A(1 + cx^2 + cy^2) \exp\left(-\frac{x^2 + y^2}{2\sigma^2}\right) dx = A'(1 + c'y^2) \exp\left(-\frac{y^2}{2\sigma^2}\right)$$
$$\text{with } A' = A\sqrt{2\pi\sigma^2}(1 + c\sigma^2) \text{ and } c' = \frac{c}{1 + c\sigma^2}.$$

Equation (4.11) is fitted to the deconvoluted radiance distributions using a least square fit procedure provided by `lsqcurvefit`. Figure 4.24 shows an example of the fitted radiance function. From the function parameters obtained from the fit the local emissivity function can be calculated. Finally, this data can be used to determine the broadened line width by interpolating the profile value at half maximum.

#### 4.2.4.5 Plasma parameter determination

**Argon resonance lines**

As previously discussed in section 3.2.6 the line width simultaneously depends on the electron temperature and density. However, a particular line width cannot be explicitly assigned to a single electron density and temperature pair. Evaluation of the line width of a single line yields an expression dependent on both parameters or, in other words, a set with possible electron density and temperature pairs. They are further referred to as temperature-density curves. Hence, a combination of multiple lines is required to determine both parameters. As was first demonstrated by Torres et al. [93] and later applied to welding arcs by Zielinska et al.[96], both temperature and density can be determined by evaluating the width of at least two Stark broadened spectral lines using the "intersection" method. Here the crossing point of two temperature-density curves determines the electron temperature and density valid for the investigated conditions.

In order to obtain temperature-density curves first the available theoretical Stark broadening data is interpolated in the temperature and density region typical for thermal plasmas. In this case a temperature range from 3000 to 20 000 K and an electron density range from $1 \times 10^{21}$ to $2 \times 10^{23}\,\mathrm{m}^{-3}$ are chosen. In the second step, all the temperature-density pairs matching the particular Stark width are extracted from the interpolated data. An exemplary evaluation of four Ar I resonance lines is demonstrated in fig. 4.25. Here argon lines with the wavelength of $\lambda_0 = 696.54$, 738.40, 763.51 and 794.82 nm are investigated. All the chosen lines are well detectable along the whole diameter of the arc. Moreover,

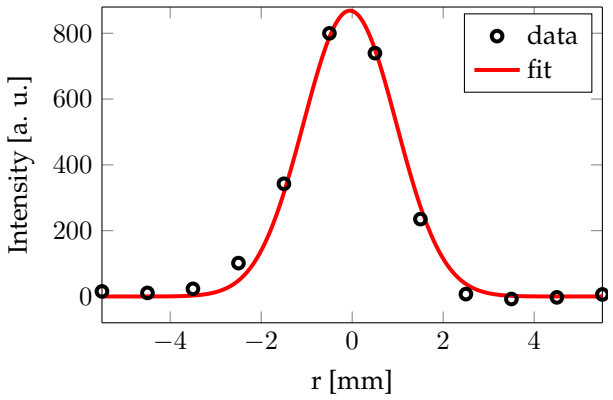


Figure 4.24: Example of a measured and fitted data for Abel inversion at $\lambda = 696.58\,\mathrm{nm}$ in a GMAW process during high current phase.

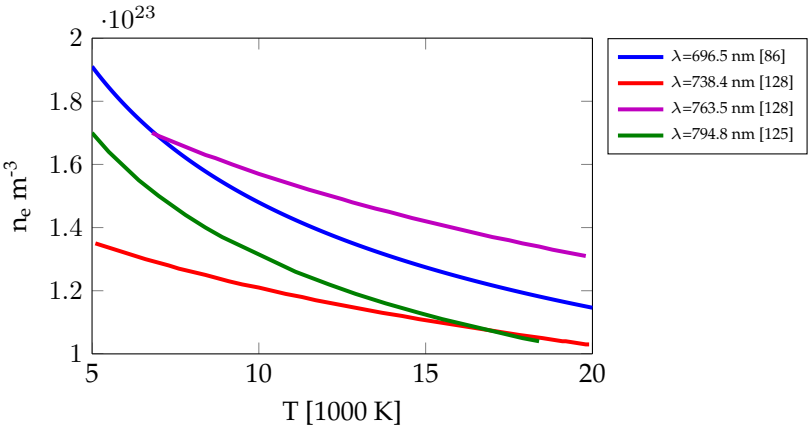


Figure 4.25: Evaluation of the electron temperature-density curves for line width of $\lambda_0 = 696.5\,\mathrm{nm}$ ($w = 0.109\,\mathrm{nm}$), $\lambda_0 = 738.4\,\mathrm{nm}$ ($w = 0.116\,\mathrm{nm}$), $\lambda_0 = 763.5\,\mathrm{nm}$ ($w = 0.158\,\mathrm{nm}$) and $\lambda_0 = 794.8\,\mathrm{nm}$ ($w = 0.136\,\mathrm{nm}$) argon resonance line measured in GMAW process operated with aluminum as a wire electrode at r=1 mm.

theoretical Stark broadening estimations are available for those lines. As $\lambda_0 = 696.5\,\mathrm{nm}$ is known to be optically thin and the broadening width density evaluation of all the lines in this investigation lies in the same range, all the lines are assumed to be optically thin.

For a successful determination of the electron temperature and density using the intersection method the gradients of particular temperature-density curves should considerably differ from each other. Yet as can be seen in fig. 4.25, temperature-density curves of different lines run almost parallel in this case. The evaluation of the curves intersections becomes very sensitive to measurement deviations and thus is not suitable for reliable temperature and density determination.

Still, fig. 4.25 illustrates, that singe temperature-density curves are more sensitive to electron density than to temperature. Therefore, the measured line width of separate spectral lines can be used to estimate at least the electron density without any further assumptions. In this case the mean electron density value is calculated from the data range given by the evaluated temperature-density curve. Additionally, the methodical uncertainty is calculated. It results from the ration between the maximum/minimum electron density contained in the dataset and the previously determined mean electron density.

Furthermore, LTE assumptions may be taken into account, when evaluating the plasma parameters from Ar I lines. In this case the Saha equation (eq. (2.10)) for the corresponding Ar-X gas mixture, with X an additional gas or metal vapor present in the plasma, is solved under consideration of the ideal gas law (eq. (2.5)) for different Ar-X concentration pairs. This dataset is used to restrict the temperature-density curves to the values possible under LTE. Thus the mean electron density and temperature values with the respective uncertainties can be calculated from the resulting restricted dataset.

An evaluation of the plasma parameters using the intersection method can still be performed, if the experimental error of the measured line width is taken into account directly in the evaluation. The deviation of the measured width results on the one hand from fluctuation in the process itself. On the other hand the noise in the signal influences the result of the fitting algorithm. The experimental error is determined by calculating the standard deviation of at least 3 consecutive measurements. In this case not a particular line width, but a line width range calculated from the mean measured line width value and its standard deviation are used to obtain temperature-density curves. Thus, the temperature-density curves extend to areas. The intersection of the areas resulting form different lines

is calculated. From this intersection area mean electron density and temperature values are determined. The methodical uncertainty is calculated in the same manner as described above for the evaluation of separate resonance lines. Figure 4.26 illustrates an example of this evaluation method. Not every temperature-density curve combination delivers an intersection area. In this specific case the $763.51\,\mathrm{nm}$ Ar I line is not considered, as the temperature-density curve resulting from the width of lines did not intersect with the areas resulting from other lines. The evaluable combination of lines however can change for different plasma compositions. For this reason different line combinations are considered for evaluation of different welding processes.

**Hydrogen resonance lines**

In contrast to argon resonance lines it is not possible to simultaneously record $H_\alpha$ and $H_\beta$ lines due to the use of the Fastie-Ebert spectrometer design. Since the GMAW arc is not very stable, the combination of the consecutively measured line width of the two hydrogen lines introduces a large error. Hence, these lines can only be evaluated separately.

Although a temperature dependence of the $H_\alpha$ and $H_\beta$ line widths exists, it is much weaker compared to the temperature dependence of the argon lines, as illustrated in fig. 4.27. Hence, the separate evaluation of these lines can at least provide the information about the electron density. Additionally, it is possible to use density dependent approximation formulas for the evaluation. Yet, as can be seen in fig. 4.27, the electron density value for the considered temperature range is underestimated, if eqs. (3.105) to (3.107) are used. Therefore, these equations are not further considered in this work.

A similar procedure, as described for the evaluation of separate argon lines, is applied for hydrogen lines as well. For this purpose the available theoretical data provided in [129] is interpolated within a temperature range from 3000 to 20 000 K and an electron density range from $1 \times 10^{21}$ to $2 \times 10^{23}\,\mathrm{m}^{-3}$. Additionally, the LTE assumptions in form of Saha equation and ideal gas law are included in order to estimate the possible temperature values.

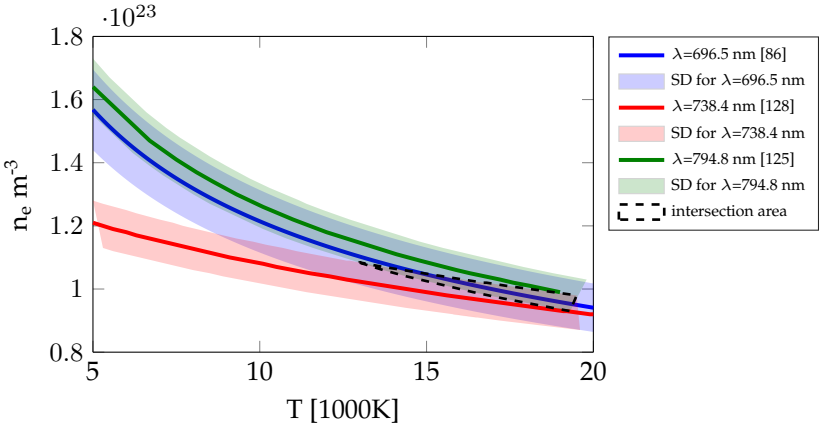


Figure 4.26: Evaluation of the electron temperature and density from mean measured width of $\lambda_0 = 696.5\,\mathrm{nm}$ ($w = 0.089 \pm 0.007\,\mathrm{nm}$), $\lambda_0 = 738.4\,\mathrm{nm}$ ($w = 0.104 \pm 0.006\,\mathrm{nm}$) and $\lambda_0 = 794.8\,\mathrm{nm}$ ($w = 0.136 \pm 0.007\,\mathrm{nm}$) argon resonance lines under consideration of the standard deviation (SD) of the data. The region marked with the black dashed line indicates the intersection area. The data is obtained from the measurement in the GMAW process operated with aluminum as wire electrode at r=$1\,\mathrm{mm}$.

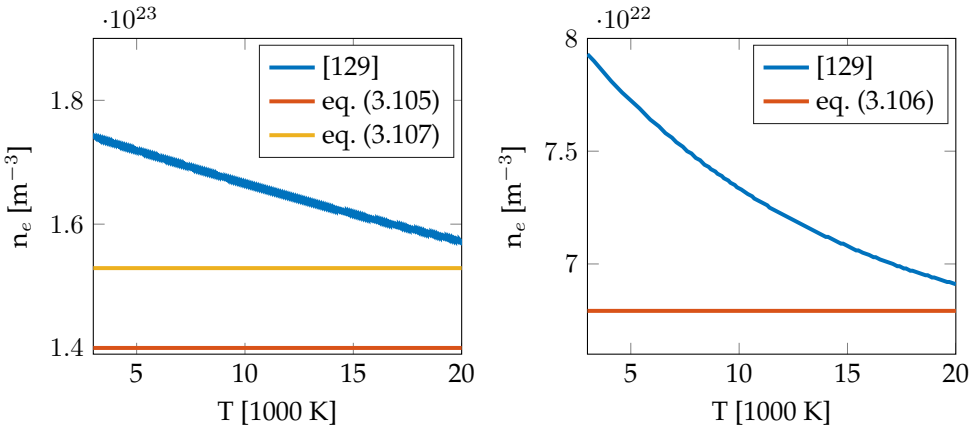


Figure 4.27: Example of the evaluation of $H_\alpha$ line width ($w = 1.38\,\mathrm{nm}$) (a) and $H_\beta$ line width ($w = 3.69\,\mathrm{nm}$) (b) using temperature and density dependent line profile data ($\mu = T_e/T_i = 1$) and different approximation formulas.

## 4.3 Setup and parameters of the welding processes

For the generation of the welding arc a stationary setup is used for both processes, so that the workpiece does not have to be moved. In both cases a cooled electrode is used as a workpiece. The distance of the welding gun and the workpiece is kept constant. The arc generating system is positioned on an automatic controlled linear axis with a stepping motor. This allows vertical movement of the arc relative to the detector unit. Thus, measurements along the whole arc length can be performed. Here ISEL LES5 type linear stage unit operated with the controller unit C142-4 is used. The accuracy of the system is $12.5\,\mu\mathrm{m/step}$. For the Stark broadening measurements a second linear axis of the same type horizontally moving the collimator is added.

All the experiments are carried out on the atmospheric pressure ($P = 10^5\,\mathrm{Pa}$) and under local exhaustion ventilation.

### 4.3.1 GTAW

Figure 4.28 shows a schematic setup of the GTAW process. In this case the arc is generated between a tungsten cathode SI1.5% $La_2O_3$, $3.2\,\mathrm{mm}$ diameter and $60°$ tip angle) and a planar water-cooled copper anode ()$100\,\mathrm{mm}$ diameter). The cooling of the anode additionally assures temporally stable arc operation. The cathode-to-anode gap is adjusted to $7\,\mathrm{mm}$. Melting of the anode is not observed in these experimental conditions. Hence, the production and entrainment of the metal vapor into the bulk plasma can be neglected.

A BINZEL ABITIG MT 500W liquid cooled robotic welding torch is used here. This torch is suitable for a stable long-lasting operation, which is necessary for the Thomson scattering measurements. An inverter type power supply EWM TETRIX 230 is operated in the DC mode at $150\,\mathrm{A}$.

Measurements with different shielding gas mixtures are performed as listed in table 4.3. The mixing ratios are given by volume percentage. Since gas bottles with predefined gas mixtures are provided, the gases are fully mixed before entering the gas nozzle of the welding gun. For all investigations a gas flow rate of $14\,\mathrm{slpm}$ and a gas nozzle with an inner diameter of $19.5\,\mathrm{mm}$ are used. The distance of the nozzle to the workpiece is $10\,\mathrm{mm}$.

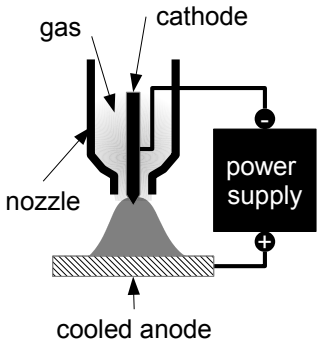


Figure 4.28: Schematic setup of the GTAW process.

| **parameter** | **value** |
|---|---|
| current (DC) | 150 A |
| cathode | W + 1.5 % $La_2O_3$, ∅ 3.2 mm, tip angle 60° |
| anode | Cu (cooled), ∅ 100 mm |
| cathode-anode gap | 7 mm |
| gas flow rate | 14 slpm |
| *diagnostics applied for shielding gas compositions* | |
| Thomson scattering | Ar, Ar (50 %) + He (50 %), Ar (98 %) + $N_2$ (2 %), Ar (94 %) + $N_2$ (6 %), Ar (98 %) + $H_2$ (2 %), Ar (94 %) + $H_2$ (6 %) |
| Stark broadening | Ar, Ar (50 %) + He (50 %) |

Table 4.3: Overview of the GTAW process parameters.

In order to obtain a two-dimensional temperature and density distribution within the arc using Thomson scattering technique, measurements along different vertical positions are performed. The starting position for measurements is set at $z = 5.5\,\mathrm{mm}$ (distance between the beam center and the anode surface). A closer position towards the cathode tip is not possible due to reflection of the laser light on the metallic surface of the cathode, which disturbed the scattering measurements. The arc is scanned in $1\,\mathrm{mm}$ steps along the z axis. Here the closest position to the anode is $z = 1.5\,\mathrm{mm}$.

Two dimensional parameter distributions from the Stark broadening measurements are obtained from a point by point scan in the region between $z = 1.5$ to $5.5\,\mathrm{mm}$ (vertical direction) and $r = -6$ to $6\,\mathrm{mm}$ (horizontal direction). The horizontal and vertical distances between the measurement points are $1\,\mathrm{mm}$.

### 4.3.2 GMAW

The schematic setup of the GMAW process is shown in fig. 4.29. The arc is ignited between a welding wire serving as an anode and a water cooled cylindrical copper cathode with a diameter of $100\,\mathrm{mm}$. The measurements are mainly conducted with an aluminum wire (AlMg 4.5 Mn). Few investigations with iron wire (G3Si1) are also performed. The wires with a diameter of $1.2\,\mathrm{mm}$ and $1\,\mathrm{mm}$ respectively are fed at a velocity of $50\,\mathrm{mm/s}$. On the central axis the copper cathode is provided with a hole of $7\,\mathrm{mm}$ in diameter. The metal droplets can fall through the hole into a collecting vessel and so prevent metal accumulation on the cathode surface.

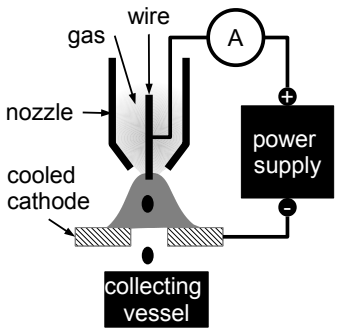


Figure 4.29: Schematic setup of the GMAW process.

A liquid cooled robotic welding torch TBI 9W AUT is used here. An inverter type power supply OTC DW 300 is operated in the pulsed DC mode. The power supply allows to program the pulse shape. Its settings for the used processes are documented in table 4.4. The current and voltage of the process are additionally monitored by a Hall sensor SS94A1F and a voltage probe.

Argon 4.6 ($99.9\,\%$ purity) is used as a shielding gas at a flow rate of $25\,\mathrm{slpm}$. The gas nozzle diameter is $16\,\mathrm{mm}$. For Stark broadening measurements less than $0.5\,\%$ of $H_2$ is added to the process. The gas nozzle standoff is set to $15\,\mathrm{mm}$ and is kept constant during the whole process.

Here investigations at $z = 5.5\,\mathrm{mm}$ above the workpiece (cathode surface) are performed. For the Stark broadening a radial range of $r = -5.5$ to $5.5\,\mathrm{mm}$ at $z = 5.5\,\mathrm{mm}$ is scanned. The horizontal distance between the single measurement locations is $1\,\mathrm{mm}$.

| **parameter** | **aluminum** | **iron** |
|---|---|---|
| pulse rate | 90 to 100 Hz | 70 to 120 Hz |
| peak current | 400 A | 320 A |
| wire | AlMg 4.5 Mn, ∅ 1.2 mm | G3Si1, ∅ 1 mm |
| feed velocity | 50 mm/s | 50 mm/s |
| stand off | 15 mm | 15 mm |
| gas flow | 25 slpm | 25 slpm |
| cathode | Cu (cooled), ∅ 100 mm | Cu (cooled), ∅ 100 mm |
| ∅ of cathode hole | 7 mm | 7 mm |
| *OTC settings* | | |
| peak current (F13) | 340 A | 300 A |
| peak time (F14) | 0.4 ms | 1 ms |
| up-slope time (F26) | 1 ms | 2 ms |
| down-slope time (F27) | 0.6 ms | 1.6 ms |
| base time (F30) | 10 ms | 10 ms |
| *Diagnostics applied for shielding gas compositions* | | |
| Thomson scattering | Ar | Ar |
| Stark broadening | Ar, Ar + $H_2$ (trace) | none |

Table 4.4: Overview of the GMAW process parameters.

# Chapter 5

# Results and discussion

In the following chapter the results of all measurement methods applied in this work are presented. Table 5.1 gives an overview over the applied measurement methods and their evaluation under different assumptions. Here the keyword LTE implies the use of Saha equation and the ideal gas law. The presentation of the results is divided in to four sections. First the measurement results originating from Thomson scattering method are presented. In the second part the results from the Stark broadening of different resonance lines are discussed. The third section compares the results of different measurement methods applied to particular processes. Moreover, the results are compared to other experimental data or modeling results available in the literature. Finally, the plasma composition reconstruction for selected processes is presented in the last section.

## 5.1 Thomson scattering results

Thomson scattering technique is applied to measure electron temperature and density independent from the assumption of LTE in GTAW and GMAW processes. Here first the results for GTAW processes with different shielding gas mixtures are shown. Afterwards measurements performed in GMAW processes with aluminum and iron electrodes are discussed.

| **method** | **assumptions** | **resulting quantities** |
|---|---|---|
| *Measurements* | | |
| Thomson scattering | Maxwell-Boltzmann distribution | $T_e, n_e$ |
| Stark broadening of a single resonance line | Maxwell-Boltzmann distribution | $n_e$ |
| | Maxwell-Boltzmann distribution, LTE | $T_e = T_i, n_e$ |
| Stark broadening of multiple resonance lines (intersection method) | Maxwell-Boltzmann distribution | $T_e, n_e$ |
| | Maxwell-Boltzmann distribution, LTE | $T_e = T_i, n_e$ |
| *Reconstruction* | | |
| Gas composition | $T_e$ and $n_e$ from Thomson scattering data, LTE | plasma composition |

Table 5.1: Overview of the applied measurement techniques and evaluation methods.

### 5.1.1 GTAW processes

In the following Thomson scattering results for the GTAW processes are presented. Figure 5.1 visualizes the region of the arc column covered by the measurement with respect to the electrodes. All the measurements represent the mean average of 3 datasets recorded under equal conditions. For all the measurements presented here the minimum measurable temperature is $5000\,\mathrm{K}$ and the minimum measurable electron density value $1 \times 10^{22}\,\mathrm{m}^{-3}$. The deviation of temperature and density values mainly arise from statistical noise of the detector and the plasma noise as described in [109]. In this setup the standard deviation of temperature and density reaches values below $5\,\%$ in the central arc region. In the edge region a lower signal intensity is detected, since the electron density decreases. Therefore, the standard deviation rises up to $30\,\%$ in this region.

#### 5.1.1.1 Pure argon GTAW process

Measurements in the GTAW process operated with pure argon are performed in order to verify the functionality of the Thomson scattering setup. Figure 5.2 shows the electron temperature and density profiles obtained from the Thomson scattering signal. Here the maximum electron density reaches $1.45 \times 10^{23}\,\mathrm{m}^{-3}$ on the central arc axis in the region below to the cathode. It decreases down to $1.2 \times 10^{23}\,\mathrm{m}^{-3}$ close to the anode region. The maximum temperature of $18\,600\,\mathrm{K}$ is also reached at the central arc axis close to the cathode. It reduces to $15\,000\,\mathrm{K}$ in the region close to the anode. The temperature and density values radially decrease towards the arc edges.

#### 5.1.1.2 GTAW processes with gas mixtures

Thomson scattering is further successfully applied to the investigation of GTAW processes with Ar-He, Ar-$H_2$ and Ar-$N_2$ gas mixtures.

Figure 5.3 shows the resulting electron temperature and density distributions in a GTAW process operated with Ar($50\,\%$)-He($50\,\%$) shielding gas mixture. The maximum electron density in the range of $8 \times 10^{22}\,\mathrm{m}^{-3}$ is reached in the near cathode region. The

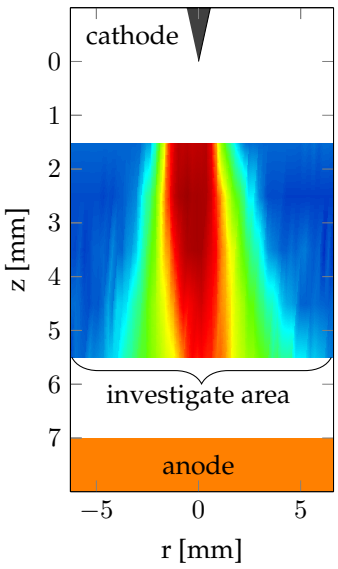


Figure 5.1: Position of the arc column region investigated by Thomson scattering with respect to the electrodes.

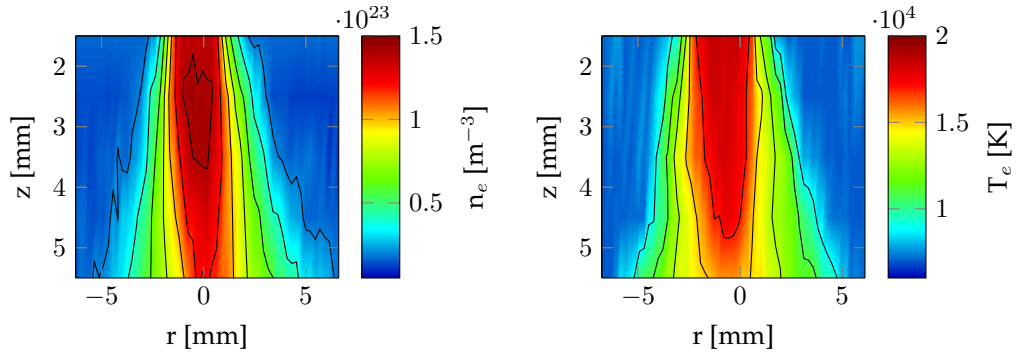


Figure 5.2: Electron density (left) and temperature (right) measured by means of Thomson scattering in the GTAW process operated with pure argon as a shielding gas. Two consecutive contour lines correspond to an increase of $2 \times 10^{22}\,\mathrm{m}^{-3}$ for the density values and 2000 K for the temperature values.

electron density drops down to $6 \times 10^{22}\,\mathrm{m}^{-3}$ when approaching the anode in the center of the arc. It lies considerably below the maximum electron density for processes with pure argon. The radial gradient of the obtained electron density distribution is reduced as well compared to the pure argon arc. This effect occurs due to the much higher ionization energy of He compared to Ar. The maximum temperature of 18 000 K is also reached in the near cathode region. However, a higher temperature drop towards the anode can be observed compared to the temperature distribution of pure argon arc. The temperature decreases down to 13 000 K when approaching the anode. The radial shape of the temperature distribution appears to be more constricted in the near anode region than it is the case for pure argon arc.

Reduction of measured electron density and temperature can be also observed for gas mixtures of argon with molecular hydrogen. This results directly from the higher enthalpy density of Ar + $H_2$, which allows to "store" a higher amount of energy in the shielding gas. If 2 % $H_2$ is added to argon, the electron temperature distribution slightly changes as can be seen in fig. 5.5(a). Its maximum value reaches up to 18 900 K. However the hottest zone is smaller compared to the case of pure argon, as illustrated by the temperature contours.

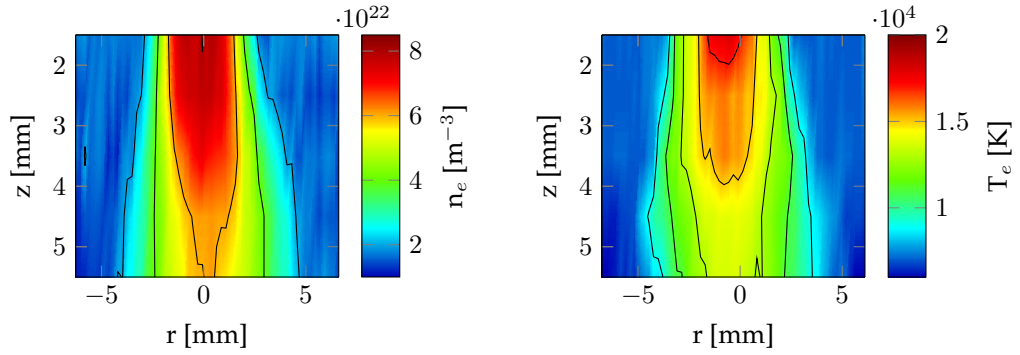


Figure 5.3: Electron density (left) and temperature (right) measured by means of Thomson scattering in the GTAW process operated with Ar(50 %)-He(50 %) shielding gas mixture. Two consecutive contour lines correspond to an increase of $2 \times 10^{22}\,\mathrm{m}^{-3}$ for the density values and 2000 K for the temperature values.

This can be explained by the higher thermal conductivity of this gas mixture for temperatures close to the dissociation temperature of $H_2$. Such higher thermal conductivity produces a higher energy flow outwards. In order to keep its high temperature the plasma column tends to constrict itself to reduce such energy loss. The maximum electron density drops to $1.25 \times 10^{23}\,\mathrm{m}^{-3}$. When $H_2$ fraction is increased to $6\,\%$ the maximum temperature drops to $17\,800\,\mathrm{K}$, while the maximum electron density decreases to $1.15 \times 10^{23}\,\mathrm{m}^{-3}$ (fig. 5.5(b)). Here the temperature and density drop towards the anode increases as well, while the arc appears to be slightly more constricted in the anode region.

The considerably lower temperature obtained in the Ar-He arc might be explained, if demixing of argon in helium is taken into account. In general demixing might be caused by mole gradients, frictional forces and thermal diffusion [145]. Figure 5.4 illustrates the temperature dependent mole fraction of an Ar-He plasma with initial concentration of $50\,\%$ Ar and $50\,\%$ He. Therefrom it can be clearly seen, that due to ionization of argon significant mole fraction gradients of Ar, $Ar^+$ and He occur, if a corresponding temperature gradient exists. Since such a gradient is present in the arc, initially the corresponding mole fraction gradients are formed. In order to compensate those gradients the argon ions in the arc center diffuse to the outer cooler regions, while the argon and helium atoms diffuse from the cooler arc regions into the arc center. Thus spatial mole fractions gradients of all species vanish. Both diffusion processes contribute to the cooling of the arc.

Moreover collisions of helium with argon atoms and ions support the diffusion of helium to the hot regions of the arc. Hence both demixing processes lead to a higher helium concentration in the arc center, which will be further discussed in section 5.4.

If mixing argon with molecular nitrogen, a similar effect can be observed. For $2\,\%$ of $N_2$ in the shielding gas mixture the electron temperature reaches up to $18\,900\,\mathrm{K}$ and the $1.31 \times 10^{23}\,\mathrm{m}^{-3}$ as depicted in fig. 5.5(c). However, compared to pure argon arc the temperature and density values decrease more rapidly towards the region close to the anode. This effect is more distinct for the temperature distribution, if the nitrogen fraction is increased to $8\,\%$. Here the maximum temperature also reaches $17\,800\,\mathrm{K}$. The electron density distribution however does not noticeably change. Its maximum value lies at $1.40 \times 10^{23}\,\mathrm{m}^{-3}$ (fig. 5.5(d)), which is comparable to the case of lower nitrogen concentration within the experimental accuracy.

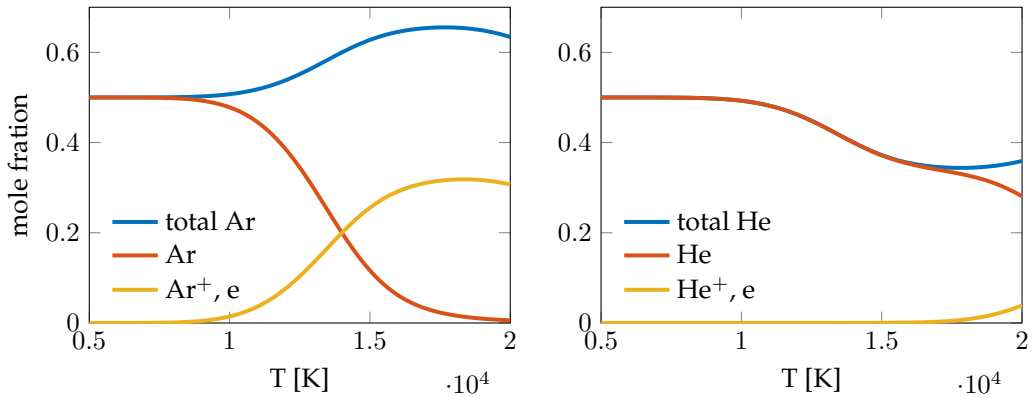


Figure 5.4: Temperature dependence of the mole fractions of argon (left) and helium (right) under LTE assumptions, if no demixing of the initial shielding gas composition occurs.

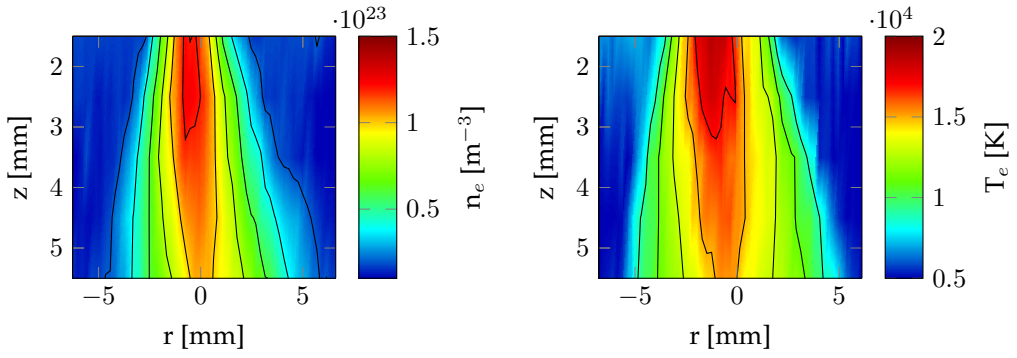


(a) Ar(98 %)-$H_2$(2 %)

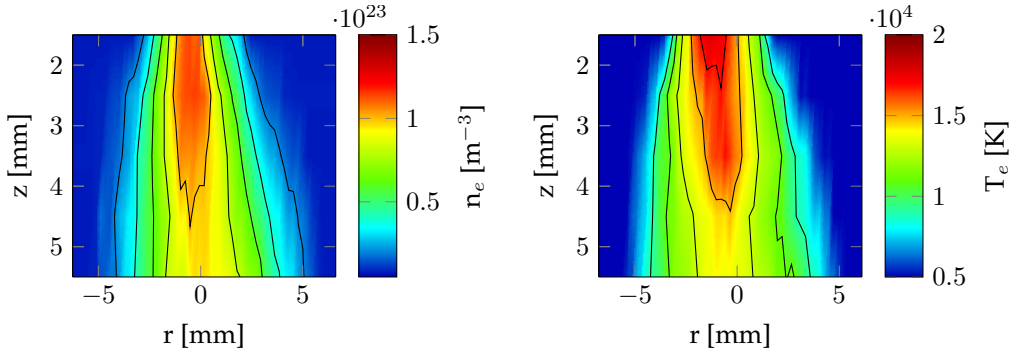


(b) Ar(94 %)-$H_2$(6 %)

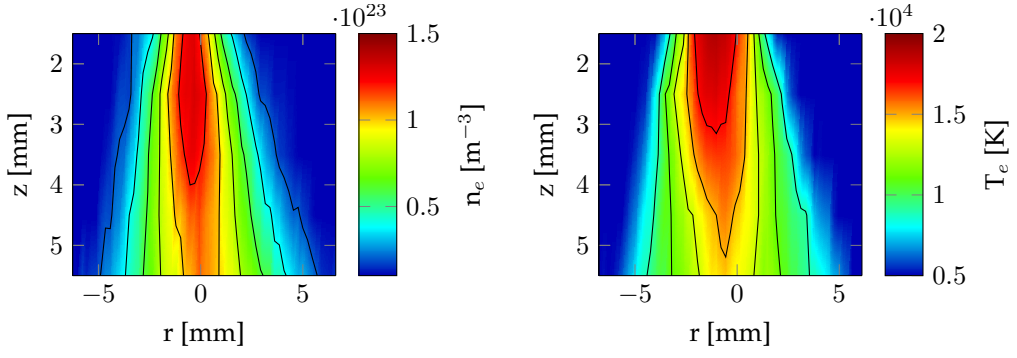


(c) Ar(98 %)-$N_2$(2 %)

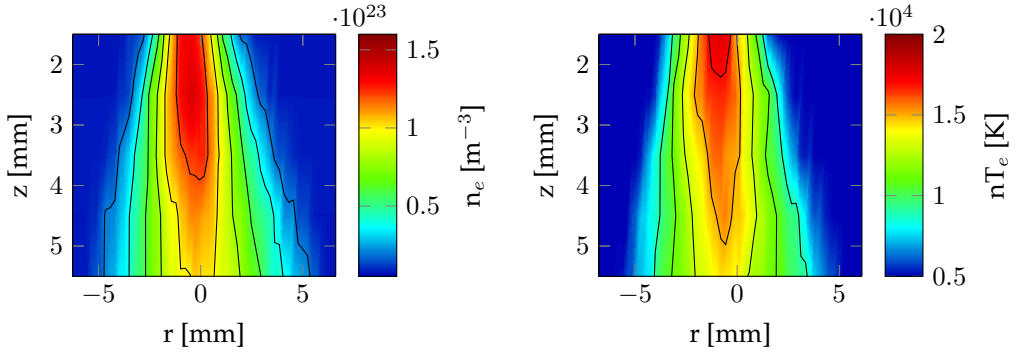


(d) Ar(92 %)-$N_2$(8 %)

Figure 5.5: Electron density (left) and temperature (right) measured by means of Thomson scattering in the GTAW process operated with different shielding gas mixtures. Two consecutive contour lines correspond to an increase of $2 \times 10^{22}\,\mathrm{m}^{-3}$ for the density values and 2000 K for the temperature values.

### 5.1.2 GMAW pocesses

In the next step Thomson scattering results for the GMAW arcs are presented. Since the conditions in the arc column of the GMAW process can change from pulse to pulse, it is generally not possible to exactly repeat a measurement. However, when comparing different measurements in the high current phase of the pulse, the overall deviation of the determined values is similar to those for GTAW arcs. In the evaluation again the temperature values below $5000\,\mathrm{K}$ and the density value below $1 \times 10^{22}\,\mathrm{m}^{-3}$ could not be measured.

#### 5.1.2.1 GMAW process with aluminum

Electron temperature and density have successfully been evaluated from Thomson scattering spectra in the case of GMAW arc operated with an aluminum wire electrode. Figure 5.6 shows an example of radially resolved measurements of the electron temperature and density in the GMAW process during the high current phase ($t_{trig}$=0.7 ms in fig. 5.7 (center)). Although the current during the measurement reaches up to $400\,\mathrm{A}$, the maximum measured electron temperature does not exceed $14\,800\,\mathrm{K}$, whereas the electron density maximum lies at about $1.6 \times 10^{23}\,\mathrm{m}^{-3}$. Here a radial decrease of electron temperature and density from the hot dense region in the center of the arc column towards the edges is observed.

The temporal investigation of the GMAW process is performed with a resolution of at least $100\,\mu\mathrm{s}$. In order to clearly present temporal evolution of electron temperatures and densities in the GMAW arc only the maximum electron temperature and density values reached in the center of the arc are plotted in fig. 5.7 (bottom). Additionally, current and voltage characteristics are shown relatively to the trigger event time $t_{trig}$ of single measurements (center). In order to visualize the shape of the arc during measurements the images for each measurement are depicted (top). The relative intensities in the images are scaled in order to visualize the shape of the arc without saturation effects. Hence the image intensities at different $t_{trig}$ are not comparable. The white dashed line in the images indicates the position of the incident laser beam.

In a first approximation it can be concluded, that the electron temperature and density are related to the arc current. The highest values are reached at the end of the high current phase. Afterwards the temperature as well as density fall with decreasing current. The last two measurements at $t_{trig}$=2.21 and $4.29\,\mathrm{ms}$ are made in the low current phase, where arc current is in the range of $10$ to $20\,\mathrm{A}$. As visualized in the images of the arc, only weak plasma radiation is visible in this phase. The lighter spots positioned above the laser beam at $t_{trig}$=2.21 ms and under the beam at $t_{trig}$=4.49 ms are aluminum metal droplets detached from the wire anode. The scattering signal level in these two measurements is lower than in the preceding ones. Thus, only signals close to the center of the arc cam be evaluated. Nevertheless, it can be concluded that the electron temperature in this phase does not exceed $5000\,\mathrm{K}$. The maximum electron density ranges between $2 \times 10^{22}$ and $2.5 \times 10^{22}\,\mathrm{m}^{-3}$.

#### 5.1.2.2 GMAW process with iron

A distinct detection of the Thomson scattering spectrum is not possible for the GMAW process operated with iron as a wire electrode. Figure 5.8 shows the spectra recorded without and with presence of the laser radiation at two different $t_{trig}$ with respect to the current pulse (bottom). Current and voltage signals (top, left) as well as the images of the plasma (top, right) for the corresponding trigger event time are represented.

For both $t_{trig}$ strong lines are present in the region around the laser wavelength. At $t_{trig} = 0\,\mathrm{ms}$ the plasma and laser radiation are approximately of the same order of magnitude (fig. 5.8(c)). The plasma radiation is weaker for $t_{trig} = 1.93\,\mathrm{ms}$ (fig. 5.8(d)), however in both cases no typical Thomson scattering spectra are visible, as is the case for GTAW or GMAW operated with aluminum. A possible explanation is, that iron resonance lines

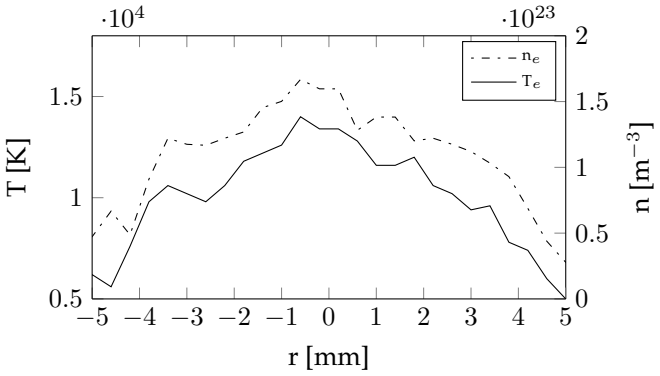


Figure 5.6: Example of the radial profile of electron temperature and density measured in the GMAW process with aluminum at $t_{trig} = 0.7\,\mathrm{ms}$ and z=5.5 mm above the cathode surface.

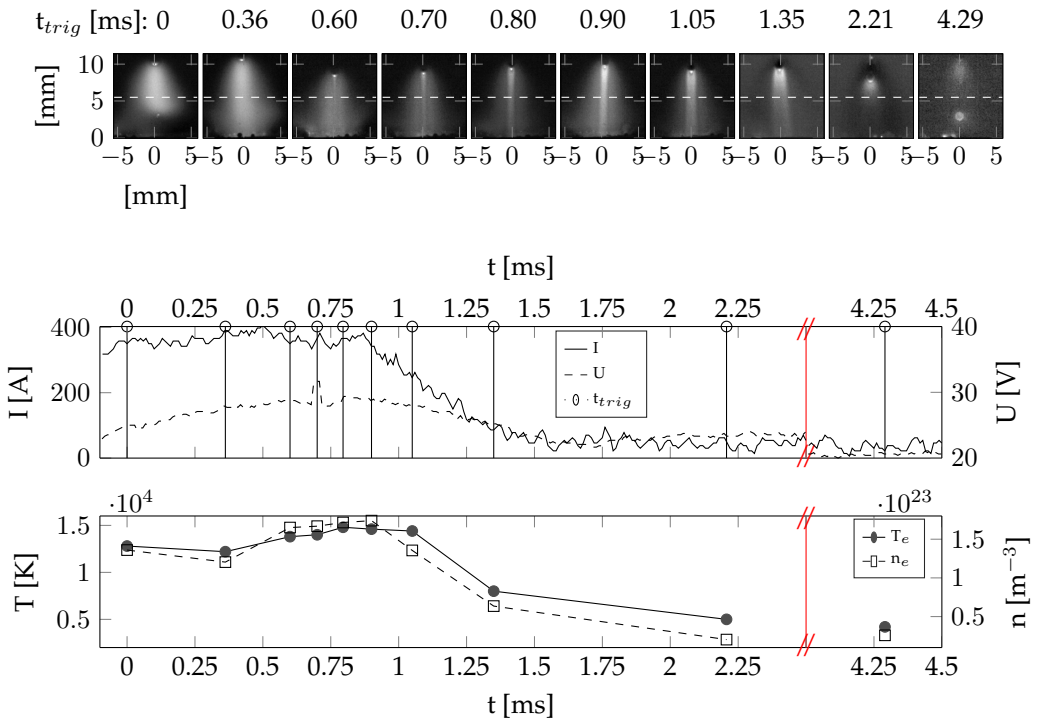


Figure 5.7: Top: images of the GMAW arc with aluminum recorded at the time point $t_{trig}$ simultaneously to the Thomson scattering measurements. The white dashed line indicates the laser beam position. Center: process current pulse and voltage, the trigger event time $t_{trig}$ is marked by the vertical bars. Bottom: time resolved maximum electron temperature and density in the center of the GMAW arc.

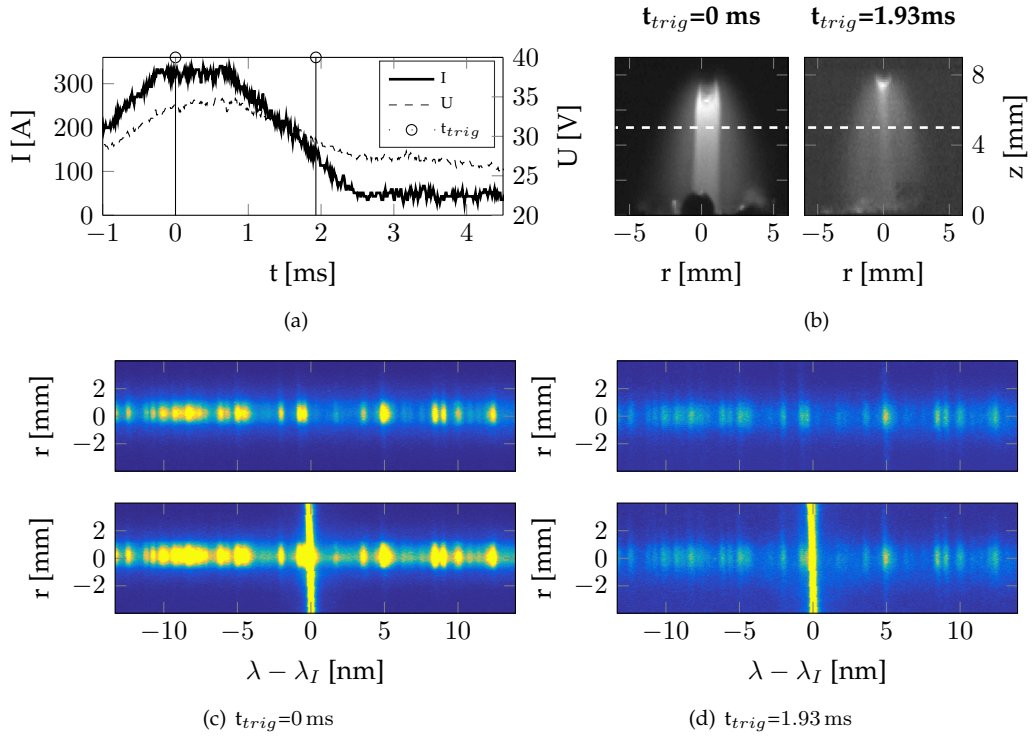


Figure 5.8: Process current pulse and voltage with the trigger event time $t_{trig}$ marked by the vertical bars (a). Images of the GMAW arc with iron wire recorded at $t_{trig}$ simultaneously to the Thomson scattering measurements (b). The white dashed line indicates the laser beam position. Spectra of GMAW arc operated with iron wire recorded at $\lambda_I = 532\,\mathrm{nm}$ without (top) and with (bottom) presence of the laser radiation for two different $t_{trig}$ (c,d). The intensities are adjusted to the typical level for Thomson scattering signal as observed for the GMAW process with aluminum.

overlap the Thomson scattering signal. The intensity of the latter is expected to be weaker than the intensity of the resonance lines. The Thomson scattering signal is not visible, even if the plasma radiation is weaker, as e.g. for $t_{trig} = 1.93\,\mathrm{ms}$. This might be an evidence for absorption of the scattered radiation.

## 5.2 Stark broadening results

Stark broadening technique is used to measure electron density and temperature without the assumption of LTE (evaluation of the electron density, while neglecting the weak temperature dependence of Stark broadening) and with assumption of LTE (Stark broadening combined with Saha equation and ideal gas law for electron temperature and density evaluation). This diagnostic method is applied to GTAW processes with pure argon and argon-helium gas mixtures. Moreover, a GMAW process with aluminum is investigated. Since no measurements with Thomson scattering could be evaluated for GMAW process with iron (see section 5.1.2.2) and several experimental works [89, 96] are already available for this process, it was not further investigated by means of Stark broadening. In the following first the results obtained for GTAW and afterwards for GMAW processes are presented.

Since the width of single resonance lines is not sufficient to obtain electron density and temperature values additional assumptions are needed to perform the evaluation. Thus,

two evaluation methods are applied for comparison. First, investigated lines are separately evaluated. If no additional assumptions are used, only electron density values could be obtained from the width data. In order to deduce both temperature and dentistry LTE assumptions are assumed, when evaluating the line width of the four separate Ar I lines. Additionally, the intersection method combining the information provided by several resonance lines is applied in order to determine electron temperature and density without and with assumption of LTE. The methodical uncertainty refers to the deviation of the determined values resulting from the evaluation method. Yet for the case of pure argon plasma in LTE it is zero. For the intersection method the total uncertainty also includes the deviation of data due to noise.

### 5.2.1 GTAW processes

Following the assumption, that the GTAW processes are stationary, two dimensional electron density and temperature profiles (radial and vertical directions) can be measured. Arcs operated with two different shielding gas mixtures, pure argon and Ar-He, and a DC current with $I = 150\,\mathrm{A}$ are investigated.

#### 5.2.1.1 Pure argon GTAW process

Figure 5.9 shows the results of the evaluation of four single Ar I lines for the GTAW process operated with pure argon as a shielding gas. For each line plasma parameter determination without and with assumption of LTE is performed.

Depending on the evaluated line the maximum electron density reaches between $9 \times 10^{22}$ and $15 \times 10^{22}\,\mathrm{m}^{-3}$ in the near cathode region (figs. 5.9(a), 5.9(c), 5.9(e) and 5.9(g)). Close to the anode the electron density drops to $8 \times 10^{22}$ – $12 \times 10^{22}\,\mathrm{m}^{-3}$. The uncertainty varies depending on the evaluated line between $16$ and $35\,\%$.

If taking into account LTE assumptions, lower electron densities are obtained (figs. 5.9(b), 5.9(d), 5.9(f) and 5.9(h)). In this case the maximum values only reach $9 \times 10^{22}$ to $12 \times 10^{22}\,\mathrm{m}^{-3}$. Additionally, plasma temperature can be determined here. The maximum values in the range of $13\,000\,\mathrm{K}$ are located close to the cathode. In the outer arc regions temperatures between $9000$ and $10\,000\,\mathrm{K}$ are estimated.

For $696.5$, $738.4$ and $794.8\,\mathrm{nm}$ lines the temperature and density values radially and vertically decrease towards the arc edges and the anode resulting in comparable spatial distributions. However, as can be seen in figs. 5.9(e) and 5.9(f) the resulting spatial profiles for $763.5\,\mathrm{nm}$ line shows inhomogeneities, which might be an indication for self-absorption of this line or measurement artifacts.

Figure 5.10 illustrates the results of the intersection method, which could only be applied when combining $696.5$ and $738.4\,\mathrm{nm}$ lines for z=$2.5$ to $5.5\,\mathrm{mm}$ without assumption of LTE. Here a density range of $1 \times 10^{22}$ to $8.9 \times 10^{22}\,\mathrm{m}^{-3}$ and a temperature range of $8100$ to $18\,000\,\mathrm{K}$ result from the evaluation of the intersections. Depending on the spatial position the uncertainty strongly varies between $5$ and $85\,\%$ for the electron density and between $4$ and $74\,\%$ for the temperature.

#### 5.2.1.2 GTAW process with Ar-He

For the GTAW process with Ar-He ($50\,\%$-$50\,\%$) shielding gas mixture electron density and temperature are determined in similar manner as for pure argon process. Figure 5.11 shows the results of the separate evaluation of the for Ar I lines.

Separate evaluation of Ar I lines delivers maximum electron densities between $5.6 \times 10^{22}$ and $8.4 \times 10^{22}\,\mathrm{m}^{-3}$ (figs. 5.11(a), 5.11(c), 5.11(e) and 5.11(g)). Here again a density decrease towards the anode is measured. The resulting values in the near anode region

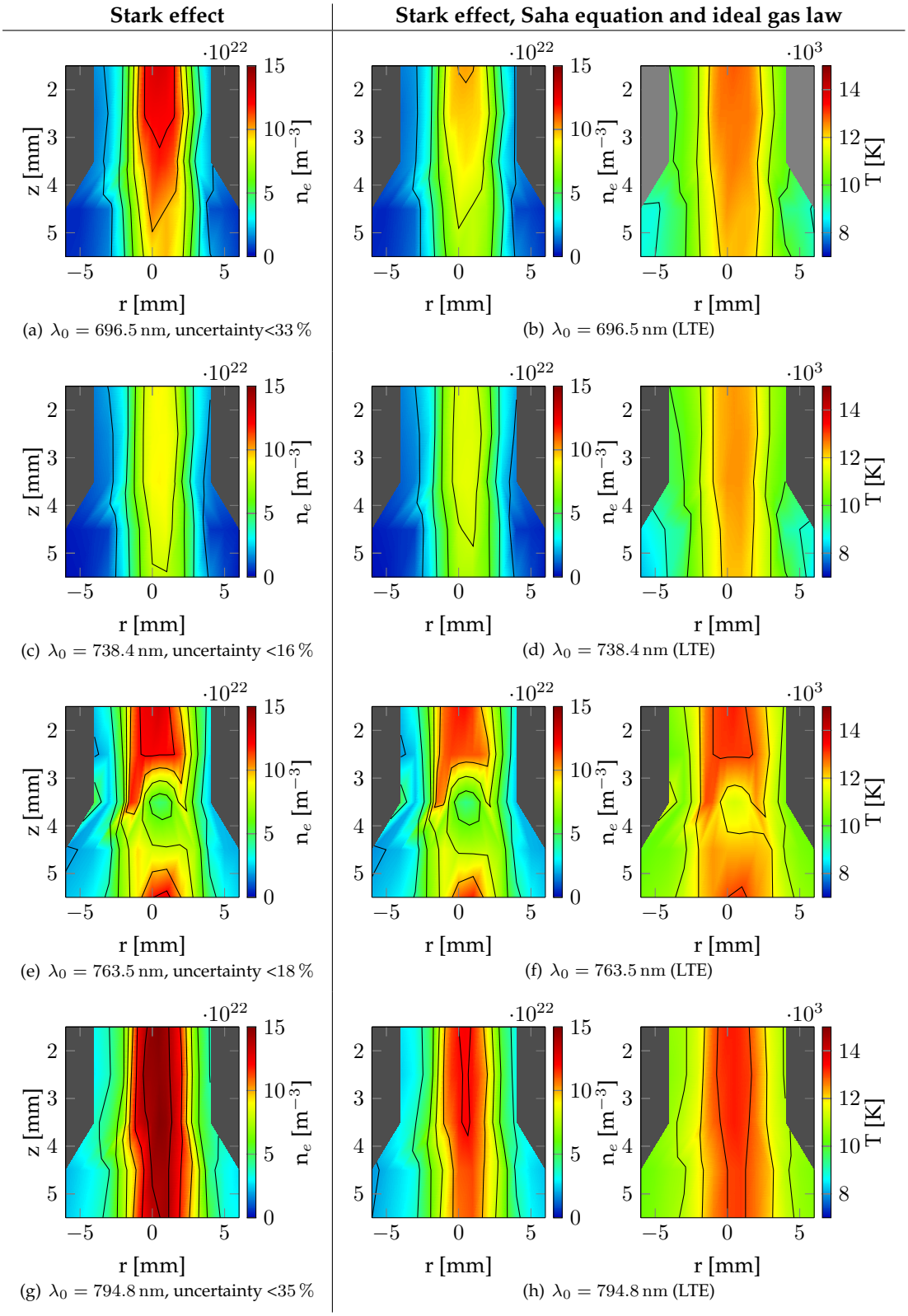


(a) $\lambda_0 = 696.5\,\mathrm{nm}$, uncertainty<33 %
(b) $\lambda_0 = 696.5\,\mathrm{nm}$ (LTE)
(c) $\lambda_0 = 738.4\,\mathrm{nm}$, uncertainty <16 %
(d) $\lambda_0 = 738.4\,\mathrm{nm}$ (LTE)
(e) $\lambda_0 = 763.5\,\mathrm{nm}$, uncertainty <18 %
(f) $\lambda_0 = 763.5\,\mathrm{nm}$ (LTE)
(g) $\lambda_0 = 794.8\,\mathrm{nm}$, uncertainty <35 %
(h) $\lambda_0 = 794.8\,\mathrm{nm}$ (LTE)

Figure 5.9: Evaluation of electron density and temperature from single Ar I resonance lines without (a,c,e,f) and with (b,d,g,h) the consideration of LTE assumptions for GTAW process operated with pure Ar as a shielding gas. The region colored in gray is not investigated. Two consecutive contour lines correspond to an increase of $2 \times 10^{22}\,\mathrm{m}^{-3}$ for the density values and 1000 K for the temperature values.

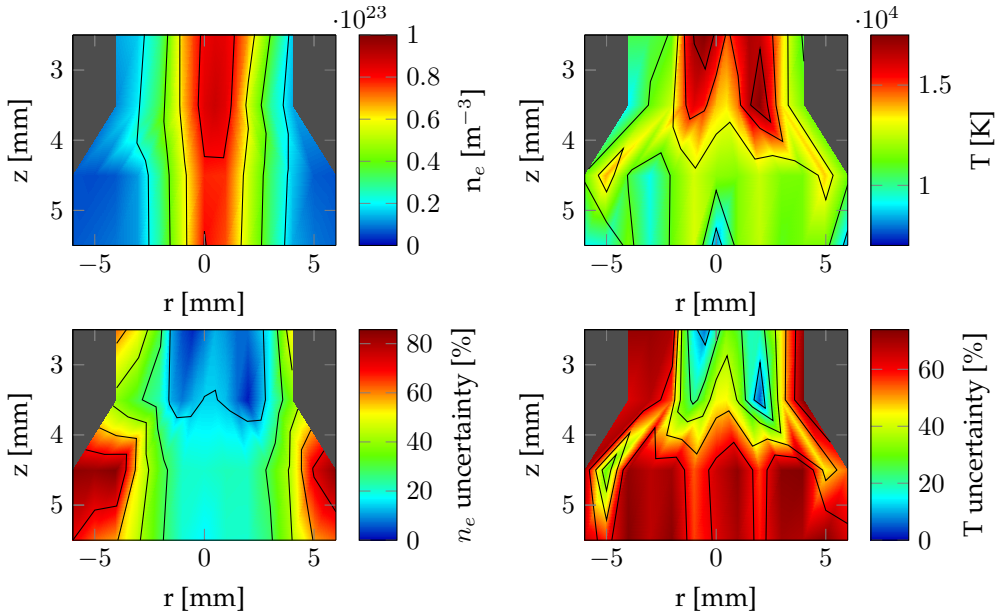


Figure 5.10: Evaluation of the Stark broadening measurement using the intersection method without the assumption of LTE for $\lambda_0$ =696.5 and 738.4 nm applied to a GTAW arc operated with pure Ar shielding gas. The region colored in gray is not investigated. Two consecutive contour lines correspond to an increase of $2 \times 10^{22}\,\mathrm{m}^{-3}$ for the density values and 2000 K for the temperature values.

are in the range of $4.3 \times 10^{22}$ to $8 \times 10^{22}\,\mathrm{m}^{-3}$. Equivalently to the case of pure argon, the methodical uncertainty varied between 16 and 35 %.

Under assumption of LTE the maximum electron density dropos to $5.3 \times 10^{22}$ – $8 \times 10^{22}\,\mathrm{m}^{-3}$. The hottest temperatures in the range of 15 000 to 16 000 K are detected in the arc center, while the values drop to 11 000 – 12 000 K in the outer arc regions (figs. 5.11(b), 5.11(d), 5.11(f) and 5.11(h)).

For all the investigated lines the temperature and density values radially and vertically decrease towards the arc edges and the anode resulting in comparable spatial distributions. Under assumption of LTE the methodical uncertainty for the electron density lies at most between 8 and 10 % and maximum 25 % for the temperature for all investigated lines.

Figure 5.12 shows the result of the intersection method, which could only be applied to the 763.5 and 794.8 nm lines pair without the assumption of LTE. Here a density range of $2 \times 10^{22}$ to $9 \times 10^{22}\,\mathrm{m}^{-3}$ and a temperature range of 3600 to 19 100 K result from the evaluation of the intersections. Depending on the spatial position the total uncertainty strongly varies between 5 and 75 % for temperature and density values.

### 5.2.2 GMAW processes

GMAW process operated with aluminum as the wire electrode is also investigated using the Stark broadening technique. In this case only one-dimensional spatial measurements at a fixed distance from the cathode are performed. Since the process is transient, temporally resolved investigations are additionally made.

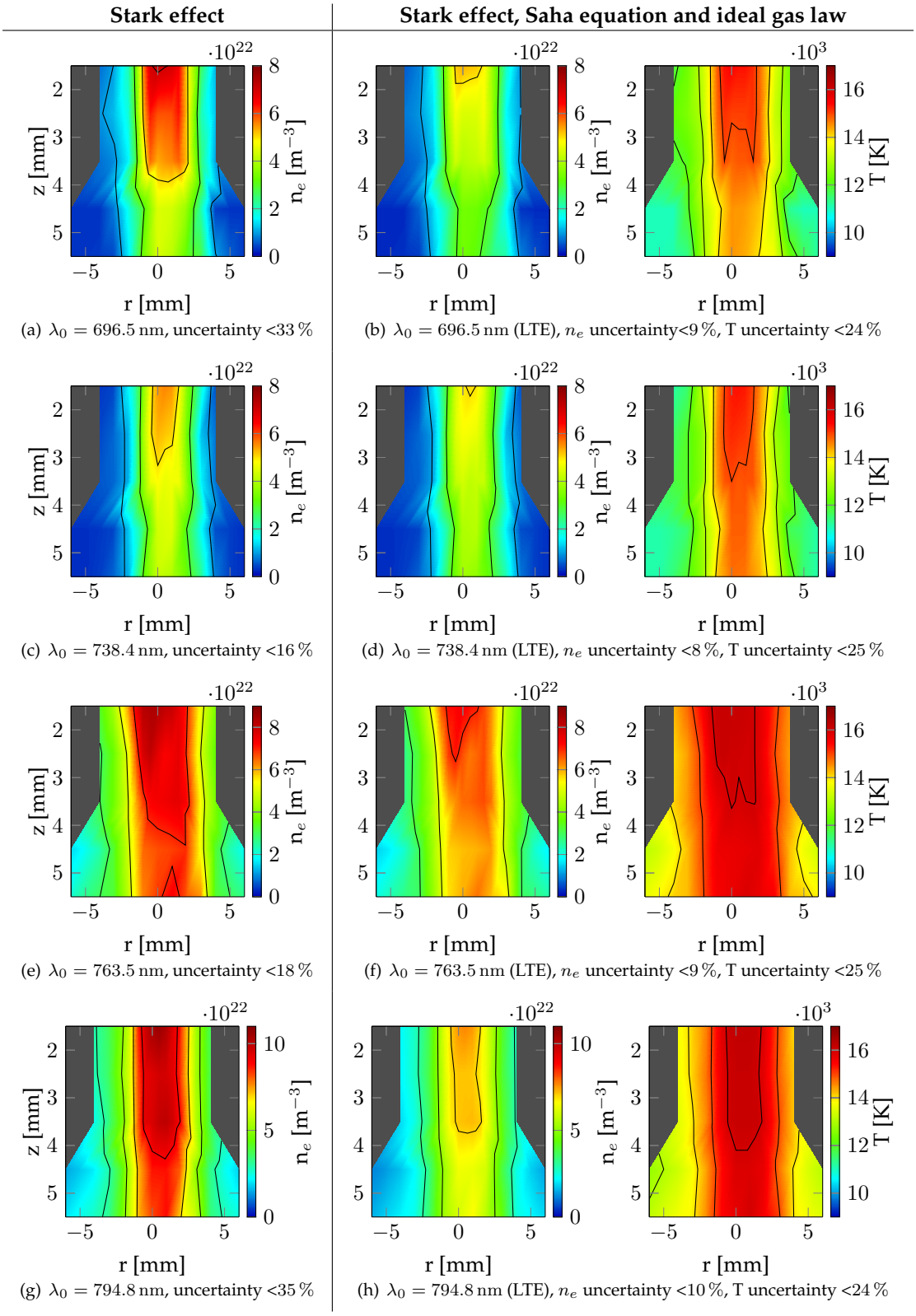


(a) $\lambda_0 = 696.5\,\mathrm{nm}$, uncertainty <33 %

(b) $\lambda_0 = 696.5\,\mathrm{nm}$ (LTE), $n_e$ uncertainty<9 %, T uncertainty <24 %

(c) $\lambda_0 = 738.4\,\mathrm{nm}$, uncertainty <16 %

(d) $\lambda_0 = 738.4\,\mathrm{nm}$ (LTE), $n_e$ uncertainty <8 %, T uncertainty <25 %

(e) $\lambda_0 = 763.5\,\mathrm{nm}$, uncertainty <18 %

(f) $\lambda_0 = 763.5\,\mathrm{nm}$ (LTE), $n_e$ uncertainty <9 %, T uncertainty <25 %

(g) $\lambda_0 = 794.8\,\mathrm{nm}$, uncertainty <35 %

(h) $\lambda_0 = 794.8\,\mathrm{nm}$ (LTE), $n_e$ uncertainty <10 %, T uncertainty <24 %

Figure 5.11: Evaluation of electron density and temperature from single Ar I resonance lines without (a,c,e,f) and with (b,d,g,h) consideration of LTE assumptions for GTAW process operated with Ar-He shielding gas mixture (50 %-50 %). The region colored in gray is not investigated. Two consecutive contour lines correspond to an increase of $2 \times 10^{22}\,\mathrm{m}^{-3}$ for the density values and 1000 K for the temperature values.

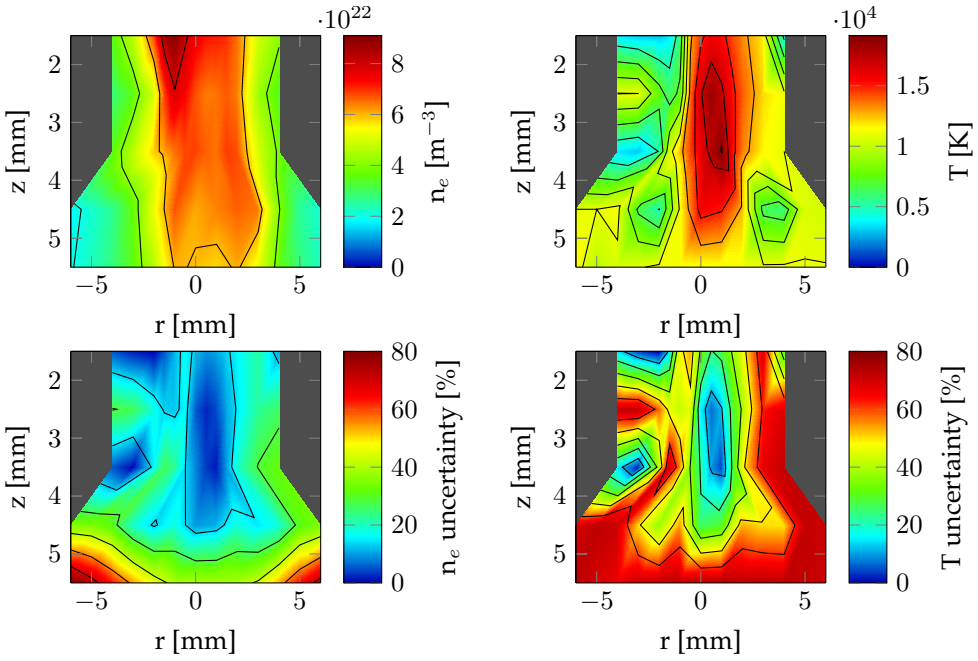


Figure 5.12: Evaluation of the Stark broadening measurement using the area intersection method for $\lambda_0$ =763.5 and 794.8 nm applied to a GTAW arc operated with pure Ar-He shielding gas mixture (50 %-50 %) and $I = 150$ A. The region colored in gray is not investigated. Two consecutive contour lines correspond to an increase of $2 \times 10^{22}\,\mathrm{m}^{-3}$ for the density values and 2000 K for the temperature values.

#### 5.2.2.1 Plasma parameters from argon resonance lines

Three different time windows are investigated using Stark width evaluation of 4 Ar I lines recorded with the ARYELLE spectrometer. Here processes with pure argon and argon with traces of hydrogen as a shielding gas are investigated. No considerable differences between the two processes are observed, if measuring the line width of Ar I lines, while less than 0.5 % of hydrogen is added. Although $H_\alpha$ line could be observed in this setup, an evaluation is not possible. For this particular ARYELLE system $\lambda_0 = 656.28\,\mathrm{nm}$ is located at the edge region of the detector. This introduced additional artifacts falsifying the shape of the line. In combination with a relatively weak signal the evaluation of the line shape in this region is not possible.

Figure 5.13 shows typical arc current and voltage signals as well as the location of the exposure windows (gray area) relative to the current pulse. The images of the GMAW process show a typical arc shape during the measurement. The spatial location of the single measurement points is indicated by green circles. The relative intensities in the images are scaled in order to visualize the shape of the arc without saturation.

The evaluation of single measurements along different pulse current phases is presented in fig. 5.14. Here 4 Ar I lines are separately evaluated for the GMAW process operated with an Al electrode. For each investigated line plasma parameter determination without and with assumption of LTE is performed.

Depending on the evaluated line during the high current phase this evaluation delivers maximum densities between $1.26 \times 10^{23}$ and $1.75 \times 10^{23}\,\mathrm{m}^{-3}$ in the central region of the arc (fig. 5.14(a)). At the arc edges the evaluation of different lines delivers more alike values. Here the density reduces to $2 \times 10^{22}$ – $3 \times 10^{22}\,\mathrm{m}^{-3}$. The uncertainty for the

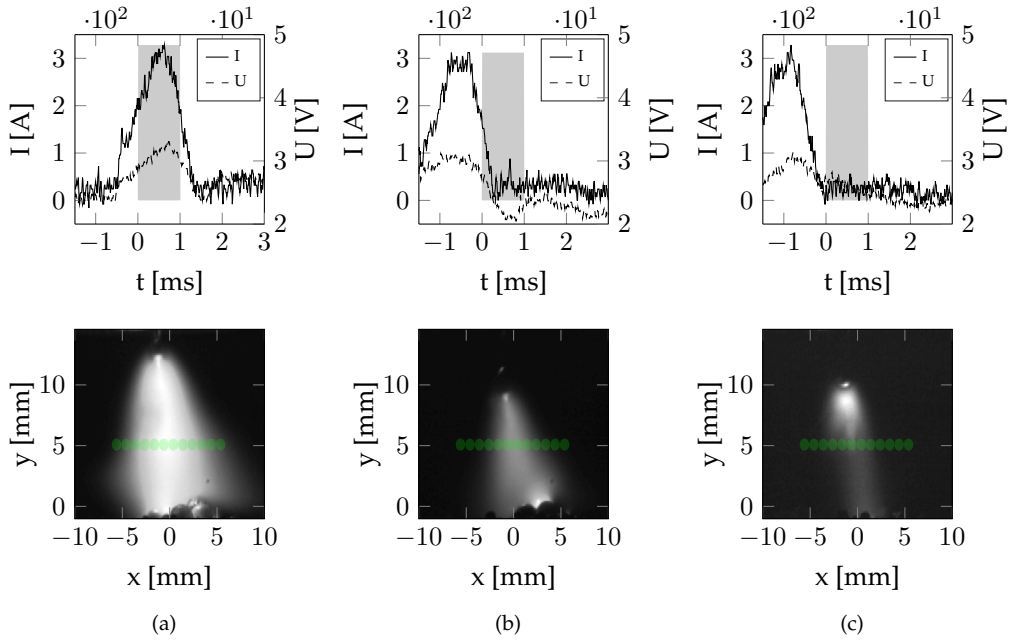


Figure 5.13: Top: Current and voltage of the GMAW process operated with Al as a wire electrode and Ar as a shielding gas for three different temporal trigger positions. The gray area indicates the location and duration of the exposure interval for the spectroscopic measurement and imaging relative to the current pulse. Bottom: images of the investigated GMAW process for the corresponding temporal trigger positions ($t_{epx} = 1\,\mathrm{ms}$). Green circles indicate the spatial position of individual measurement points.

whole region does not exceed $18\,\%$ for the $738.4$ and $763.5\,\mathrm{nm}$ lines and $33\,\%$ for the $696.5$ and $794.8\,\mathrm{nm}$ lines. Figure 5.14(b) shows the evaluated temperatures and densities, if the LTE assumptions are valid. Here the peak electron densities lower to $1.6 \times 10^{23}\,\mathrm{m}^{-3}$. The plasma temperature is estimated to $10\,000\,\mathrm{K}$ in the arc center and $8000\,\mathrm{K}$ at the arc edges. For all the evaluated lines comparable temperature and density profiles are obtained. Here the values steadily reduce from the center to the edges. The methodical uncertainty for all electron density estimations however drops to $5$ – $15\,\%$ depending on the evaluated line. The temperature uncertainty is in the range of 30 to $35\,\%$ depending on the radial location.

For the measurement starting at the falling edge of the current pulse (fig. 5.14(c)) peak electron densities in the range of $5.4 \times 10^{22}$ to $3 \times 10^{22}\,\mathrm{m}^{-3}$ are determined. At the edges the electron densities reduce to $0.5 \times 10^{22}$ – $1 \times 10^{22}\,\mathrm{m}^{-3}$. When introducing LTE assumptions the resulting densities only change slightly. In this case peak temperatures of $8000$ to $8500\,\mathrm{K}$ are obtained. They lower to $6500$ – $7000\,\mathrm{K}$ at the arc edges (fig. 5.14(d)). The relative uncertainties for these measurements are comparable to the high current phase.

The measurement in the low current phase delivers peak densities of $3 \times 10^{22}$ to $1 \times 10^{22}\,\mathrm{m}^{-3}$ in the arc center (fig. 5.14(e)). Here the temperature and density profiles differ from the preceding measurements. The oscillation in the profiles can be explained by the relatively weak signal at this current phase. The resulting density distribution does not change with additional LTE assumption. The obtained temperatures lie in the range of $6000$ to $8000\,\mathrm{K}$ (fig. 5.14(f)). The relative uncertainties for these measurements are comparable to the high current phase.

Moreover, the measurements are evaluated using the intersection method with and without assumption of LTE. Here only the $\lambda_0$ =696.54, 738.40 and $794.82\,\mathrm{nm}$ lines can be

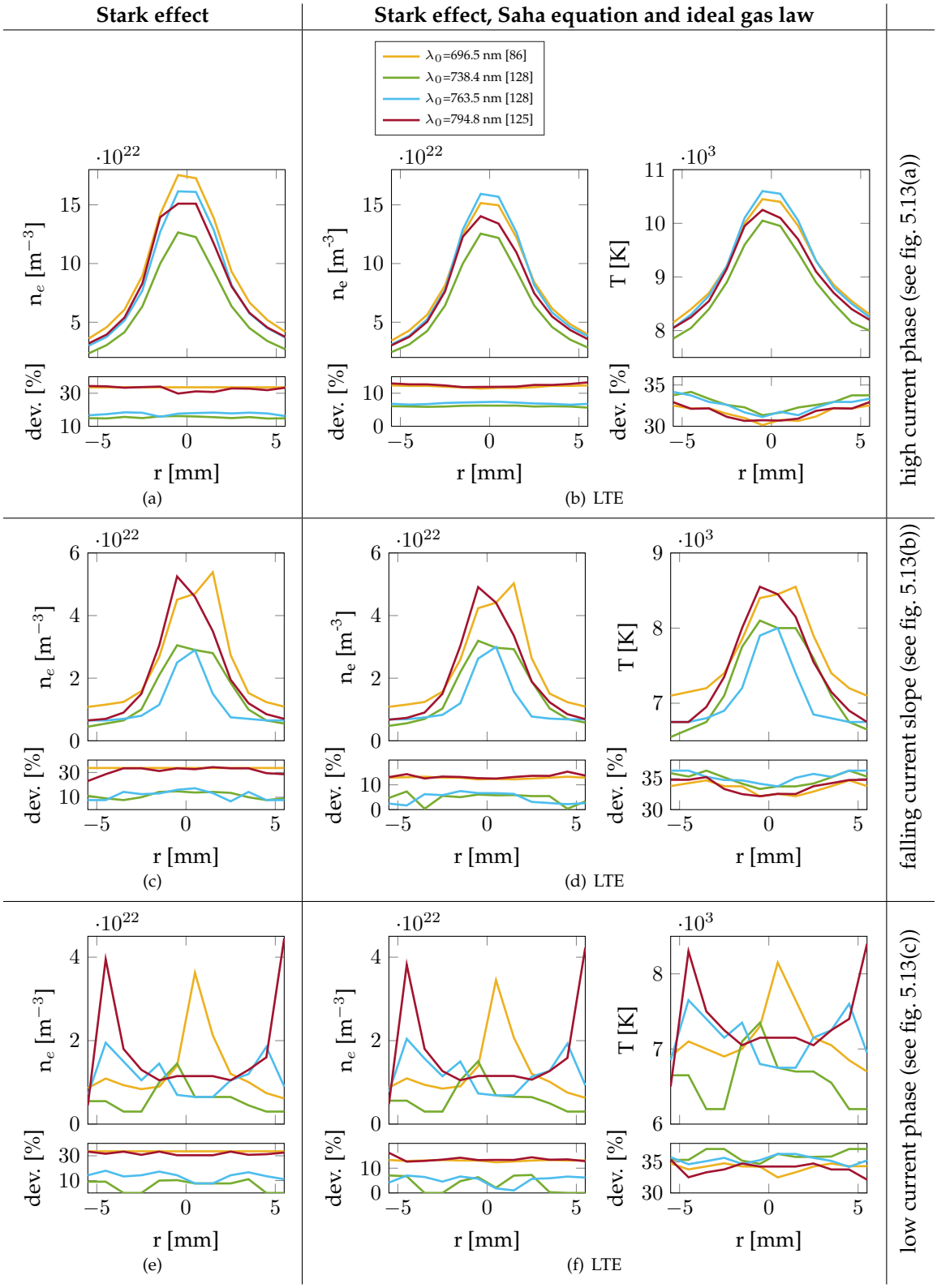


Figure 5.14: Resulting electron density and temperature (top of each subfigure) separately evaluated from Ar I lines without (a,c,e) and with (b,d,f) consideration of LTE conditions for three different temporal trigger positions. For each measured parameter the methodical uncertainty (dev. [%]) is indicated (bottom of each subfigure).

used, because $\lambda_0$ =763.5 nm resonance line delivers a significantly higher estimation for plasma temperature and density. This might be an evidence of absorption in this wavelength region.

The results for high current phase of the process are shown in fig. 5.15. Here three different line combinations can be evaluated without consideration of LTE. Depending on the combination of the lines peak electron temperatures reach $1.4 \times 10^{23}\,\mathrm{m}^{-3}$ (fig. 5.15(a)) and $1 \times 10^{23}\,\mathrm{m}^{-3}$ (figs. 5.15(b) and 5.15(c)). The uncertainty in the center varies between 2 and 26 %. At the arc edges the electron density drops down to $2 \times 10^{22}$ – $3 \times 10^{22}\,\mathrm{m}^{-3}$. The total uncertainty varies between 26 and 47 %. Higher uncertainties compared to the evaluation of separate lines arise, because the standard deviation of the measurements is directly taken into account in the evaluation method.

In all the three cases the line combinations are not sensitive to the temperature, as can be seen from the error bars in the graphs. For 696.5, 738.4 and 794.8 nm lines the total uncertainty appears to be relatively small in the arc center. Here however the results are limited by the assumed temperature range for the evaluation.

If considering LTE assumptions, the intersection method can only be evaluated for a combination of two lines in the high current phase as shown in figs. 5.15(d) and 5.15(e). Here the maximum electron densities lower to $1.1 \times 10^{23}$ – $1.3 \times 10^{23}\,\mathrm{m}^{-3}$ with a total uncertainty of 5 to 13 %. Here the evaluation method is more sensitive to temperature. Peak values in the range of 10 000 to 11 000 K with an accuracy between 13 and 30 % arise from the evaluation. The temperatures at the edges reach up to 8000 K. Here the accuracy lies below 36 %.

The results of the evaluation of the intersection method at the falling current slope without the consideration of LTE are shown in figs. 5.16(a) to 5.16(c). Here again three different line combinations are evaluated. Maximum electron densities around $4.1 \times 10^{22}$ to $6.2 \times 10^{22}\,\mathrm{m}^{-3}$ are reached. The total uncertainty lies between 10 and 38 %. The electron densities drop down to up to $1 \times 10^{22}\,\mathrm{m}^{-3}$ at the arc edges. Here again the uncertainty decrease to 65 – 80 %. The consideration of LTE assumptions does not drastically changes the resulting electron densities as can be seen in figs. 5.16(d) to 5.16(f). The peak electron density values lie at $4.5 \times 10^{22}$ to $5.6 \times 10^{22}\,\mathrm{m}^{-3}$, while the accuracy improves to 5 – 20 %.

Without the assumption of LTE the intersection method did not deliver any temperature values with an acceptable accuracy. Yet when considering LTE, plasma temperatures with an accuracy comparable to evaluation of single lines can be obtained. In the arc center temperatures in the range of 8700 to 11 000 K with a total uncertainty of 10 to 33 % are obtained. At the edges the temperature drops down to 6600 – 7100 K with a total uncertainty of 40 to 47 %.

The evaluation of the third dataset in the low current phase (figs. 5.13(c) and 5.14(e)) using the intersection method could not be performed, since none of the line combinations delivered an intersection area for all spatial points.

#### 5.2.2.2 Plasma parameters from hydrogen lines

Since the minimum temporal resolution of the ARYELLE spectrometer is not sufficient for the time domain of the pulsed GMAW process, additional measurements as described in section 4.2.2 are performed. The resolution of the Fastie-Ebert spectrometer is only precise enough for the investigation of the $H_\alpha$ and $H_\beta$ lines.

As has been previously mentioned, $H_\beta$ line is superposed by lines of other elements and continuum radiation. If only a small amount of hydrogen is added, the magnitude of the $H_\beta$ radiation and the background are still quite similar in strength. Yet the continuum shape is too similar to the broadened line shape. Hence, even if the complete spectrum including the contribution of the continuum and the resonance lines of other element is fitted to the measured data, it is not possible to reliably extract the contribution of $H_\beta$ line. The fitting algorithm often converges into a local minimum, which however does not fit

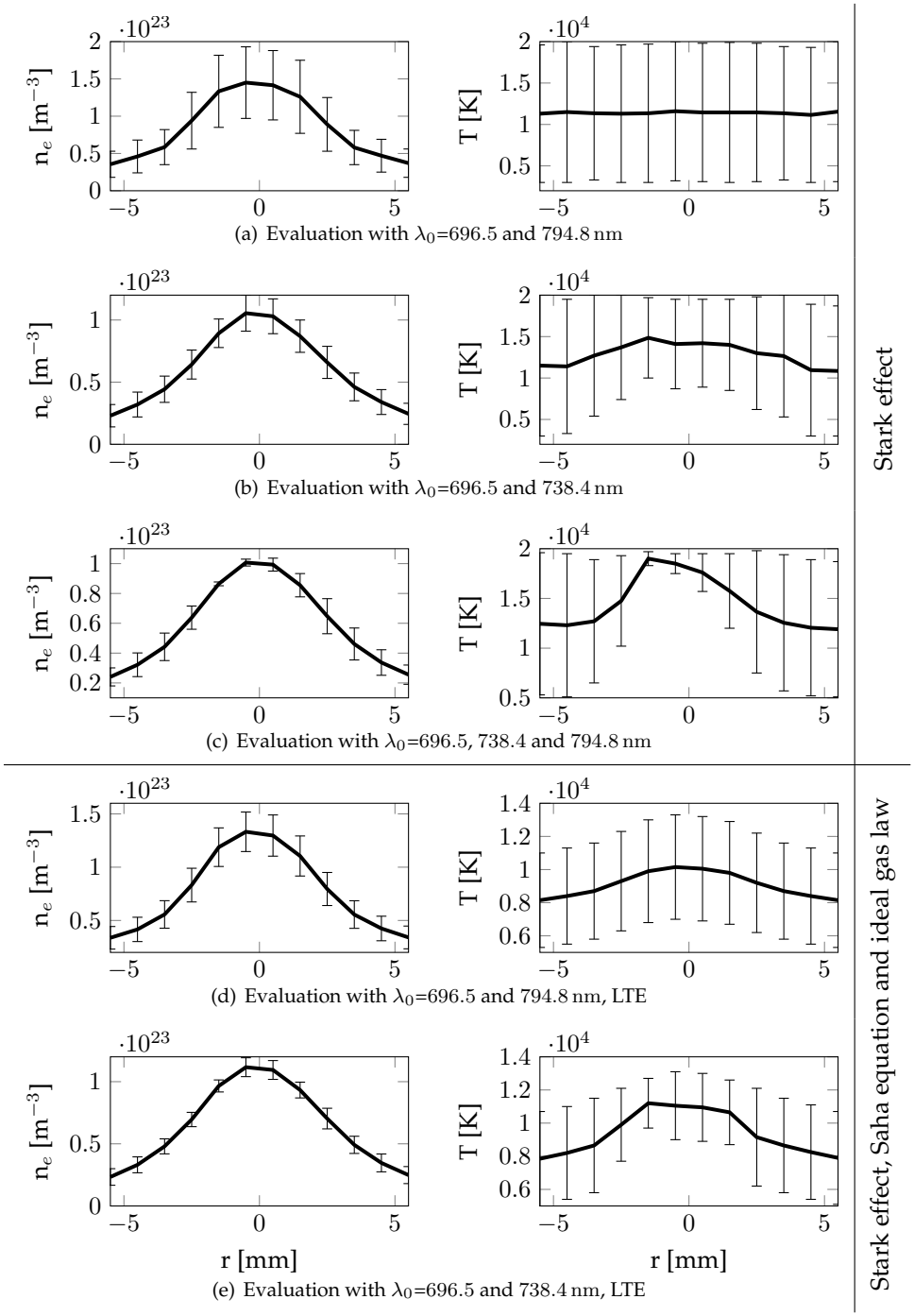


(a) Evaluation with $\lambda_0$=696.5 and 794.8 nm

(b) Evaluation with $\lambda_0$=696.5 and 738.4 nm

(c) Evaluation with $\lambda_0$=696.5, 738.4 and 794.8 nm

(d) Evaluation with $\lambda_0$=696.5 and 794.8 nm, LTE

(e) Evaluation with $\lambda_0$=696.5 and 738.4 nm, LTE

Figure 5.15: Evaluation of electron density and temperature using the intersection method for 3 different line combinations without (a-c) and with (d-e) assumption of LTE for a dataset recorded during the high current phase under conditions as indicated in fig. 5.13(a).

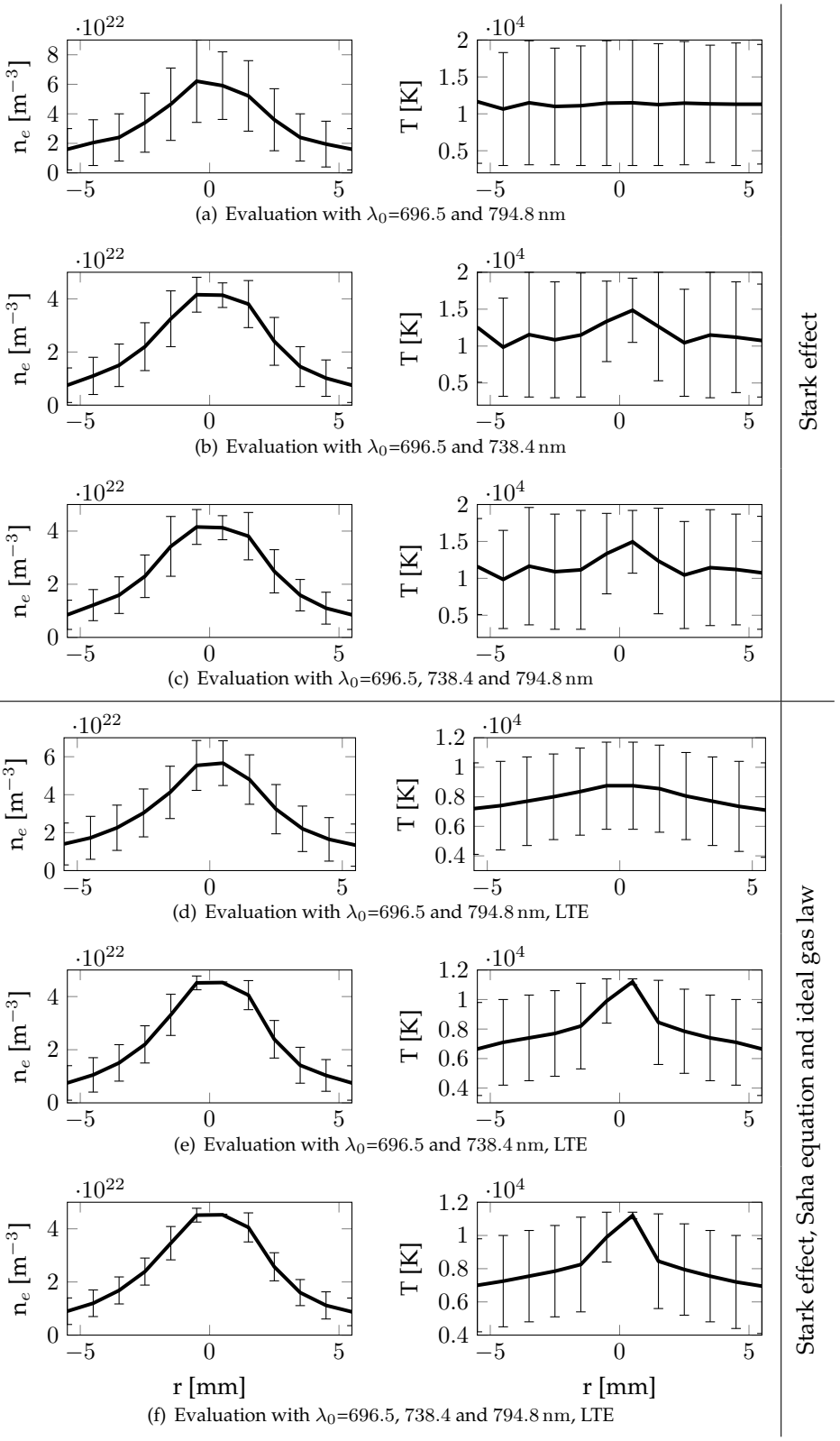


(a) Evaluation with $\lambda_0$=696.5 and 794.8 nm

(b) Evaluation with $\lambda_0$=696.5 and 738.4 nm

(c) Evaluation with $\lambda_0$=696.5, 738.4 and 794.8 nm

(d) Evaluation with $\lambda_0$=696.5 and 794.8 nm, LTE

(e) Evaluation with $\lambda_0$=696.5 and 738.4 nm, LTE

(f) Evaluation with $\lambda_0$=696.5, 738.4 and 794.8 nm, LTE

Figure 5.16: Evaluation of electron density and temperature using the intersection method for 3 different line combinations without (a-c) and with (d-f) assumption of LTE for a dataset recorded at the falling current slope under conditions as indicated in fig. 5.13(b).

the real line shape well enough. Hence, the data containing this line could not be used for further evaluation.

Figure 5.17 shows the evaluation of 5 consecutive measurements at the same trigger event time at the beginning of the high current phase. In figs. 5.17(a) and 5.17(b) the $H_\alpha$ line is used to evaluate the electron density without the assumption of LTE. For the evaluation the simulated line profiles provided in [129] for $\mu$ =1 and 1.5, which is equivalent to $T_e = T_i$ (a) and $T_e = 1.5T_i$ (b), are used. The maximum electron density values for $\mu = 1$ lie in the range of $8.7 \times 10^{22}$ to $10.1 \times 10^{22}\,\mathrm{m}^{-3}$ in the arc center. The electron densities steadily drop down towards the edges up to around $3 \times 10^{22}\,\mathrm{m}^{-3}$. For the slight deviation from temperature equilibrium ($\mu = 1.5$) the evaluated maximum electron densities rise to $9.4 \times 10^{22}$ – $11.5 \times 10^{22}\,\mathrm{m}^{-3}$. The electron densities at the edge lie at $4 \times 10^{22}\,\mathrm{m}^{-3}$. The methodical uncertainty varies between 7 and 10 %. The variation of the reconstructed electron densities for the single measurements might be explained with the instability of the process.

The theoretical dataset for the calculation of the $H_\alpha$ line allows to consider LTE as well as pLTE assumptions with different electron and heavy particles temperatures. Here two evaluations for $T_e = T_i$ (fig. 5.17(c)) and $T_e = 1.5T_i$ (fig. 5.17(d)) are conducted. In order to obtain electron density-temperature pairs Saha equation for Ar-Al plasma for $T_e = T_i$ (c) and $T_e = 1.5T_i$ (d) is solved for various Ar-Al concentrations. The presence of hydrogen is neglected here.

The resulting electron densities do not considerably differ from the non LTE case, while the accuracy improves to 2 – 4 %. Resulting peak temperatures rage between 9400 and 9700 K in the arc center for $\mu$ =1 and 1.5. The temperature falls off to 8000 K at the arc edge region. The methodical uncertainty is 32 to 34 %.

The temporal investigation of the $H_\alpha$ line width is performed with a resolution of at least 250 $\mu$s. In order to clearly present temporal evolution of the electron temperature and densities along the pulse only the maximum values of each measurement are presented in fig. 5.18 (bottom). Besides the evaluated plasma parameters, the process current and voltage together with the trigger event time represented by the vertical bars are shown (center). Additionally images of the arc are depicted for each trigger point. The relative intensities in the images are scaled in order to visualize the shape of the arc without saturation.

In the high current phase the resulting electron densities and temperatures approximately follow the shape of the pulse. The values obtained on the descending slope unexpectedly rise, while in the low current phase they considerably reduce again. A plausible explanation for this results can be found, when taking a closer look on the arc images. In the first 5 measurements ($t_{trig}$=0 to 1 ms) no droplets are present below the measurement volume. For $t_{trig}$=1.25 and 1.5 ms the situation is different. In both cases a metal droplet is visible below the measurement volume, which probably leads to increased metal vapor concentration in the plasma. The $H_\alpha$ line is very sensitive to ion dynamics or in other words collisions between the emitters and heavy perturbers [93]. This means, that if the plasma composition changes, this may lead to a considerable modification of the line shape and hence to apparently higher electron densities. In order to verify these assumptions precise simulations of the line shape for the particular plasma composition would be necessary.

In the low current phase and in the absence of metal droplets ($t_{trig}$=6.9 ms) the results for electron densities and temperatures correlate well with the results obtained in other measurements.

## 5.3 Discussion and comparison of results

In the following sections results obtained by different methods are compared with each other and with other measurements or simulation results available in the literature. Again

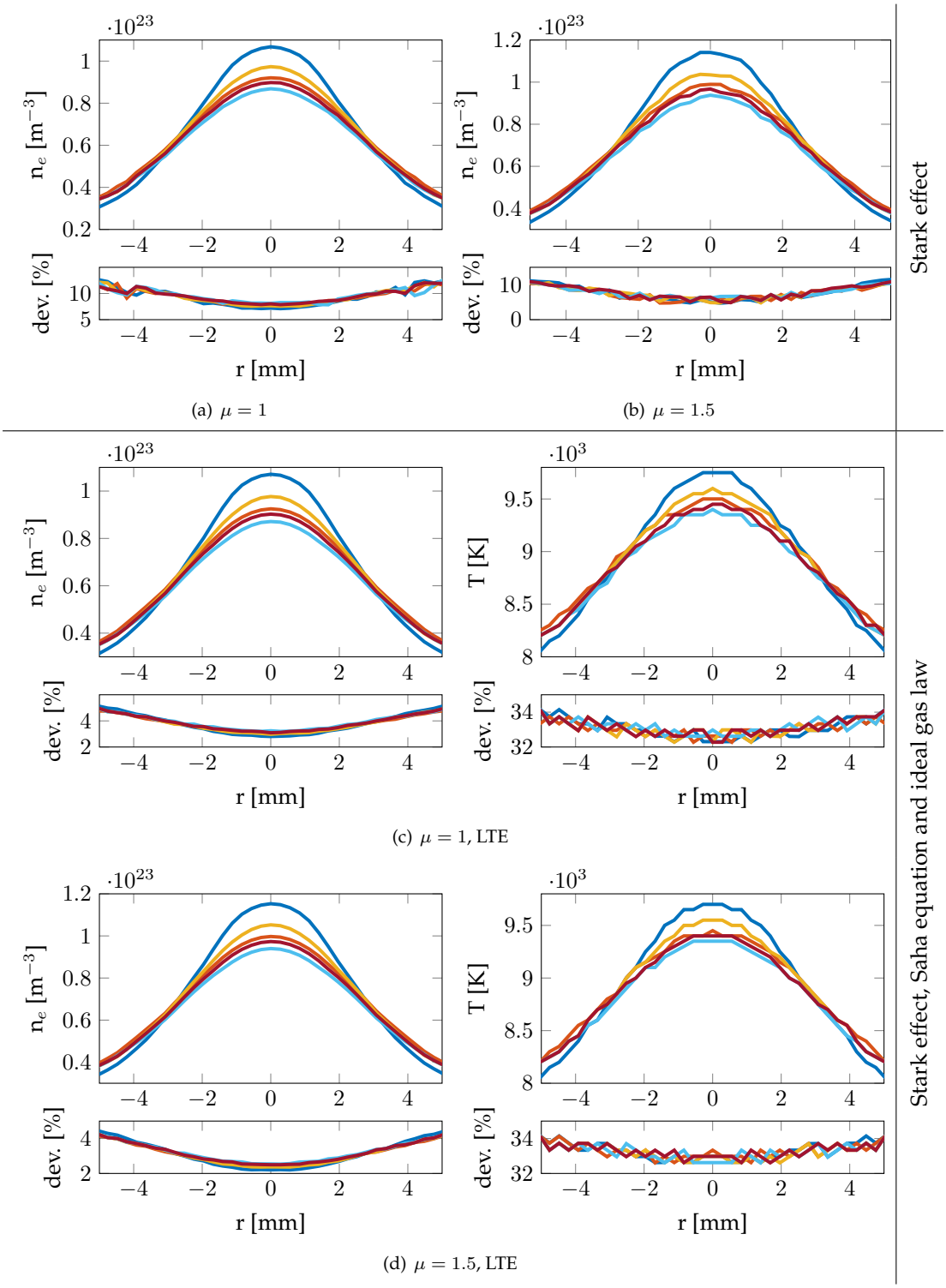


(a) $\mu = 1$ (b) $\mu = 1.5$

(c) $\mu = 1$, LTE

(d) $\mu = 1.5$, LTE

Figure 5.17: Evaluation of electron density without consideration of LTE (a,b) and electron density and temperature under consideration of LTE (c,d) from the $H_\alpha$ line. The measurement are consecutively performed at the beginning of the high current phase ($t_{trig}$=0.25 ms). The methodical uncertainty (dev. [%]) is depicted below each evaluation graph.

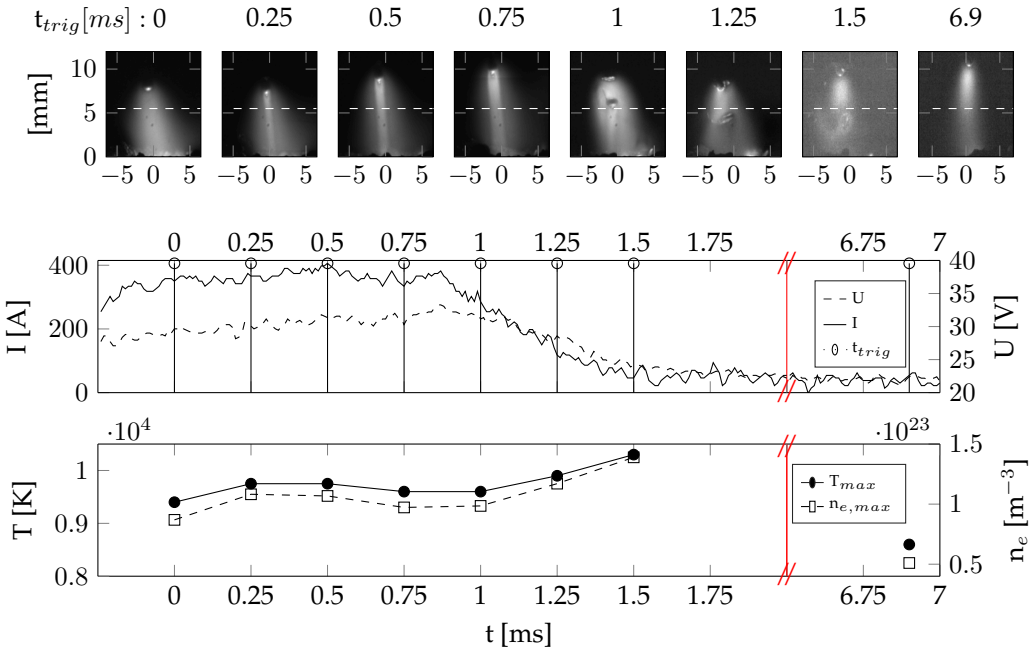


Figure 5.18: Temporal development of the maximum electron temperature and density evaluated at a particular trigger event time (bottom) along the arc current and voltage signal (center). The arc images illustrate the position of droplets relative to the measurement volume (top). The white dashed line in the images marks the measurement volume.

first the results for GTAW arc and afterwards for GMAW processes are discussed.

### 5.3.1 GTAW processes

#### 5.3.1.1 Pure argon GTAW process

Electron densities obtained by Thomson scattering measurements are in good agreement with results of Stark broadening of $\lambda_0$=696.5 and 794.8 nm without consideration of LTE (Saha equation and ideal gas law). If implementing these equations together with consideration LTE assumptions, the data is reasonably close to the results of $\lambda_0$=763.5 and 794.8 nm at least in the region close to the cathode. Results obtained from evaluation of $\lambda_0$=738.4 nm lie considerably below the values of Thomson scattering. Consequently, the electron densities obtained from the intersection method are also much lower, since $\lambda_0$=738.4 nm is used for the evaluation here. For $\lambda_0$=763.5 nm the comparison is difficult due to the presence of artifacts.

In the case of temperature it seems, that the Stark method is not very sensitive. Figure 5.19 contradicts the results of the Thomson scattering and Stark broadening methods taking into consideration of LTE evaluated for a pure argon arc. As illustrated for the evaluation of $\lambda_0 = 696.5\,\mathrm{nm}$ line, resulting temperature distributions of all the evaluated lines lie below the values obtained in the arc center using Thomson scattering, while the values close to the arc fringes are slightly higher than the results obtained by Thomson scattering. The temperature evaluated from the intersection method close to the cathode however agree well with the Thomson scattering results. The accuracy of the intersection method is in an acceptable range in this area.

The overall discrepancy between results obtained by Stark broadening and Thomson

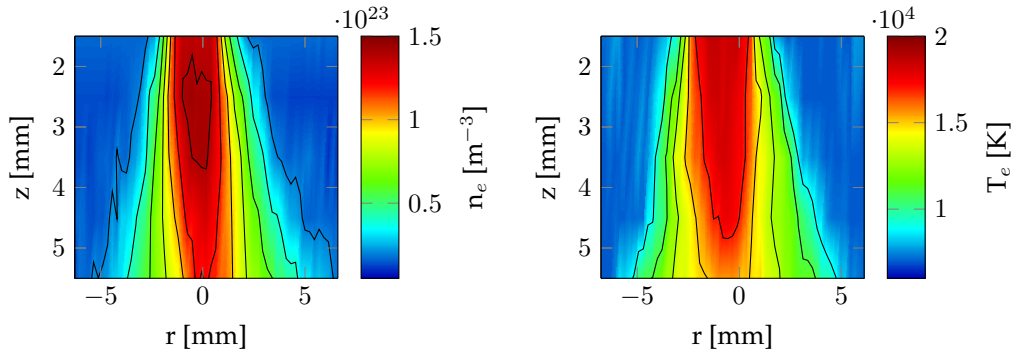


(a) Thomson scattering results

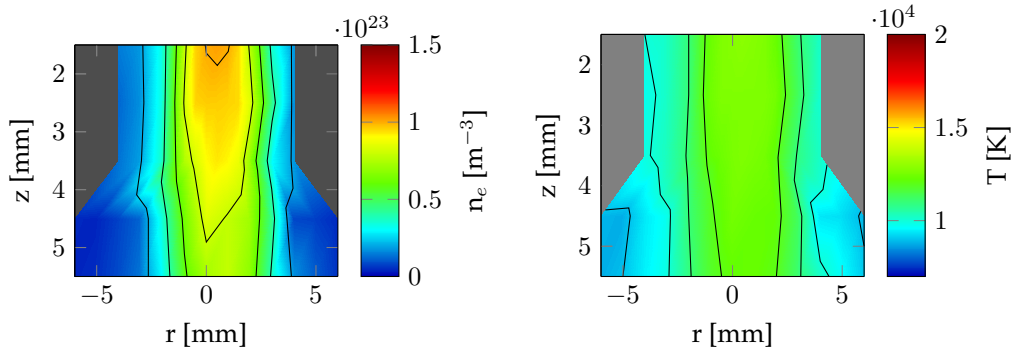


(b) Stark broadening results for $\lambda_0 = 696.5\,\mathrm{nm}$

Figure 5.19: Comparison of Thomson scattering and Stark broadening evaluated under consideration of LTE for GMAW process operated with pure argon as a shielding gas.

scattering for the particular processes can be linked to errors, which occur during Stark broadening evaluation. Besides stochastic errors, such as detector noise or arc fluctuation, uncertainty may arise from the assumptions needed for Abel inversion (definite type of intensity profile, axial symmetry). Apart from that, the model applied to obtain the relation between the line width and the electron density and temperature may not be precise enough for the processes investigated in this work. Moreover, slight deviation from LTE in some arc regions would lead to errors as well. Finally it has to be taken into account, that the accuracy of temperature and density determination is lower in the case of Stark broadening compared to Thomson scattering.

Pure argon arcs in comparable conditions were also investigated by other groups. Here mainly temperature results were published. Electron temperatures obtained using Thomson scattering in comparable conditions published by Tanaka et al. [29] reach over 20 000 K in the center of the arc, which lies considerably above the values obtained in this work. However, the Tanaka et al. use a laser pulse energy, which is 16 times higher than the laser used in this work, so heating of plasma by the laser radiation may not be negligible. Yet the linear extrapolation to zero laser energy as suggested by Tanaka et al. still overestimates the electron temperature as shown by Murphy [146]. When using the correction procedure suggested by Murphy, electron temperature values in the range of the values obtained using Thomson scattering in this work are achieved.

Still, the temperature distribution obtained by Thomson scattering in this work is comparable to the temperature distribution determined by emission spectroscopy methods e.g. by Bachmann et al. [74] in process operated in very similar conditions.

#### 5.3.1.2 GTAW process with Ar-He gas mixture

The comparison of Thomson scattering and the Stark broadening results for the GTAW process operate with Ar-He shielding gas mixture reveals a strong correlation between the electron density values determined within the accuracy range. In particular the agreement is good for the separate evaluation of $763.5$ and $794.8\,\mathrm{nm}$ lines with and without the assumption of LTE, for evaluation of the $696.5\,\mathrm{nm}$ line without LTE restriction and the density values obtained by the intersection method. For $738.4\,\mathrm{nm}$ line again the density values lie below Thomson scattering results.

If comparing the temperature distributions resulting from the two measurement methods, the agreement of the results is only good near the central axis of the arc. Towards the arc edges the values obtained by Stark broadening lie above the values obtained by Thomson scattering. Only for the intersection method the temperature values lie closer to the temperatures obtained by Thomson scattering. However, in the outer regions the accuracy of the intersection method is quite low.

The temperature and density in Ar-He arcs were also spectroscopically investigated in two other works. Hiraoka [69] investigated GTAW process operated with Ar-He ($50\,\%$-$50\,\%$), I=$100\,\mathrm{A}$ and an arc length of $5\,\mathrm{mm}$. Here maximum electron densities slightly above $1 \times 10^{23}\,\mathrm{m}^{-3}$ using IR-spectroscopy technique and temperatures below $17\,000\,\mathrm{K}$ using a two Ar line intensity correlation were determined $1\,\mathrm{mm}$ below the cathode tip. Although the resulting densities are higher than obtained in this work, the resulting temperatures are in the expected range for a process operated with a lower current.

Xiao et al. [71] have reported temperatures and densities of a GTAW process operated with the same shielding gas mixtures, I=$200\,\mathrm{A}$ and an arc length of $5\,\mathrm{mm}$. Here Fowler-Milne method, Boltzmann plot and correlation of two Ar lines were used to measure plasma temperature $1\,\mathrm{mm}$ below the cathode tip. The maximum temperatures above $20\,000\,\mathrm{K}$ were reached. Maximum electron densities in the range of $1.1 \times 10^{23}\,\mathrm{m}^{-3}$ were evaluated from the Stark broadening measurement of Ar II 480.6 nm line. The measurements seem to be in reasonable agreement with the values obtained in this work for lower currents.

A numerical investigation of a GTAW process with pure Ar in comparison with Ar-He shielding gas, I=$180\,\mathrm{A}$, but only $3\,\mathrm{mm}$ arc length was performed by Traidia et al. [147]. Here the resulting temperature distribution shape of the pure Ar arc and the Ar-He arc agree with distribution shapes obtained in this work. However the simulation delivers higher plasma temperatures for the Ar-He gas mixtures compared to pure argon. The results of modeling a $5\,\mathrm{mm}$ GTAW arc operated with a Ar($70\,\%$)-He($30\,\%$) shielding gas mixtures and I=$150\,\mathrm{A}$ [148] deliver a temperature distribution similar to the results obtained in this work. However, it has to be noted, that in both modeling the demixing of the shielding gas components is not considered.

#### 5.3.1.3 GTAW process with Ar-$H_2$ and Ar-$N_2$ gas mixtures

Comparable studies of GTAW processes operated with Ar-$H_2$ and Ar-$N_2$ gas mixtures were performed by Hiraoka[68, 82]. Here the arc was operated with I=$100\,\mathrm{A}$ and an arc length of $5\,\mathrm{mm}$.

For the arc operated with $5\,\%$ of $H_2$ maximum measured temperatures in the range of $16\,500\,\mathrm{K}$ [82] and $16\,000\,\mathrm{K}$ [68] for $10\,\%$ of $H_2$ using the two-line intensity correlation method are reported. The arc shape determined in this work is comparable to the results delivered by Thomson scattering. The maximum reported electron densities of $1.6 \times 10^{23}\,\mathrm{m}^{-3}$ determined by Stark broadening of $H_\beta$ line and $2 \times 10^{23}\,\mathrm{m}^{-3}$ determined by infrared emission spectroscopy are considerably higher than the values obtained in this work. However, the author reports a temperature and density decrease compared to the measurements in the arc with pure argon, which is also observed in this work.

Hiraoka [82] has also detected slight decrease of temperature in the arc, when adding $5\,\%$ of $N_2$ to the shielding gas. Similar effects are also observed in this work. Murphy [26] has measured a maximum temperature of around $18\,000\,\mathrm{K}$ $2\,\mathrm{mm}$ below the cathode in a $5\,\mathrm{mm}$ long GTAW arc operated with I=200 A and $12\,\%$ $N_2$ mixed to argon shielding gas. When considering the higher currents the electron temperatures of about $16\,000\,\mathrm{K}$ in the arc center for $8\,\%$ of $N_2$ in the shielding gas mixture obtained in this work reach a plausible value.

### 5.3.2 GMAW process

If comparing the electron density results obtained from Thomson scattering and Stark broadening of single resonance lines, good agreement within the accuracy of the measurements methods for the high current phase of the pulse can be shown. Here electron densities of up to $1.6 \times 10^{23}\,\mathrm{m}^{-3}$ for Thomson scattering and densities between $1.26 \times 10^{23}$ and $1.75 \times 10^{23}\,\mathrm{m}^{-3}$ for Stark broadening are obtained. The assumption of LTE does not have a strong influence on the results.

The variation of results delivered by Stark broadening method is mainly due to the choice of the evaluated spectral line. While the results obtained from the $696.5$, $763.5$ and $794.8\,\mathrm{nm}$ Ar I lines lie in a comparable range, the results for $738.4\,\mathrm{nm}$ line are noticeably below. Since this observation can be made for all the measurement, it might be assumed that the theoretical dataset used for the evaluation underestimates the plasma parameters in the welding arcs.

The electron densities obtained by the intersection method ranging from $1 \times 10^{23}$ to $1.4 \times 10^{23}\,\mathrm{nm}$ lie slightly below the other results. Yet when not considering the results including the evaluation of the $738.4\,\mathrm{nm}$ line, maximum values of $1.4 \times 10^{23}\,\mathrm{m}^{-3}$ are reached. The deviation from to the values obtained by Thomson scattering can be explained by the different temporal resolution of both methods. While for Thomson scattering extremely short exposure times of up to $15\,\mathrm{ns}$ are used, the measured spectra are averaged over $1\,\mathrm{ms}$ in the case of Stark broadening detection with the ARYELLE spectrometer. Considering the more coarse spatial resolution of the Stark broadening results, both methods deliver comparable spatial electron density distributions.

The maximum temperatures evaluated from the Stark broadening of approximately $10\,000\,\mathrm{K}$ lie below the maximum values obtained by the Thomson scattering method ($14\,000\,\mathrm{K}$). However the deviation of the results can be explained by the relatively high uncertainty of the former method and the time averaging of the results. Here no strong deviations between the results of single lines are observed. The evaluation of intersection method combined with the assumption of LTE deliver comparable results. All in all the Stark method is more sensitive to the temperature in the case of Ar-Al plasma. Considering the uncertainty of the Stark method the temperature profiles of the Stark broadening and the Thomson scattering are comparable.

The results of Thomson scattering measurement for the electron density lie above the values obtained from the evaluation of the $H_\alpha$ line. However, as was already discussed, this line is sensitive to the ion dynamics in the plasma. The comparison of the two different electron-ion temperature ratios (parameter $\mu$) indicates, that the theoretical dataset might not precisely describe the broadening mechanism for the conditions in the Ar-Al plasma. The obtained temperature values, their spatial distribution and uncertainty are however comparable to the results obtained from evaluation of single Ar lines.

When comparing the temporal evaluation of Thomson scattering results with the evaluation of Ar I lines similar development of the electron temperature and density is obtained. In both measurements the values behave accordingly to the magnitude of the current. For the temporal evolution obtained from the width measurement of $H_\alpha$ line this is only true for the values measured during the high current and low current phase. As was previously explained, the temporary increase of the temperature and density values in the

presence of metal droplets might again be an evidence for a changed ion dynamics and eventually absorption.

The electron temperatures measured in the high current phase of the GMAW process are slightly higher than plasma temperatures spectroscopically measured by Goecke [9] using the Barthels method. Here as well, measurements in the high current phase were performed using a comparable pulsed GMAW process operated with aluminum welding wire with a diameter of $1\,\mathrm{mm}$ and argon as a shielding gas. Radial temperature profiles were recorded at $3\,\mathrm{mm}$ above the workpiece. For pure argon an arc length of approximately $5\,\mathrm{mm}$ was measured. The radial temperature distribution displays a slight minimum at the central axis of the arc. Here the measured temperature in the center of the arc lies at approximately $11\,000\,\mathrm{K}$, whereas the maximum temperature of the radial distribution reaches $11\,300\,\mathrm{K}$. The results of the emission coefficient method deliver a much lower temperature minimum in the center of the arc. However as already stated by the author, this method is sensitive to self absorption of the spectral lines. The fact that the used spectral lines are optically thin, was not experimentally confirmed.

Maximum temperatures in the center of an aluminum GMAW arc with a DC current of $95\,\mathrm{A}$ obtained from a 3D simulation model by Murphy [149] reach $9800\,\mathrm{K}$, when considering the influence of the metal vapor. A temperature minimum in the radial temperature distribution is only visible close to the wire electrode. This might be an explanation for the absence of a temperature minimum in the center of the radial profile measured by the Thomson scattering technique. Due to a longer arc with a length of $8$ to $9\,\mathrm{mm}$ and hence different spatial temperature distribution the region with the on-axis temperature minimum might be shifted or even vanish.

## 5.4 Gas composition reconstruction

As was previously shown by modeling and experimental approaches [145, 150] demixing of shielding gas components is taking place in GTAW and GMAW arcs. Since Thomson scattering delivers reliable electron temperature and density values, they can be used to estimate the concentration of species in a two component plasma, if LTE assumptions are valid. Molecular gases are assumed to be fully dissociated, which is reasonable for the considered temperature range. If solving the Saha equation, correlations between plasma temperature, density and component concentration are obtained. These correlations are used to identify concentrations matching the temperature density pairs.

Figure 5.20 visualizes the temperature electron density relation resulting from the solution of the Saha equation for different argon concentrations in a two component plasma. In the case of Ar-He (fig. 5.20(a)) the resulting sensitivity as a function of the argon concentration is significantly high in the temperature range from $10\,000$ to $20\,000\,\mathrm{K}$. This makes it possible to perform an accurate gas composition reconstruction in the central region of the arc. For Ar-Al plasma (fig. 5.20(b)) the density sensitivity as a function of the argon concentration is significant in the temperature range from $5000$ to $15\,000\,\mathrm{K}$, which also makes the reconstruction of the Al concentration possible.

For argon-hydrogen or argon-nitrogen plasmas however the electron density does not considerably change for LTE condition with $T_e = T_i$, if changing the argon concentration. Hence, the reconstruction is not possible, if only information about the electron density and temperature is available.

Figure 5.21 shows the results of the helium concentration reconstruction. The concentration drastically increases in the arc center to up to $77 - 80\,\%$, although the original gas mixture contains only $50\,\%$ He. It confirms the assumption (see section 5.1.1.2), that demixing of argon and helium is taking place in the Ar-He arc. The concentrations measured by Hiraoka [69] for a an GTAW arc operated with I=$100\,\mathrm{A}$ lie in the range of $70\,\%$. The values

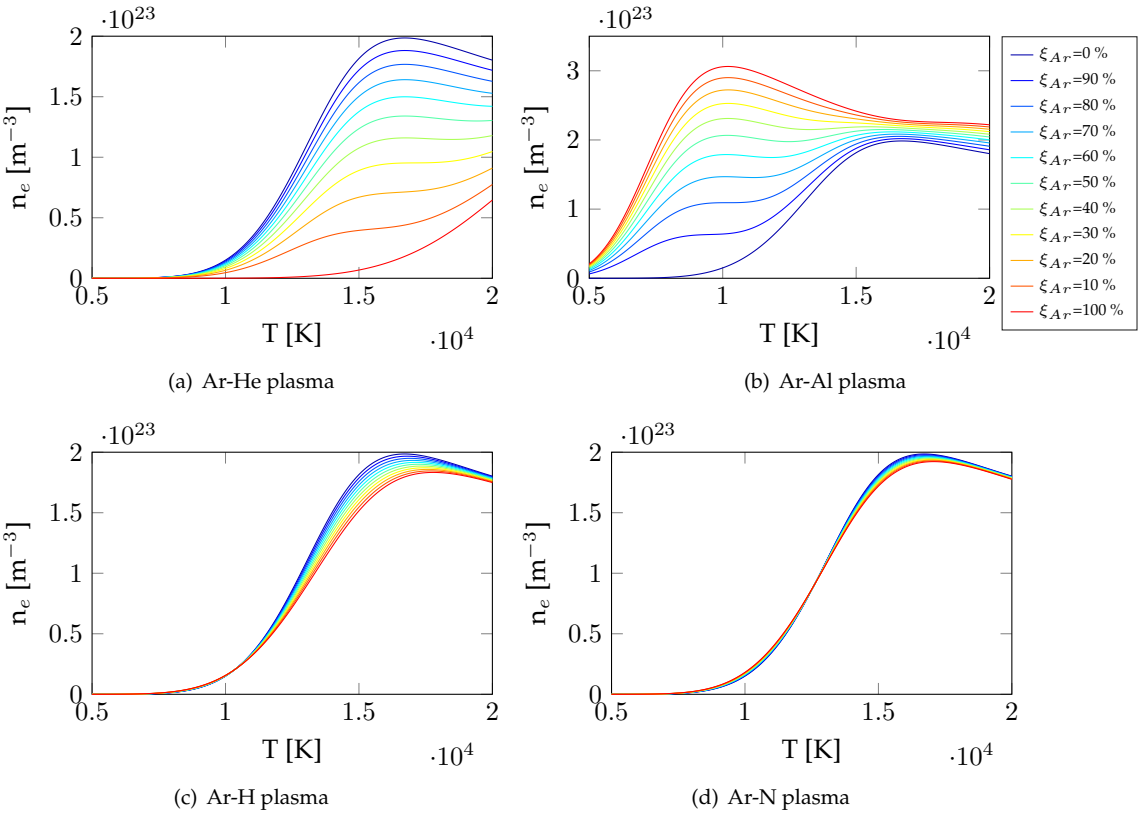


(a) Ar-He plasma

(b) Ar-Al plasma

(c) Ar-H plasma

(d) Ar-N plasma

Figure 5.20: Temperature-electron density characteristics for different concentration fo Ar in the two component plasma under consideration of LTE.

predicted by Murphy [145] for an arc with I=200 A rise up to 77 % in the arc center. This corresponds very well with the result of the reconstruction performed in this work.

An example of a radial distribution of aluminum concentration in the GMAW arc is shown in fig. 5.22. The estimation yields metal concentrations in the range of 20 % in the inner region of the arc. Metal concentrations estimated from spectroscopic measurements reported by Goecke [9] are in the similar range for a pulsed GMAW process operated in comparable conditions. The aluminum vapor concentration simulated in [149] however range at a much higher level (80 %) for a process operated with a DC current of 95 A and a feed rate of 72 mm/s. Yet it has to be considered, that in contrast to the simulation the workpiece is cooled during the Thomson scattering measurement reducing the vaporization. Moreover, the arc length in the experiment is estimated to be twice as long as in the simulation (approx. 4 mm), which might as well influence the vaporization process.

Figure 5.23 depicts the average aluminum concentration reconstructed in the arc center over the duration of the current pulse. It can be seen that estimated aluminum concentration reaches 10 to 20 % during the high current phase of the pulse. Higher aluminum concentration values in the range of 33 to 72 % are estimated in the low current phase in the center of the arc. This accumulation of aluminum possibly arises due to its low ionization energy, which is necessary to still maintain the plasma state even for the reduced electric arc current.

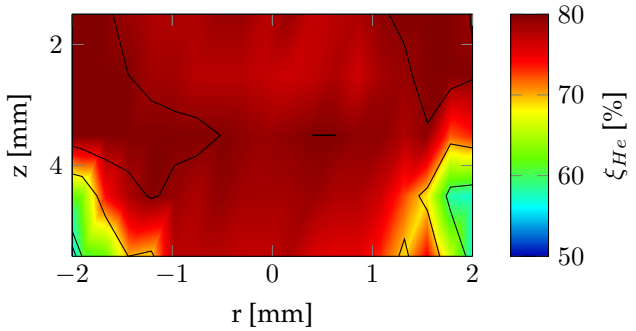


Figure 5.21: Reconstructed concentration of helium by volume fraction in the GTAW arc operated with Ar-He shielding gas mixture. Two consecutive contour lines correspond to an increase of He concentration of $10\,\%$.

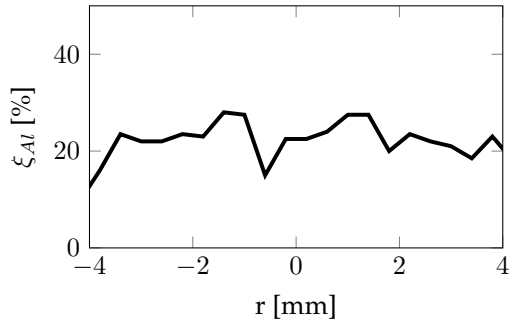


Figure 5.22: Example of aluminum concentration reconstruction in the GMAW arc recorded at t=$0.7\,\mathrm{ms}$.

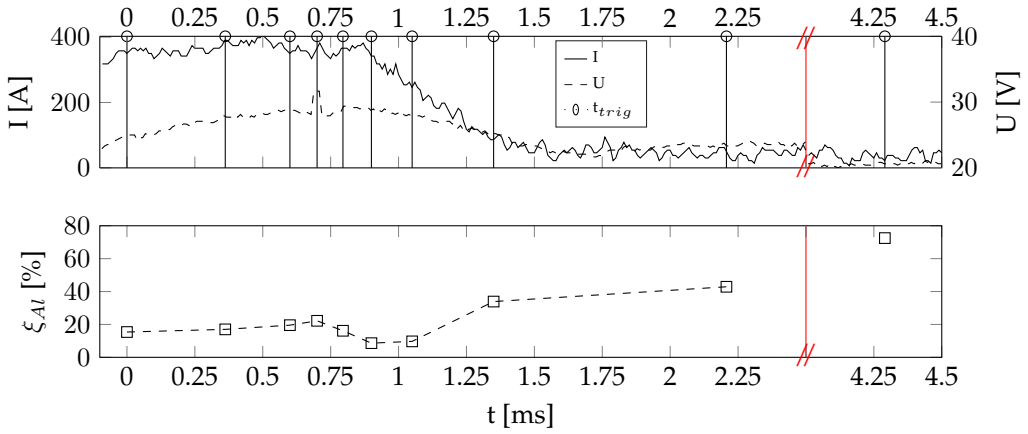


Figure 5.23: Temporal evolution of reconstructed mean metal vapor concentration in the center of the arc GTAW arc operated with aluminum wire (bottom). Process current pulse and voltage with the measurement time $t_{meas}$ marked by the vertical bars (top).

# Chapter 6

# Conclusions and outlook

In this work two diagnostic techniques, Thomson scattering and Stark broadening, have been applied for the measurement of electron density and temperature of stationary as well as transient welding processes operated with different shielding gas mixtures.

Firstly, Thomson scattering technique has been set up for the investigation of stationary GTAW processes with inert and molecular shielding gas mixtures. Thereafter, it has been extended for application to pulsed GMAW processes operated with aluminum and iron wire electrodes. It has been demonstrated, that this technique can be applied to transient GMAW processes in the presence of metal vapor. For all the processes, where the electron feature could be clearly detected, the signal has been evaluated by fitting theoretical scattering profiles to the measured scattering patterns. The fits have yielded spatially resolved electron density and temperature profiles without previous knowledge of plasma composition, the arc column shape and partially without the assumption of LTE. The temporal resolution for transient processes has been achieved using an additional logic circuit for shifted trigger pulse generation.

From the obtained results it can be deduced, that the main requirement for a successful detection of the scattering spectra in welding plasmas is the absence of strong plasma background radiation in the region of the laser wavelength. Yet as several strong lines are present in the wavelength region of interest, the detection of electron feature with the current setup was not possible for the GMAW processes with iron wire electrode.

Since the electron densities and temperatures have been evaluated independently, the measurement data could be used for spatially and temporally resolved plasma composition estimation. However, these calculations could only be performed for gas mixtures with sufficiently different ionization energies and under assumption of LTE.

In the second step, the emission spectra of stationary GTAW processes operated with pure argon and with argon-helium gas mixture as well as the pulsed GMAW processes operated with aluminum as the wire electrode have been recorded in order to evaluate the Stark broadening of selected spectral lines. Temporal resolution for the transient GMAW process has been implemented using the trigger logic previously applied for Thomson scattering setup. A clear advantage of this technique is, that it is a passive diagnostic technique with a relatively simple experimental setup. It has been successfully applied for the electron density determination without assumption of LTE. Temperature values have been additionally estimated, when LTE restrictions were taken into account. The intersection method using several broadened lines for electron temperature and density evaluation however has only delivered results with a reasonable accuracy for the electron density without the assumption of LTE.

The comparison of Thomson scattering and Stark broadening techniques has shown, that both methods deliver comparable results for electron density within the experimental error of the respective methods. Good agreement with the experimental results available in

the literature could be also found for both techniques at least for the stationary processes, since not much data for transient processes exist.

**Additional improvements of the diagnostic techniques**
The Thomson scattering signal is in general relatively weak. Yet its magnitude additionally drops with the decreasing electron density. This introduces a higher experimental error in the low density regions of the arc or makes the estimation of plasma parameters impossible. In order to improve the S/N ratio and simultaneously widen the region, where Thomson scattering can be applied, several features of the experimental setup can still be optimized.

Among others, the magnitude of the scattering signal depends on the power of incident laser radiation. Yet starting from certain radiation power level the heat-up of the plasma by inverse bremsstrahlung becomes significant. Thus the pulse laser energy cannot be considerably increased above the pulse energies used in this work without modifying the conditions in the investigated plasma volume. Still an increase of laser frequency from several $\mathrm{Hz}$ to $\mathrm{kHz}$ range with laser per pulse energies in the range of several $\mathrm{mJ}$ may significantly improve the S/N ratio of the resulting spectrum, when on chip integration mode of the camera is used. This was already demonstrated in [60] for argon streamer plasmas. Thus, the total CCD chip integration time can be reduced, while the number of integrated pulses is increased, which improves an overall S/N ratio.

It should be taken into account, that increase of the Thomson scattering signal implies a simultaneous increase of the magnitude of Rayleigh scattering and the parasitic reflections. If this part of the spectrum is not filtered out, it not only might cause saturation of the CCD detector, but also damaged the image intensifier. To prevent this effect gas reference vapor cells can be used as notch filters. A rubidium vapor cell [151] or sodium vapor cell [152] were successfully applied as a notch filter in a Thomson scattering setup using tunable lasers as the radiation source. However, the drawback of those cells is, that their absorption properties vary with ambient conditions, such as temperature and pressure. Hence, special care has to be taken to maintain comparable cell conditions for reproducible measurements.

Another possibility to filter out the Rayleigh scattering signal is to implement a mechanical notch filter by using a triple grating spectrometer as e.g. proposed by van de Sande [153]. The accurate realization of this type of filter apparatus is more complex, since three diffraction gratings and a narrow stripe are used to block the undesired wavelength. The advantage yet is, that the blocked wavelength can be adjusted for any required spectral region. Moreover, once set up, the triple grating spectrometer is less sensitive to change of ambient conditions.

In the case of Stark broadening the applied experimental technique may be further improved. The possibility of recording a wide spectral range with a simultaneously high wavelength resolution, which was realized by the Echelle spectrometer, proved to be very advantageous. However by replacing the current CCD detector by an ICCD camera would improve the sensitivity and allow faster gating times for better temporal resolution during the transient sections. Additionally, the inner configuration of the imaging optics within the spectrometer must be adjusted, so that all the lines of interest are positioned not on the edges of the detector to prevent optical artifacts.

It might be also useful to replace the fiber optics by lenses imaging the investigated volume on the spectrometer slit. Thus, a one-dimensional more precise spatial resolution can be obtained in a single measurement, which is important for less stable processes.

The discrepancies in the results of Thomson scattering and Stark broadening suggest, that the theoretical model delivering line profiles and hence the broadening width of the Stark effect for different emitters needs to be adapted to conditions prevailing in welding plasmas. The comparison of the evaluation of different resonance lines clearly indicates,

that the accuracy and reliability of particular evaluated electron densities and temperatures are determined by the employed theoretical data delivering the correlation of those parameters and spectral line shape. Moreover, the applicability of the intersection method, which theoretically allows simultaneous measurement of electron temperature and density, strongly depends on the choice of the spectral lines. Due to lack of theoretical data for detectable lines of other emitting species mainly Ar I lines could be evaluated by this method. Additionally, the investigations have shown that depending on plasma conditions spectral line shape might be sensitive to ion dynamics. This was clearly observed for the $H_\alpha$ line, while the Ar I lines showed less sensitivity to different plasma compositions.

Hence, a more detailed theoretical estimation of line shapes is required in order to correctly estimate the plasma parameters depending on the particular conditions. This can be achieved by extending the approach proposed by Gigosos et al. in [129] to the particular conditions present in the investigated welding process. Theoretical estimations of lines shapes of well detectable spectral lines of other species might be as well helpful in order to improve the performance of intersection method, so that the electron temperatures and densities can be deduced without any further assumptions.

**Further applicability for industrial processes**

All in all it can be concluded, that the Thomson scattering technique delivers more reliable measurement results and can be applied for different plasma composition without additional modification. Due to its complicated experimental setup this technique is only suitable for basic investigation of the process under careful controlled conditions in a laboratory. Yet the Stark broadening with its more simple experimental setup may be adopted to perform measurements of electron temperature and density in processes operated under industrial conditions. However, for a reliable plasma parameter determination an improved theoretical model for each particular process condition is required, if the Stark broadening technique has to be used.

# Appendix A

# Supplementary material

## A.1 Stark Broadening Parameters for isolated argon lines

Line width for argon resonance lines according to the impact approximation and under consideration of the ion impact parameters are given in the table A.1 for specific electron temperatures and densities.

(a) $\lambda_0 = 794.8\,\mathrm{nm}$

| $T$ [K] | $w$ [nm] | $a$ |
|---|---|---|
| 5000 | 0.00361 | 0.028 |
| 10000 | 0.0048 | 0.023 |
| 20000 | 0.00649 | 0.018 |
| 40000 | 0.00843 | 0.015 |

(b) $\lambda_0 = 696.54\,\mathrm{nm}$

| $T$ [K] | $w$ [nm] | $a$ |
|---|---|---|
| 2500 | 3.27e-3 | 0.047 |
| 5000 | 4.09e-3 | 0.04 |
| 10000 | 5.37e-3 | 0.032 |
| 20000 | 7.1e-3 | 0.026 |
| 40000 | 8.73e-3 | 0.023 |

Table A.1: Broadening width parameters for $n_e = 10^{22}\,\mathrm{m}^{-3}$ and for two resonance lines $\lambda_0 = 794.8\,\mathrm{nm}$ [125] and $\lambda_0 = 696.54\,\mathrm{nm}$ [101].

For some data a fitting function

$$\log(w_i) = a_0 + a_1 \log(T) + a_2 (\log(T))^2 \tag{A.1}$$

with $w_i$ the line width in Å. The index $i$ denotes the width obtained for a specified collider. The total width is simply $w = \sum_i w_i$ as the line profile is assumed to be Lorentzian. The fitting coefficients for different argon resonance lines are given in the table A.2.

| | | electron | | | Ar II | | |
|---|---|---|---|---|---|---|---|
| $\lambda_0$ [nm] | $n_e$ [$m^{-3}$] | $a_0$ | $a_1$ | $a_2$ | $a_0$ | $a_1$ | $a_2$ |
| 696.54 | $10^{21}$ | -0.77841 | -1.0172 | 0.16496 | -2.65189 | 0.01701 | -0.0016 |
| | $10^{22}$ | 0.22159 | -1.0172 | 0.16496 | -1.84825 | 0.10643 | -0.01178 |
| | $10^{23}$ | 1.22159 | -1.0172 | 0.16496 | -1.02443 | 0.16605 | -0.01645 |
| 738.40 | $10^{21}$ | -0.62722 | -1.02105 | 0.1596 | -2.5426 | -0.01722 | 0.0027 |
| | $10^{22}$ | 0.37278 | -1.02105 | 0.1596 | -1.74533 | 0.07539 | -0.00785 |
| | $10^{23}$ | 1.35898 | -1.01499 | 0.15894 | -1.07938 | 0.21072 | -0.02157 |
| 763.51 | $10^{21}$ | -0.50925 | -1.11654 | 0.17688 | -2.52303 | -0.00255 | 0.00062 |
| | $10^{22}$ | 0.49075 | -1.11654 | 0.17688 | -1.75809 | 0.10547 | -0.01175 |
| | $10^{23}$ | 1.47199 | -1.10769 | 0.17584 | -1.10765 | 0.24441 | -0.02547 |

Table A.2: Fitting coefficients for the calculation of broadened line width using eq. (A.1) according to [128].

## A.2 Experimental setup

A photograph and a 3D model of the improved mobile experimental setup is shown in figs. A.1 and A.2.

Figure A.1: Photograph of the optimized Thomson scattering setup.

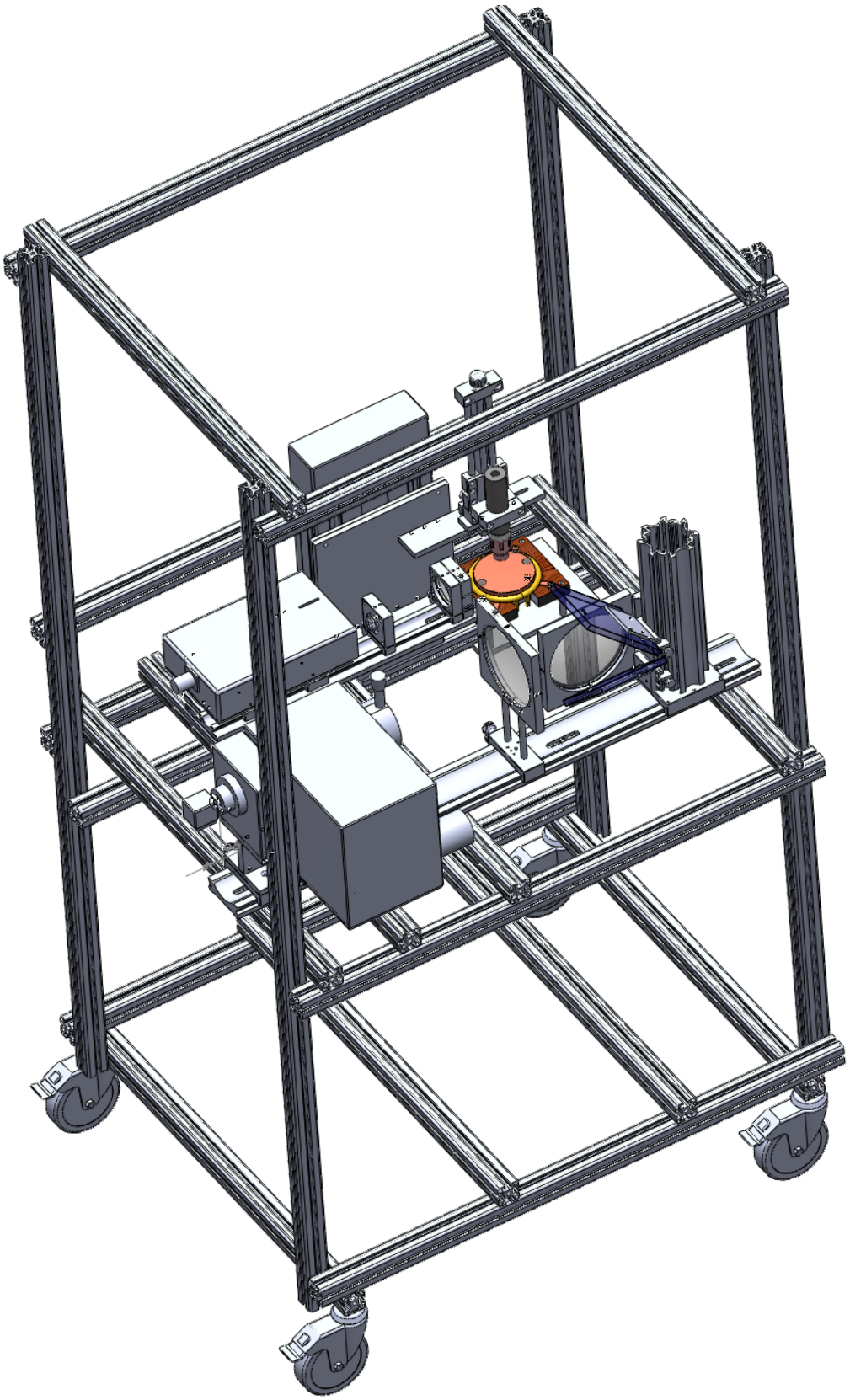

Figure A.2: 3D Model of the optimized Thomson scattering setup.

## A.3 MATLAB scripts and functions for data evaluation

In the following selected MATLAB scripts and functions, which has been used for the data evaluation, are given.

### A.3.1 Thomson scattering

File A.1: Generate '*.mat' files from '*.rtv' files provided by the 4SPEC software

```
function [file_name]=create_spectrum_1(dir_list,flag,dir_shift) %field mode start with next, no trig
      framgrabber
%define image width and height
%function creates integrated spectra from .rtv images recorded by the 4picos cameara.
%the spectras are saved in .mat files

%input parameter:
%dir_list: directory with signal and back folders/files
%flag: select between *.rtv (=0) and .*tif (=1) file list
%dir_shift (optionial): correct the astigmatism of the entrance slit

%output: name of the generated *.mat file

tic
width=350+2;      %width=pixel_width+2; width=pixel_width  %for 10bit
height=572;

if nargin<3
    shift=zeros(1,height/2);
else
    load(dir_shift);
end

if nargin<2
    flag=1;
end
%determine signal frame
if flag==1
    buf_field=integrate_images_seq(dir_list,width,height);    %integrate signal
elseif flag==0
    buf_field=integrate_images_rtv(dir_list,width,height);
    %check whether the sign of the spectrum is correct
    spec_h_1=sum(buf_field(1:2:height,:),1);
    spec_h_2=sum(buf_field(2:2:height,:),1);
    spec_h_1_s=sum(spec_h_1(70:110));
    spec_h_2_s=sum(spec_h_2(70:110));
    if spec_h_1_s<0 && abs(spec_h_1_s)>abs(spec_h_2_s)
        buf_field=-buf_field;
    elseif spec_h_2_s<0 && abs(spec_h_2_s)>abs(spec_h_1_s)
        buf_field=-buf_field;
    end
end

frm1=astg_corr(buf_field,height,width,1,shift); %correct spectrograph astigmatism and separate frames
frm2=astg_corr(buf_field,height,width,2,shift);

width=size(frm1,2);

spec_h_1=sum(frm1(100:200,:),1);
spec_h_2=sum(frm2(100:200,:),1);
file_name=[dir_list 'frm.mat'];

if max(spec_h_1)>max(spec_h_2)
    figure;
%    max_s=max(spec_h_1);
    subplot (4,4,14:16); plot((1:width).*0.15,spec_h_1); xlim([0,width*0.15]);
    spec_v_1=sum(frm1(:,80:110),2);                                %vertical median filter
    spec_v_1=smooth(spec_v_1,10);
    subplot (4,4,[1 5 9]); plot(spec_v_1); view(90,90);xlim([0,height/2]);
    subplot(4,4,[2:4 6:8 10:12]); imagesc(frm1)
    colormap('Gray')

    title(dir_list,'Interpreter','none')
    save(file_name,'frm1')
else
    figure;
```

```
%    max_s=max(spec_h_2);
    subplot (4,4,[14:16]); plot((1:width).*0.15,spec_h_2); xlim([0,width*0.15]);
    spec_v_2=sum(frm2(:,80:110),2);                              %vertical median filter
    spec_v_2=smooth(spec_v_2,10);
    subplot (4,4,[1 5 9]); plot(spec_v_2); view(90,90);xlim([0,height/2]);
    subplot(4,4,[2:4 6:8 10:12]); imagesc(frm2)
    colormap('Gray')

    title(dir_list,'Interpreter','none')

    save(file_name,'frm2')
end
toc

%%%%%%%%%%%%%%%%%%%%%%%%%%%%%%%%%%%%%%%%%%%%%%%%%%%%%%%%%%%%%%%%%%%%%%%%%%%%%%%
%subfunctions
%%%%%%%%%%%%%%%%%%%%%%%%%%%%%%%%%%%%%%%%%%%%%%%%%%%%%%%%%%%%%%%%%%%%%%%%%%%%%%%
function[img_out] = astg_corr(img_in,height,width,i_start,shift)
%geometrical correction of the spectral line shape based on the asumption
%of parabolic shape of the line
%i_start indicates the first or second half-frame

%correction shift
img_out=zeros(height/2,width+max(shift));   %preallocate memory
for i=1:height/2-1
img_out(i,1+shift(i):width+shift(i))=img_in((i-1)*2+i_start,:);
%img_out(i,1+shift(i):width+shift(i))=img_in(i,:);
end
max_shift=max(shift);
if max_shift==0
    max_shift=1;
end
img_out=img_out(:,max_shift:width);                          %cut edges
```

File A.2: Generate correction matrix for curvature correction of the spectra

```
function[shift,shift_file]= astg_shift(file,line_interv)
%geometrical correction of the spectral line shape based on the asumption
%of parabolic shape of the line
%file: *.mat
%line_interv indicates the interval which has to be corrected as follows [start:end]

%output: name of the generated *.mat file

%define image width and height
var=whos('-file', file);
frm=load(file,var.name);
frm=frm.(var.name);
height=size(frm,1);

[~,max_i]=max(frm(:,line_interv),[],2);
p_coef=polyfit(15:height-2,max_i(15:end-2)',2);              %quadratic polynomial fit
line_fit=ceil(line_interv(1)+polyval(p_coef,1:height));
line_peak=max(line_fit);
shift=line_peak-line_fit;                   %define cell shift for each row
[pathstr, name, ~] = fileparts(file);
shift_file=[pathstr '\' name '_shift.mat'];
save(shift_file,'shift')
```

File A.3: Fit theoretical Thomson spectra to the measured data

```
 function[T,n]=thomson_auswertung_lsqr(spectrum,gauss_data,M_spec,p)

dl=0.04;        %resolution of the monochromator nm/pix => dl=0.04; old1 dl=0.07; old2 dl=0.15

[height,width]=size(spectrum);

%load data for correlation with measured spectra
var=whos('-file', gauss_data);
frm=load(gauss_data,var.name);
frm=frm.(var.name);
spec_h=sum(frm(150:200,:),1);
spec_h=spec_h-mean(spec_h(1:200));
```

```
spec_h=spec_h./max(spec_h);
sig1=find(spec_h>=exp(-0.5),1,'first');
sig2=find(spec_h>=exp(-0.5),1,'last');
width_i=abs(sig1-sig2).*dl;
sig1=sig1+(exp(-0.5)-spec_h(sig1-1))/(spec_h(sig1)-spec_h(sig1-1));
sig2=sig2+(exp(-0.5)-spec_h(sig2+1))/(spec_h(sig2+1)-spec_h(sig2));
sig=dl*(sig2-sig1)/2;
%[~,M_spec]=max(spectrum,[],2);

DwX=-20:0.01:20;        %precalculation of the Dawson integral
DwY=mfun('dawson',DwX);  %precalculation of the Dawson integral

thomson=@(f,x)(1e3.*f(3).*thomson_fun(sig,f(1).*1e3,f(2),x,DwX,DwY));
gauss=@(f,x)(f(1)*1e4.*exp(-0.5.*((x-f(2))./f(3)).^2));
lor = @(f,x)(1e4.*f(1)*f(3)./(pi*((x-f(2)).^2+f(3)^2)));
voigt=@(f,x)(1e4.*f(4)*(f(1).*(1./(1+((x-f(2))./f(3)).^2))+(1-f(1)).*(exp(-log(2).*((x-f(2))./f(3)).^4))));

test=@(f,x)(thomson(f(1:3),x)+voigt(f(4:7),x));


T=zeros(1,height);
n=zeros(1,height);


k_b=1.3806504e-23;  %J/K
m_e=9e-31;          %electron mass kg
phi=pi/2;           %scattering angle in rad
lambda_0=532e-9;    %laser wavelength in nm
k=4*pi*sin(phi/2)/lambda_0;
c=3e8;
alpha_s=c.*4.*pi./((lambda_0.^2).*2.5.*k.*sqrt(k_b.*1e4./m_e));       %constant for initial alpha value

for i=1:height
    spectrum(i,:)=spectrum(i,:)-mean(spectrum(i,1:40));
    %M_spec=round((1:width)*spectrum(i,:)'./sum(spectrum(i,:)));
    x=linspace(0,width*dl,width);
    x=x-x(M_spec);
    sh=fix(1.3/dl);
    x_ind=[1:M_spec-sh,M_spec+sh:width];

    f0g=[0.5,0,sig,max(spectrum(i,:)).*1e-4];
    %f0g=[max(spectrum(i,:)).*1e-4,0,sig];
    %f0g=[1e-4.*max(spectrum(i,:)).*pi*width_i./2,0,width_i/2];

    [sMax,sMaxI]=max(spectrum(i,x_ind));

    f0=[1e1,min(5,max(1.2,alpha_s.*(abs(x(x_ind(sMaxI))).*1e-9))),1e-3.*100];
    lb=[0.3e1,0.8,1e-3.*sMax*0.6];
    ub=[5e1,5,1e-3.*sMax*1.1];

%     lbg=[1e-4.*max(spectrum(i,:)).*0.95,-0.5,sig*0.8];
%     ubg=[1e-4.*max(spectrum(i,:)).*1.05,0.5,sig*1.2];
     %lbg=[(1e-4.*max(spectrum(i,:)).*pi*width_i./2).*0.55,-0.5,width_i*0.5*0.5];
     %ubg=[(1e-4*max(spectrum(i,:)).*pi*width_i./2).*0.75,0.5,width_i*0.5*1.5];
        lbg=[0.27,-0.5,0.015,max(spectrum(i,:)).*0.95.*1e-4];
        ubg=[1,.5,1,max(spectrum(i,:)).*1.05.*1e-4];

    options=optimset('Display','off','TolFun',1e-6,'TolX',1e-6,'MaxFunEval',2e4,'MaxIter',4e4);

    x_ind=1:width;
    [f_par]= lsqcurvefit(test,[f0,f0g],x(x_ind),spectrum(i,x_ind),[lb,lbg],[ub,ubg],options);
    T(i)=f_par(1);
    n(i)=f_par(2);
    if p
         figure;
         [y_fit]=test(f_par,x(x_ind));
         plot(x(x_ind),spectrum(i,x_ind),x(x_ind),y_fit,'Linewidth',1.5)
         ylim([min(spectrum(i,:)) max(spectrum(i,:))./10])
         xlim([x(1),x(end)])
         xlabel('\lambda-\lambda_0 [nm]')
         ylabel('Intensity [a.u.]')
    end
end
```

File A.4: Generate electron feature convoluted with an instrumental profile for an array of T and $\alpha$

```
function[]= gen_thomson_data(gauss_data)
%generate calculated Thomson spectral datan in dependence of T_e and n_e
%input: instrumental function
T_e=3000:200:25000;
%n_e=7e21:5e21:3e23;
l_T=length(T_e);
%l_n=length(n_e);

k_b=1.3806504e-23;  %J/K
m_e=9e-31;          %electron mass kg
phi=pi/2;           %scattering angle in rad
lambda_0=532e-9;    %laser wavelength in nm
eps_0=8.8e-12;      %As/Vm
Q_e=1.6e-19;        %electron charge in C
c0=3e8;             %speed of light m/s

%lambda_d=sqrt(eps_0*k_b/Q_e^2).*sqrt(T_e'*(1./n_e));
k=4*pi*sin(phi/2)/lambda_0;
%alpha=1./(k.*lambda_d);
alpha=1:0.05:3.5;
l_n=length(alpha);

%determine instrumental profile width (measured data on cold atmosphere/gasflow)
dl=0.027;                           %spectral resolution in nm/pix => old2 dl=0.15 old1=0.07 dl=0.04;
var=whos('-file', gauss_data);
frm=load(gauss_data,var.name);
frm=frm.(var.name);
spec_h=sum(frm(1:100,:),1);
m=mean(spec_h(1:100));
spec_h=spec_h-m;
spec_h=spec_h./max(spec_h);

sig1=find(spec_h>=0.5,1,'first');
sig2=find(spec_h>=0.5,1,'last');
sig1=(0.5-sig1*spec_h(sig1-1)+(sig1-1)*spec_h(sig1))/(spec_h(sig1)-spec_h(sig1-1));
sig2=(0.5-(sig2+1)*spec_h(sig2)+(sig2)*spec_h(sig2+1))/(spec_h(sig2+1)-spec_h(sig2));
sig=dl*(sig2-sig1)/(2*sqrt(2*log(2)));

x_e=-4:0.01:4;
l=length(x_e);
a=sqrt(2.*k_b.*T_e./m_e);
a_3d=permute(repmat(a,[l_n 1 l]),[2 1 3]);
x_e_3d=permute(repmat(x_e,[l_T 1 l_n]),[1 3 2]);
x_el=x_e_3d.*2.*lambda_0.*sin(phi/2).*a_3d/c0*1e9;   %transofrm x_e to lambda in [nm]
gauss=exp(-0.5*(x_el./sig).^2);

%salpeter approximation
alpha_2_3d=repmat(alpha,[l_T 1 l]);
alpha_2_3d=alpha_2_3d.^2;
G_e_n=(1-2.*x_e.*mfun('dawson',x_e)-1i.*(x_e.*sqrt(pi).*exp(-x_e.^2)));
G_e_3d=permute(repmat(G_e_n,[l_T 1 l_n]),[1 3 2]);
G_e=alpha_2_3d.*G_e_3d;

S_e=(1./(k.*a_3d.*sqrt(pi))).*(abs(1./(1+G_e)).^2).*exp(-x_e_3d.^2);%electron scattering spectrum tranformed
      for lambda as input parameter
%consideration of the instrumental width
S_e_conv=ifft(fft(S_e,2*l-1,3).*fft(gauss,2*l-1,3),2*l-1,3);       %extende convoluted vectors to prevent the
      wrap around of the data

%transformation into the wavelength scale (scaling factor)
S_0=zeros(l_T,l_n,l*2-1);
S_0(:,:, l:l*2-1)=2*sqrt(pi)*c0/(k.*lambda_0^2.*a_3d);
S_0(:,:,1:l-1)=flipdim(S_0(:,:,l+1:l*2-1),3);

S_e_conv=S_0.*S_e_conv;

[M dx]=max(S_e_conv(:,:,l:l*2-1),[],3);
Hwhm=zeros(l_T,l_n);
P_V=zeros(l_T,l_n);
P_V1=zeros(l_T,l_n);
%determine HWHM
for i=1:l_T
    for j=1:l_n
    Hwhm(i,j)=find(S_e_conv(i,j,l-1+dx(i,j):l*2-1)<M(i,j)/2,1,'first');
    P_V(i,j)=M(i,j)./S_e_conv(i,j,800+fix(dx(i,j).*0.5));
    end
```

```
end
%M=M./S_e_conv(:,:,801);
dx=0.01.*(dx).*2.*lambda_0.*sin(phi/2).*a_3d(:,:,1)/c0*1e9; %transofrm x_e to lambda in [nm]
Hwhm=0.01.*(Hwhm).*2.*lambda_0.*sin(phi/2).*a_3d(:,:,1)/c0*1e9;

[A,T]=meshgrid(alpha,T_e);
save([gauss_data '_thomson_data.mat'],'Hwhm','dx','T','A','S_e_conv','P_V');
```

File A.5: Generate temperature density profiles valid in LTE assumptions (Solution of the Saha equation along with ideal gas law)

```
function[]= gen_thomson_data(gauss_data)
%generate calculated Thomson spectral datan in dependence of T_e and n_e
%input: instrumental function
T_e=3000:200:25000;
%n_e=7e21:5e21:3e23;
l_T=length(T_e);
%l_n=length(n_e);

k_b=1.3806504e-23;  %J/K
m_e=9e-31;          %electron mass kg
phi=pi/2;           %scattering angle in rad
lambda_0=532e-9;    %laser wavelength in nm
eps_0=8.8e-12;      %As/Vm
Q_e=1.6e-19;        %electron charge in C
c0=3e8;             %speed of light m/s

%lambda_d=sqrt(eps_0*k_b/Q_e^2).*sqrt(T_e'*(1./n_e));
k=4*pi*sin(phi/2)/lambda_0;
%alpha=1./(k.*lambda_d);
alpha=1:0.05:3.5;
l_n=length(alpha);

%determine instrumental profile width (measured data on cold atmosphere/gasflow)
dl=0.027;                           %spectral resolution in nm/pix => old2 dl=0.15 old1=0.07 dl=0.04;
var=whos('-file', gauss_data);
frm=load(gauss_data,var.name);
frm=frm.(var.name);
spec_h=sum(frm(1:100,:),1);
m=mean(spec_h(1:100));
spec_h=spec_h-m;
spec_h=spec_h./max(spec_h);

sig1=find(spec_h>=0.5,1,'first');
sig2=find(spec_h>=0.5,1,'last');
sig1=(0.5-sig1*spec_h(sig1-1)+(sig1-1)*spec_h(sig1))/(spec_h(sig1)-spec_h(sig1-1));
sig2=(0.5-(sig2+1)*spec_h(sig2)+(sig2)*spec_h(sig2+1))/(spec_h(sig2+1)-spec_h(sig2));
sig=dl*(sig2-sig1)/(2*sqrt(2*log(2)));

x_e=-4:0.01:4;
l=length(x_e);
a=sqrt(2.*k_b.*T_e./m_e);
a_3d=permute(repmat(a,[l_n 1 l]),[2 1 3]);
x_e_3d=permute(repmat(x_e,[l_T 1 l_n]),[1 3 2]);
x_el=x_e_3d.*2.*lambda_0.*sin(phi/2).*a_3d/c0*1e9;   %transofrm x_e to lambda in [nm]
gauss=exp(-0.5*(x_el./sig).^2);

%salpeter approximation
alpha_2_3d=repmat(alpha,[l_T 1 l]);
alpha_2_3d=alpha_2_3d.^2;
G_e_n=(1-2.*x_e.*mfun('dawson',x_e)-1i.*(x_e.*sqrt(pi).*exp(-x_e.^2)));
G_e_3d=permute(repmat(G_e_n,[l_T 1 l_n]),[1 3 2]);
G_e=alpha_2_3d.*G_e_3d;

S_e=(1./(k.*a_3d.*sqrt(pi))).*(abs(1./(1+G_e)).^2).*exp(-x_e_3d.^2);%electron scattering spectrum tranformed
      for lambda as input parameter
%consideration of the instrumental width
S_e_conv=ifft(fft(S_e,2*l-1,3).*fft(gauss,2*l-1,3),2*l-1,3);       %extende convoluted vectors to prevent the
      wrap around of the data

%transformation into the wavelength scale (scaling factor)
S_0=zeros(l_T,l_n,l*2-1);
S_0(:,:, l:l*2-1)=2*sqrt(pi)*c0/(k.*lambda_0^2.*a_3d);
S_0(:,:,1:l-1)=flipdim(S_0(:,:,l+1:l*2-1),3);

S_e_conv=S_0.*S_e_conv;
```

```
64
65 [M dx]=max(S_e_conv(:,:,l:l*2-1),[],3);
66 Hwhm=zeros(l_T,l_n);
67 P_V=zeros(l_T,l_n);
68 P_V1=zeros(l_T,l_n);
69 %determine HWHM
70 for i=1:l_T
71     for j=1:l_n
72     Hwhm(i,j)=find(S_e_conv(i,j,l-1+dx(i,j):l*2-1)<M(i,j)/2,1,'first');
73     P_V(i,j)=M(i,j)./S_e_conv(i,j,800+fix(dx(i,j).*0.5));
74     end
75 end
76 %M=M./S_e_conv(:,:,801);
77 dx=0.01.*(dx).*2.*lambda_0.*sin(phi/2).*a_3d(:,:,1)/c0*1e9; %transofrm x_e to lambda in [nm]
78 Hwhm=0.01.*(Hwhm).*2.*lambda_0.*sin(phi/2).*a_3d(:,:,1)/c0*1e9;
79
80 [A,T]=meshgrid(alpha,T_e);
81 save([gauss_data '_thomson_data.mat'],'Hwhm','dx','T','A','S_e_conv','P_V');
```

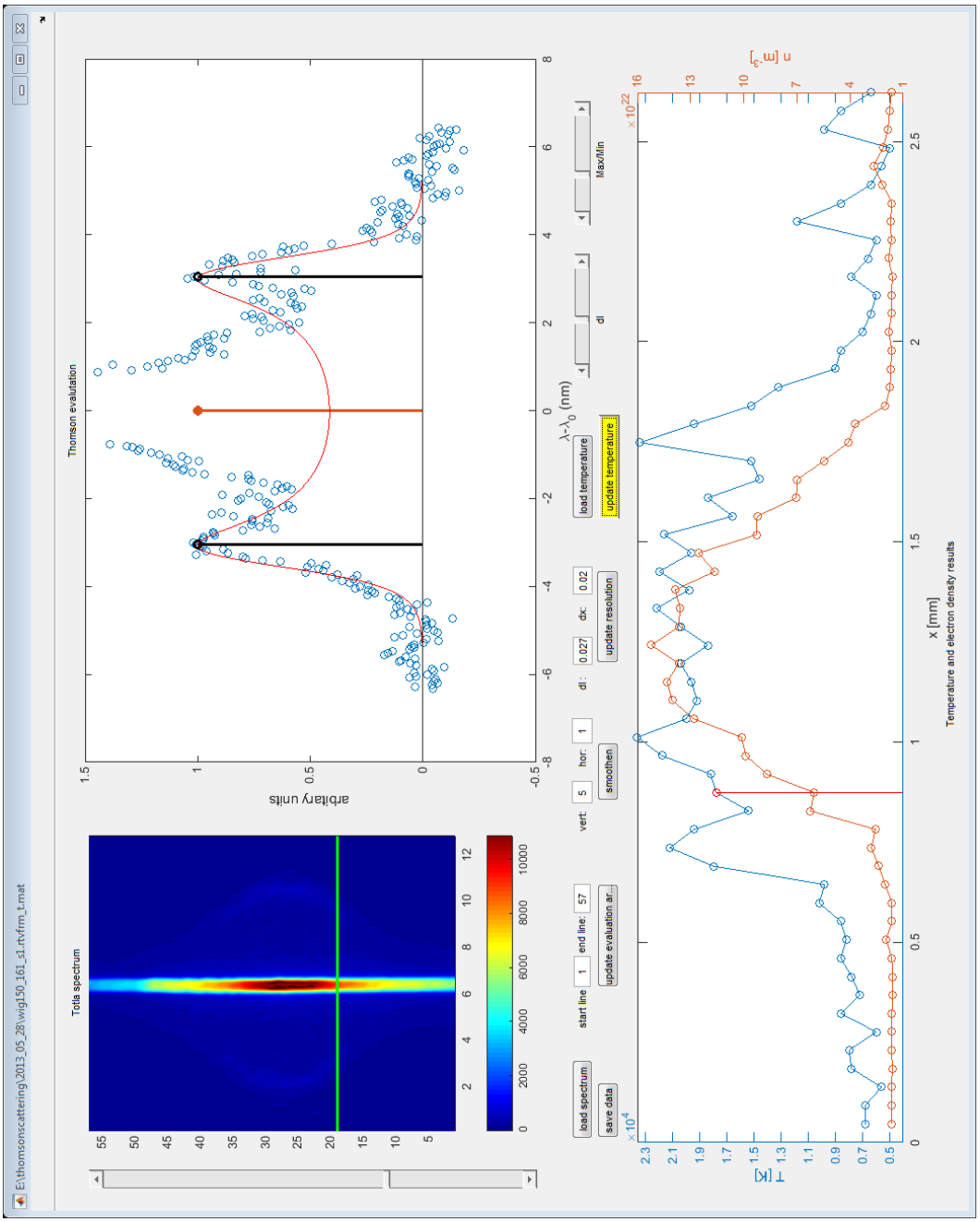


Figure A.3: Screen-shot of an interactive evaluation tool for correction of the false minima of the fitting algorithm. The tool is implemented using MATLAB.

### A.3.2 Stark broadening

File A.6: Generate '*.mat' files from '*.esf' files provided by the software of the ARYELLE spectrometer

```
function[split]=split_spec_esf(fid_xe,export)
%fid_xe: spex file name
%export=1 eport option is activatedted, export=0 no export

xe=importdata(fid_xe);              %reda original file
lambda_ind=xe.data(:,4);            %assign order data
lambda_spl=xe.data(:,1);            %assign wavelength data
spec_spl=xe.data(:,3);              %assign intensity data

%initialise serch parameters
len_xe=length(xe.data(:,3));
ind=lambda_ind(1);
pos=1;
split=cell(1,len_xe/sum(lambda_ind==ind));
count=1;

%prepare folder for export option
folder=[fid_xe(1:end-4) '\'];
if ~isdir(folder) && export
    mkdir(folder);
end

while pos<len_xe
    spec=spec_spl(lambda_ind==ind);
    lambda=lambda_spl(lambda_ind==ind);
    if export
        fid=fopen([folder num2str(ind) '.bin'],'w');
        fwrite(fid,[lambda spec]','float32');
        fclose(fid);
    end
    split{count}=[lambda spec];
    count=count+1;
    pos=find(lambda_ind==ind,1,'last')+1;
    if pos<len_xe
        ind=lambda_ind(pos);
    end
end
save([folder(1:end-1) '.mat'],'split')
```

File A.7: Determine instrumental profile

```
function[f_par,width_i,lambda,width_a]=instrumental(file,lambda0,res)
%routine to determin instrumental function for lambda0

var=whos('-file', file);
img=load(file,var.name);
img=img.(var.name);

%load spectral line of interest
[~,c]=max(img(142,:));
lambda=res.*((1:length(img))-c)+lambda0;
x=lambda(c-30:c+30);
y=sum(img(125:175,c-30:c+30),1);

back=polyfit(x([1:15 end-15:end]),y([1:15 end-15:end]),1);

y=y-(back(1).*x+back(2));
gauss=@(f,x)(f(1).*exp(-0.5.*((x-f(2))./f(3)).^2));
mu=(x*y')./sum(y);
gamma=mu-x(find(y>max(y)/2,1,'first'));
f0=[abs(max(y));mu;gamma]; % [nu, mean value, deviation, amplitude]
options=optimset('Display','off');
lb=[abs(max(y)).*0.8,lambda0-0.05,0.0001];
ub=[abs(max(y)).*1.01,lambda0+0.05,0.5];
%f_par= nlinfit(x,y,lor,f0,options);
f_par= lsqcurvefit(gauss,f0,x,y,lb,ub,options); %fit instrumental line profile to a gauussian

x_fit=x(1):0.001:x(end);
y_fit=gauss(f_par,x_fit);
width_i=sqrt(8*log(2)).*f_par(3); %fullwidth half maximum
```

```

total=sum(0.001.*y_fit);
diag=tril(ones(length(y_fit))).*repmat(y_fit,length(y_fit),1);
S=sum(diag.*0.001./total,2);
width_a=x_fit(find(S>0.75,1,'first'))-x_fit(find(S>0.25,1,'first'));
figure; plot(x,y,x_fit,y_fit)
end
```

File A.8: Analytical Abel inversion procedure

```
function[f]=abel(h_meas,x)

%assumption f is a Gaussian
%first Step: Gaussian fit to measured data
%second step: determination of amplitude

%determmin deviation
f_par=zeros(4,length(h_meas));
p=0;                            %plot parameter for debugging
for i=1:size(h_meas,2)
    f_par(:,i)=fit_gauss(x,h_meas(:,i)',p);
end
sigma=f_par(3,:);
mu=f_par(2,:);
h_max=f_par(1,:);
c=f_par(4,:);

%factor for the abel transform
cn=c./(1-c.*sigma.^2);
amp=h_max./((1+cn.*sigma.^2).*sqrt(2*pi*sigma.^2));
%amp=h_max./sqrt(2*pi*sigma.^2);
X=repmat(x',1,length(h_meas));
MU=repmat(mu,length(x),1);
SIGMA=repmat(sigma,length(x),1);
CN=repmat(cn,length(x),1);
AMP=repmat(amp,length(x),1);
f=AMP.*(1+CN.*(X-MU).^2).*exp(-0.5.*((X-MU)./SIGMA).^2);
if p
    xlim([-5.5,5.5])
    %ylim([-0.1*max(y),1.1*max(y)])
    xlabel('x [mm]')
    ylabel('Intensity [a. u.]')
    legend('data','fit')
end
end

function[f_par]=fit_gauss(x,y,p)
    %modified gauss distribution
    %gauss = @(f,x)(f(1).*(exp(-0.5.*((x-f(2))./f(3)).^2)));
    gauss = @(f,x)(f(1).*(1+f(4).*(x-f(2)).^2).*(exp(-0.5.*((x-f(2))./f(3)).^2)));
    y=y;
    f0=[max(y); x(fix(end/2)); 1;1e-9];
    options=optimset('Display','off','TolFun',1e-10,'TolX',1e-10);
    lb=[max(y).*0.85;-5.1;0.01;0];
    ub=[max(y).*1.15;5.1;100;0.1];
    [f_par,resn]= lsqcurvefit(gauss,f0,x,y,lb,ub,options);
    x_fit=x(1):0.01:x(end);
    y_fit=gauss(f_par,x_fit);
    if p
        resn;
        plot(x,y,'ko',x_fit,y_fit,'r','Linewidth',1.5)
        xlim([x(1), x(end)])
        ylim([-0.1*max(y),1.1*max(y)])
        xlabel('x [mm]')
        ylabel('Intensity [a. u.]')
        legend('data','fit')
    end
end
```

File A.9: Evaluate the line width from the emission spectra

```
function[ne,resnorm]=stark1(lambda,spec_abl,abl,lambda0,std,width_i,line_sim)
%%
```

```
%spec_abl: data
%abl: different kind of abelisaiton procedure
%lambda0: stark wavelength
%shift: halfwidth of the investigation window
%std: region which should be fitted
%width_i: FWHM of the instrumental broadening

[~,width]=size(spec_abl);
ne=zeros(1,width);
x=(0:(width-1))-(width-1)/2;
I=zeros(length(lambda(1):0.0005:lambda(end)),width);
resnorm=zeros(length(lambda),width);
back=fix(length(lambda)/6);

for j=1:width
     if lambda0==486.13
        r2=find(lambda>475,1,'first');
        r3=find(lambda>476.2,1,'first');
        r4=find(lambda>477.4,1,'first');
        r5=find(lambda>480,1,'first');
        r6=find(lambda>493.4,1,'first');
        r7=find(lambda>494.1,1,'first');
        fit_range=[r2:r3, r4:r5, r6:r7];
        std1=union(fit_range,std);
        [lambda_fit,I(:,j)]=lor_fit(lambda,spec_abl(:,j),lambda0,std,width_i,fit_range,line_sim);    %perfome
             deconvolution
     elseif lambda0==656.28
         fit_range=[1:back back*6-back:back*6];
        [lambda_fit,I(:,j),resnorm(:,j)]=lor_fit(lambda,spec_abl(:,j),lambda0,std,width_i,fit_range);    %
             perfome deconvolution
     else
         p=polyfit(lambda([1:back end-back:end]),spec_abl([1:back end-back:end],j),1);     %remove linear
              shift
         spec_abl(:,j)=spec_abl(:,j)-(p(1).*lambda+p(2));
         [lambda_fit,I(:,j)]=lor_fit(lambda,spec_abl(:,j),lambda0,std,width_i);
     end
end

%figure; pcolor(I'); shading interp; colorbar
if abl==1
    step=fix(length(I)/200);
    I=I(1:step:end,:);
    [~,m]=max(I,[],2);
    x=x-x(round(mean(m)));
    %x=x-mean((I(:,:)*x')./sum(I(:,:),2));
    lambda_fit=lambda_fit(1:step:end);
    I=abel(I',x)';  %abel inversion of a gaussian profile
elseif abl==0
   I=I; %no abel inversion in case the object profile is not known
elseif abl==2
   I=abel_spline_2half(I',x)'; %abel inversion with the spline methode
elseif abl==3
   I=abel_spline(spec_abl',x)';  %abel inversion with the spline methode with half of the data
end

%figure; pcolor(I'); shading interp; colorbar
%% identify line and extract data

for j=1:width
    ne(j)=fwhm_spline(lambda_fit',I(:,j));
end
end

function[x_fit,y_dc,residual]=lor_fit(x,y,lambda0,std,width_i,fit_range,line_sim)
    lor = @(f,x)(f(1)*f(3)./(pi*((x-f(2)).^2+f(3)^2)));
    voigt=@(f,x)(f(4)*(f(1).*(1./(1+((x-f(2))./f(3)).^2))+(1-f(1)).*exp(-log(2).*((x-f(2))./f(3)).^2)));     %
         pseudefoigtprofile (siehe wikipedia)
    gauss=@(f,x)(f(1).*exp(-0.5.*((x-f(2))./f(3)).^2));


    mu=(x'*y)./sum(y,1);
    gamma=mu-x(find(y>max(y)/2,1,'first'));
    options=optimset('Display','off','TolFun',1e-10,'TolX',1e-10);
    c=find(x>=lambda0,1,'first');
    f0=[0.5;mu;gamma;abs(max(y))]; % [nu, mean value, deviation, amplitude]
    lb=[1e-9,lambda0-0.1,0.015,abs(max(y(c-10:c+10))).*0.95];
    ub=[1-1e-9,lambda0+0.1,4,abs(max(y(c-10:c+10))).*1.05];

    x_fit=x(1):0.0005:x(end);
```

```
78  if lambda0==486.13
79      y=y/1e3;
80      test=@(f,x)(voigt(f(1:4),x)+lor(f(5:7),x)+gauss(f(8:10),x)+...
81          gauss(f(11:13),x)+gauss(f(14:16),x)+gauss(f(17:19),x)+...
82          +gauss(f(20:22),x)+gauss(f(23:25),x)+polyval(f(26:28),x));
83
84
85      p0=polyfit(x(fit_range),y(fit_range),2);        % scale y to improve polyfit presicision
86      y0=y-polyval(p0,x);                             %rescale the coefficients to fit back to y
87      lbp=-[5e-2,0,1.5e3].*1e0;                                       %background (polynomial)
            boundaries
88      ubp= [0,10,0].*1e0;
89
90      f0=[0.5;mu;gamma;abs(max(y0))]; % [nu, mean value, deviation, amplitude]
91      lb=[0.9+1e-9,lambda0-0.3,0.015,abs(max(y0(c-10:c+10))).*0.98];
92      ub=[1,lambda0+0.05,3.8,abs(max(y0(c-10:c+10))).*1.2];
93      c=zeros(1,size(line_sim,2));mi=c;m=c;
94      cb=-[5,5,3,5,3,3,5];
95      ce=[5,15,3,5,3,3,10];
96      for i=1:size(line_sim,2)
97          c(i)=find(x>=line_sim(1,i),1,'first');
98          [m(i),mi(i)]=max(y0(c(i)+cb(i):c(i)+ce(i)));
99      end
100     m(m<0)=0.1.*m(2);
101     m([1,5:6])=ones(1,3).*0.1.*m(2);
102     mi=mi+c+cb-1;
103
104     f0g=[m.*pi*width_i./2;x(mi)';ones(1,size(line_sim,2)).*width_i./2];  %spectral line boundaries
105     lbg=[m.*0.9.*pi*width_i./2;line_sim(1,:)-[.1,.1,.1,.2,.1,.1,.3];ones(1,size(line_sim,2)).*0.95.*
            width_i./2];
106     ubg=[m.*5*pi*width_i./2;line_sim(1,:)+[.1,.3,.1,.2,.1,.1,.3];ones(1,size(line_sim,2)).*3.*width_i./2];
107
108     gl=[2,3,4,5,6,7];
109     f0g([1,3],gl)=[m(gl);ones(1,length(gl)).*width_i./sqrt(8*log(2))];
110     lbg([1,3],gl)=[m(gl).*0.3;ones(1,length(gl)).*width_i./sqrt(8*log(2)).*0.7]; lbg(1,[1,5:6])=zeros(1,3)
            ;
111     ubg([1,3],gl)=[m(gl).*1.05;ones(1,length(gl)).*width_i./sqrt(8*log(2)).*1.5];
112
113     f0g=reshape(f0g,size(line_sim,2)*3,1);
114     lbg=reshape(lbg,size(line_sim,2)*3,1);
115     ubg=reshape(ubg,size(line_sim,2)*3,1);
116
117
118
119     std=union(c(1)-20 :c(end),fit_range);                       %unify fit region for H-beta and
            background
120
121     [f_par_sim,resnorm,residual,exitflag]=lsqcurvefit(test,[f0;f0g;p0'],x(std),y(std),[lb';lbg;lbp'],[ub';
            ubg;ubp'],options);
122     f_par=f_par_sim(1:4);                                           %extract fit aprameters for later
            plotting
123     spec_sim=test(f_par_sim,x);
124
125 elseif lambda0==656.28
126     y=y/1e3;
127     test=@(f,x)(voigt(f(1:4),x)+polyval(f(5:6),x));
128     p0=polyfit(x(fit_range),y(fit_range),1);        % scale y to improve polyfit presicision
129     y0=y-polyval(p0,x);                             %rescale the coefficients to fit back to y
130     lbp=-[1,0];                                             %background (polynomial) boundaries
131     ubp= [0,100];
132
133     f0=[0.5;mu;gamma;abs(max(y0))]; % [nu, mean value, deviation, amplitude]
134     lb=[1e-9,lambda0-0.3,0.015,abs(max(y0(c-10:c+10))).*0.99];
135     ub=[1,lambda0+0.05,1.8,abs(max(y0(c-10:c+10))).*1.2];
136     [f_par_sim,resnorm,residual]= lsqcurvefit(test,[f0' p0],x,y,[lb lbp],[ub ubp],options);
137     spec_sim=test(f_par_sim,x);
138     f_par=f_par_sim(1:4);
139 else
140     if max(y)>max(y(c-10:c+10))
141
142         [f_par,resnorm]= lsqcurvefit(voigt,f0,x(std),y(std),lb,ub,options);
143         y_fit=voigt(f_par,x_fit);
144         spec_sim=y_fit;
145     else
146         [f_par,resnorm]= lsqcurvefit(voigt,f0,x(std),y(std),lb,ub,options);
147         y_fit=voigt(f_par,x_fit);
148         spec_sim=y_fit;
149     end
150 end
```

```
    y_fit=voigt(f_par,x_fit);
    w=fwhm_spline(x_fit,y_fit);
    if w<=width_i
        w=width_i+0.001;
    end
    if lambda0==486.13
        wn=w;%(w.^1.4-width_i.^1.4).^(1/1.4);                          %approximated formula for deconvoluted
              FWHA for H beta
    else
        %deconvolution
        c1=.5346;
        c2=.2169;
        wn=-c1.*w./(c2-c1^2)-sqrt((c1.*w./(c2-c1^2)).^2-(width_i.^2-w.^2)./(c2-c1^2)); %for a Voigt profile
        %wn=w;
    end;
     y_dc=lor([max(y_fit)*pi*wn/2,f_par(2),wn/2],x_fit); %deconvoluted profile
%      figure; plot(x,spec_sim,x(std),y(std),'o',x,y,'.','Linewidth', 1.5)
%      resnorm
%      f_par_sim'
%      xlabel('\lambda [nm]')
%      ylabel('Intensity [a.u.]')
%      legend('fitted spectrum','fit region','raw data')
%      x;
end

function [width]=fwhm_spline(x,y)
        %determine FWHM using linear interpolation at f(x)=0.5
        [my,myi]=max(y);
        if my<1e-10
            width=0;
        else
            y=y./(my);
            s1=find(diff(y(1:myi))>1e-6,1,'first');
            sp1 = interp1(y(s1:myi),x(s1:myi),0.5);

            e1=find(abs(diff(y(myi:end)))>1e-6,1,'last');
            sp2 = interp1(y(myi:myi+e1),x(myi:myi+e1),0.5);
            width=sp2-sp1;
        end
end
```

# Nomenclature

**Abbreviations**

| | |
|---|---|
| AC | alternating current |
| Ar I, Ar II | neutral and ionized argon |
| CCD | charge-coupled device |
| DC | direct current |
| $f/n$ | f-number |
| FWHM | full width half maximum |
| GMAW | gas metal arc welding |
| GTAW | gas tungsten arc welding |
| $H_\alpha$, $H_\beta$ | Balmer series hydrogen lines |
| ICCD | intensified charge-coupled device |
| LTE | local thermal equilibrium |
| MCP | micro channel plate |
| Nd:YAG | neodymium-doped yttrium aluminium garnet |
| S/N | signal to noise ratio |
| SVD | singular value decomposition |
| TE | thermal equilibrium |

**Constants**

| | |
|---|---|
| $c$ | $= 2.998 \times 10^8\,\mathrm{ms}^{-1}$, speed of light |
| $e$ | $= 1.602 \times 10^{-19}\,\mathrm{C}$, electron charge |
| $h$ | $= 6.626 \times 10^{-34}\,\mathrm{Js}$, Planck's constant |
| $\hbar$ | $= h/2\pi$, reduced Plank's constant |
| $k_\mathrm{B}$ | $= 1.380 \times 10^{-23}\,\mathrm{JK}^{-1}$, Boltzmann constant |
| $\mu_0$ | $= 4\pi \times 10^{-7}\,\mathrm{Hm}^{-1}$, vacuum permeability |
| $\varepsilon_0$ | $= 8.854 \times 10^{-12}\,\mathrm{Fm}^1 - 1$, vacuum permittivity |

**Symbols**

| | |
|---|---|
| $_e$ | index denoting quantities related to electrons |
| $_I$ | index denoting quantities of incident radiation |
| $_i$ | index denoting quantities related to ions |
| $_q$ | index denoting quantities related to a species with a charge $q$ |
| $_S$ | index denoting quantities of scattered radiation |
| $A$ | area |
| $\vec{A}$ | vector potential |
| $\vec{a}$ | acceleration |
| $\vec{B}$ | magnetic field |
| $\mathcal{C}$ | correlation function of the emitted light amplitude |
| $d$ | diameter |
| $\vec{E}$ | electric field |
| $E_L$ | per pulse laser energy |
| $E_n$ | energy level of the state $n$ |
| $E_j$ | ionization energy |
| $E_{u,q}$ | excited energy state of the species with a charge $q$ |
| $f$ | focal length |
| $\vec{F}$ | force |
| $F_q$ | distribution function of the species with a charge $q$ |
| $f_{col}$ | particle collision frequency |
| $g_n$ | number of polarizations of a photon |
| $g_{u,q}$ | the statistical weight of the species with a charge $q$ |
| $H$ | Hamiltonian operator |
| $H_0$ | Hamiltonian of the unperturbed system |
| $H_{int}$ | Hamiltonian of the perturbed system |
| $\vec{i}$ | direction of incident radiation |
| $\hat{\imath}$ | imaginary unit |
| $\vec{j}$ | total current density |
| $\vec{k}$ | wave number |
| $L$ | radiance |
| $\mathcal{L}$ | spectral profile of the emitted line |
| $\mathcal{L}_{\mathrm{G}}$ | Gauss spectral line profile |

| | |
|---|---|
| $\mathcal{L}_{\mathrm{Lor}}$ | Lorentz spectral line profile |
| $\mathcal{L}_{\mathrm{V}}$ | Gauss spectral line profile |
| $m_e$, $m_i$ | electron or ion mass |
| $N$ | number of particles |
| $\|n\rangle$ | state function |
| $n_e$, $n_i$ | electron or ion density |
| $P$ | power |
| $p$ | pressure |
| $\underline{p}$ | momentum operator |
| $q$ | charge of a species |
| $\underline{q}$ | position operator |
| $R$ | observation distance |
| $r$ | radius |
| $\vec{r}$ | spatial position |
| $r_L$ | laser beam radius |
| $\vec{S}$ | Poynting vector |
| $\vec{s}$ | direction of scattered radiation |
| $S_e, S_i$ | electron and ion feature of the Thomson scattering spectrum |
| $t$ | time coordinate |
| $\mathcal{T}$ | time interval |
| $T$, $T_e$, $T_i$ | particle, electron or ion temperature |
| $V$ | observed volume |
| $\vec{v}$ | velocity |
| $v_q$ | velocity of the species with a charge $q$ |
| $w$ | profile half width in $\mathrm{nm}$ |
| $x$ | space coordinate |
| $x_e$, $x_i$ | normed electron and ion frequency scales |
| $Z$ | charge number of ions |
| $Z_q$ | the partition function of the species with a charge $q$ |
| $\alpha$ | scattering parameter |
| $\varepsilon$ | local emissivity |
| $\varepsilon_{m\to n}$ | the emission coefficient of the transition $m \to n$ |

| | |
|---|---|
| $\epsilon$ | longitudinal dielectric function |
| $\theta$ | observation angle of scattered radiation with respect to the incident radiation |
| $\Delta\lambda$ | FWHM of the line profile in the wavelength scale |
| $\lambda$ | radiation wavelength |
| $\lambda_0$ | central wavelength of the emitted line profile |
| $\lambda_D$ | Debye length |
| $\mu$ | $= T_e/T_i$ |
| $\nu$ | the frequency of the photon emitted by a bound electron transition |
| $\Delta\omega$ | FWHM of the line profile in the frequency scale |
| $\omega_{mn}$ | angular frequency of the radiation emitted during the transition $m \rightarrow n$ |
| $\rho$ | total charge density |
| $\sigma_{col}$ | effective collision cross section |
| $\varphi_n, \Phi_n$ | state function |
| $\phi$ | scalar potential |
| $\chi_e, \chi_i$ | electron and ion susceptibilities |
| $\Omega$ | solid angle |
| $\omega$ | angular frequency |
| $\omega_0$ | central angular frequency of the emitted line profile |
| $\omega_{pe}$ | free electron plasma frequency |
| I | current |
| U | voltage |

# Bibliography


[1] Davy, S. H. "Additional Experiment on Galvanic electricity". *Nicholson's Journal of Natural Philosophy, Chemistry and the Arts.* 4 (1801), p. 326. URL: https://archive.org/stream/ajournalnatural10nichgoog#page/n360/mode/2up.

[2] Benardos, N. N. and Olszewski, S. *Process of and apparatus for working metals by the direct application of the electric current*. US Patent 363,320. 1887. URL: http://www.google.de/patents/US363320.

[3] Norrish, J. *Advanced welding processes*. Woodhead Publishing, 2006.

[4] Lancaster, J. *The physics of welding*. Ed. by Lancaster, J. Second Edition. Pergamon, 1986. ISBN: 9780080340760. DOI: http://dx.doi.org/10.1016/B978-0-08-034076-0.50002-5.

[5] Fritz, A. H. *Fertigungstechnik*. Ed. by Schulze, G. 10th. Vol. 3. Springer, 2012, pp. 117–256. URL: http://link.springer.com/book/10.1007/978-3-642-29786-1.

[6] *EWM-Schweißlexikon*. EWM higtech welding GmbH. 2009. URL: https://www.ewm-group.com/de/service/downloads/broschueren-prospekte-und-handbuecher/1192-ewm-schweisslexikon/download.html.

[7] Trube, S. and Miklos, E. "Metall-Aktivgasschweißen MAG / Metall-Inertgasschweißen MIG". *29. Sondertagung: Schweißen im Anlagen und Behälterbau; Basis-Info: MAG / MIG*. 2001.

[8] Scherreiks, J. "Untersuchung der Tropfenablösung während eines Metall-Schutzgas Schweißprozesses (BA-thesis)". MA thesis. Universität der Bundeswehr München, 2014.

[9] Goecke, S. "Auswirkungen von Aktivgaszumischungen im vpm-Bereich zu Argon auf das MIG-Impulsschweißen on Aluminium". PhD thesis. Technische Universität Berlich, 2004. URL: http://opus4.kobv.de/opus4-tuberlin/frontdoor/index/index/docId/723.

[10] Subramaniam, S., White, D. R., Scholl, D. J., and Weber, W. H. "In situ optical measurement of liquid drop surface tension in gas metal arc welding". *Journal of Physics D: Applied Physics* 31.16 (1998), p. 1963. URL: http://stacks.iop.org/0022-3727/31/i=16/a=004.

[11] Fan, H. and Kovacevic, R. "Droplet formation, detachment, and impingement on the molten pool in gas metal arc welding". English. *Metallurgical and Materials Transactions B* 30.4 (1999), pp. 791–801. ISSN: 1073-5615. DOI: 10.1007/s11663-999-0041-6.

[12] Ferraresi, V. A., Figueiredo, K. M., and Ong, T. H. "Metal transfer in the aluminum gas metal arc welding". en. *Journal of the Brazilian Society of Mechanical Sciences and Engineering* 25 (2003), pp. 229–234. ISSN: 1678-5878. URL: http://www.scielo.br/scielo.php?script=sci_arttext&pid=S1678-58782003000300003&nrm=iso.

[13] Siewert, E., Schein, J., and Forster, G. "Determination of enthalpy, temperature, surface tension and geometry of the material transfer in PGMAW for the system argon?iron". *Journal of Physics D: Applied Physics* 46.22 (2013), p. 224008. URL: http://stacks.iop.org/0022-3727/46/i=22/a=224008.

[14] Moreira, P. M. G. P., Frazão, O., Tavares, S. M. O., de Figueiredo, M. A. V., Restivo, M. T., Santos, J. L., and de Castro, P. M. S. T. "Temperature field acquisition during gas metal arc welding using thermocouples, thermography and fibre Bragg grating sensors". *Measurement Science and Technology* 18.3 (2007), p. 877. URL: http://stacks.iop.org/0957-0233/18/i=3/a=041.

[15] Yamazki, K., Yamamoto, E., Suzuki, K., Koshishi, F., miyazako, S., Tashiro, S., Tanaka, M., and Nakata, K. "The Surface Temperature Measurement of Weld Pool by Infrared Two-Color Pyrometry". *Quaterly Journal of the Japan Welding Society* 27.1 (2009), pp. 34–40. DOI: 10.2207/qjjws.27.34.

[16] Soderstorm, E. J., Scott, K. M., and Mendez, P. F. "Calorimetric Measurement of Droplet Temperature in GMAW". *Welding Journal* 90.4 (2011), p. 77. URL: http://www.aws.org/wj/supplement/S-2011.html.

[17] Schnick, M., Dreher, M., Zschetzsche, J., Füssel, U., and Spille-Kohoff, A. "Visualization and Optimization of Shielding Gas Flows in Arc Welding". English. *Welding in the World* 56.1-2 (2012), pp. 54–61. ISSN: 0043-2288. DOI: 10.1007/BF03321146.

[18] Lin, M. and Eagar, T. "Pressures produced by gas tungsten arcs". English. *Metallurgical Transactions B* 17.3 (1986), pp. 601–607. ISSN: 0360-2141. DOI: 10.1007/BF02670227.

[19] Gick, A. E. F., Quigley, M. B. C., and Richards, P. H. "The use of electrostatic probes to measure the temperature profiles of welding arcs". *Journal of Physics D: Applied Physics* 6.16 (1973), p. 1941. URL: http://stacks.iop.org/0022-3727/6/i=16/a=314.

[20] Sanders, N. and Pfender, E. "Measurement of anode falls and anode heat transfer in atmospheric pressure high intensity arcs". *Journal of Applied Physics* 55.3 (1984), pp. 714–722. ISSN: 0021-8979. DOI: 10.1063/1.333129.

[21] Tanaka, M. and Ushio, M. "Observations of the anode boundary layer in free-burning argon arcs". *Journal of Physics D: Applied Physics* 32.8 (1999), p. 906. URL: http://stacks.iop.org/0022-3727/32/i=8/a=011.

[22] Muraoka, K. and Kono, A. "Laser Thomson scattering for low-temperature plasmas". *Journal of Physics D: Applied Physics* 44.4 (2011), p. 043001. URL: http://stacks.iop.org/0022-3727/44/i=4/a=043001.

[23] Farmer, A. J. D. and Haddad, G. N. "Rayleigh scattering measurements in a free-burning argon arc". *Journal of Physics D: Applied Physics* 21.3 (1988), p. 426. URL: http://stacks.iop.org/0022-3727/21/i=3/a=008.

[24] Murphy, A. B. and Farmer, A. J. D. "Temperature measurement in thermal plasmas by Rayleigh scattering". *Journal of Physics D: Applied Physics* 25.4 (1992), p. 634. URL: http://stacks.iop.org/0022-3727/25/i=4/a=009.

[25] Snyder, S. C., Lassahn, G. D., and Reynolds, L. D. "Direct evidence of departure from local thermodynamic equilibrium in a free-burning arc-discharge plasma". *Phys. Rev. E* 48 (1993), pp. 4124–4127. DOI: 10.1103/PhysRevE.48.4124.

[26] Murphy, A. B. "Laser-scattering temperature measurements of a free-burning arc in nitrogen". *Journal of Physics D: Applied Physics* 27.7 (1994), p. 1492. URL: http://stacks.iop.org/0022-3727/27/i=7/a=022.

[27] Snyder, S. C. and Bentley, R. E. "A measurement of axial velocity and temperature in a free-burning arc using Thomson scattering". *Journal of Physics D: Applied Physics* 29.12 (1996), p. 3045. URL: http://stacks.iop.org/0022-3727/29/i=12/a=017.

[28] Bentley, R. E. "A departure from local thermodynamic equilibrium within a freely burning arc and asymmetrical Thomson electron features". *Journal of Physics D: Applied Physics* 30.20 (1997), p. 2880. URL: http://stacks.iop.org/0022-3727/30/i=20/a=015.

[29] Tanaka, M. and Ushio, M. "Plasma state in free-burning argon arc and its effect on anode heat transfer". *Journal of Physics D: Applied Physics* 32.10 (1999), p. 1153. URL: http://stacks.iop.org/0022-3727/32/i=10/a=312.

[30] Terasaki, H., Tanaka, M., and Ushio, M. "Effects of metal vapor on electron temperature in helium gas tungsten arcs". English. *Metallurgical and Materials Transactions A* 33.4 (2002), pp. 1183–1188. ISSN: 1073-5623. DOI: 10.1007/s11661-002-0219-x.

[31] Snyder, S. C., Crawford, D., and Fincke, J. R. "Dependence on the scattering angle of the electron temperature and electron density in Thomson-scattering measurements on an atmospheric-pressure plasma jet". *Phys. Rev. E* 61 (2000), pp. 1920–1924. DOI: 10.1103/PhysRevE.61.1920.

[32] Tanaka, M. and Tashiro, S. "Electron temperature measurement of tungsten inert gas arcs". *Thin Solid Films* 516.19 (2008). 20th Symposium on Plasma Science for Materials (SPSM-20), pp. 6628–6633. ISSN: 0040-6090. DOI: 10.1016/j.tsf.2007.11.036.

[33] Reiche, J. "Nichtresonante Laserstreudiagnostik an Hochdruckgasentladungen". PhD thesis. Universität Hannover, 2003. URL: http://d-nb.info/970679874.

[34] Reiche, J., Könemann, F., Mende, W., and Kock, M. "Diagnostics of discharge modes of a free-burning low-current argon arc". *Journal of Physics D: Applied Physics* 34.21 (2001), p. 3177. URL: http://stacks.iop.org/0022-3727/34/i=21/a=310.

[35] Uchino, K., Muraoka, K., and Akazaki, M. "Laser Scattering Diagnostics of an Atmospheric Impulse Arc". *Japanese Journal of Applied Physics* 20.6 (1981), p. 1165. URL: http://stacks.iop.org/1347-4065/20/i=6/a=1165.

[36] Uchino, K., Muraoka, K., and Akazaki, M. "Temperature Measurement of an Atmospheric Impulse Arc Using Ruby Laser Scattering". *Japanese Journal of Applied Physics* 21.9R (1982), p. 1388. URL: http://stacks.iop.org/1347-4065/21/i=9R/a=1388.

[37] Uchino, K., Itsumi, Y., Muraoka, K., and Akazaki, M. "Ruby-Laser Scattering Diagnostics of DC-Arcs in Atmospheric Air". *Japanese Journal of Applied Physics* 23.5R (1984), p. 662. URL: http://stacks.iop.org/1347-4065/23/i=5R/a=662.

[38] Forster, G. "Bestimmung von Parametern thermischer Plasmen mittels Thomsonstreuung". PhD thesis. Universität der Bundeswehr München, 1995. URL: http://www.unibw.de/eit2/Forschung/chronik/dissertationen/index_html.

[39] Gregori, G., Schein, J., Schwendinger, P., Kortshagen, U., Heberlein, J., and Pfender, E. "Thomson scattering measurements in atmospheric plasma jets". *Phys. Rev. E* 59 (1999), pp. 2286–2291. DOI: 10.1103/PhysRevE.59.2286.

[40] Gregori, G., Kortshagen, U., Heberlein, J., and Pfender, E. "Analysis of Thomson scattered light from an arc plasma jet". *Phys. Rev. E* 65 (2002), p. 046411. DOI: 10.1103/PhysRevE.65.046411.

[41] Schinköth, D. "Laser–Streu–Diagnostik im Vergleich mit Emissionsspektroskopie an einem Freistrahlplasma". PhD thesis. Universität Stuttgart, 2001. URL: http://elib.uni-stuttgart.de/opus/volltexte/2001/834/.

[42] Snyder, S. C., Reynolds, L. D., Fincke, J. R., Lassahn, G. D., Grandy, J. D., and Repetti, T. E. "Electron-temperature and electron-density profiles in an atmospheric-pressure argon plasma jet". *Phys. Rev. E* 50 (1994), pp. 519–525. DOI: 10.1103/PhysRevE.50.519.

[43] Kopainsky, J. "Laser scattering with a rapidly tuned dye laser". English. *Applied physics* 8.3 (1975), pp. 229–239. ISSN: 0340-3793. DOI: 10.1007/BF00896616.

[44] Yang, G. and Heberlein, J. "Anode attachment modes and their formation in a high intensity argon arc". *Plasma Sources Science and Technology* 16.3 (2007), p. 529. URL: http://stacks.iop.org/0963-0252/16/i=3/a=012.

[45] Dzierizega, K., Zawadzki, W., Pokrzywka, B., and Pellerin, S. "Experimental investigations of plasma perturbation in Thomson scattering applied to thermal plasma diagnostics". *Phys. Rev. E* 74 (2006), p. 026404. DOI: 10.1103/PhysRevE.74.026404.

[46] Murphy, A. B. "Thomson scattering diagnostics of thermal plasmas: Laser heating of electrons and the existence of local thermodynamic equilibrium". *Phys. Rev. E* 69 (2004), p. 016408. DOI: 10.1103/PhysRevE.69.016408.

[47] Murphy, A. B. "Reinterpretation of Laser Scattering Measurements of Welding Arc Temperature and the Existence of Local Thermodynamic Equilibrium in Arcs (Physics, Processes, Instruments & Measurements, International Symposium of JWRI 30th Anniversary)". *Transactions of JWRI* 32.1 (2003), pp. 1–9. ISSN: 03874508. URL: http://ci.nii.ac.jp/naid/110006486165/en/.

[48] Tomita, K., Gojima, D., Nagai, K., Uchino, K., Kamimae, R., Tanaka, Y., Suzuki, K., Iijima, T., Uchii, T., and Shinkai, T. "Thomson scattering diagnostics of decay processes of Ar/SF 6 gas-blast arcs confined by a nozzle". *Journal of Physics D: Applied Physics* 46.38 (2013), p. 382001. URL: http://stacks.iop.org/0022-3727/46/i=38/a=382001.

[49] Tomita, K., Yoshitake, S., Uchino, K., Takenaka, D., Toda, H., Hikita, M., and Suzuki, K. "Measurements of Electron Density and Electron Temperature of Arc Discharge Plasmas Containing Metallic Vapors using Laser Thomson Scattering". *IEEJ Transactions on Fundamentals and Materials* 133.9 (2013), pp. 458–464. DOI: 10.1541/ieejfms.133.458.

[50] Tomita, K., Nagai, K., Shimizu, T., Bolouki, N., Yamagata, Y., Uchino, K., and Kaneko, T. "Thomson scattering diagnostics of atmospheric plasmas in contact with ionic liquids". *Applied Physics Express* 7.6 (2014), p. 066101. URL: http://stacks.iop.org/1882-0786/7/i=6/a=066101.

[51] Sesi, N. N., Mackenzie, A., Shanks, K. E., Yang, P., and Hieftje, G. M. "Fundamental studies of mixed-gas inductively coupled plasmas". *Spectrochimica Acta Part B: Atomic Spectroscopy* 49.12-14 (1994), pp. 1259–1282. ISSN: 0584-8547. DOI: http://dx.doi.org/10.1016/0584-8547(94)80108-8.

[52] Van Gessel, A. F. H., Carbone, E. A. D., Bruggeman, P. J., and van der Mullen, J. J. A. M. "Laser scattering on an atmospheric pressure plasma jet: disentangling Rayleigh, Raman and Thomson scattering". *Plasma Sources Science and Technology* 21.1 (2012), p. 015003. URL: http://stacks.iop.org/0963-0252/21/i=1/a=015003.

[53] Hübner, S., Carbone, E., Palomares, J. M., and van der Mullen, J. "Afterglow of Argon Plasmas with H2, O2, N2, and CO2 Admixtures Observed by Thomson Scattering". *Plasma Processes and Polymers* 11.5 (2014), pp. 482–488. ISSN: 1612-8869. DOI: 10.1002/ppap.201300190.

[54] Diwakar, P. and Hahn, D. "Study of early laser-induced plasma dynamics: Transient electron density gradients via Thomson scattering and Stark Broadening, and the implications on laser-induced breakdown spectroscopy measurements". *Spectrochimica Acta Part B: Atomic Spectroscopy* 63.10 (2008). A collection of papers presented at the Euro Mediterranean Symposium on Laser Induced Breakdown Spectroscopy (EMSLIBS 2007), pp. 1038–1046. ISSN: 0584-8547. DOI: http://dx.doi.org/10.1016/j.sab.2008.07.003.

[55] Kieft, E. R., van der Mullen, J. J. A. M., Kroesen, G. M. W., Banine, V., and Koshelev, K. N. "Collective Thomson scattering experiments on a tin vapor discharge in the prepinch phase". *Phys. Rev. E* 70 (2004), p. 056413. DOI: 10.1103/PhysRevE.70.056413.

[56] Van der Mullen, J., van de Sande, M., de Vries, N., Broks, B., Iordanova, E., Gamero, A., Torres, J., and Sola, A. "Single-shot Thomson scattering on argon plasmas created by the Microwave Plasma Torch; evidence for a new plasma class". *Spectrochimica Acta Part B: Atomic Spectroscopy* 62.10 (2007), pp. 1135–1146. ISSN: 0584-8547. DOI: http://dx.doi.org/10.1016/j.sab.2007.07.006.

[57] Dzierizega, K., Mendys, A., Pellerin, S., Thouin, E., Travaille, G., Bousquet, B., Canioni, L., and Pokrzywka, B. "Thomson scattering from laser induced plasma in air". *Journal of Physics: Conference Series* 227.1 (2010), p. 012029. URL: http://stacks.iop.org/1742-6596/227/i=1/a=012029.

[58] Nedanovska, E., Nersisyan, G., Morgan, T. J., Huwel, L., Lewis, C. L. S., Riley, D., and Graham, W. G. "Comparison of the electron density measurements using Thomson scattering and emission spectroscopy for laser induced breakdown in one atmosphere of helium". *Applied Physics Letters* 99.26, 261504 (2011), p. 261504. DOI: 10.1063/1.3672817.

[59] Kieft, E. R., Groothuis, C. H. J. M., van der Mullen, J. J. A. M., and Banine, V. "Subnanosecond Thomson scattering setup for space and time resolved measurements with reduced background signal". *Review of Scientific Instruments* 76.9, 093503 (2005), p. 093503. DOI: 10.1063/1.2038667.

[60] Hübner, S., Hofmann, S., van Veldhuizen, E. M., and Bruggeman, P. J. "Electron densities and energies of a guided argon streamer in argon and air environments". *Plasma Sources Science and Technology* 22.6 (2013), p. 065011. URL: http://stacks.iop.org/0963-0252/22/i=6/a=065011.

[61] Wiese, W. "Spectroscopic diagnostics of low temperature plasmas: techniques and required data". *Spectrochimica Acta Part B: Atomic Spectroscopy* 46.6–7 (1991), pp. 831–841. ISSN: 0584-8547. DOI: http://dx.doi.org/10.1016/0584-8547(91)80084-G.

[62] Haddad, G. N. and Farmer, A. J. D. "Temperature determinations in a free-burning arc. I. Experimental techniques and results in argon". *Journal of Physics D: Applied Physics* 17.6 (1984), p. 1189. URL: http://stacks.iop.org/0022-3727/17/i=6/a=015.

[63] Thornton, M. F. "Spectroscopic determination of temperature distributions for a TIG arc". *Journal of Physics D: Applied Physics* 26.9 (1993), p. 1432. URL: http://stacks.iop.org/0022-3727/26/i=9/a=014.

[64] Haddad, G. N. and Farmer, A. J. D. "Temperature Measurements in Gas Tungsten Arcs". *Welding Research Supplement* 12 (1985), p. 339.

[65] Haddad, G., Farmer, A., Kovitya, P., and Cram, L. "Physical Processes in Gas-Tungsten Arcs". *Plasma Science, IEEE Transactions on* 14.4 (1986), pp. 333–336. ISSN: 0093-3813. DOI: 10.1109/TPS.1986.4316559.

[66] Farmer, A. J. D., Haddad, G. N., and Cram, L. E. "Temperature determinations in a free-burning arc. III. Measurements with molten anodes". *Journal of Physics D: Applied Physics* 19.9 (1986), p. 1723. URL: http://stacks.iop.org/0022-3727/19/i=9/a=016.

[67] Murphy, A. B. "Modified Fowler–Milne method for the spectroscopic measurement of temperature and composition of multielement thermal plasmas". *Review of Scientific Instruments* 65.11 (1994), pp. 3423–3427. DOI: 10.1063/1.1144516.

[68] Hiraoka, K. "Plasma structures of Ar-H2 mixed gas tungsten arcs determined by spectroscopic measurements". *TWLD* 12.3 (1998), pp. 186–194. ISSN: 0950-7116. DOI: 10.1080/09507119809448472.

[69] Hiraoka, K. "Demixing in Argon-Helium Mixed Gas Tungsten Welding Arcs". *11th International Sympo-sium on Plasma Chemistry, Loughborough, England*. Ed. by Harry, J. E. Vol. 1. 1993, pp. 440–445.

[70] Xiao, X., Hua, X., Li, F., and Wu, Y. "A modified Fowler-Milne method for monochromatic image analysis in multi-element arc plasma welding". *Journal of Materials Processing Technology* 214.11 (2014), pp. 2770–2776. ISSN: 0924-0136. DOI: 10.1016/j.jmatprotec.2014.05.026.

[71] Xiao, X., Hua, X., and Wu, Y. "Comparison of temperature and composition measurement by spectroscopic methods for argon-helium arc plasma". *Optics and Laser Technology* 66 (2015), pp. 138–145. ISSN: 0030-3992. DOI: 10.1016/j.optlastec.2014.08.017.

[72] Ma, S., Gao, H., Wu, L., and Zheng, S. "Time and spatially resolved spectroscopic measurement of temperatures in a free-burning arc by monochromatic imaging". *Measurement Science and Technology* 19.10 (2008), p. 105602. URL: http://stacks.iop.org/0957-0233/19/i=10/a=105602.

[73] Zhang, G., Xiong, J., and Hu, Y. "Spectroscopic diagnostics of temperatures for a non-axisymmetric coupling arc by monochromatic imaging". *Measurement Science and Technology* 21.10 (2010), p. 105502. URL: http://stacks.iop.org/0957-0233/21/i=10/a=105502.

[74] Bachmann, B., Kozakov, R., Goett, G., Ekkert, K., Bachmann, J.-P., Marques, J.-L., Schoepp, H., Uhrlandt, D., and Schein, J. "High-speed three-dimensional plasma temperature determination of axially symmetric free-burning arcs". *Journal of Physics D: Applied Physics* 46.12 (2013), p. 125203. URL: http://stacks.iop.org/0022-3727/46/i=12/a=125203.

[75] Mills, G. S. "Use of emission spectroscopy for welding arc analysis". *Welding Research Supplement* 3 (1977), pp. 93–96.

[76] Glickstein, S. S. "Temperature Measurements in a Free Burning Arc". *Welding Research Supplement* 54.8 (1976), p. 222. URL: aws.org/w/a/wj/supplement/WJ_1976_08_s222.pdf.

[77] Pellerin, S., Musiol, K., Pokrzywka, B., and Chapelle, J. "Investigation of a cathode region of an electric arc". *Journal of Physics D: Applied Physics* 27.3 (1994), p. 522. URL: http://stacks.iop.org/0022-3727/27/i=3/a=014.

[78] Razafinimanana, M., Hamidi, L. E., Gleizes, A., and Vacquie, S. "Experimental study of the influence of anode ablation on the characteristics of an argon transferred arc". *Plasma Sources Science and Technology* 4.3 (1995), p. 501. URL: http://stacks.iop.org/0963-0252/4/i=3/a=021.

[79] Akbar, S. and Etemadi, K. "Impact of copper vapor contamination on argon arcs". English. *Plasma Chemistry and Plasma Processing* 17.2 (1997), pp. 251–262. ISSN: 0272-4324. DOI: 10.1007/BF02766818.

[80] Gonzalez, J. J., Bouaziz, M., Razafinimanana, M., and Gleizes, A. "The influence of iron vapour on an argon transferred arc". *Plasma Sources Science and Technology* 6.1 (1997), p. 20. URL: http://stacks.iop.org/0963-0252/6/i=1/a=004.

[81] Key, J., Chan, J. W., and .McIlwa, M. E. "Process variable influence on arc temperature distribution". *Welding Journal* 62 (1983), p. 179.

[82] Hiraoka, K. "Study on Characteristics of Gas Tungsten Arc Shielded by Mixed Gases (Report 2). Evaluation of Local Plasma Composition and Temperature in Mixed Gas Tungsten Arc Plasma Column by Light Spectroscopy." *Quaterly Journal of the Japan Welding Society* 11.1 (1993), pp. 68–74. ISSN: 0288-4771. DOI: 10.2207/qjjws.11.68.

[83] Megy, S., Baronnet, J. .-.-M., and Ershov-Parlov, E. A. "Distribution of plasma parameters in a nitrogen transferred DC arc". *Journal of Physics D: Applied Physics* 28.2 (1995), p. 344. URL: http://stacks.iop.org/0022-3727/28/i=2/a=018.

[84] Etemadi, K. and Pfender, E. "Impact of anode evaporation on the anode region of a high-intensity argon arc". English. *Plasma Chemistry and Plasma Processing* 5.2 (1985), pp. 175–182. ISSN: 0272-4324. DOI: 10.1007/BF00566213.

[85] Wiese, W. L., Kelleher, D. E., and Paquette, D. R. "Detailed Study of the Stark Broadening of Balmer Lines in a High-Density Plasma". *Phys. Rev. A* 6 (1972), pp. 1132–1153. DOI: 10.1103/PhysRevA.6.1132.

[86] Pellerin, S., Musiol, K., Pokrzywka, B., and Chapelle, J. "Stark width of4s-4p Ar I transition (696.543 nm)". *Journal of Physics B: Atomic, Molecular and Optical Physics* 29.17 (1996), p. 3911. URL: http://stacks.iop.org/0953-4075/29/i=17/a=014.

[87] Ton, H. "Physical properties of the plasma-MIG welding arc". *Journal of Physics D: Applied Physics* 8.8 (1975), p. 922. URL: http://stacks.iop.org/0022-3727/8/i=8/a=006.

[88] Valensi, F., Pellerin, S., Boutaghane, A., Dzierzega, K., Zielinska, S., Pellerin, N., and Briand, F. "Plasma diagnostics in gas metal arc welding by optical emission spectroscopy". *Journal of Physics D: Applied Physics* 43.43 (2010), p. 434002. URL: http://stacks.iop.org/0022-3727/43/i=43/a=434002.

[89] Rouffet, M. E., Wendt, M., Goett, G., Kozakov, R., Schoepp, H., Weltmann, K. D., and Uhrlandt, D. "Spectroscopic investigation of the high-current phase of a pulsed GMAW process". *Journal of Physics D: Applied Physics* 43.43 (2010). MSG, p. 434003. URL: http://stacks.iop.org/0022-3727/43/i=43/a=434003.

[90] Goecke, S. F., Metzke, E., Spille-Kohoff, A., and Langula, M. *ChopArc. MSG-Lichtbogenschweißen für den Ultraleichtbau*. Fraunhofer IRB Verlag, 2005. URL: http://www.choparc.de/haupt.html.

[91] Bartels, H. "Eine neue Methode zur Temperaturmessung an hochtemperierten Bogensäulen (Teil 1 und 2)". German. *Zeitschrift für Physik* 127 (1950), pp. 243–273. ISSN: 0044-3328. DOI: 10.1007/BF01338590.

[92] Wilhelm, G., Gött, G., Schöpp, H., and Uhrlandt, D. "Study of the welding gas influence on a controlled short-arc GMAW process by optical emission spectroscopy". *Journal of Physics D: Applied Physics* 43.43 (2010), p. 434004. URL: http://stacks.iop.org/0022-3727/43/i=43/a=434004.

[93] Torres, J., Jonkers, J., van de Sande, M. J., van der Mullen, J. J. A. M., Gamero, A., and Sola, A. "An easy way to determine simultaneously the electron density and temperature in high-pressure plasmas by using Stark broadening". *Journal of Physics D: Applied Physics* 36.13 (2003), p. L55. URL: http://stacks.iop.org/0022-3727/36/i=13/a=101.

[94] Torres, J., van de Sande, M., van der Mullen, J., Gamero, A., and Sola, A. "Stark broadening for simultaneous diagnostics of the electron density and temperature in atmospheric microwave discharges". *Spectrochimica Acta Part B: Atomic Spectroscopy* 61.1 (2006), pp. 58–68. ISSN: 0584-8547. DOI: http://dx.doi.org/10.1016/j.sab.2005.11.002.

[95] Torres, J., Palomares, J. M., Sola, A., van der Mullen, J. J. A. M., and Gamero, A. "A Stark broadening method to determine simultaneously the electron temperature and density in high-pressure microwave plasmas". *Journal of Physics D: Applied Physics* 40.19 (2007), p. 5929. URL: http://stacks.iop.org/0022-3727/40/i=19/a=023.

[96] Zielinska, S., Musiolfl, K., Dzierzega, K., Pellerin, S., Valensi, F., de Izarra, C., and Briand, F. "Investigations of GMAW plasma by optical emission spectroscopy". *Plasma Sources Science and Technology* 16.4 (2007), p. 832. URL: http://stacks.iop.org/0963-0252/16/i=4/a=019.

[97] Zielinska, S., Pellerin, S., Dzierzega, K., Valensi, F., Musiol, K., and Briand, F. "Measurement of atomic Stark parameters of many Mn I and Fe I spectral lines using GMAW process". *Journal of Physics D: Applied Physics* 43.43 (2010), p. 434005. URL: http://stacks.iop.org/0022-3727/43/i=43/a=434005.

[98] Boulos, M. I., Fauchais, P., and Pfender, E. *Thermal Plasmas, Fundamentals and Application*. Vol. 1. Plenum Press, 1994.

[99] Chen, F. F. *Introduction to Plasma Physics and Controlled Fusion*. Vol. 1. Plenum Press, 1974.

[100] Van der Mullen, J. "Exitation in equilibria plasmas". *Physics Reports* 191.2-3 (1990), pp. 109–220. DOI: http://dx.doi.org/10.1016/0370-1573(90)90152-R.

[101] Griem, H. R. *Plasma spectroscopy*. New York: McGraw-Hill, 1964. URL: http://adsabs.harvard.edu//abs/1964plsp.book.....G.

[102] Kunze, H.-J. *Introduction to Plasma Spectroscopy*. Springer Series on Atomic. Dordrecht: Springer, 2009.

[103] Van de Sanden, M. C. M., Schram, P. P. J. M., Peeters, A. G., van der Mullen, J. A. M., and Kroesen, G. M. W. "Thermodynamic generalization of the Saha equation for a two-temperature plasma". *Phys. Rev. A* 40 (1989), pp. 5273–5276. DOI: 10.1103/PhysRevA.40.5273.

[104] Gleizes, A., Gonzalez, J. J., and Freton, P. "Thermal plasma modelling". *Journal of Physics D: Applied Physics* 38.9 (2005), R153. URL: http://stacks.iop.org/0022-3727/38/i=9/a=R01.

[105] Conn, W. M. *Die Technische Physic der Lichtbogenschweissung*. Springer verlag, 1958.

[106] Benilov, M. S., Benilova, L. G., Li, H.-P., and Wu, G.-Q. "Sheath and arc-column voltages in high-pressure arc discharges". *Journal of Physics D: Applied Physics* 45.35 (2012), p. 355201. URL: http://stacks.iop.org/0022-3727/45/i=35/a=355201.

[107] Uhrlandt, D., Baeva, M., Pipa, A., Kozakov, R., and Gött, G. "Cathode fall voltage of TIG arcs from a non-equilibrium arc model". English. *Welding in the World* (2014), pp. 1–9. ISSN: 0043-2288. DOI: 10.1007/s40194-014-0188-x.

[108] Salpeter, E. E. "Electron Density Fluctuations in a Plasma". *Phys. Rev.* 120 (1960), pp. 1528–1535. DOI: 10.1103/PhysRev.120.1528.

[109] Froula, D. H., Glenzer, S. H., Luhmann Jr, N. C., and Sheffield, J. *Plasma Scattering of Electromagnetic Radiation*. 2nd ed. Academic Press, Elsevier, 2011. URL: http://www.sciencedirect.com/science/book/9780123748775.

[110] Landau, L. and Lifshitz, E. *The classical theory of fields*. English. Pergamon Press, 1962.

[111] Jackson, J. D. *Classical Electrodynamics*. de Gruyter, 1983.

[112] Schiff, L. I. *Quantum mechanics*. McGraw-Hill, 1968.

[113] Wertheim, G. K., Butler, M. A., West, K. W., and Buchanan, D. N. E. "Determination of the Gaussian and Lorentzian content of experimental line shapes". *Review of Scientific Instruments* 45.11 (1974), pp. 1369–1371. DOI: http://dx.doi.org/10.1063/1.1686503.

[114] Behringer, K. *Einführunghrung in die Plasmaspektroskopie*. Universität Augsburg. 2000.

[115] Sobelman, I. I., Vainshtein, L., and Yukov, E. A. *Excitation of Atoms and Broadening of Spectral Lines*. Springer, Berlin, Heidelberg, 1995.

[116] Oliveira, C., Souza Corrêa, J. A., Gomes, M. P., Sismanoglu, B. N., and Amorim, J. "Hyperthermal hydrogen atoms in argon-hydrogen atmospheric pressure microplasma jet". *Applied Physics Letters* 93.4, 041503 (2008). DOI: http://dx.doi.org/10.1063/1.2967016.

[117] Qiuping, Z., Cheng, C., and Yuedong, M. "Electron Density and Temperature Measurement by Stark Broadening in a Cold Argon Arc-Plasma Jet at Atmospheric Pressure". *Plasma Science and Technology* 11.5 (2009), p. 560. URL: http://stacks.iop.org/1009-0630/11/i=5/a=09.

[118] Baranger, M. "Simplified Quantum-Mechanical Theory of Pressure Broadening". *Phys. Rev.* 111 (1958), pp. 481–493. DOI: 10.1103/PhysRev.111.481.

[119] Anderson, P. W. "Pressure Broadening in the Microwave and Infra-Red Regions". *Phys. Rev.* 76 (1949), pp. 647–661. DOI: 10.1103/PhysRev.76.647.

[120] Büscher, S. "Untersuchungen Stark-verbreiterter Spektrallininen von Wasserstoff und Helium II". PhD thesis. Ruhr-Universität Bochum, 2000.

[121] Holtsmark, J. "Über die Verbreiterung von Spektrallinien". *Annalen der Physik* 363.7 (1919), pp. 577–630. ISSN: 1521-3889. DOI: 10.1002/andp.19193630702.

[122] Hooper, C. F. "Electric Microfield Distributions in Plasmas". *Phys. Rev.* 149 (1966), pp. 77–91. DOI: 10.1103/PhysRev.149.77.

[123] Hooper, C. F. "Low-Frequency Component Electric Microfield Distributions in Plasmas". *Phys. Rev.* 165 (1968), pp. 215–222. DOI: 10.1103/PhysRev.165.215.

[124] Griem, H. R. "Stark Broadening of Isolated Spectral Lines from Heavy Elements in a Plasma". *Phys. Rev.* 128 (1962), pp. 515–523. DOI: 10.1103/PhysRev.128.515.

[125] Griem, H. R. *Spectral line broadening by plasmas*. Academic Press, New Yourk and London, 1974.

[126] Dimitrijevic, M. S., Christova, M., and Sahal-Brechot, S. "Stark broadening of visible Ar I spectral lines". *Physica Scripta* 75.6 (2007), p. 809. URL: http://stacks.iop.org/1402-4896/75/i=6/a=011.

[127] Dimitrijevic, M. S., Skuljan, L., and Djenie, S. "Stark Broadening of the Ar I Spectral Lines 763.51, 738.39 and 696.54 nm". *Physica Scripta* 66.1 (2002), p. 77. URL: http://stacks.iop.org/1402-4896/66/i=1/a=012.

[128] Sahal-Bréchot, S., Dimitrijevic, M., and N., M. *Stark-B database*. online. Observatory of Paris, LERMA and Astronomical Observatory of Belgrade. 2014. URL: http://stark-b.obspm.fr.

[129] Gigosos, M. A., Gonzalez, M., and Cardenoso, V. "Computer simulated Balmer-alpha, -beta and -gamma Stark line profiles for non-equilibrium plasmas diagnostics". *Spectrochimica Acta Part B: Atomic Spectroscopy* 58.8 (2003). 5th European Furnace Symposium and 10th International Solid Sampling Colloquium with Atomic Spectroscopy, pp. 1489–1504. ISSN: 0584-8547. DOI: http://dx.doi.org/10.1016/S0584-8547(03)00097-1.

[130] Kepple, P. and Griem, H. R. "Improved Stark Profile Calculations for the Hydrogen Lines $H_\alpha$, $H_\beta$, $H_\gamma$, $H_\delta$". *Phys. Rev.* 173 (1968), pp. 317–325. DOI: 10.1103/PhysRev.173.317.

[131] Vidal, C. R., Cooper, J., and Smith, E. W. "Hydrogen Stark-Broadening Tables". *Astrophysical Journal Supplement* 25 (1973), p. 37.

[132] Stehlé, C. and Hutcheon, R. "Extensive tabulations of Stark broadened hydrogen line profiles". *Astron. Astrophys. Suppl. Ser.* 140.1 (1999), pp. 93–97. DOI: 10.1051/aas:1999118.

[133] Konjevic, N., Ivkovic, M., and Sakan, N. "Hydrogen Balmer lines for low electron number density plasma diagnostics". *Spectrochimica Acta Part B: Atomic Spectroscopy* 76 (2012). Honoring Issue: A Collection of Papers on Plasma and Laser Spectrochemistry. Dedicated to Gary M. Hieftje on the occasion of his 70th birthday., pp. 16–26. ISSN: 0584-8547. DOI: http://dx.doi.org/10.1016/j.sab.2012.06.026.

[134] Gigosos, M. A. and Cardenoso, V. "New plasma diagnosis tables of hydrogen Stark broadening including ion dynamics". *Journal of Physics B: Atomic, Molecular and Optical Physics* 29.20 (1996), p. 4795. URL: http://stacks.iop.org/0953-4075/29/i=20/a=029.

[135] Oks, E. *Stark Broadening of Hydrogen And Hydrogenlike Spectral Lines in Plasmas: The Physical Insight*. Alpha Science International Ltd, 2006.

[136] Büscher, S., Wrubel, T., Ferri, S., and Kunze, H.-J. "The Stark width and shift of the hydrogen $H_\alpha$ line". *Journal of Physics B: Atomic, Molecular and Optical Physics* 35.13 (2002), p. 2889. URL: http://stacks.iop.org/0953-4075/35/i=13/a=304.

[137] *Athomic spectral database*. NIST.

[138] Olsen, H. "The electric arc as a light source for quantitative spectroscopy". *Journal of Quantitative Spectroscopy and Radiative Transfer* 3.4 (1963), pp. 305–333. ISSN: 0022-4073. DOI: 10.1016/0022-4073(63)90015-3.

[139] Lochte-Holtgreven, W., Richter, J., G., T., and Zwicker, H. *Plasma Diagnostics*. North-Holland Publishing Company, Amsterdam, 1968.

[140] Evans, D. E. and Katzenstein, J. "Laser light scattering in laboratory plasmas". *Reports on Progress in Physics* 32.1 (1969), p. 207. URL: http://stacks.iop.org/0034-4885/32/i=1/a=305.

[141] Pedrotti, F., Pedrotti, L., Bausch, W., and Schmidt, H. *Optik für Ingenieure*. Berlin-Heidelberg: Springer-Verlag, 2005. URL: http://www.springer.com/engineering/electronics/book/978-3-540-73471-0.

[142] Karzas, W. J. and Latter, R. "Electron Radiative Transitions in a Coulomb Field." *The Astrophysical Journal Supplement Series* 6 (1961), p. 167. DOI: 10.1086/190063.

[143] Wall, M. E., Rechtsteiner, A., and Rocha, L. M. "Singular Value Decomposition and Principal Component Analysis". English. *A Practical Approach to Microarray Data Analysis*. Ed. by Berrar, D., Dubitzky, W., and Granzow, M. Springer US, 2003, pp. 91–109. ISBN: 9781402072604. DOI: 10.1007/0-306-47815-3_5.

[144] *Manual ARYELLE - Spectrograph Series*. 7.3.0. Lasertechnik Berlin. Am Studio 2c D-12489 Berlin, 2013. URL: http://www.ltb-berlin.de/Aufbau-Funktionsweise.101.0.html?&L=0.

[145] Murphy, A. B. "Demixing in free-burning arcs". *Phys. Rev. E* 55 (1997), pp. 7473–7494. DOI: 10.1103/PhysRevE.55.7473.

[146] Murphy, A. B. "Electron Heating in the Measurement of Electron Temperature by Thomson Scattering: Are Thermal Plasmas Thermal?" *Phys. Rev. Lett.* 89 (2002), p. 025002. DOI: 10.1103/PhysRevLett.89.025002.

[147] Traidia, A., Roger, F., Chidley, A., Schroeder, J., and Marlaud, T. "Effect of Helium-Argon Mixtures on the Heat Transfer and Fluid Flow in Gas Tungsten Arc Welding". *World Academy of Science, Engineering and Technology* 5.1 (2011), pp. 896–901. ISSN: 1307-6892. URL: http://waset.org/Publications?p=49.

[148] Murphy, A. B., Tanaka, M., Yamamoto, K., Tashiro, S., Sato, T., and Lowke, J. J. "Modelling of thermal plasmas for arc welding: the role of the shielding gas properties and of metal vapour". *Journal of Physics D: Applied Physics* 42.19 (2009), p. 194006. URL: http://stacks.iop.org/0022-3727/42/i=19/a=194006.

[149] Murphy, A. B. "Influence of metal vapour on arc temperatures in gas metal arc welding: convection versus radiation". *Journal of Physics D: Applied Physics* 46.22 (2013), p. 224004. URL: http://stacks.iop.org/0022-3727/46/i=22/a=224004.

[150] Murphy, A. B. and Hiraoka, K. "A comparison of measurements and calculations of demixing in free-burning arcs". *J. Phys. D: Appl. Phys.* 33.17 (2000), pp. 2183–2188. ISSN: 1361-6463. DOI: 10.1088/0022-3727/33/17/313.

[151] Miles, R. B., Yalin, A. P., Tang, Z., Zaidi, S. H., and Forkey, J. N. "Flow field imaging through sharp-edged atomic and molecular 'notch' filters". *Measurement Science and Technology* 12.4 (2001), pp. 442–451. ISSN: 1361-6501. DOI: 10.1088/0957-0233/12/4/308.

[152] Bakker, L. P., Freriks, J. M., de Hoog, F. J., and Kroesen, G. M. W. "Thomson scattering using an atomic notch filter". *Review of Scientific Instruments* 71.5 (2000), p. 2007. ISSN: 0034-6748. DOI: 10.1063/1.1150569.

[153] Van de Sande, M. "Laser scattering on low temperature plasmas". PhD thesis. Technische Universiteit Eindhoven, 2002. URL: http://repository.tue.nl/554040.